



# Nuclear Fusion of Advanced Fuels Using Converging Focused Ion Beams

Brian James Egle

December 2010

UWFDM-1406

Ph.D. thesis.

**FUSION TECHNOLOGY INSTITUTE  
UNIVERSITY OF WISCONSIN  
MADISON WISCONSIN**

# **Nuclear Fusion of Advanced Fuels Using Converging Focused Ion Beams**

Brian James Egle

Fusion Technology Institute  
University of Wisconsin  
1500 Engineering Drive  
Madison, WI 53706

<http://fti.neep.wisc.edu>

December 2010

UWFDM-1406

Ph.D. thesis.

# **Nuclear Fusion of Advanced Fuels Using Converging Focused Ion Beams**

by

Brian James Egle

A dissertation submitted in partial fulfillment of  
the requirements for the degree of

Doctor of Philosophy

Nuclear Engineering and Engineering Physics

at the

University of Wisconsin – Madison

2010



## Abstract

The Six Ion Gun Fusion Experiment (SIGFE) was designed and built to investigate a possible avenue to increase the reaction rate efficiency of the D-D and D-<sup>3</sup>He nuclear fusion reactions in Inertial Electrostatic Confinement (IEC) devices to the levels required for several non-electric applications of nuclear fusion. The SIGFE is based on the seminal IEC experiment published by Hirsch in 1967, and is the first experiment to recreate the results and unique features of the Hirsch device.

The SIGFE used six identical ion beams to focus and converge deuterium and helium-3 ions into a sphere of less than 2 mm at nearly mono-energetic ion energies up to 150 keV. With improved ion optics and diagnostics, the SIGFE concluded that within the investigated parameter space, the region where the ion beams converged accounted for less than 0.2% of the total D-D fusion reactions. The maximum D-D fusion rates were observed when the ion beams were intentionally defocused to strike the inside surface of the cathode lenses. In this defocused state, the total D-D fusion rate increased when the chamber pressure was decreased. The maximum D-D fusion rate was  $4.3 \times 10^7$  neutrons per second at a cathode voltage of -130 kV, a total cathode current of 10 mA, and a chamber pressure of 27 mPa.

The D and <sup>3</sup>He ion beams were produced in six self-contained ion gun modules. The modules were each capable of at least 4 mA of ion current while maintaining a main chamber pressure as low as 13 mPa. The theoretically calculated extractable ion current agreed with the experiment within a factor of 2.

A concept was also developed and evaluated for the production of radioisotopes from the 14.7 MeV D-<sup>3</sup>He fusion protons produced in an IEC device. Monte Carlo simulations of this concept determined that a D-<sup>3</sup>He fusion rate on the order of  $10^{11} \text{ s}^{-1}$  would be required for an IEC device to produce 1 mCi of the <sup>11</sup>C radioisotope.

## Acknowledgements

During the course of my PhD and time at the University of Wisconsin – Madison, there have been numerous people that I am forever grateful to. This has been a wonderful experience that has shaped me both professionally and personally.

First and foremost are my amazing parents and family. They have loved and supported me in all of my crazy adventures. It is much easier to take risks when I know there is a strong safety net waiting to catch me.

I would like to express my deepest thanks to my advisor Gerald Kulcinski and to John Santarius for their patience in shaping me as a scientist. This dissertation would not have been possible without hard work, dedication and humor of the whole IEC team. I would like to express special thanks to Matt Michalak for all of his help building the SIGFE. The students of the IEC team that I have had the pleasure to work with include Greg Piefer, Ross Radel, Dave Boris, Eric Alderson, Sam Zenobia, David Donovan, Gabriel Becerra, Craig Schuff, Lauren Garrison, Logan Campbell, Carlos Paz-Soldan and John Sorebo. I would like to thank the IEC lab managers, Bob Ashley and Richard Bonomo, and the other members of the IEC team, Joan Welc-Lepain and Dennis Bruggink.

I would like to thank David Grainger and the Grainger Foundation for their generous financial support that made this experiment possible. Our future is brighter because of your selfless investment into the education of so many students past and present.

I would also like to thank Robert Hirsch for his insight and discussions about this work.

Finally, graduate school was such an enjoyable experience only because of good friends to celebrate successes, to help recover from setbacks, and to play volleyball with.

## Table of contents

<b>Abstract .....</b>	<b>i</b>
<b>Acknowledgements .....</b>	<b>ii</b>
<b>Table of contents .....</b>	<b>iii</b>
<b>Table of figures.....</b>	<b>v</b>
<b>Table of tables.....</b>	<b>xiv</b>
<b>Chapter 1. Introduction .....</b>	<b>1</b>
<b>Chapter 2. Past contributions to IEC research and the production of isotopes in IEC devices .....</b>	<b>7</b>
2.1. Review of past experiments in Inertial Electrostatic Confinement (IEC) .....	8
<i>2.1.1. Measurement of fusion reaction regimes .....</i>	<i>15</i>
<i>2.1.2. Measurements and experimental evidence of virtual electrode formation.....</i>	<i>19</i>
2.2. Past theoretical contributions to IEC operation and virtual electrode formation .....	22
2.3. Previous experiments for the production of radioisotopes in IEC devices .....	31
2.4. References for Chapter 2.....	35
<b>Chapter 3. Ion extraction and ion gun theory .....</b>	<b>39</b>
<b>Chapter 4. Six Ion Gun Fusion Experiment (SIGFE) design and construction.....</b>	<b>47</b>
4.1. Ion gun module design and construction .....	49
<i>4.1.1. Plasma source and extraction .....</i>	<i>50</i>
<i>4.1.2. Electrostatic optics design and ion trajectory simulations.....</i>	<i>55</i>
<i>4.1.3. Assembly and alignment techniques .....</i>	<i>60</i>
<i>4.1.4. Electrode and insulator design and fabrication .....</i>	<i>63</i>
<i>4.1.5. Prototype ion gun .....</i>	<i>66</i>
4.2. SIGFE infrastructure.....	72
<i>4.2.1. Ion gun mounting and alignment .....</i>	<i>73</i>
<i>4.2.2. 200 kV high-voltage feed-through .....</i>	<i>77</i>
<i>4.2.3. Boron nitride 200 kV insulator design .....</i>	<i>81</i>
<i>4.2.4. Cathode design for electron trapping .....</i>	<i>87</i>
<i>4.2.5. Power supplies .....</i>	<i>90</i>
<i>4.2.6. Computerized control, monitoring and data logging.....</i>	<i>94</i>
<i>4.2.7. Vacuum system .....</i>	<i>98</i>
4.3. Diagnostics .....	104
<i>4.3.1. Neutron detection .....</i>	<i>104</i>
<i>4.3.2. Fusion ion Doppler shift (FIDO) diagnostic.....</i>	<i>108</i>
<i>4.3.3. One-axis movable collimated proton detector.....</i>	<i>114</i>
<i>4.3.4. Proton detector for D-<sup>3</sup>He fusion reactions.....</i>	<i>121</i>

4.3.5. Optical cameras .....	126
4.4. References for Chapter 4 .....	129
<b>Chapter 5. Extractable ion current from the ion source and extraction system.....</b>	<b>131</b>
5.1. Results of plasma parameter study of the ion source .....	131
5.2. Extractable ion current.....	136
5.3. Discussion of plasma parameters and extractable ion current .....	138
<b>Chapter 6. Six Ion Gun Fusion Experiment results and discussion .....</b>	<b>142</b>
6.1. D-D fusion results.....	144
6.1.1. <i>Energy spectrum of D-D fusion protons.</i> .....	155
6.2. D- <sup>3</sup> He fusion results.....	162
6.3. Discussion of SIGFE results .....	168
6.3.1. <i>Implications for the existence of potential well structures in the SIGFE device.....</i>	168
6.3.2. <i>Comments on the D-<sup>3</sup>He fusion rate .....</i>	177
6.3.3. <i>Scaling of D-D neutron rate with pressure and ion beam focus.....</i>	178
6.3.4. <i>Comparison of the SIGFE to the Hirsch experiment .....</i>	180
6.4. References for Chapter 6 .....	185
<b>Chapter 7. Design and simulation for the production of radioisotopes in from a D-<sup>3</sup>He fusion device.....</b>	<b>187</b>
7.1. Radioisotope activity, cross-sections, and gas target design considerations .....	187
7.2. Gas target design .....	189
7.3. Monte Carlo simulations .....	191
7.3.1. <i>Model geometry, materials, and parameters.....</i>	191
7.3.2. <i>Results of the baseline (4 atm, 0.5 mm) design.....</i>	192
7.3.3. <i>Results of a pressure scan of the target gas pressure .....</i>	193
7.3.4. <i>Results of titanium foil thickness scan.....</i>	195
7.3.5. <i>Results of the optimized case (10 atm, 0.3 mm).....</i>	196
7.4. Finite element analysis of mechanical strength and prototype testing .....	196
7.5. Conclusions for the production of PET Radioisotopes in an IEC fusion device ....	198
7.6. References for Chapter 7 .....	199
<b>Chapter 8. Conclusions .....</b>	<b>200</b>
<b>Chapter 9. Recommendation for future work.....</b>	<b>204</b>

## Table of figures

Figure 2-1: Nuclear fusion cross-sections as a function of center-of-mass energy for D-T, D-D, D- <sup>3</sup> He, and <sup>3</sup> He- <sup>3</sup> He reactions.....	8
Figure 2-2: a) Neutron production rates in the Hirsch experiment as a function of voltage and gas pressure of D <sub>2</sub> gas or D-T gas mixture at 10 mA of ion current. Adapted from Figure 11 of Hirsch-1967. b) Neutron production rate as function of pressure at 100 kV for Hirsch and UW-IEC, note difference in total experimental current. (1 micron = 1 mTorr = 0.13 Pa).....	9
Figure 2-3: Results of collimated neutron and x-ray measurements scaled from the original paper. The results are overlaid on a sketch of the experiment device to provide scale. ....	10
Figure 2-4: Comparison of steady-state D-D fusion neutron rates per kilowatt of high voltage power (meter current times cathode voltage) for various IEC experiments listed by author and year reported.....	11
Figure 2-5: Scale drawing of the Hirsch ion gun and cathode with details of the electrostatic lenses. Drawing created by this author by directly scaling the figures published by Hirsch and Meeks-1967. ....	13
Figure 2-6: Scale drawing of the Hirsch device. The anode diameter was 178 mm and the Cathode diameter was 114 mm. Drawing created by this author by directly scaling the figures published by Hirsch and Meeks-1967. ....	14
Figure 2-7: Sketch of UW IEC experiment, HOMER. It is shown with a 50 cm wire gridded anode, and a 10 cm wire gridded cathode. The chamber is cylindrical with a diameter of 95 cm and a height of 65 cm. Figure adapted from Figure 3-1 of Cipiti 2004. ....	15
Figure 2-8: Comparison of gridded wire cathode to solid metal cathodes in D gas. Adapted from Figure 6-7 of Cipiti-2004.....	17
Figure 2-9: Comparison of W solid cathode versus gridded W-Re wire gridded cathode in D- <sup>3</sup> He gas mixture. Adapted from Figure 6-9 of Cipiti-2004. ....	17
Figure 2-10: Percentage of fusion protons blocked by eclipse disks for D-D reactions and D- <sup>3</sup> He reactions. Figure taken from Figure 6-11 of Cipiti-2004 .....	18
Figure 2-11: Spatially resolved electron density on the interior of the cylindrical device as determined with a laser heterodyne system. Figure taken from Figure 9 of Verdeyen-1975.....	21
Figure 2-12: A) Shallow potential well profile used in the computational model to determine ion energy spectrum. This profile shape is similar to the experimentally measured potential profile. Figure taken directly from Figure 1 of Black-1974 .....	24

Figure 2-13: Ion energy spectrum predicted by the computation code at infinite vacuum, 0.12 Pa, and 0.68 Pa of background pressure. This figure was taken from Figure 3 of Black-1974 .....	25
Figure 2-14: Normalized depth of the potential well inside the cathode with an applied potential of -5.5 kV and a grid transparency of 85%. Chart A shows the predicted well depth as a function of the deviation of the cathode shape from a true sphere at various ion currents, and at a gas pressure of 0.12 Pa. Chart B shows the well depth as a function of gas pressure for two different amounts of deviation in cathode shape, and at an ion current of 10 mA. These figures were taken directly from figure 4 and 6 of Black-1974. (1 mTorr = 0.13 Pa) .....	26
Figure 2-15: Simulated neutron production rate as a function of ion current for two different values of radial ion energy spread, a) 5 keV and b) 10 keV. These figures were taken directly from figure 9 of Ohnishi.....	28
Figure 2-16: Calculated neutron production rate as a function of pressure, including ionization and charge exchange in the accelerating region. Figure and caption taken directly from figure 3 of Baxter-1982 (1 micron = 1 mTorr = 0.13 Pa).....	30
Figure 2-17: Picture of radiator device for producing radioisotopes in an IEC device. Figure taken from Figure 3.11 of Weidner-2003. ....	33
Figure 2-18: Picture of thin walled, water filled, stainless steel tube acting as the cathode for the production of $^{13}\text{N}$ . Figure taken from Figure 10-7 of Cipiti 2004. ....	34
Figure 3-1: Schematic of ion extraction test setup with simulated ion trajectories .....	39
Figure 3-2: Graph of $\alpha^2$ values from table 2.1 of Forrester. ....	42
Figure 3-3: Sample result of SIMION <sup>®</sup> simulations to determine the starting locations of ions that could be accelerated and focused through the orifice in the extraction electrode	45
Figure 4-1: Comparison of the CAD models of the Hirsch device (A) to the final SIGFE design (B) .....	48
Figure 4-2: Pictorial timeline of the SIGFE development.....	48
Figure 4-3: Cross-section drawing of ion gun module. Major components highlighted with operating voltages and pressures listed where appropriate.....	49
Figure 4-4: Photo of an ion gun module. White paper square is for scale and is 25 x 25 mm (1 x 1 inch). Boron nitride spacer replaced with quartz spacer to show extraction electrode.....	50
Figure 4-5: Photo of internal components of plasma source, including the tungsten filament and Langmuir probe.....	52
Figure 4-6: Original drawings of the Hirsch device, reproduced from Hirsch (1967).....	56

Figure 4-7: Comparison of simulated ion optics between A) the Hirsch device with spacer added to adjust focal length and B) the SIGFE device with the focus lens set to 7.2 kV. Both cathode voltages set to 150 kV.....	57
Figure 4-8: Graph of ion trajectory simulation results showing the relative number of particles that were predicted to strike the different lens surfaces defined in Table 4-1. ....	60
Figure 4-9: Ion gun module alignment details. A) Cross-section view of the full module showing boron nitride mounting rods, alignment rod and jigs, B) cross-section view of cathode lens highlighting mounting rod attachment, C) view of 1 of 5 optic mounts with lens alignment set screws shown, and D) view of magnet mount .....	62
Figure 4-10: Picture of the prototype ion gun.....	67
Figure 4-11: Pictures of the prototype ion gun in operation. A) View of the quartz target placed at future center of SIGFE device. B) View from below the ion gun. ....	69
Figure 4-12: Typical result from a voltage scan of the collector voltage for a fixed extraction voltage.....	70
Figure 4-13: A) Schematic of materials test setup. The quartz target seen in Figure 4-11A was replaced with a test sample. B) Micrograph of the unirradiated W-needle to be tested. C) Micrograph of the W-needle after a fluence of $1.3 \times 10^{19}$ He <sup>+</sup> ions per cm <sup>2</sup> . Pictures courtesy of Sam Zenobia. ....	71
Figure 4-14: Photo of the internal components of the Six Ion Gun Fusion Experiment. All six ion gun modules are shown in their adjustable mounts attached to the super structure.....	72
Figure 4-15: Photo of external SIGFE infrastructure.....	73
Figure 4-16: Details of the ion gun module mounting and adjustment hardware. Yellow straight arrows denote adjustment by adding or removing shims. Red curved arrows denote set screw adjust around the pivot points. ....	74
Figure 4-17: Photo illustrating the technique used to align the ion gun modules. Note that the location of each alignment rods was constrained by the extraction aperture and the cathode lens. ....	76
Figure 4-18: Photo of the alignment rods to show the level of accuracy the modules were aligned to. The rods are precision ground to $1.829 \pm 0.008$ mm ( $0.072 \pm 0.0003$ inch). ....	76
Figure 4-19: Photo of ion beams of all six ion gun modules converging at the center of the SIGFE device. The width of the beams just before the center is estimated at 1.6 mm. ....	77
Figure 4-20: Details of the isolated nut high voltage feed-through design .....	79

Figure 4-21: Cross-section views of the high-voltage feed though for A) HOMER and B) SIGFE .....	79
Figure 4-22: Simulated electric field strength for an applied voltage of -1000 kV for A) HOMER and B) SIGFE. The areas shown in red are above the dielectric strength of boron nitride at $6.69 \times 10^7$ V/m. The SIGFE design showed a factor of 2.2 improvement in the maximum magnitude of the electric field .....	80
Figure 4-23: Infinitely long cylindrical geometry used for the analytic calculations of the electric field inside the high voltage stalk.....	82
Figure 4-24: Radial electric field for an applied voltage of 300 kV and dimensions of $r_1=2.4$ mm, $r_3=12.7$ mm, and $r_4=13$ mm. The size of the vacuum gap between the inner electrode and the inside diameter of the dielectric ( $gap=r_2-r_1$ ) was varied.....	84
Figure 4-25: Maximum electric fields in the dielectric and vacuum gap as a function of the inner radius of the dielectric for an applied voltage of 300 kV, and dimensions of $r_1=2.4$ mm, $r_3=12.7$ mm, and $r_4=13$ mm. ....	85
Figure 4-26: Sketch of the new high voltage stalk design.....	86
Figure 4-27: Photo of the 110 mm diameter spherical cathode region form by the final electrostatic lenses of the ion gun modules. One of the modules was removed for viewing.....	88
Figure 4-28: A) Photo of the electron shields installed. An 8 $\mu\text{m}$ Al foil is shown at the corner of the lenses to allow fusion protons to reach the detectors, and a quartz window was installed for optical viewing inside the cathode. B) Illustration of the fit of the shields, note the gap between the shield and the lens. C) Photo of the electron shield. The ends of the shields were formed to hold the various styles of corner shields .....	90
Figure 4-29: Schematic of vacuum system for vacuum conductance calculations.....	100
Figure 4-30: Layout of UW-IEC's hot cell. The location of the two neutron detectors is shown in relation to the SIGFE experiment.....	105
Figure 4-31: Schematic of electronics used for both the main and secondary neutron detector setups.....	107
Figure 4-32: Cross-section view of the Fusion Ion Doppler Shift (FIDO) diagnostic installed on SIGFE. The cone-of-view of the system is highlighted. The distance from the detector face to the device center was 825 mm. An 8 $\mu\text{m}$ Al foil was placed between the device center and the detector.....	110
Figure 4-33: Predicted fusion proton spectrum for 125 keV $D_1^+$ , $D_2^+$ , and $D_3^+$ ions after passing through 8 $\mu\text{m}$ of Al foil. Energy loss through foil was simulated in SRIM. [27] The height of the predicted peaks were adjust to match experimental data.	

Experimental data set shown was taken at a cathode voltage of 125 kV and 40 mPa (300 $\mu$ Torr).....	112
Figure 4-34: Schematic of collimated detector system .....	114
Figure 4-35: Probability of a proton striking the detector from a distance $b$ from the axis of collimation and on a plane perpendicular to that axis and that intersected the origin of the SIGFE device. All of the cases in Table 4-7 are plotted. Note that the distance between aperture 1 and the origin remained fixed while aperture 2 was moved in the various cases.....	117
Figure 4-36: Cut-away view of the movable collimated detector system installed on the SIGFE. The inside diameter of the cathode was 110 mm, and the gaps between the cathode lenses were 8 mm.....	118
Figure 4-37: Cross-section view of the collimated detector head assembly. ....	118
Figure 4-38: Schematic of the collimated proton detector electronics.....	121
Figure 4-39: Diagram of wide-view D- $^3$ He proton detector setup. The 1200 $\text{mm}^2 \times 700 \mu\text{m}$ thick Si based detector had 360 $\mu\text{m}$ of Pd and 8 $\mu\text{m}$ of Al between it and the center of the device, which was 543 mm away. ....	123
Figure 4-40: Predicted energy spectrum deposited in a 700 $\mu\text{m}$ thick Si detector after 8 $\mu\text{m}$ of Al and 360 $\mu\text{m}$ of Pb for 14.7 MeV $^3\text{He}(d, p)^4\text{He}$ fusion protons resulting from 130 keV ions fusing with stationary targets. All four combinations of $^3\text{He}^+$ , $D_1^+$ , $D_2^+$ , and $D_3^+$ ions on $^3\text{He}$ and D targets are plotted .....	125
Figure 4-41: A) Diagram of video camera setup showing the mirrors used to direct the camera view through quartz window at the bottom of the cathode electrode. B) Photo of typical view from camera 1.....	128
Figure 4-42: Still photo taken from camera 2. Light emitted from the heated extraction lenses was visible along with DC plasma discharges along the insulating spacers. .	128
Figure 5-1: Contour plot of the plasma density versus filament voltage drop and gas flow. The red dot on the plot represents an experimental data point. (10 uncalibrated sccm = 0.9 sccm) .....	133
Figure 5-2: Contour plot of the plasma density versus filament voltage drop and filament bias voltage. The red dot on the plot represents an experimental data point. ....	134
Figure 5-3: Contour plot of the plasma electron temperature versus filament voltage drop and filament bias voltage.....	135
Figure 5-4: Contour plot of the plasma potential versus filament voltage drop and gas flow. (10 uncalibrated sccm = 0.9 sccm) .....	135
Figure 5-5: Schematic of the ion extraction test setup with simulated ion trajectories .....	136

Figure 5-6: Extracted ion current and the total current on the extraction lens plotted versus the voltage across the filament. Relationship between the filament voltage and the plasma density was described in section 4.1.....	137
Figure 5-7: Extracted ion current for three extraction lens voltages versus the filament voltage.....	137
Figure 5-8: Maximum extracted ion current and corresponding plasma density at various extraction electrode voltages.....	138
Figure 5-9: Comparison of the experimental current extracted from the plasma and the theoretical current calculated by Eqn 3-13.....	140
Figure 6-1: Parameter space of the Six Ion Gun Fusion Experiment.....	144
Figure 6-2: D-D neutron production rate in the SIGFE versus cathode voltage at different focus lens voltages.....	146
Figure 6-3: D-D neutron production rate from the SIGFE versus pressure at 3 different focus lens voltages. ....	147
Figure 6-4: Result of a focus lens voltage scan showing the neutron rate and total cathode current. The cathode voltage was -100 kV, chamber pressure was 80 mPa, and the extraction voltage was -8 kV. The extraction and ion source input parameters were constant. The total cathode current was the sum of the ion to and secondary electron current from the cathode. ....	148
Figure 6-5: Contour plot showing lines of equal neutron rate for combinations of different voltages applied to the focus and extraction lenses. Contours are the result of a Design of Experiment that was setup and analyzed in the statistical software package Design-Expert® .....	149
Figure 6-6: Plot of neutron rate versus focus voltage. The plasma source parameters were adjusted to provide a total cathode current of 10 mA for each data point. The experimental data and fit curve are a subset of the data shown in Figure 6-5 at an extraction voltage of 10 kV.....	150
Figure 6-7: Single ion gun operation compared to full six ion gun operation as a function of focus.....	151
Figure 6-8: D-D neutron production rate versus total cathode current at two focus lens voltages. Data was taken at a cathode voltage of -100 kV and a chamber pressure of 27 mPa. The total cathode current was the sum of the ion current to and secondary electron from the cathode.....	152
Figure 6-9: D-D neutron production rate versus total cathode current at two chamber pressures. Data was taken at a cathode voltage of -100 kV and a focus lens voltage of 100%. The total cathode current was the sum of the ion current to and secondary electron current from the cathode.....	152

Figure 6-10: Time dependence of the neutron rate.....	153
Figure 6-11: Effects of lens alignment on neutron rate. Misalignment of the extraction lenses was on the order of 1 mm.....	154
Figure 6-12: Comparison the neutron rate performance before and after the installation of the electron shields at the seams of the cathode.....	155
Figure 6-13: Cross-section of fusion ion Doppler shift diagnostic (FIDO) installed on SIGFE. The cone-of-view of the system is highlighted in green. The distance from the detector face to the device center is 825 mm. An 8 $\mu\text{m}$ Al foil was between the device center and the detector.....	156
Figure 6-14: Energy spectrum for 3.02 MeV D-D fusion protons deposited in a 500 $\mu\text{m}$ thick Si detector after an 8 $\mu\text{m}$ thick Al foil. Data was obtained with the FIDO diagnostic at a cathode voltage of -125 kV and count time of 2000 seconds.....	158
Figure 6-15: Predicted energy deposited in a detector by D-D fusion protons after a Doppler shift from 125 keV $\text{D}_1^+$ , $\text{D}_2^+$ , and $\text{D}_3^+$ ions and after 8 $\mu\text{m}$ thick Al foil. Initial ion energies after Doppler shift used in SRIM simulations are shown in Table 4-6. The peak heights of the various ions are adjusted for clarity to match experimental peak heights in Figure 6-14.....	158
Figure 6-16: Comparison of the energy spectra of D-D protons collected by the FIDO diagnostic at three different cathode voltages. An 8 $\mu\text{m}$ Al foil was between the cathode region and the detector.....	159
Figure 6-17: Predicted energy deposited by $\text{D}_2^+$ ions into a 500 $\mu\text{m}$ thick Si detector after an 8 $\mu\text{m}$ thick Al foil. Initial ion energies after Doppler shift used in SRIM simulations are shown in Table 4-6. The peak heights of the various energy ions adjusted for clarity to match experimental peak heights in Figure 6-16.....	159
Figure 6-18: Comparison of the energy spectrum of the 3.02 MeV D-D protons collected by the FIDO diagnostic at three different chamber pressures. An 8 $\mu\text{m}$ Al foil was between the cathode region and the detector.....	160
Figure 6-19: Calibrated D-D proton rate from the cone-of-view defined in Figure 6-13, which included the center of the cathode, compared to the total calibrated neutron rate at focus voltages of 3.0 keV (65% focus) and 5.8 keV (125% focus). .....	161
Figure 6-20: Calibrated D-D proton rate from the cone-of-view defined in Figure 6-13, which included the center of the cathode, compared to the total calibrated neutron rate for three different chamber pressures.....	162
Figure 6-21: Energy spectrum for 14.7 MeV $\text{D}-{}^3\text{He}$ fusion protons deposited in a 700 $\mu\text{m}$ thick Si detector after 8 $\mu\text{m}$ Al foil and 650 $\mu\text{m}$ Pb foil.....	164
Figure 6-22: Predicted energy spectrum deposited in a 700 $\mu\text{m}$ thick Si detector after 8 $\mu\text{m}$ of Al and 360 $\mu\text{m}$ of Pb for 14.7 MeV ${}^3\text{He}(\text{d}, \text{p}){}^4\text{He}$ protons resulting from 130 keV ions	

fusing with stationary targets. All four combinations of ${}^3\text{He}^+$ , $\text{D}_1^+$ , $\text{D}_2^+$ , and $\text{D}_3^+$ ions on ${}^3\text{He}$ and D targets are plotted.....	164
Figure 6-23: Comparison of the energy spectra of D- ${}^3\text{He}$ fusion protons at three cathode voltages. 8 $\mu\text{m}$ of Al foil and 360 $\mu\text{m}$ of Pb foil were between the center of the cathode and the detector.....	165
Figure 6-24: Calibrated D- ${}^3\text{He}$ fusion proton rate from the cone-of-view defined in Figure 4-39, which included the center of the cathode, compared to the total calibrated D-D neutron rate for the three cathode voltages. ....	166
Figure 6-25: Comparison of the energy spectra of the 14.7 MeV D- ${}^3\text{He}$ fusion protons at three chamber pressures with a 1:1 mixture of D and ${}^3\text{He}$ gas. 8 $\mu\text{m}$ of Al foil and 360 $\mu\text{m}$ of Pb foil were between the center of the cathode and the detector. ....	167
Figure 6-26: Calibrated D- ${}^3\text{He}$ fusion proton rate from the cone-of-view defined in Figure 4-39, which included the center of the cathode, compared to the total calibrated D-D neutron rate for the three chamber pressures. ....	167
Figure 6-27: Experimental and predicted fusion proton spectrum of D-D fusion protons Doppler shifted by 125 keV $\text{D}_1$ , $\text{D}_2$ , and $\text{D}_3$ ions after passing through 8 $\mu\text{m}$ of Al foil. Energy loss through foil was simulated in SRIM. The height of the predicted peaks were adjusted to match experimental data. Experimental data set shown was taken at a cathode voltage of 125 kV and 40 mPa (300 $\mu\text{Torr}$ ). ....	169
Figure 6-28: Estimated upper bound of the percentage of the total D-D fusion reactions that originated from reactions between the primary ion beams and the background gas in the main vacuum chamber.....	171
Figure 6-29: Comparison of experimental D-D neutron production rates at cathode voltages of -90 kV and -100 kV to the number of particles that strike all areas of the cathode lenses as predicted by the ion trajectory simulations.....	174
Figure 6-30: Graph of ion trajectory simulation results showing the relative number of particles that were predicted to strike the different lens surfaces defined in Table 4-1. ....	175
Figure 6-31: Experimental D-D neutron production rate versus cathode voltage at various pressures for comparison of the SIGFE, the Hirsch device, and the UW gridded IEC device. All data was taken at a total cathode current (including ion and electron current) of 10 mA. ....	180
Figure 6-32: Normalized D-D neutron production and D-D fusion cross-sections for comparison of voltage scaling. Values normalized to 1 at a cathode voltage of -50 kV or a lab frame ion energy of 50 keV. The SIGFE data was taken at 70% focus. [3, 7] .....	181
Figure 6-33: Comparison of D-D neutron production rate versus pressures for the SIGFE, the Hirsch device, and the UW gridded IEC device. The UW gridded data was linearly	

scaled down to 10 mA from 30 mA of total cathode current. The Hirsch data was interpolated to 100 kV from the data shown in Figure 6-31.....	182
Figure 6-34: Comparison of D-D fusion neutron rates per kilowatt of high voltage power (meter current times cathode voltage) for various IEC experiments listed by author and year reported. *SIGFE-2009 is the result of this dissertation.....	184
Figure 7-1: Summary of the multi-stage process for the production of $^{11}\text{C}$ using the D- $^3\text{He}$ fusion reaction .....	188
Figure 7-2: Cross-section of the $^{14}\text{N}(\text{p}, \alpha)^{11}\text{C}$ reaction.....	188
Figure 7-3: A) Cutaway view of the $^3\text{HeCTRE}$ IEC device with gas targets installed. B) Cross-section view of the IEC from the top. C) Cutaway view of the gas target .....	190
Figure 7-4: Simplified geometry for simulations showing tally locations .....	192
Figure 7-5: Comparison of proton spectrum entering the gas (after Ti foil) and exiting the gas (after Ti and gas) for 0.5 mm Ti foil and 4 atm of pure $^{14}\text{N}$ gas with the $^{14}\text{N}(\text{p}, \alpha)^{11}\text{C}$ cross-section. ....	193
Figure 7-6: Multiplication factor, M, asymptotes above 10 atm. The Ti foil thickness held constant at 0.5 mm and target depth held at 77.5 mm. ....	194
Figure 7-7: Comparison of peak energy entering (after Ti foil) and exiting gas cell (after foil and gas) as a function of gas pressure with the cross-section of the $^{14}\text{N}(\text{p}, \alpha)^{11}\text{C}$ reaction. Ti foil thickness held constant at 0.5 mm and target depth held at 77.5 mm. ....	194
Figure 7-8: Multiplication factor, M, is reduced by increasing the Ti foil thickness. The gas pressure and cell depth held constant at 4 atm and 77.5 mm. ....	195
Figure 7-9: Comparison of peak proton energy entering (after Ti foil) and existing the gas (after Ti foil and gas) as a function of foil thickness with the cross-section of the $^{14}\text{N}(\text{p}, \alpha)^{11}\text{C}$ reaction. Gas pressure and cell depth held constant at 4 atm and 77.5 mm.....	196
Figure 7-10: Picture of prototype gas target .....	198



## Table of tables

Table 1-1: Relevant nuclear fusion reactions, energy released per reaction (reaction Q-value), and maximum fusion cross-section within a center-of-mass energy range of 1 to 400 keV. *The cross-sections of the D-D reactions are increasing without a maximum below 400 keV. ....	3
Table 2-1: Estimated contribution of various geometric regions in the UW gridded IEC device to the total fusion rate. ....	18
Table 2-2: Properties of Radioisotopes for Positron Emission Tomography .....	32
Table 3-1: Values of $\alpha^2$ for the spherically converging case, $r_o > r_e$ . Values reproduced from table 2.1 of Forrester.....	42
Table 4-1: Visual representation of ion trajectory simulations.....	59
Table 4-2: Simulation and experimental comparison of three cathode electrode designs. The lower electrode was set to 0 V and the upper electrode was at -150 kV. A 0.1 mm vertical gap was modeled between the insulating rod and the top electrode to represent fabrication tolerances. Simulations performed in Ansoft Maxwell SV <sup>®</sup> ....	65
Table 4-3: Experimental parameters displayed and recorded by custom LabVIEW <sup>®</sup> program .....	96
Table 4-4: Values of variables for the pressure difference calculation. *for hydrogen .....	103
Table 4-5: Details of the two neutron detector systems including model number and settings of equipment. LLD and ULD are the Lower and Upper Level Discriminator setting for the Single Channel Analyzer (SCA). Note that the TC246 is a combination amplifier and SCA. *Values of the course adjust, multi-turn potentiometer, **Value of the multi-turn potentiometer. ....	107
Table 4-6: Energy of fusion protons in the lab frame after the Doppler shift as calculated by Eqn 4-20 for 70, 100 and 125 keV ions with stationary D <sup>0</sup> . The average proton energy after attenuation through 8 $\mu\text{m}$ of Al foil is also shown as calculated by SRIM. ....	111
Table 4-7: The effect of multiple design parameter choices on the spatial resolution and required count times for the collimated detector setup.....	116
Table 4-8: Details of D- <sup>3</sup> He proton detector equipment and settings. *Values of the course adjust, multi-turn potentiometer. ....	122
Table 4-9: Energy of a 14.7 MeV D- <sup>3</sup> He fusion proton in the lab frame after the Doppler shift resulting from 100, 130, and 150 keV ions reacting with stationary targets. The proton energy after 8 $\mu\text{m}$ of Al and 360 $\mu\text{m}$ of Pb was determined by SRIM. The 700 $\mu\text{m}$ thick Si detector was predicted to completely stop the proton after the foils. All energy values are in MeV and masses are in AMU.....	125

Table 6-1: Typical ion energy, fusion cross-section, and contribution to total cathode current for ions that struck various locations inside the SIGFE device. The locations are defined in Table 4-1.....	175
Table 6-2: Summary of the estimated percentage of fusion reactions from possible mechanisms of fusion reactions in the SIGFE device .....	177
Table 6-3: Visual comparison of the simulated ion trajectory of the SIGFE device at 70% focus to the Hirsch device. Simulation performed in SIMION® .....	183

## Chapter 1. Introduction

The application of nuclear fusion science and technology to non-electric applications has been the goal of the Inertial Electrostatic Confinement (IEC) laboratory at the University of Wisconsin – Madison for more than 15 years. [1] The Six Ion Gun Fusion Experiment (SIGFE) was designed and built to explore a possible avenue to increase the D-D and D-<sup>3</sup>He nuclear fusion reaction rates to the levels required for several possible commercial applications. The concept of using six ion beams to focus and spherically converge deuterium ions for nuclear fusion was first experimentally investigated by Hirsch in 1967. [2] To date, the Hirsch device reported the highest efficiency of D-D reactions in an IEC style device and utilized several features that had not been repeated in the more than 40 years of international IEC experiments that followed it. The SIGFE, built for this dissertation, was the first experiment to recreate both the unique features and the results of the Hirsch experiments. The more advanced ion optics design, control and instrumentation systems, and diagnostics of the SIGFE device allowed this dissertation to go beyond the original Hirsch experiments and more definitely determine the mechanisms by which D-D and D-<sup>3</sup>He fusion reaction were and were not occurring in the SIGFE device.

Nuclear fusion can produce several unique and potentially useful forms of radiation depending on the fuel used. These include high energy neutrons (2-14 MeV), thermal neutrons, high energy protons (3-15 MeV), and electromagnetic radiation (microwave to x-ray to  $\gamma$ -rays). These fusion products have many potential commercial applications, including but not limited to:

- production of radioisotopes for medical applications and research, including isotopes for positron emission tomography (PET)

- detection of specific elements and isotopes in complex environments, including explosives in the form of improvised explosive devices (IEDs), landmines, fissile material, and concealed nuclear weapons
- radiotherapy
- alteration of the electrical, optical, or mechanical properties of solids
- destruction of long-lived radioactive waste
- destruction of fissile material from nuclear warheads
- production of tritium for military and civilian applications
- food and equipment sterilization
- pulsed neutron, proton, and x-ray sources.

Some of these applications are attractive even at very low ratios of fusion energy output versus energy in ( $Q \ll 1$ ); whereas electrical power plants generally require  $Q$  greater than 10. Development of the commercial opportunities for fusion science will, and has, attracted private investment. The inclusion of private resources through the commercialization of short-term applications will augment the large public effort and accelerate the development of nuclear fusion as a viable electrical energy source. [1]

Depending on the requirements of the specific application, different fusion reactions can be used and devices can be tailored to meet the needs of the specific reaction and application. Table 1-1 lists the four fusion reactions most relevant to the applications mentioned. Devices based on IEC technology are well suited for some of these commercial applications in several ways. Current IEC devices fit in an area the size of a hospital exam room and could be designed to be mounted on a truck, or even smaller. IEC-based technology has an advantage in utilizing the fusion reactions beyond D-T that require higher

ion energies. This capability is a result of the direct acceleration of the ions to fusion energies. This is in contrast to other technologies, which operate by heating large Maxwellian plasmas to high, keV range temperatures and then relying on the ions in the high energy tail of the distribution to produce the fusion reactions.

Table 1-1: Relevant nuclear fusion reactions, energy released per reaction (reaction Q-value), and maximum fusion cross-section within a center-of-mass energy range of 1 to 400 keV.

\*The cross-sections of the D-D reactions are increasing without a maximum below 400 keV.  
[3, 4]

Nuclear Fusion Reaction	Energy Released per Reaction	Maximum Cross-section @ Center-of-Mass Energy
D + T $\rightarrow$ <sup>4</sup> He (3.5 MeV) +n (14.1 MeV)	17.6 MeV	5000 mb @ 70 keV
D + D $\rightarrow$ <sup>3</sup> He (0.8 MeV) +n (2.5 MeV)	3.3 MeV	87 mb @ 400 keV*
D + D $\rightarrow$ T (1.0 MeV) +p (3.0 MeV)	4.0 MeV	70 mb @ 400 keV*
D + <sup>3</sup> He $\rightarrow$ <sup>4</sup> He (3.7 MeV) +p (14.7 MeV)	18.4 MeV	810 mb @ 250 keV

With concerns of terrorism within the United States and where our troops are stationed abroad, the development of new technologies for the detection of improvised explosive devices (IEDs), landmines, and small explosives concealed inside items like luggage is receiving increased attention. The main constituents of explosives, carbon, nitrogen, and oxygen are difficult to detect with conventional x-ray techniques. These elements do, however, produce a specific gamma-ray signature when actively interrogated with neutrons. It is estimated that a D-D neutron source of approximately  $5 \times 10^{11}$  neutrons per second (n/s) would be required for this application. [1]

The production of radioisotopes for use in Positron Emission Tomography (PET) is also an attractive market for fusion-based technology. PET is a medical technique used to image abnormalities, such as tumors, and dynamic processes, such as blood and air flow, inside the human body. The cross-sections of the radioisotopes desired by the medical community, <sup>11</sup>C ( $t_{1/2} = 20.4$  min), <sup>13</sup>N (9.97 min) and <sup>15</sup>O (2.05 min), are well matched to the

14.7 MeV proton produced by the D-<sup>3</sup>He fusion reaction. [5] The short half-life of these isotopes dictates they be produced within 100s of meters of the location where they will be used. Many of the PET radioisotopes are currently produced using charged particle accelerators. These are immobile, multi-million dollar installations that only larger hospitals and clinics in urban areas can justify, thus significantly limiting isotope availability to a fraction of the U.S. population. It may be possible to design a device utilizing IEC technology and D-<sup>3</sup>He fusion reactions that can be integrated in a mobile semi-trailer to be shared among multiple hospitals and clinics in rural communities. [6] This would improve the availability of short-lived radioisotopes to smaller clinics and hospitals. Previous work at the University of Wisconsin has produced radioisotopes in an IEC device at a proof-of-concept level. In separate experiments, 1 nCi of <sup>13</sup>N and 1.5 nCi of <sup>94m</sup>Tc were produced. [7] The design and simulated performance of a newly proposed IEC-based radioisotope production device will be discussed in detail in Chapter 7. Based on the Monte Carlo analysis of this system, it is estimated that a D-<sup>3</sup>He fusion rate on the order of  $10^{11}$  protons per second (p/s) would be required for a commercially viable system.

Two of the most promising short-term applications of IEC devices, explosive detection and radioisotope production, both require fusion rates on the order  $10^{11}$  to  $10^{12}$  s<sup>-1</sup>. For explosive detection, which could use the neutrons from the D-D or D-T reactions, this is a two to three orders-of-magnitude increase over the present pulsed D-D IEC record of  $5 \times 10^9$  n/s, and four orders of magnitude more than the  $2.4 \times 10^8$  n/s D-D steady state record [8]. Switching to D-T would increase the steady state neutron rate to approximately  $4 \times 10^{10}$  n/s. A larger increase in D-<sup>3</sup>He fusion rate is required for isotope production. A five orders-of-magnitude increase in the rate of 14.7 MeV fusion protons is required over the current  $5 \times 10^7$  p/s steady-state IEC record. [7]

The main goal of this dissertation was to build the Six Ion Gun Fusion Experiment and to determine if this Hirsch-like device was a viable approach to increasing the D-D and D-<sup>3</sup>He fusion reaction rates to the levels required for many near-term applications. This work also provided valuable experimental data that will help to resolve conflicts in the theoretical papers surrounding beam convergence in IEC type devices. The strategy of this dissertation was to first reverse engineer the original Hirsch device. The next step was to design and build the SIGFE device based upon detailed modeling, simulation, and on the previous experimental and theoretical literature. The SIGFE improved the diagnostics and ion optics of the original Hirsch device to develop a better understanding of the mechanisms of the D-D and D-<sup>3</sup>He nuclear reactions that occurred in the SIGFE device.

## References for Chapter 1

- 
1. Kulcinski, G. L. (1996). Near term commercial opportunities from long range fusion research. *Fusion Technology*, 30(3) 411-21.
  2. Hirsch, R. L. (1967). Inertial-electrostatic confinement of ionized fusion gases. *Journal of Applied Physics*, 38(11), 4522-4534.
  3. Huba, J. D. (Ed.). (2007) NRL Plasma Formulary. Washington, DC 20375: Naval Research Laboratory.
  4. Bosch, H. S., & Hale, G. M. (1992). Improved formulas for fusion cross-section and thermal reactivities. *Nuclear Fusion*, 32(4), 611-31.
  5. Owunwanne, A., Patel, M., & Sadek, S. (1995). The handbook of radiopharmaceuticals. London New York: Chapman & Hall Medical.
  6. Weidner, J. W. (2003). The production of N-13 from inertial electrostatic confinement fusion. (Doctoral dissertation, University of Wisconsin - Madison).
  7. Cipiti, B. B. (2004). The fusion of advanced fuels to produce medical isotopes using inertial electrostatic confinement. (Doctoral dissertation, University of Wisconsin – Madison)
  8. Radel, R. F. (2007). Detection of highly enriched uranium and tungsten surface damage studies using a pulsed inertial electrostatic confinement fusion device. (Doctoral dissertation, University of Wisconsin - Madison).



## Chapter 2. Past contributions to IEC research and the production of isotopes in IEC devices

The idea of confining plasma with an electrostatic potential well was first published by Elmore, Tuck and Watson in 1959. [1] In this scheme for nuclear fusion, high energy electrons were injected toward a spherical anode. The electrons produced a potential well, which in turn attracted the ions. The analysis of this system was discouraging due to the large electron current required and predicted ion instabilities. In the 1950s, P.T. Farnsworth conceived of the reverse of this idea, which he patented in 1966. [2] Farnsworth proposed injecting ions into an electrostatic well instead of injecting electrons; this idea is the basis of the present research into the Inertial Electrostatic Confinement (IEC) concept.

In a gridded IEC device, a negative potential well on the order of 1 to 100's of kilovolts is established between two concentric spherical or cylindrical electrodes. Cool ions, on the order of a few electron volts (eV), are born at the outer grounded electrode (anode). These positive ions accelerate through the potential well toward the central negatively biased cathode. As the ions reach fusion energies, they have a probability of fusing with other ions converging on the center from all directions and with the background gas as they stream through the cathode and recirculate in the potential well. Figure 2-1 shows the cross-section for fusion versus the center-of-mass energy of the colliding particles. This is a much idealized picture of the physics inside an IEC device. In the past 40 years substantial advancements in the understanding of the “non-ideal” physical effects governing IEC have been made, including the role of atomic and molecular processes. [3, 4]

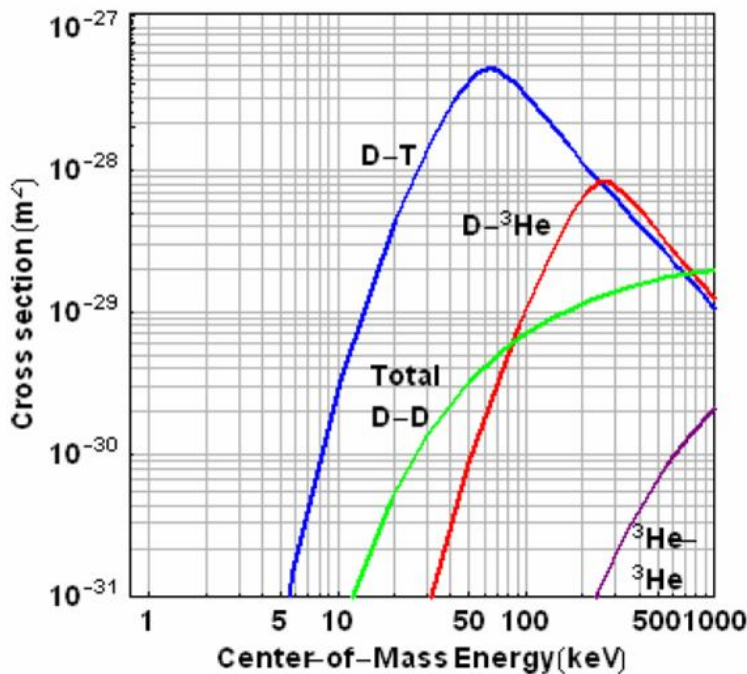


Figure 2-1: Nuclear fusion cross-sections as a function of center-of-mass energy for D-T, D-D, D- $^3\text{He}$ , and  $^3\text{He}$ - $^3\text{He}$  reactions. [5] Nuclear fusion cross-section values adapted from the compilation published by Bosch [6] of multiple experimental data sets.

## 2.1. Review of past experiments in Inertial Electrostatic Confinement (IEC)

Supported by Farnsworth, R. L. Hirsch published the first experimental work on the IEC concept in 1967 [7] and had very encouraging results. In steady-state, Hirsch observed  $5 \times 10^7$  neutrons per second (n/s) from D-D reactions, and  $3 \times 10^9$  n/s from D-T reactions. Figure 2-2 shows the neutron production rate (NPR) of this experiment as a function of cathode voltage and gas pressure. Of note in Figure 2-2 is the increase in NPR as the pressure of  $\text{D}_2$  decreased from 1.0 Pa (7.8 mTorr) to 0.013 Pa (0.1 mTorr). This inverse relationship is contrary to present day D-D experiments. The present IEC devices at the University of Wisconsin (UW) have an optimal  $\text{D}_2$  pressure of approximately 0.2 to 0.5 Pa [8]. This suggests that the Hirsch experiment was operating in a different mode than the present day gridded experiments, which have been shown to be operating in a beam-background mode. [9] In the beam-background mode, reactions between energetic ions and

fast neutrals with the nearly stationary background gas is the dominate mechanism of the fusion reactions to occur. [10, 3, 4]

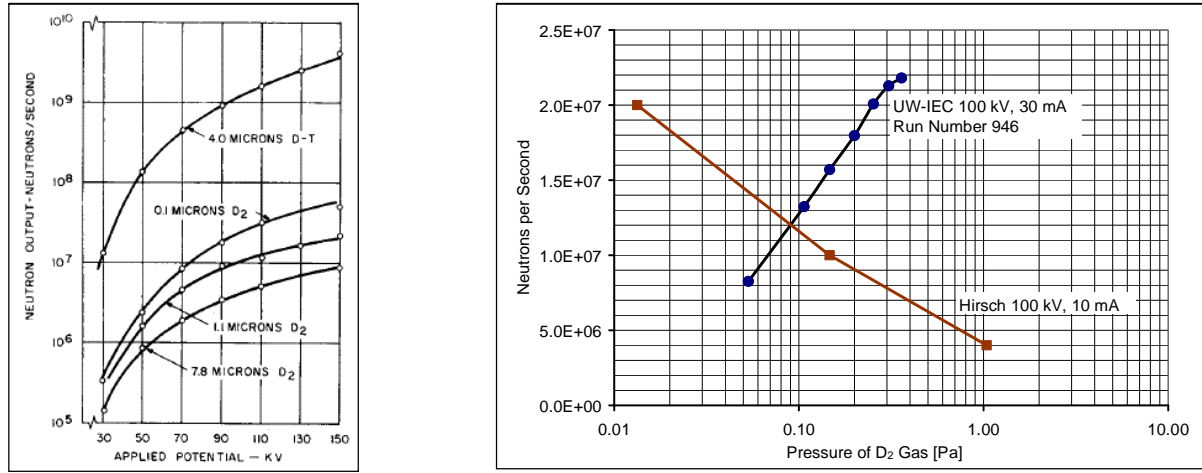


Figure 2-2: a) Neutron production rates in the Hirsch experiment as a function of voltage and gas pressure of D<sub>2</sub> gas or D-T gas mixture at 10 mA of ion current. Adapted from Figure 11 of Hirsch-1967. [7] b) Neutron production rate as function of pressure at 100 kV for Hirsch and UW-IEC, note difference in total experimental current. (1 micron = 1 mTorr = 0.13 Pa) [7, 8]

Hirsch used both a collimated neutron detector and a collimated x-ray detector to diagnose the source of fusion reactions and to infer the shape of the electrical potential structure inside the cathode. The spatial distribution of the D-D fusion reactions was determined from direct measurements of the spatial distribution of 2.45 MeV fusion neutrons. The second diagnostic looked at the x-rays from bremsstrahlung radiation caused by fast electrons slowing down in regions of high ion density. Figure 2-3 overlays a reproduction of the original graphs from both diagnostics with a scaled sketch of the device. The graph was scaled from the original paper and the units were changed to match. Hirsch believed the peaks in both diagnostics were caused by the formation of virtual anodes and cathodes. In his theory, the virtual electrodes caused regions of higher ion density and thus higher fusion rates. He extended a solution to the Poisson equation that assumed the presence of both electrons and mono-energetic ions with only radial velocity. This solution

predicted the formation of these virtual electrodes from the space charge and energy associated with the ions and electrons. Hirsch's theory, along with several other theoretical papers which do not assume purely radial velocity for the ions, will be summarized in Section 2.2.

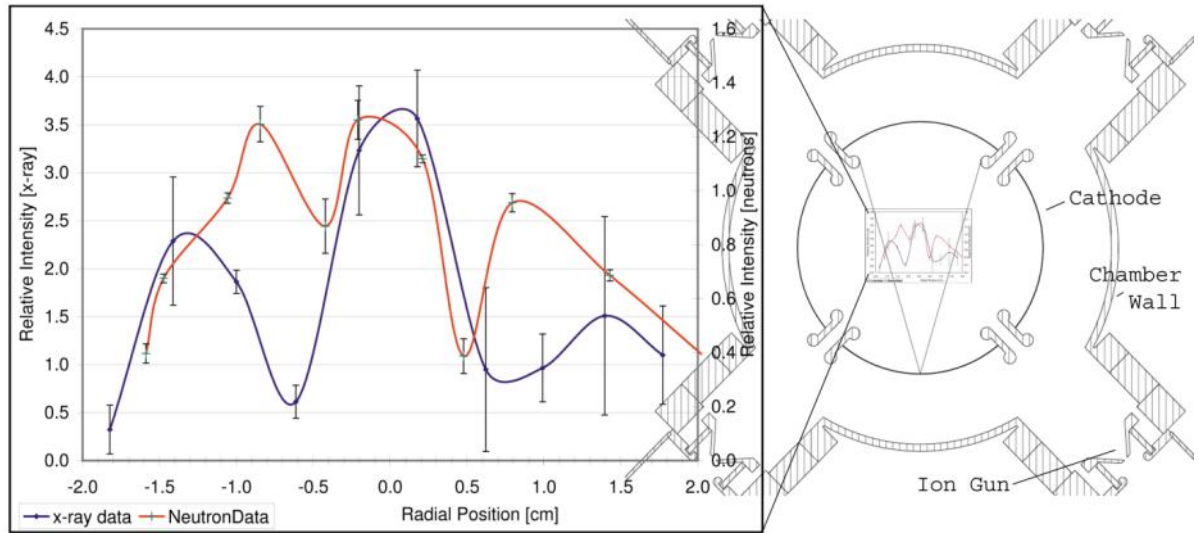


Figure 2-3: Results of collimated neutron and x-ray measurements scaled from the original paper. The results are overlaid on a sketch of the experiment device to provide scale. [7]

Hirsch's theory for the operation of this experiment predicted the fusion rate should increase as the current squared ( $I^2$ ). However, the experiment showed only linear scaling with current. Hirsch postulated that this was due to space-charge spreading of the ion beam outside the parameters required for ion trapping, and that improvements in the ion optics of the systems may alleviate this issue.

The high fusion rates reported by Hirsch in 1967 motivated many other researchers to investigate IEC as a viable option for producing nuclear fusion. However, in the past 40 years the original results of Hirsch have not been reproduced in their entirety. Only in the last 5 years has the research group at the UW surpassed the number of D-D neutrons produced in 1967. The UW record of  $2.4 \times 10^8$  n/s was achieved at a cathode voltage of

168 kV and total cathode current of 75 mA, versus the  $5 \times 10^7$  n/s at a cathode voltage of 150 kV and a total cathode current of 10 mA reported by Hirsch. Total cathode current, or meter current, is the net electrical charge flow from the high voltage power supply. It includes both the ions that impact the cathode and the secondary electrons generated at the cathode that are accelerated back to ground. Figure 2-4 compares many of the IEC experiments that have been conducted over the last 40 years. [7, 13, 26-37] Since each device operated at different voltage and current conditions, the performance was normalized by dividing the neutron production rate by the total high voltage power.

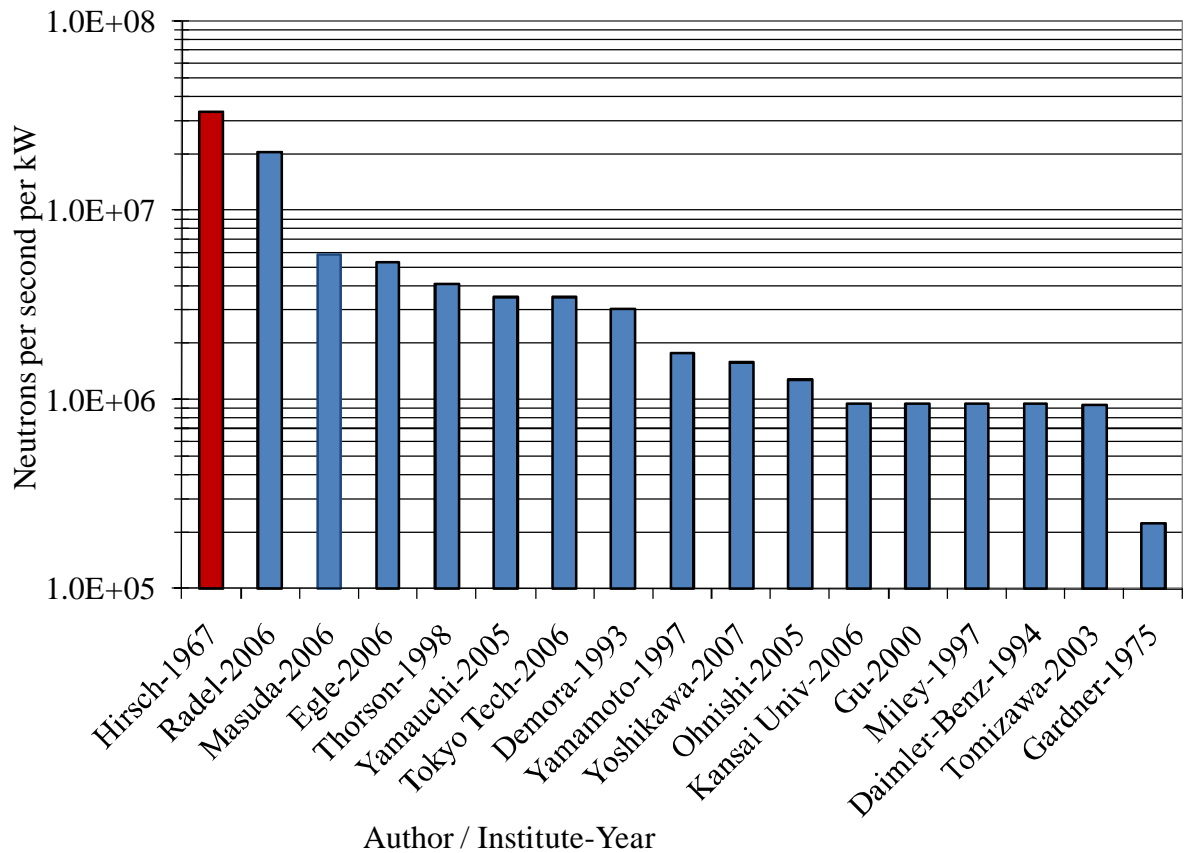


Figure 2-4: Comparison of steady-state D-D fusion neutron rates per kilowatt of high voltage power (meter current times cathode voltage) for various IEC experiments listed by author and year reported. [7, 13, 26-37]

The higher efficiency of the Hirsch device, excluding SIGFE-2009 which will be described in chapter 4, was likely due to the unique features of this device. Several of these

unique features had not been repeated in their entirety prior to this dissertation. First, the Hirsch design utilized an opaque spherical cathode that confined the majority of the secondary electrons produced inside of the cathode region. Any area of the cathode, with the exception of the six ion ports, that required an opening was covered with a double mesh biased at approximately -500 volts. These electrons were essential to the formation of the virtual electrodes of Hirsch's theory. Also, the trapping of the electrons prevented high voltage power from being wasted in the acceleration of electrons toward the anode. Second, he operated at pressures on the order of 0.01 Pa, which is at least an order of magnitude less than the majority of the other IEC experiments from around the world, which typically operate between 0.1 Pa and 1.3 Pa. This lower pressure was achieved by employing ion guns, which provided a higher pressure region to allow a plasma to form as an ion source behind a small aperture. The aperture functioned as both an electrostatic extraction system for the ions, since it was biased to -10 kV, and as a 1.5 mm diameter orifice for maintaining the pressure difference between the main vacuum chamber and the ion source region. A schematic of the Hirsch ion gun is shown in Figure 2-5. Six ion guns were used; each placed opposing each other on the three axes of a spherical chamber to approximate a spherical converging system. Figure 2-5 and Figure 2-6 were created by this author by scaling the drawing included by Hirsch in the original publications. [7,11]

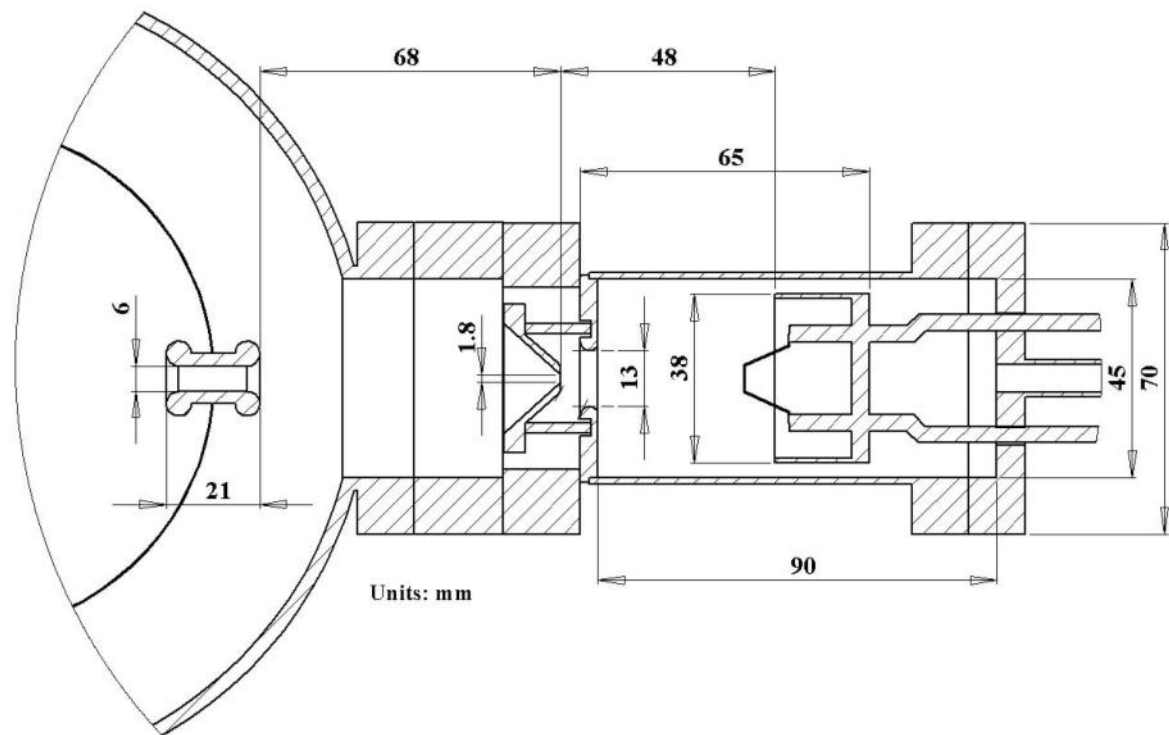


Figure 2-5: Scale drawing of the Hirsch ion gun and cathode with details of the electrostatic lenses. Drawing created by this author by directly scaling the figures published by Hirsch and Meeks-1967. [11]

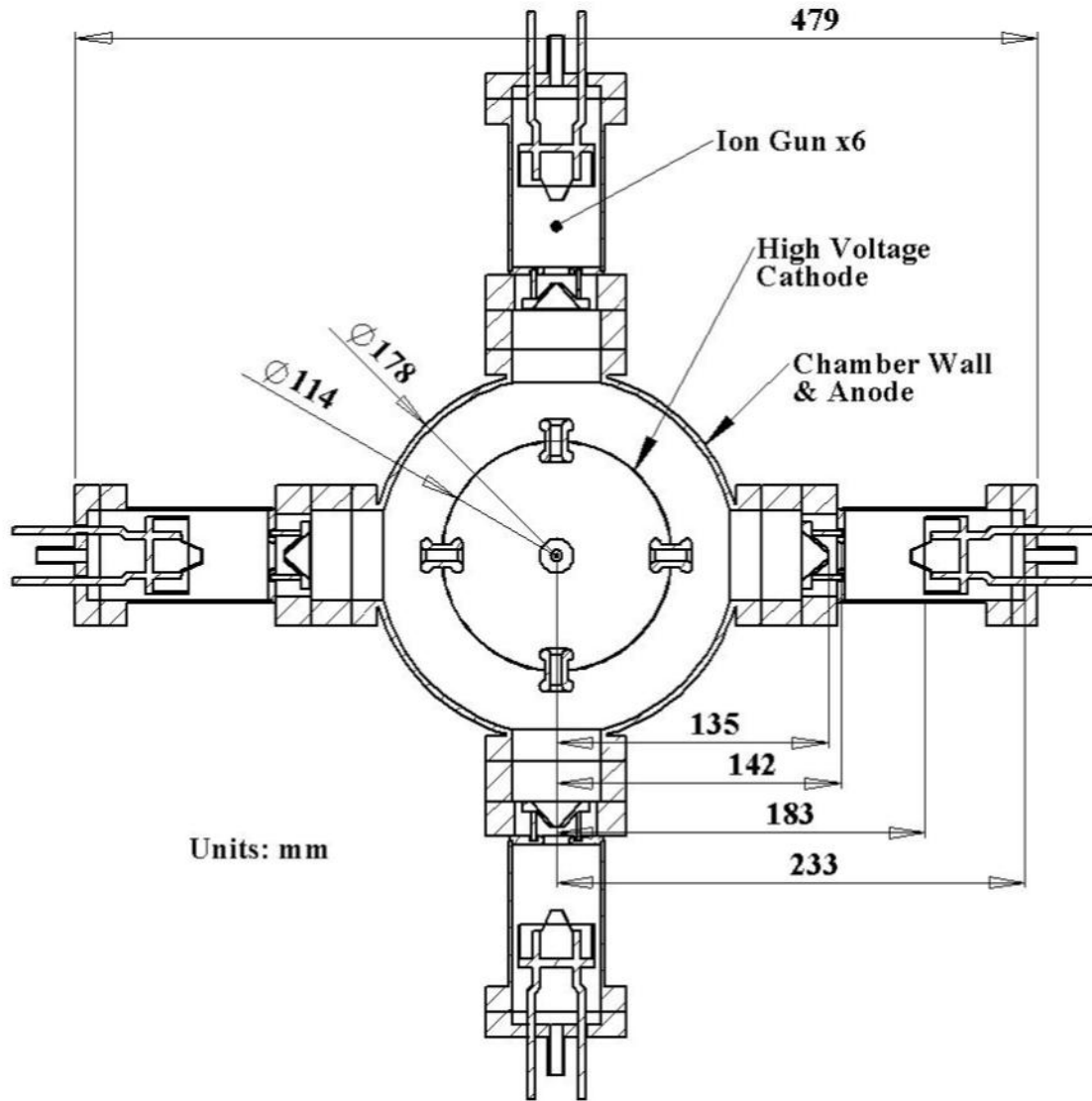


Figure 2-6: Scale drawing of the Hirsch device. The anode diameter was 178 mm and the Cathode diameter was 114 mm. Drawing created by this author by directly scaling the figures published by Hirsch and Meeks-1967. [11, 7]

In contrast to the Hirsch design, the majority of the present IEC experiments use a transparent (>90%) spherical wire grid for the cathode, and either a wire grid or the inside of the vacuum vessel for the anode. Many of the gridded IEC devices operate at pressures greater than 0.8 Pa and rely on electrical breakdown between the anode and cathode to ionize the background gas. This creates a dependence between the gas pressure, voltage and current, which qualitatively follows the Paschen theory of electrical breakdown in gas, thus greatly limiting the operating regimes in which these experiments can operate. One of the

IEC experiments at the UW, called HOMER, used a heated, negatively-biased filament to produce energetic electrons (10 to 500 eV) that ionize the background gas. This allowed the current to be adjusted while the voltage and pressure are held constant, thus greatly increasing the operating parameter space available for experimentation. A sketch of this device is shown in Figure 2-7. [9]

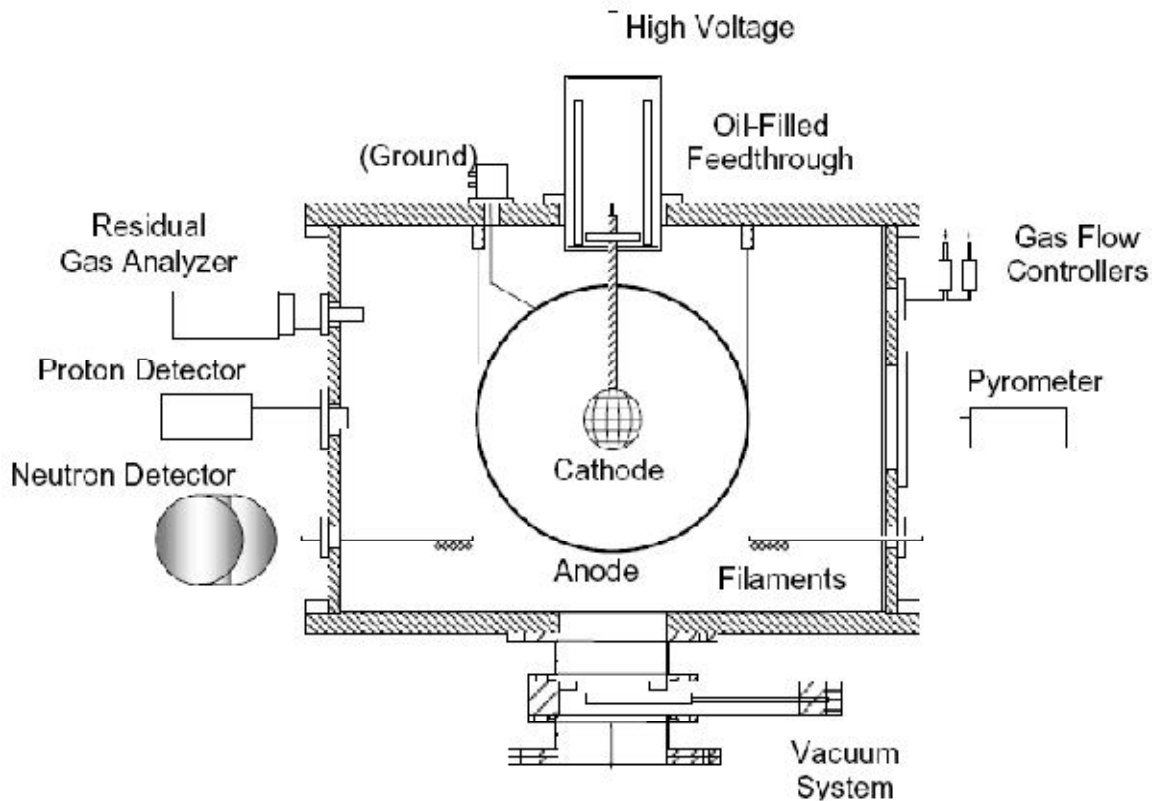


Figure 2-7: Sketch of UW IEC experiment, HOMER. It is shown with a 50 cm wire gridded anode, and a 10 cm wire gridded cathode. The chamber is cylindrical with a diameter of 95 cm and a height of 65 cm. Figure adapted from Figure 3-1 of Cipiti 2004. [9]

### 2.1.1. Measurement of fusion reaction regimes

As alluded to previously, there are various modes in which fusion can occur in an IEC device. These different modes can be diagnosed from the spatial distribution of fusion reactions. The research team at the UW employed three experimental techniques for both D-D and D-<sup>3</sup>He for this purpose: (1) experiments comparing fusion rates when the gridded

cathode was replaced by a solid sphere, (2) eclipse disk experiments where various regions of the device were blocked from the view of the proton detector, and (3) comparison of a proton detector aligned on the axis of the cathode to a second detector aligned off-axis, out of the view of the cathode. All of these experiments were conducted at 0.24 Pa of gas and 30 mA of high-voltage meter current.

The premise of the first technique was to determine the contribution of the inter-cathode region and the number of fusion reactions that occurred when D or  $^3\text{He}$  became embedded in the cathode wires and was impacted by high energy ions. Figure 2-8 and Figure 2-9 show the results of these experiments for both D-D and D- $^3\text{He}$ . For D-D, the gridded cathode outperformed the solid cathode by a factor of 4 to 10. This indicated that multiple ion passes through a semi-transparent grid and the total path length of fast, charge-exchange neutrals may contribute to the total fusion rate. For D- $^3\text{He}$ , however, the solid cathode's performance was virtually identical to the gridded system, implying that the center region of the cathode provided a very small contribution to the total reaction rate. This was consistent with later findings that the majority of D- $^3\text{He}$  reactions occur as ions embedded in the electrodes.

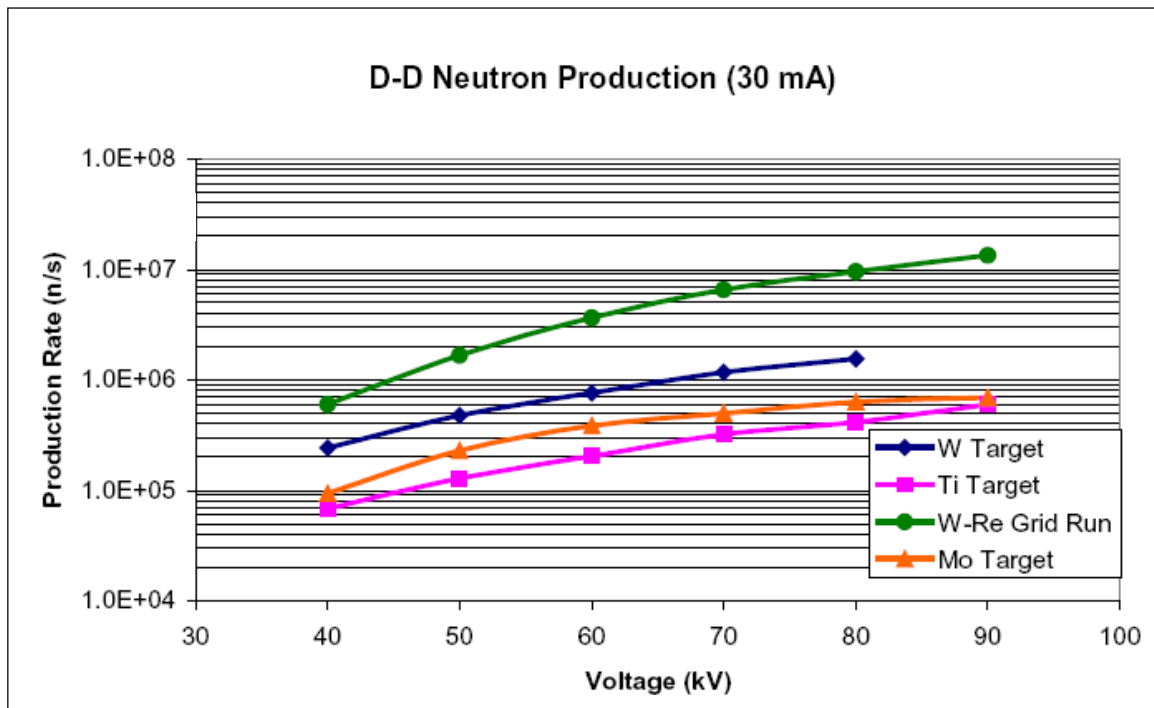


Figure 2-8: Comparison of gridded wire cathode to solid metal cathodes in D gas. Adapted from Figure 6-7 of Cipiti-2004. [7]

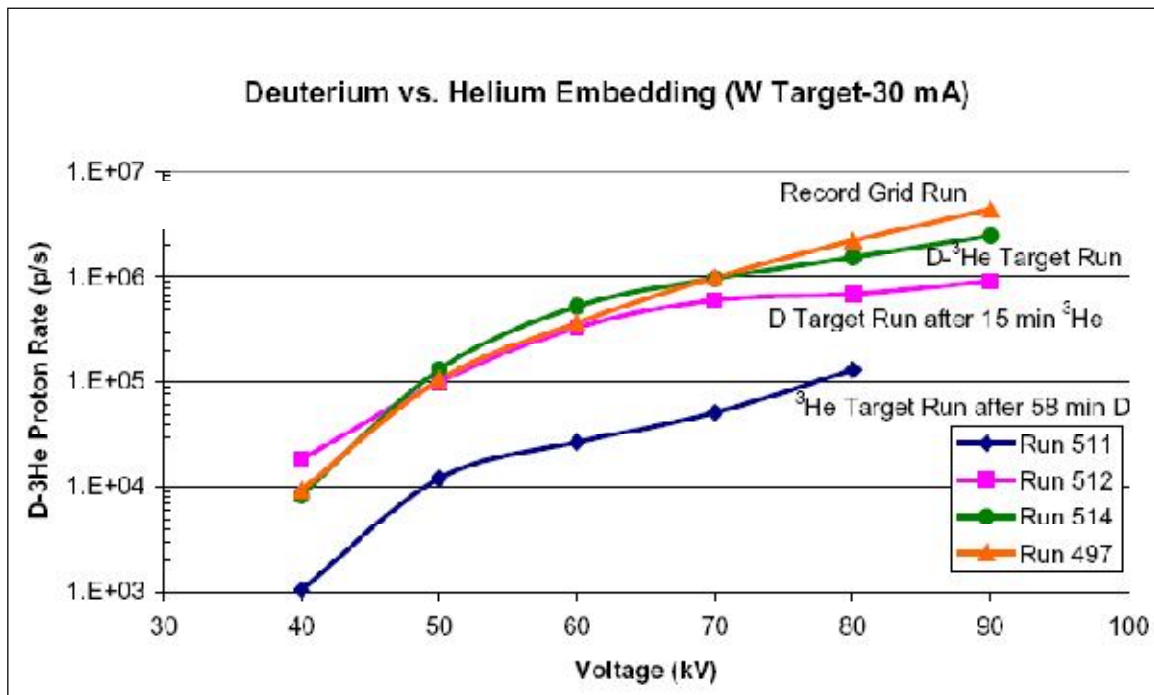


Figure 2-9: Comparison of W solid cathode versus gridded W-Re wire gridded cathode in D-<sup>3</sup>He gas mixture. Adapted from Figure 6-9 of Cipiti-2004. [7]

The second and third techniques further study the reaction regions by allowing a proton detector to only see specific regions. Three different-sized disks were used to block increasing amounts of a gridded cathode. Figure 2-10 shows the results of the eclipse disk experiments. Cipiti combined the results of all three experimental techniques to estimate the contributions from the center region of the cathode, the grid wires, and the volume. Table 2-1 summarizes his estimates. [9]

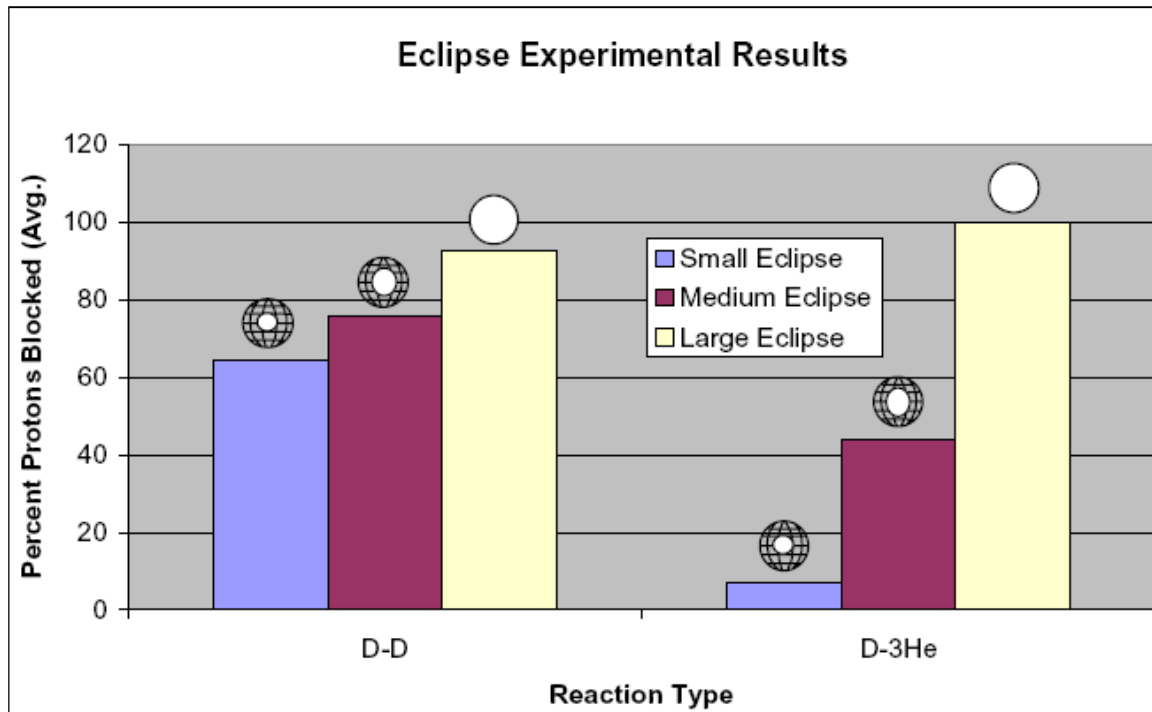


Figure 2-10: Percentage of fusion protons blocked by eclipse disks for D-D reactions and D-<sup>3</sup>He reactions. Figure taken from Figure 6-11 of Cipiti-2004 [9]

Table 2-1: Estimated contribution of various geometric regions in the UW gridded IEC device to the total fusion rate. [9]

	Cathode Center	Embedded	Volume
D-D	22%	8%	70%
D- <sup>3</sup> He	5%	95%	Negligible

The 2003 results of the UW research group pertaining to the spatial regions in which D-<sup>3</sup>He fusion occurred were verified by T. Fujimoto from Kyoto University in 2007. [12]

Using a movable mask in front of a proton detector, the Kyoto group estimated that ~60% of the D-<sup>3</sup>He fusion protons were originating from the cathode surface and ~40% from the surface of the metal high-voltage feed-through. Therefore, 99% of the fusion reactions were embedded, while less than 1% was from the volume inside the cathode.

### *2.1.2. Measurements and experimental evidence of virtual electrode formation*

As ions in a spherical or cylindrical IEC device converge at the center, assuming a modest amount of focusing, a region of positive space charge is predicted to form. Several of the experiments to be discussed observed this positively charged region. The theory proposed by Hirsch [7] goes beyond simple ion convergence. He proposed that the region of positive charge could attract electrons which in turn could create a region of negative space charge inside the positive region. This interaction between the ions and electrons could create spatially oscillating virtual anode-cathode pairs, multiple potential wells, at the center of the physical cathode. This may explain the experimentally observed spatial distribution of neutrons and x-rays shown in Figure 2-3. Several separate experiments, using various techniques, have attempted to directly measure the electrostatic potential structures inside the physical cathode and observe the predicted virtual electrode pairs.

The electron density inside the cathode region was measured by Gardner in 1975 [13] with the original experimental equipment used by Hirsch. Gardner attempted to measure a change in the electron density by looking for a shift in the microwave resonance frequency of the cathode as the current of the IEC system was increased. An increase in electron density would support the theory of ion convergence and electron confinement inside the cathode. However, Gardner did not find a conclusive resonance frequency shift over the operating pressures he was able to explore. A brief note was made in the paper referring to experimental difficulties in obtaining as low an operating pressure as Hirsch; “the orifices

were somewhat enlarged with use and the pressure could not be further reduced while still maintaining an output current of one mA per gun.” The enlargement of the orifices due to electron and ion bombardment over time may have had a larger effect on the device’s operation than just pressure. Even a small enlargement of the orifices could greatly affect the ion focus and thus adversely affect the ion convergence of the system. The adverse effect of small changes in the extraction orifices is experimentally supported in the results sections of this dissertation.

Experiments done at the University of Illinois and reported by Verdeyen in 1975 [14] examined the potential structure and charge densities inside an IEC device. They used an electron beam to probe the potential well created when electrons were injected toward an anode with an applied potential between +0.5 and +2 kV and a current of 10 to 250 mA. Potential wells of approximately 20-80% of the applied voltage were measured when only electrons were injected into a  $10^{-6}$  Pa vacuum. The absolute depth of the well was found to be a linear function of the injection current and was insensitive to the anode voltage. A background pressure of  $2 \times 10^{-3}$  Pa of D<sub>2</sub> gas was introduced to produce D<sub>2</sub><sup>+</sup> ions in the system. Verdeyen concluded that the deflection of the electron-beam-probe observed in the presence of D<sub>2</sub><sup>+</sup> ions strongly suggested a region of positive space charge, and established that stable, multiple potential wells could exist.

In the same 1975 paper, Verdeyen [14] also presented the results of a cylindrical IEC device in which the electron density was measured directly using a laser heterodyne system. This measurement technique integrated the electron density along the axis of the cylinder and provided a spatial resolution of approximately 1 mm along the radius. The results of these measurements, as seen in Figure 2-11, show spatial variations in electron density that qualitatively agree with the collimated neutron and x-ray results of Hirsch. The experiments

presented by Verdelyen unfortunately are not a one-to-one comparison to Hirsch or to fusion reactors of usable scale since these experiments were conducted at electrode voltages of 1 to 3 kV.

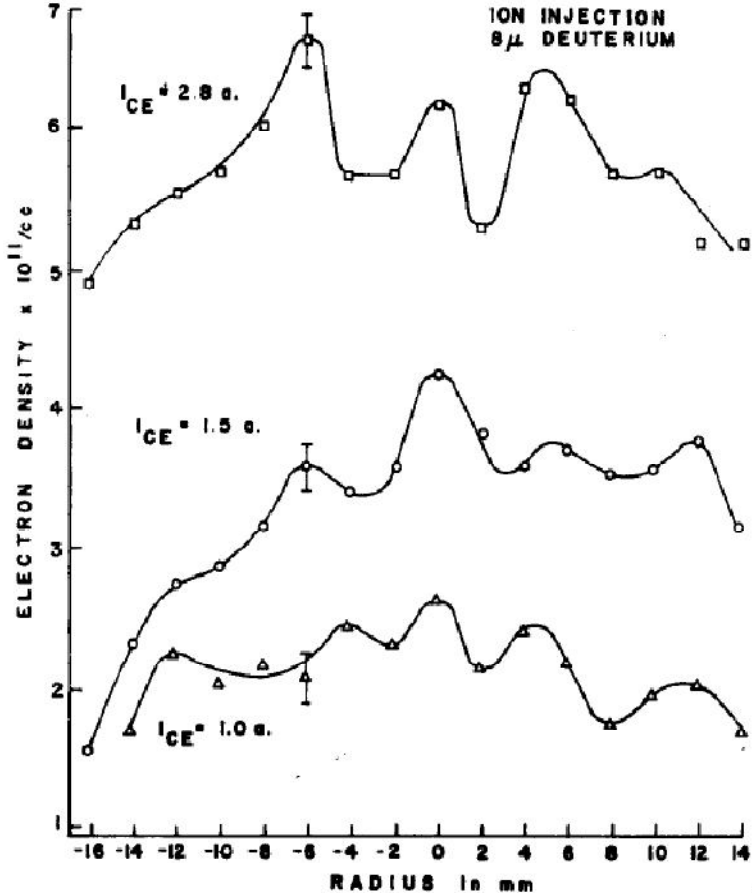


Figure 2-11: Spatially resolved electron density on the interior of the cylindrical device as determined with a laser heterodyne system. Figure taken from Figure 9 of Verdelyen-1975. [14]

The electron-beam probing technique used by Verdelyen to measure the potential structures was limited to low applied potentials due to the unavailability of an electron beam of sufficient energy. Black in 1974 [15] described using radioactive <sup>109</sup>Cadmium as a source of 62.2 keV and 84.2 keV electrons. Black concluded that by using this source and a collimated detector, the potential profile of a gridded spherical IEC device with an applied voltage of up to a few tens of kilovolts could be measured within an error of a few percent.

At ion currents comparable to Hirsch and 2 to 10 kV applied voltages, a shallow double potential well structure was observed. However, the depth of the potential well was less than 5% of the applied voltage.

The spatially resolved results of Verdeyen [14] and Hirsch [7] differ from the results of Cipiti [9] and Fujimoto [12] presented in Section 2.1.3. This difference is an indication of the sensitivity of the system to many variables. The two sets of experiments operated in pressure regimes separated by at least an order of magnitude and had several key design differences. From these papers it appears that ion current, background gas pressure and ion focusing were essential parameters to consider when designing an IEC device in which virtual potential well structures significantly contributed to the fusion reaction rate.

## **2.2. Past theoretical contributions to IEC operation and virtual electrode formation**

Along with the publication of his experimental results in 1967, Hirsch [7] also presented a solution of the Poisson equation with space charge coupled to the kinetic energy equations for both the injected ions and the trapped secondary electrons. Ions were assumed to be born with zero energy at the anode of the system; these ions accelerated purely radially toward the center of the cathode. As they converged, positive space charge at the center of the device increased and created a virtual anode. This virtual anode decelerated subsequent incoming ions and eventually turning them around to exit the cathode on the same path they entered on. In this hypothesis, the virtual anode also attracted secondary electrons that formed as stray ions impacted the inside of the cathode. These electrons were then radially focused and accelerated toward the virtual anode. The converging electrons formed a region of negative space charge, a virtual cathode, inside the virtual anode. In theory, this process can repeat itself to form an infinite number of increasing smaller radius virtual anode-cathode pairs. In this initial hypothesis, Hirsch ignored all non-radial velocity components and the

atomic interaction that occurred with the background gas. Therefore all the ions were assumed to be mono-energetic at the energy corresponding to the cathode potential and to have no angular momentum.

In Hirsch's hypothesis, the infinite number of virtual anode-cathode pairs would have focused an increasingly larger density of ions and electrons. At the center, the ion density was predicted to go to infinity. This, of course, is non-physical, and was a result of assuming the ions had no angular momentum. In reality the ions and electrons must have a finite amount of both radial energy spread and angular momentum. With this, the ions and electrons are no longer focused at an infinitesimally small point, but at a finite volume. The radius of this volume, called the radius of closest approach, was theoretically estimated by Rosenberg and Krall [16] from the angular momentum the ions were born with and transported to the cathode by assuming angular momentum was conserved. Assuming conservation of angular momentum implied that there are no non-radial forces. However, the electrostatic lenses used in the Hirsch device would have produced such non-radial forces.

Ignoring the transverse velocity of the ions has been a major criticism of Hirsch's hypothesis. Several researchers have extended this hypothesis using slightly different models to include distributions of both angular momentum and radial energy spread. Dolan [17] solved the equations with square distributions of ion energy and angular momentum from zero to their maximum allowed values. This very large spread in energies and angular momentum prevented the formation of virtual potential wells. Cherrington [18] continued the work of Dolan by analyzing cases with "relatively small" ion energy spreads and with much smaller square distributions of angular momentum. In these restricted cases, he predicted the formation of a single virtual anode-cathode pair. He was concerned, however, with the uniqueness of his solution and stated that his results were "far from definitive."

Black and Klevans [20] used a more sophisticated distribution function than Dolan or Cherrington. More accurate radial energy spread and angular momentum distribution functions were developed by first assuming the shallow well potential profile shown in Figure 2-12. This profile was similar to experimental measurements Black made in a gridded spherical IEC device. A computational model was developed to predict the radial ion energy spectrum at the entrance of the cathode region. Their model incorporated the measured potential profile, the background gas pressure and the energy dependent ion charge-exchange cross-section.

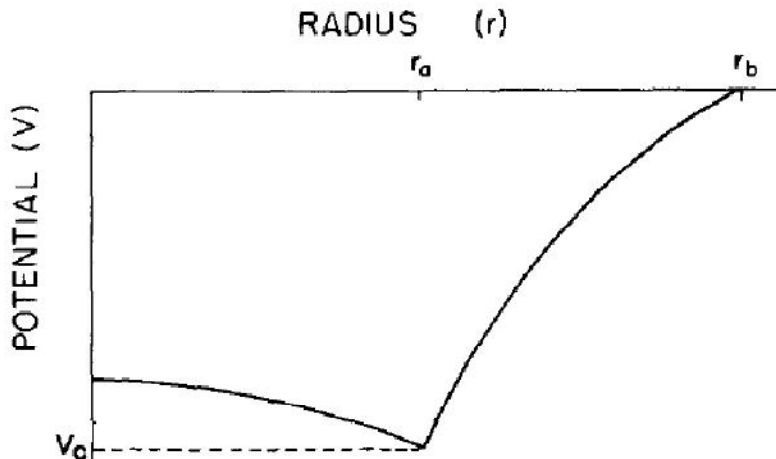


Figure 2-12: A) Shallow potential well profile used in the computational model to determine ion energy spectrum. This profile shape is similar to the experimentally measured potential profile. Figure taken directly from Figure 1 of Black-1974 [19]

The computed spectrum was divided into three distinct regions or types of ions: low energy ions, intermediate ions and beam ions. A different angular momentum distribution function was used for each type of ion. 1) For the beam ions, Black identified two main sources of angular momentum; spherical focusing error caused by deviations of the grids from a true sphere (grid error), and the attraction of the ions to the grid wires. A square distribution function with its maximum determined as a function of the two sources of angular momentum was used for this ion type. 2) For the intermediate ions a square

distribution was also used, but with a maximum of one-half the maximum of the beam ions.

3) The low energy ions were assumed to be isotropic. Figure 2-13 shows the computed ion energy spectrum at various chamber pressures of helium gas.

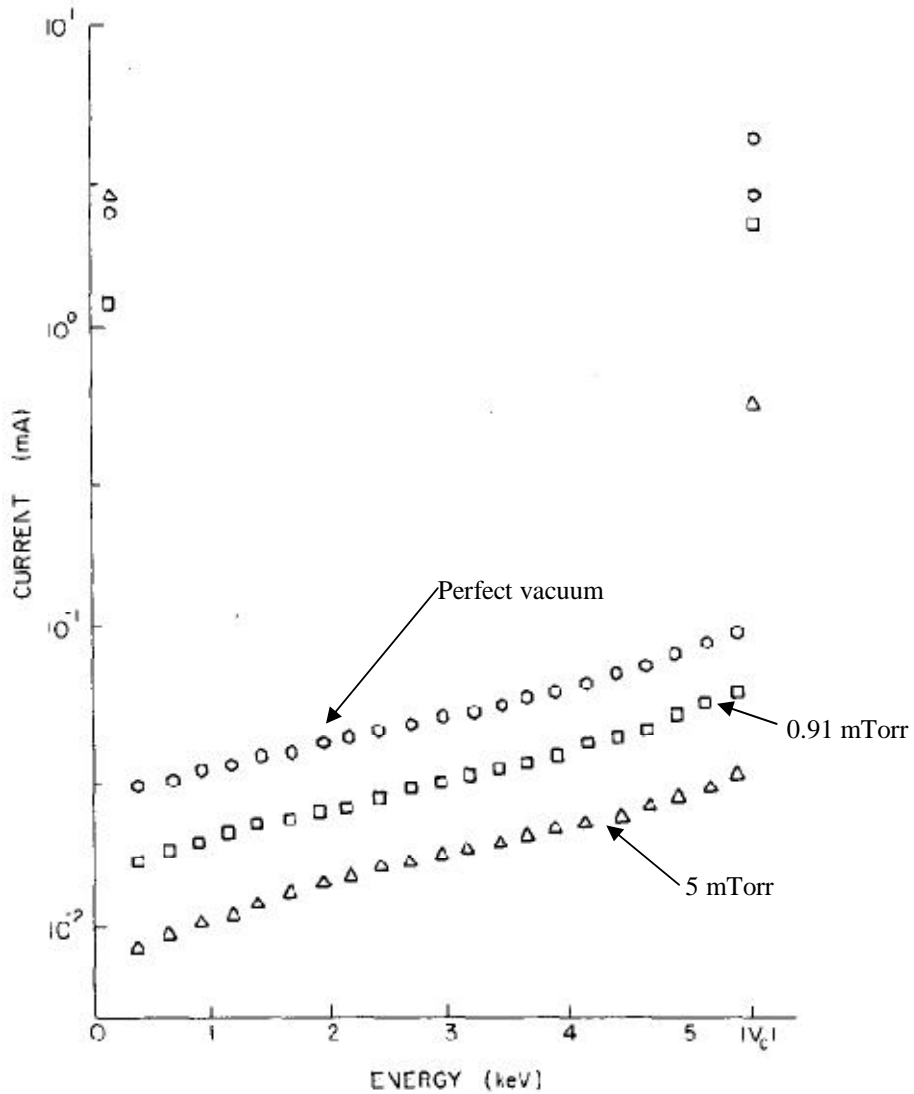


Figure 2-13: Ion energy spectrum predicted by the computation code at infinite vacuum, 0.12 Pa, and 0.68 Pa of background pressure. This figure was taken from Figure 3 of Black-1974 [19]

The radial energy and angular momentum distribution functions were then substituted into the Poisson equation. The resultant solution agreed with the original potential profile shown in Figure 2-12. With this model, Black adjusted key experimental parameters to gain insight into which parameters were most important for the creation of deep potential wells.

At ion currents on the order of 10 mA, inadequate spherical focusing and charge neutralization were the most critical factors. In order for factors such as grid transparency and background pressure to play a role, the grids must be spherical within a few percent. As the ion current was increased, the effect of non-spherical focusing was diminished and a deep potential well was predicted to form more easily. Figure 2-14 is a sample of the paper's results. Even though this model was used to explore how deep wells could be formed, Black pointed out that the underlying assumption of the model was a shallow well; therefore the validity of the model for deep wells is uncertain since the ion energy spectrum may change with well depth. [19]

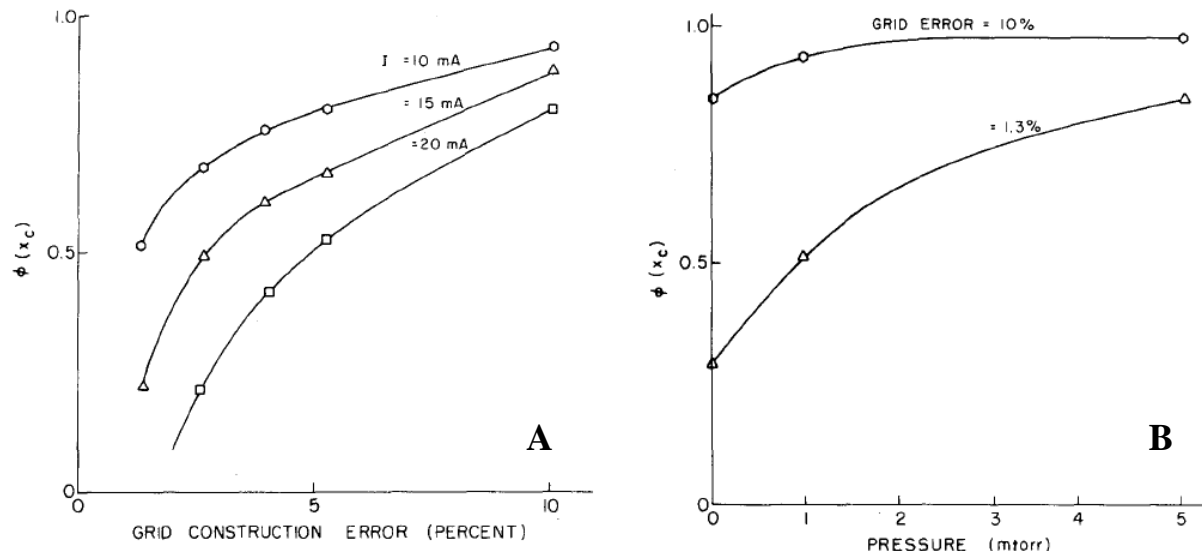


Figure 2-14: Normalized depth of the potential well inside the cathode with an applied potential of -5.5 kV and a grid transparency of 85%. Chart A shows the predicted well depth as a function of the deviation of the cathode shape from a true sphere at various ion currents, and at a gas pressure of 0.12 Pa. Chart B shows the well depth as a function of gas pressure for two different amounts of deviation in cathode shape, and at an ion current of 10 mA. These figures were taken directly from figure 4 and 6 of Black-1974. (1 mTorr = 0.13 Pa) [19]

With the increased availability of computer power and advanced simulation techniques, a 1997 paper by Ohnishi [20] investigated potential well formation using a particle-in-cell (PIC) technique. Ohnishi reported the results of a time dependent 1D spatial

and 2D velocity space PIC code along with a steady-state analytic solution. His results showed that single, double, and triple wells could be formed with mono-energetic ions, and the depth of the potential well was dependent on the injected ion current. As ion energy spread and angular momentum were added to the model, double well formation could still be achieved; however it required an injected ion current above a threshold value. Below the threshold there was a linear dependence between the ion current and the neutron output. Note that the Hirsch experiment observed linear scaling of the neutron output with current. Above the threshold, the neutron output scaled as multiple powers of the ion current. [7] The power of the scaling was a function of the amount of radial energy spread and the angular momentum of the injected ions. The neutron production rate scaled at a lesser power of the ion current as the radial energy spread of the ions increased. Examples of these results are shown in Figure 2-15. In addition, the neutron output was found to be inversely proportional to the radius of the ion focus area. As the focusing of the ions improved and as the ion energy spectrum became closer to the mono-energetic case the ion current threshold decreased and the neutron rate scaling with current increased. Therefore, to achieve these results experimentally, an experimental device would need to be well focused and operate at low enough pressures to minimize ion interactions with the background gas.

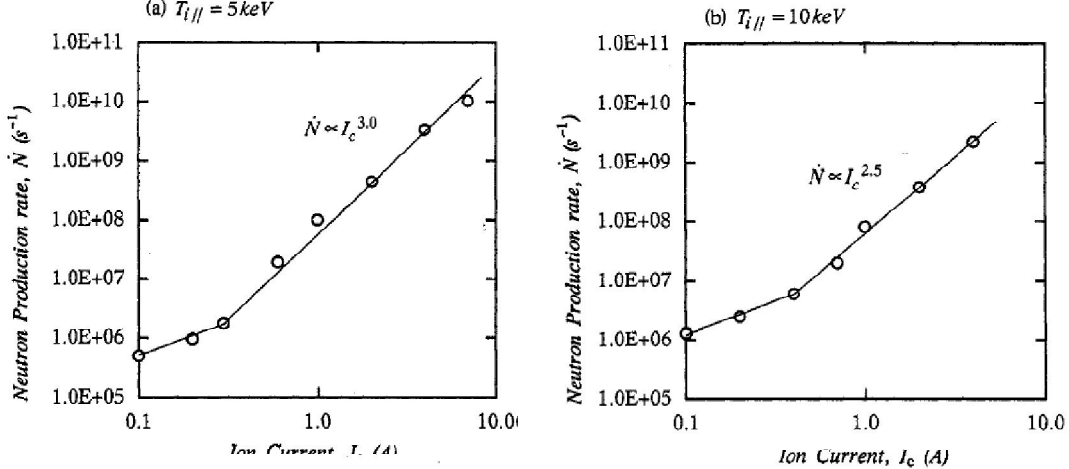


Figure 2-15: Simulated neutron production rate as a function of ion current for two different values of radial ion energy spread, a) 5 keV and b) 10 keV. These figures were taken directly from figure 9 of Ohnishi. [20]

In a 1973 article, Hu and Klevans [21] presented and refuted several non-virtual-potential-well explanations for Hirsch's results. The first explanation proposed that the fusion reactions were occurring inside the ion guns. The second was that the neutron production was caused by embedded fusion in the metal of the cathode. Hu argued that these hypotheses could not explain the sensitivity of the neutron rate to the alignment of the ion guns. If the fusion was dominated by reactions in the ion guns, it should be independent of the cathode alignment. If it was dominated by embedded reaction in the cathode the total neutron yield should have remained constant or even increased as more of the ions were allowed to directly strike the cathode in a mis-aligned state. [21] This author believes Hu's argument against fusion occurring by embedded ions in the cathode may be clouded by the effects of secondary electron emission from the cathode. Misalignment could have caused more ions to strike the outside surfaces of the cathode. Ion strikes on the outside of the cathode would produce secondary electrons that would not be trapped, and that would be accelerated toward the anode and contribute to the total current on the high voltage power supply. This would decrease the ion current, and thus the fusion rate, for the same high

voltage power and skew the neutron yield per unit of power. This argument will be further developed in the discussion section of this dissertation, Section 6.3.

Another theory dismissed by Hu, was that a cold neutral plasma formed at the center of the device and interacted with the beam. He calculated that a cold plasma density of  $10^{15}$  to  $10^{16}$  cm<sup>-3</sup> would be required to account for the observed neutron output. This is an unrealistically high density for this device. In addition, the plasma density would therefore be expected to increase, and thus increase the fusion rate, as a function of pressure. This, however, was not the experimental observation. [21]

In a 1982 paper, Baxter [22] further developed the hypothesis that the Hirsch experiential results could be explained by the effects of charge exchange and ionization with the background gas within the acceleration region of the ion guns. According to Baxter, a virtual potential well may have been formed but was unlikely to be the dominant source of fusion. Baxter presented a 1-D position and 1-D velocity space analysis of the effects of atomic charge exchange and atomic ionization cross-sections on a Hirsch-like system. He explained Hirsch's observation of the increase in fusion rate with decreased pressure by a hardening of the ion energy spectrum due to less atomic interactions with the neutral background gas. The lower energy spectrum at higher pressures would have a lower fusion cross-section and thus have a lower neutron production rate. Figure 2-16 shows Baxter's predicted neutron rate as a function of pressure in the acceleration region of a Hirsch like device. The inverse neutron rate to pressure scaling in Figure 2-16 is only at pressures greater than approximately 2.7 Pa. The Hirsch device operated below 2.7 Pa at pressures between 13 mPa and 1 Pa. Baxter attempted to explain the pressure discrepancy by the location of the pressure gauge relative to the acceleration region of the device.

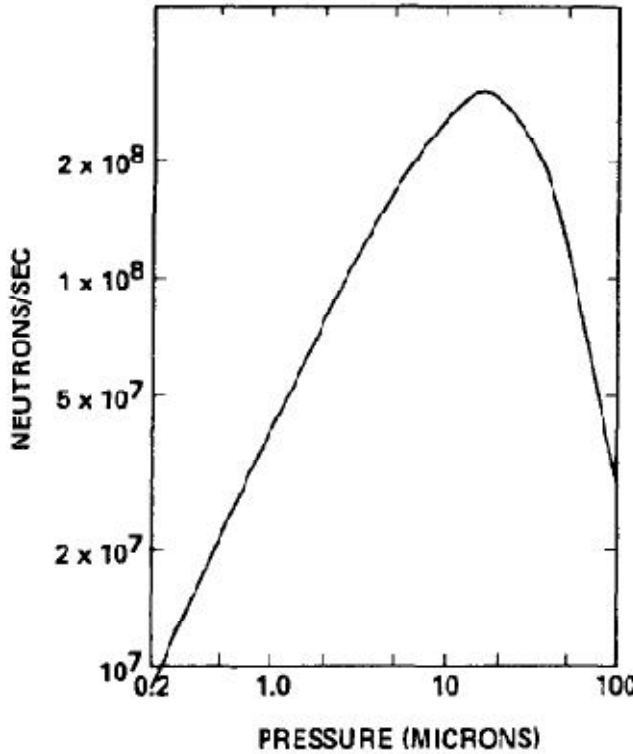


Figure 2-16: Calculated neutron production rate as a function of pressure, including ionization and charge exchange in the accelerating region. Figure and caption taken directly from figure 3 of Baxter-1982 [22] (1 micron = 1 mTorr = 0.13 Pa)

Since Hirsch's publication, [7] there have been multiple attempts to explain his experimental results and to further explore the hypothesis of producing a virtual potential well with spherically converging ions and electrons. From the body of theoretical and experiment papers on the IEC concept this author gleaned several key points that were used to guide the development of the Hirsch-like device constructed for this dissertation, the SIGFE. These key points included the following.

- Multiple potential well formations have been shown to be theoretically possible, even when finite amounts of radial ion energy spread and angular momentum were included.
- Experiments have shown that virtual electrodes can form and that the electrical potential of these virtual electrodes is dependent on the ion current, radius of ion

focus, radial ion energy spread and angular momentum of the ions. It is only weakly dependent on the applied cathode potential.

- Well formation may exhibit an injected ion current threshold. The value of this threshold is directly proportional to the amount of radial energy spread and the magnitude of the angular momentum.

Based on these key points, the design of the SIGFE emphasized the ability to focus and align the ion beams at the center of the device, and the ability to operate at pressures that minimized ion interactions with the background gas.

### **2.3. Previous experiments for the production of radioisotopes in IEC devices**

The production of radioisotopes for Positron Emission Tomography (PET) is a relatively mature, yet still growing field. The annual sales of  $^{18}\text{F}$  in the form FDG was \$398 million in 2007 and is expected to grow to \$1.36 billion by 2014. [23] Charged particle accelerators are the main source for  $^{18}\text{F}$  and other PET radioisotopes. They are capable of synthesizing several hundred different compounds by accelerating protons, deuterons, and alpha particles to energies in the range of 10 to 30 MeV. Table 2-2 lists various attributes for four PET isotopes of interest for production in an IEC device. They are of interest due to their short half-lives, which require they be produced locally. Two separate researchers at the UW have produced radioisotopes at the proof-of-concept level using an IEC device; Weidner in 2003, [25] and Cipiti in 2004. [9]

Table 2-2: Properties of Radioisotopes for Positron Emission Tomography [24]

Isotope	Production Reaction	Half-life [minutes]	Maximum $\beta^+$ Energy	Compounds	Approximate Dosage
$^{11}\text{C}$	$^{14}\text{N}(\text{p},\alpha)^{11}\text{C}$ $^{10}\text{B}(\text{d},\text{n})^{11}\text{C}$ $^{11}\text{B}(\text{p},\text{n})^{11}\text{C}$	20.4	960 keV	Carbon dioxide Hydrogen cyanide Methane	2-10 mCi (74-370 MBq)
$^{13}\text{N}$	$^{16}\text{O}(\text{p},\alpha)^{13}\text{N}$ $^{12}\text{C}(\text{d},\text{n})^{13}\text{N}$	9.97	1.19 MeV	Ammonia Nitrogen Nitrous oxide	10-15 mCi (370-555 MBq)
$^{15}\text{O}$	$^{15}\text{N}(\text{p},\text{n})^{15}\text{O}$ $^{14}\text{N}(\text{d},\text{n})^{15}\text{O}$	2.05	1.72 MeV	Oxygen Water Carbon dioxide	1 mCi (37 MBq)
$^{18}\text{F}$	$^{18}\text{O}(\text{p},\text{n})^{18}\text{F}$ $^{20}\text{Ne}(\text{d},\alpha)^{18}\text{F}$	109.8	635 keV	Fluorine Fluorodeoxyglucose Fluoridic acid	2-10 mCi (74-370 MBq)

Using a flux of 14.7 MeV protons from D- $^3\text{He}$  fusion reactions created in the gridded, spherical IEC device shown in Figure 2.7, Weidner produced  $^{13}\text{N}$  in the form of  $^{13}\text{NH}_3$  contained in 1.6 L of water. The fusion protons reacted with the  $^{16}\text{O}$  in high purity water contained in the radiator-type device shown in Figure 2-17. The radiator was constructed of thin-walled, 0.013 cm thick, stainless tubing. The original design used 0.036 cm thick aluminum tubes; however these tubes quickly developed pinholes caused by focused electron jets accelerated out of the cathode. During the isotope production experiments, the fusion rate was  $7.5 \times 10^6$  protons per second (p/s) at operating conditions of 145 kV, 35 mA and 0.2 Pa. This was maintained for 20 and 15 minutes in separate experimental runs that produced 0.20 nCi and 0.12 nCi samples of  $^{13}\text{N}$ . [25]



Figure 2-17: Picture of radiator device for producing radioisotopes in an IEC device. Figure taken from Figure 3.11 of Weidner-2003. [25]

Cipiti took a different approach to producing isotopes. Using the knowledge that 99% of the D-<sup>3</sup>He fusion reactions are embedded in the cathode, he replaced the cathode with the reactant need for the desired isotope. In his first experiments, the cathode was replaced by a solid sphere of Mo. Natural Mo contains 10% <sup>94</sup>Mo, which through the <sup>94</sup>Mo(p, n)<sup>94m</sup>Tc reaction produces <sup>94m</sup>Tc. Running the experiment at 110 kV and 30 mA with a fusion rate of  $6 \times 10^6$  p/s for 15 minutes he produced 1.5 nCi of <sup>94m</sup>Tc.

To produce <sup>13</sup>N, Cipiti replaced the cathode with a stainless steel tube of wall thickness 0.13 cm as shown in Figure 2-18. D-<sup>3</sup>He fusion occurred in the tubing wall. Roughly half the resulting 14.7 MeV fusion protons traversed the center of tube and the purified water that circulated in the tubing. Maximum operating parameters of -85 kV and

30 mA (approximately  $4 \times 10^6$  p/s) were reached for a short time and produced 1.0 nCi of  $^{13}\text{N}$ . Cipiti estimated the maximum performance of this design, if it could be operated at -200 kV, to be approximately 1.2  $\mu\text{Ci}$  per mA of high voltage current. Therefore, to reach commercial production levels ( $\sim 1 \text{ mCi}$ ) 800 mA of current would be required, or 160 kW of power. This amount of electric power would present engineering difficulties and increase the cost of a commercial device. Based on these results, Cipiti conjectured that to meet the design goals of a portable, low cost radioisotope production device, IEC technology would have to move beyond the beam-embedded fusion mode to a converged-core mode like suggested by the Hirsch experiment. [9]

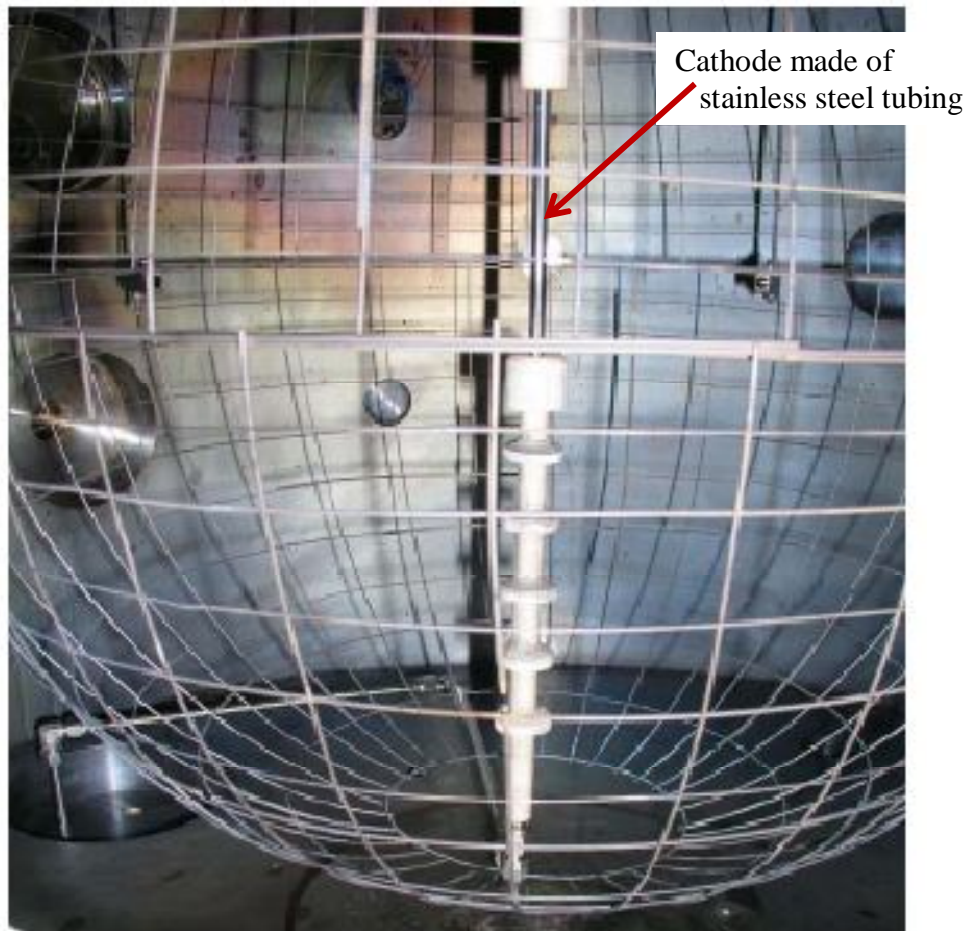


Figure 2-18: Picture of thin walled, water filled, stainless steel tube acting as the cathode for the production of  $^{13}\text{N}$ . Figure taken from Figure 10-7 of Cipiti 2004. [9]

## 2.4. References for Chapter 2.

---

1. Elmore, W. C., Tuck, J. L., & Watson, K. M. (1959). On the inertial-electrostatic confinement of a plasma. *Physics of Fluids*, 2(3), 239-246.
2. Farnsworth, P. T. (1962). Electric Discharge Device for Producing Interactions between Nuclei. Patent Number: 3,258,402. June 28, 1966
3. Emmert, G. A., & Santarius, J. F. (2010). Atomic and molecular effects on spherically convergent ion flow. I. Single atomic species. *Physics of Plasmas*, 17
4. Emmert, G. A., & Santarius, J. F. (2010). Atomic and molecular effects on spherically convergent ion flow. II. Multiple molecular species. *Physics of Plasmas*, 17
5. Santarius, J.F. (2008). Personal communication. University of Wisconsin – Madison
6. Bosch, H. S., & Hale, G. M. (1992). Improved formulas for fusion cross-section and thermal reactivities. *Nuclear Fusion*, 32(4), 611-31.
7. Hirsch, R. L. (1967). Inertial-electrostatic confinement of ionized fusion gases. *Journal of Applied Physics*, 38(11), 4522-4534.
8. University of Wisconsin-IEC unpublished results
9. Cipiti, B. B. (2004). The fusion of advanced fuels to produce medical isotopes using inertial electrostatic confinement. (PhD dissertation, University of Wisconsin – Madison)
10. Boris, D.R. (2009). Novel diagnostic approaches to characterizing the performance of the Wisconsin Inertial Electrostatic Confinement plasma. (PhD dissertation, University of Wisconsin – Madison)
11. Hirsch, R. L., & Meeks, G. A. (1967). Highly efficient, inexpensive, medium current ion source. *Review of Scientific Instruments*, 38(5), 621-624.
12. T. Fujimoto, T. Oishi, H. Zen, K. Masuda, and K. Yoshikawa, (2007). Intensity Distribution of D-3He Fusion Reaction Rate in an IEC Device, *22nd IEEE/NPSS Symposium on Fusion Engineering*, Albuquerque, NM, USA, 134-137
13. Gardner, A. L., Hatch, D. M., Chan, A. I. Y., & Evans, R. P. (1974). Measurements on a Spherical Electrostatic Confinement System Employing Six Ion Guns. *Annals of the New York Academy of Sciences*, 251, 179-189.
14. Verdeyen, J. T., Cherrington, B. E., Swanson, D. A., & Meeker, D. J. (1974). Recent Developments in Electrostatic Confinement - Experimental. *Annals of the New York Academy of Sciences*, 251, 126-138.
15. Black, W. M., & Robinson, J. W. (1974). Measuring rotationally symmetric potential profiles with an electron-beam probe. *Journal of Applied Physics*, 45(6), 2497-501.
16. Rosenberg, M., & Krall, N. A. (1992). The effect of collisions in maintaining a non-maxwellian plasma distribution in a spherically convergent ion focus. *Physics of Fluids B (Plasma Physics)*, 4(7), 1788-94.
17. Dolan, T. J., Verdeyen, J. T., Meeker, D. J., & Cherrington, B. E. (1972). Electrostatic-inertial plasma confinement. *Journal of Applied Physics*, 43(4), 1590-600.

- 
18. Cherrington, B. E., Verdeyen, J. T., & Swanson, D. A. (1975). Recent Developments in Electrostatic Confinement-Theoretical. *Annals of the New York Academy of Science*, 251, 139-151.
  19. Black, W. M., & Klevans, E. H. (1974). Theory of potential-well formation in an electrostatic confinement device. *Journal of Applied Physics*, 45(6), 2502-11.
  20. Ohnishi, M., Sato, K. H., Yamamoto, Y., & Yoshikawa, K. (1997). Correlation between potential well structure and neutron production in inertial electrostatic confinement fusion. *Nuclear Fusion*, 37(5), 611-619.
  21. Hu, K. M., & Klevans, E. H. (1974). On the Theory of Electrostatic Confinement of Plasmas with Ion Injection. *Physics of Fluids*, 17(1), 227-231.
  22. Baxter, D.C., & Stuart, G.W. (1982). The effect of charge exchange on ion guns and an application to inertial electrostatic confinement devices. *Journal of Applied Physics*, 53(7), 4597-4601
  23. BIO-TECH report #270, The US market for Diagnostic Radiopharmaceuticals. (2007). Retrieved 2-2-2010 from biotechsystems.com/reports/270/default.asp
  24. Cherry, S. R., Sorenson, J. A., & Phelps, M. E. (Eds.). (2003). *Physics in nuclear medicine (3rd ed.)*. Philadelphia, Pennsylvania: Saunders.
  25. Weidner, J. W. (2003). The production of N-13 from inertial electrostatic confinement fusion. (M.S. dissertation, University of Wisconsin - Madison).
  26. Radel, R. F. (2007). Detection of highly enriched uranium and tungsten surface damage studies using a pulsed inertial electrostatic confinement fusion device. (Doctoral dissertation, University of Wisconsin - Madison).
  27. Masuda, K. et. al., (2007), Anti-personnel landmine detection by use of an IEC neutron source, Presented at US-Japan IEC workshop 2007, Argonne National Lab
  28. Thorson, T.A., Durst, R. D., Fonck, R.J., & Sontag, A.C., (1998). Fusion reactivity characteristics of a spherically convergent ion focus. *Nuclear Fusion*. 38(4), 495-507
  29. Yamauchi, K., Tashiro, A., & Shura, S., (2005). Performance characteristics of ion-source-assisted cylindrical IEC fusion neutron/proton source, Presented at US-Japan IEC workshop 2005. Los Alamos National Lab
  30. Demora, J. M., (1999). *Cathode grid optimization studies for the spherical IEC device*. (Master's thesis University of Illinois-Urbana)
  31. Yamamoto, Y., Hasegawa, M. and Ohnishi, M., (1997). Preliminary studies of potential well measurement in IEC fusion experiment, Presented at IEEE-SOFE 1998.
  32. Yoshikawa, K, Masuda, K, Takamatsu, T, et. al. (2007). Anti-personnel landmine detection by use of an IEC neutron source, presentation at the US-Japan IEC workshop- 2007, Argonne National Lab
  33. Ohnishi, M. Osawa, H. Tabata, T. & Yoshimura, S. (2005). Neutron yield in IEC fusion, presentation at the US-Japan IEC workshop-2005, Los Alamos National Lab

34. Gu, Y., & Miley, G.H., (2000). Experimental study of potential structure in a spherical IEC fusion device, *IEEE Trans on Plasma Science*. 28(1) 331-346
35. Miley, G. (1997). The IEC approach to fusion power, Current Trends in International Fusion Research edited by Panarella, *Plenum Press*, New York, NY
36. Daimler-Benz Aerospace, (1994). Preliminary announcement: Fusion Star IEC-PS1, Bremen Germany
37. Tomizawa, T., Higashi, T. Daino, M. & Yamamoto, Y., (2003). Characteristics of the cylindrical IECF experiments of low gas pressure operation, Presented at US-Japan IEC workshop-2003. Tokyo Institute of Technology.



### Chapter 3. Ion extraction and ion gun theory

The ion source and extraction system used for the Hirsch experiments [1] and developed by Hirsch and Meeks [2], was able to focus the 1 to 10 mA of ions produced in a simple filament-assisted DC discharge plasma through a small orifice (~1.5 mm diameter) by optimizing the shape of the plasma emissive area to act as a lens. Neither of two papers published by Hirsch or Meeks on this source discussed the theory of how the plasma boundary formed to focus the ions through the aperture in the extraction electrode. This section will compile the theory of how the plasma sheath forms a concave surface in response to the plasma density, plasma temperature, and extraction voltage. Figure 3-1 is a schematic of the electrode configuration of the ion source. A detailed description of the experimental hardware can be found in Chapter 4.

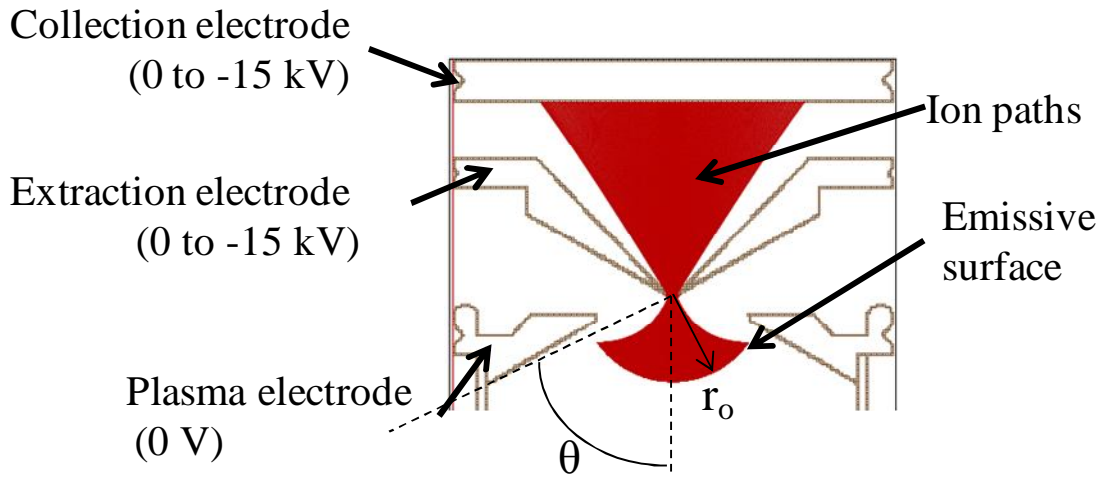


Figure 3-1: Schematic of ion extraction test setup with simulated ion trajectories

Within the limits of this system, the amount of steady-state ion current that can be extracted from the plasma is simultaneously constrained by both the emission limit of the plasma and space-charge current limit between the plasma boundary and the extraction

electrode. The emission limit of the plasma is shown in eqn 3-1 and is called the Bohm current density,  $J$ .

$$J = \frac{I}{A} = 0.4 n_e e \sqrt{\frac{2 k T_e}{M_i}} \approx 8.9 \times 10^{-14} n_e \sqrt{\frac{T_e}{M_i [AMU]}} \left[ \text{Amps/cm}^2 \right] \quad \text{Eqn 3-1}$$

Where  $I$  is the extractable ion current,  $A$  is the surface area of the plasma boundary,  $T_e$  is plasma electron temperature in eV,  $n_e$  is plasma density in  $\text{cm}^{-3}$ ,  $M_i$  is the ion mass, and  $e$  is electron charge. The factor of 0.4 in front of the equation is dependent on the characteristics of the bulk plasma, namely the uniformity of ionization and geometry. It may vary from 0.3 to 0.9. A value of 0.4 was arbitrarily chosen, since it was the most common value cited in the literature. [3, 4]

The amount of current that can be transported between the plasma boundary and the extraction electrode is limited by the space charge of the transported charge particles; this is known as the Child-Langmuir limit. For this analysis, the extraction electrode is assumed to be a small sphere at the tip of the extraction electrode with a radius,  $r_e$ , which is assumed to be the same as the radius of the circular orifice in the center of the electrode. The emissive electrode is assumed to be the boundary of the plasma. For a plasma boundary radius,  $r_o$ , much larger than the orifice radius, spherical coordinates are a good approximation to the symmetry of the system. The derivation of the space charge current limit between the plasma and the extraction aperture begins with the radial component of the Poisson equation in spherical coordinates, shown in eqn 3-2, where  $V$  is potential at any radius,  $r$ , between the electrodes, and  $\rho$  is the charge density.

$$\frac{1}{r^2} \frac{d}{dr} \left( r^2 \frac{dV}{dr} \right) = -\frac{\rho}{\epsilon_0} \quad \text{Eqn 3-2}$$

The charge density is given by eqn 3-3 and is function of the charged particle current,  $I$ , and the velocity of the particles,  $v$ .

$$\rho = \frac{I}{4\pi r^2 v} \quad \text{Eqn 3-3}$$

The particle velocity at radius  $r$  can be given as a function of the potential at that radius and the particle's mass as shown in eqn 3-4

$$v = \left( \frac{2eV}{M_i} \right)^{1/2} \quad \text{Eqn 3-4}$$

Combining eqns 3-2, 3-3, and 3-4 yields

$$\frac{1}{r^2} \frac{d}{dr} \left( r^2 \frac{dV}{dr} \right) = - \frac{I}{4\pi\epsilon_0 r^2} \left( \frac{M_i}{2eV} \right)^{1/2} \quad \text{Eqn 3-5}$$

A closed solution of equation 3-5 has not been found, but a numerical solution was expressed by Langmuir and Blodgett [5] as seen in eqn 3-6 in terms of  $\alpha^2$ .

$$I_{4\pi} = \frac{16\pi\epsilon_0}{9} \sqrt{\frac{2e}{M_i}} \frac{V_e^2}{\alpha^2}^{3/2} \quad \text{Eqn 3-6}$$

$V_e$  is the voltage applied to the extraction electrode. The emissive surface of the plasma was assumed to be at 0 V. Eqn 3.6 is the space charge current limit between two complete concentric spheres. Eqn 3.7 is a scaled version of eqn 3.6 to include only the fraction of the sphere of interest, where  $\theta$  is the angle between the z-axis and the grounded plasma aperture as seen in Figure 3-1.

$$I = \frac{16\pi\epsilon_0}{9} \sqrt{\frac{2e}{M_i}} \frac{V_e^2}{\alpha^2}^{3/2} \sin^2 \left( \frac{\theta}{2} \right) \quad \text{Eqn 3-7}$$

The value of  $\alpha^2$  was determined from Table 2-1, which is a tabulation of either the series or integral form of  $\alpha^2$  reproduced by Forrester [4] from the Langmuir-Blodgett paper.

Table 3-1: Values of  $\alpha^2$  for the spherically converging case,  $r_o > r_e$ . Values reproduced from table 2.1 of Forrester [4]

$\frac{r_o}{r_e}$	$\alpha^2$	$\frac{r_o}{r_e}$	$\alpha^2$	$\frac{r_o}{r_e}$	$\alpha^2$
1.0	0	2.0	0.75	14	51.86
1.1	0.0096	2.5	1.531	20	93.24
1.2	0.0372	3.0	2.512	30	178.2
1.3	0.0809	4.0	4.968	50	395.3
1.4	0.1396	5.0	7.976	70	663.3
1.5	0.2118	6.0	11.46	100	1144
1.6	0.2968	8.0	19.62	200	3270
1.8	0.502	10	29.19	500	13015

Over the specific range of values of interest for this system the values in Table 2-1 are well behaved and were fit with a least squares method as eqn 3-7 within the accuracy required for this application.

$$\alpha^2 \cong 0.668 \left( \frac{r_o}{r_e} \right)^{1.645} \text{ for } 10 < \frac{r_o}{r_e} < 30 \quad \text{Eqn 3-8}$$

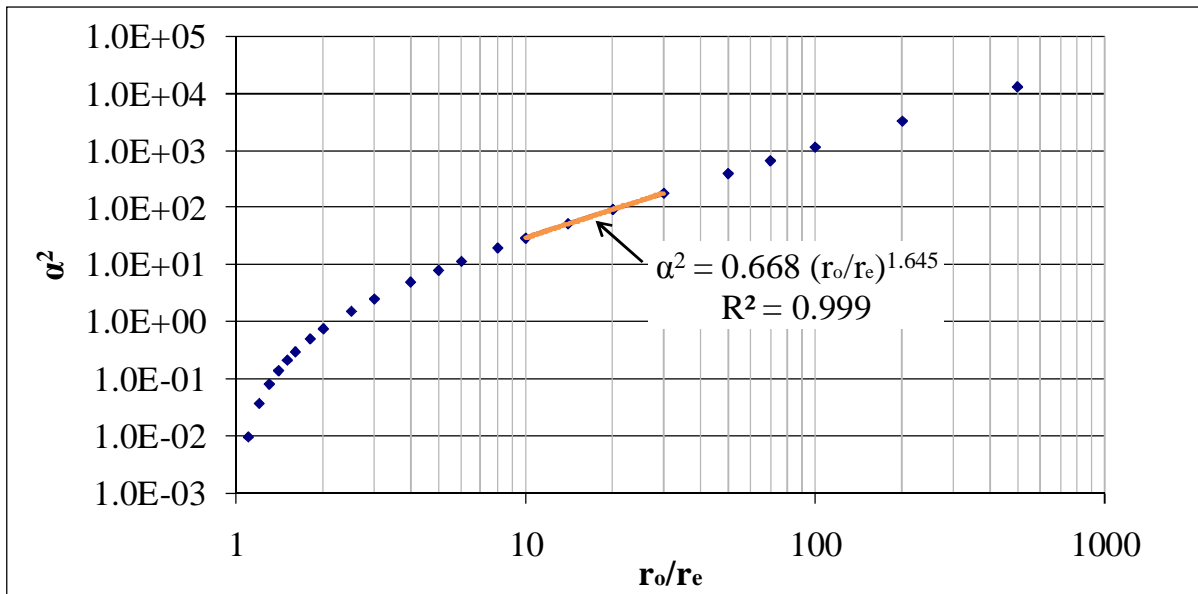


Figure 3-2: Graph of  $\alpha^2$  values from table 2.1 of Forrester [4]. The fit between  $\frac{r_o}{r_e}$  values of 10 and 30 is shown.

The Child-Langmuir current limit for this system can be approximated from eqn 3-9, which is a result of combining eqn 3-7 and 3-8, changing to AMU for mass units, and simplifying.

$$I \cong 1.03 \times 10^{-6} \frac{V_e^{\frac{3}{2}}}{\sqrt{M_i[\text{AMU}]}} \left(\frac{r_e}{r_o}\right)^{1.645} \sin^2\left(\frac{\theta}{2}\right) \text{ for } 10 < \frac{r_o}{r_e} < 30 \quad \text{Eqn 3-9}$$

The shape and position of the plasma boundary adjusts to simultaneously satisfy the plasma emissive current limit, eqn 3-1, and the space charge current limit, eqn 3-9, when the plasma and extraction parameters are within the limits that allow for the spherical geometry assumption and when the system has reached steady-state. The approximate shape of the plasma boundary can be calculated by solving eqn 3-1 for  $I$  and setting it equal to 3-9.  $A$  is the surface area of the plasma boundary and is in  $\text{cm}^2$ .

$$8.9 \times 10^{-14} A n_e \sqrt{\frac{T_e}{M_i[\text{AMU}]}} \cong 1.03 \times 10^{-6} \frac{V_e^{\frac{3}{2}}}{\sqrt{M_i[\text{AMU}]}} \left(\frac{r_e}{r_o}\right)^{1.645} \sin^2\left(\frac{\theta}{2}\right)$$

$$\text{for } 10 < \frac{r_o}{r_e} < 30 \quad \text{Eqn 3-10}$$

Based on the geometry of the system shown in Figure 3-1,  $A$  is approximated as the portion of a sphere of radius  $r_o$  subtended by the angle,  $\theta$ , between the z-axis and the grounded plasma aperture. This is likely a good assumption beyond several Debye lengths from the plasma aperture. Equation 3-11 gives the value of  $A$  used for the remaining calculations.

$$A = 2\pi r_o^2 (1 - \cos \theta) \quad \text{Eqn 3-11}$$

Substituting eqn 3-11 into eqn 3-10 and solving for  $r_o$  yields

$$r_o = 43.3 r_e^{0.451} \left( \frac{V_e^{\frac{3}{2}}}{n_e \sqrt{T_e}} \right)^{0.274} \text{ for } 10 < \frac{r_o}{r_e} < 30 \quad \text{Eqn 3-12}$$

The maximum total extractable ion current can be calculated by substituting eqn 3-12 back into either 3-1 or 3-9. The result from 3-1 is shown below, with  $I$  in amps,  $n_e$  in  $\text{cm}^{-3}$ ,  $T_e$  in eV,  $r_e$  in cm, and  $V_e$  in volts.

$$I [\text{amps}] = 1.05 \times 10^{-9} \frac{(1-\cos\theta)}{\sqrt{M_i[\text{AMU}]}} ( n_e \sqrt{T_e} )^{0.452} r_e^{0.902} V_e^{0.822} \quad \text{Eqn 3-13}$$

For typical experimental values of  $M_{i\text{AMU}} = 4$ ,  $\theta = 55^\circ$ ,  $n_e = 5 \times 10^9 \text{ cm}^{-3}$ ,  $T_e = 7 \text{ eV}$ ,  $r_e = 0.09 \text{ cm}$ , and  $V_e = 10 \text{ kV}$ , the ion current was calculated to be  $I = 1.5 \text{ mA}$ , which is in quantitative agreement with experimentally observed values. For the same values, the radius of the plasma boundary was calculated to be  $r_o = 1.1 \text{ cm}$ , which is a reasonable value in that it is larger than the plasma aperture and smaller than the dimension to the tube wall. Also,  $\frac{r_o}{r_e} = 12.2$ , which is within the range of validity of the approximation made for  $\alpha^2$ .

Equation 3-13 can calculate the total ion current drawn to the extraction electrode, however it does not have information about how much of that current can be successively extracted through the small orifice in the electrode versus the amount of current which would strike the physical electrode and be lost. To explore this relationship, the charged particle trajectory tracking code, SIMION® [6] was employed. A simplified version of the electrode geometry was imported into SIMION® from the more detailed SolidWorks® CAD model. To evaluate each set of electrode geometries a grid of ions was started at possible locations for the plasma meniscus to form. The geometries were ranked by the number of ions that started on a single radius that were extracted through the orifice in the extraction electrode. The range of valid radii was determined from equation 3-12. The geometries were also ranked on their insensitivity to changes in radius. Figure 3-3 shows an example of the analysis. The points on the graph indicate the locations inside the source region where free ions with zero energy would be accelerated through the extraction orifice. Several different

shapes of the plasma electrode were simulated before building an electrode with the shape seen in Figure 3-1. Several of the shapes investigated were adapted from designs found in the literature. [7, 8]

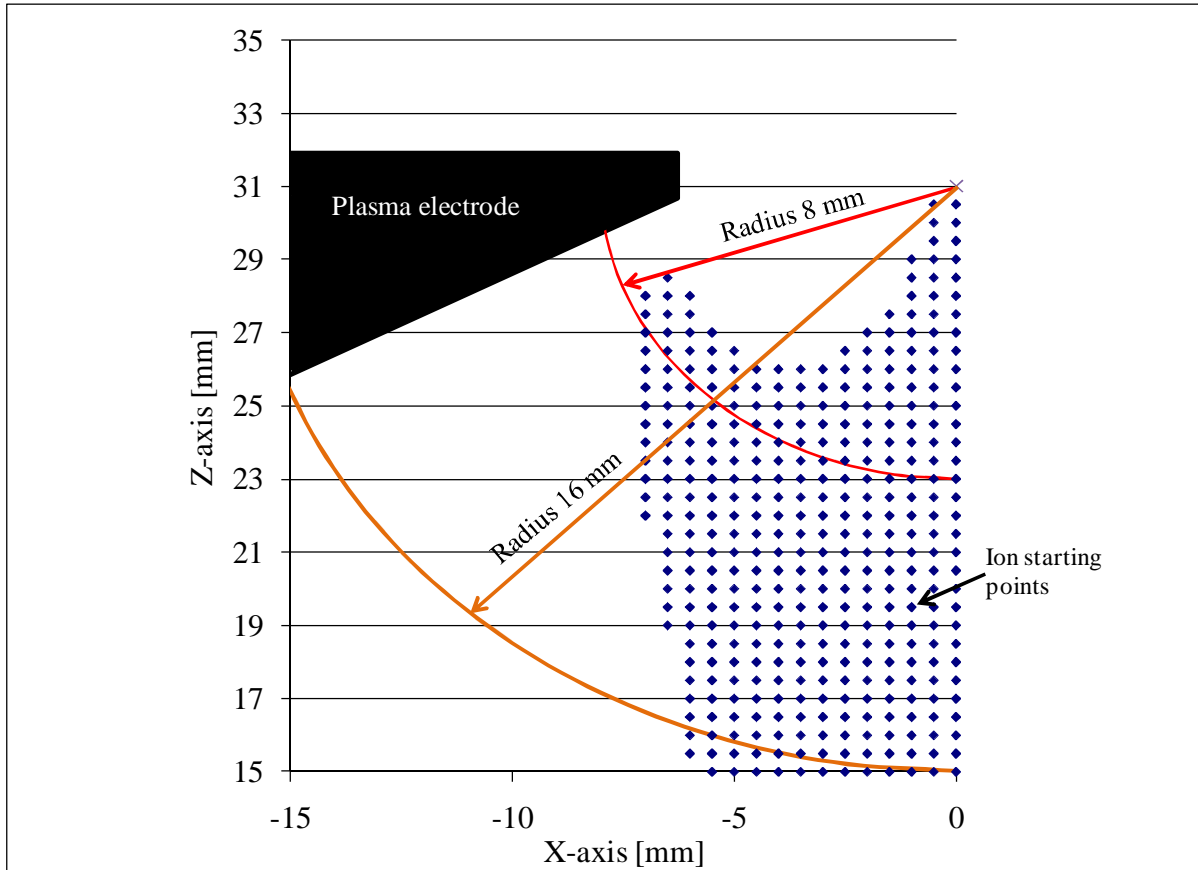


Figure 3-3: Sample result of SIMION<sup>®</sup> simulations to determine the starting locations of ions that could be accelerated and focused through the orifice in the extraction electrode

The theory governing the extractable ion current from a plasma guided the design of the experimental device and gave estimates of the performance that could be expected from a given design. Estimating the performance helped to evaluate possible designs so only the most promising designs were physically tested. The understanding gained was also valuable in interpreting the operation of the experiment.

## References for Chapter 3.

- 
1. Hirsch, R. L., & Meeks, G. A. (1967). Highly efficient, inexpensive, medium current ion source. *Review of Scientific Instruments*, 38(5), 621-624.
  2. Hirsch, R. L. (1967). Inertial-electrostatic confinement of ionized fusion gases. *Journal of Applied Physics*, 38(11), 4522-4534.
  3. Zhang, H., (1999) *Ion Sources*. Science Press Beijing. ISBN: 7-03-007351-7/O-1092
  4. Forrester A. T., (1988) *Large Ion Beams, Fundamentals of Generation and Propagation*, John Wiley & Sons Inc. New York, ISBN 0-471-62557-4
  5. Langmuir, I. and Boldgett, K.B. (1924). Currents limited by space charge between concentric spheres, *Phys. Rev.* 23(49) Reprinted in Suits (1961), Vol. 3, p. 125
  6. *SIMION Version 8.0*, (2009) Scientific Instrument Services, Inc, Ringoes, NJ, [www.simion.com](http://www.simion.com)
  7. L.R. Grisham, C.C. Tsai, J.H. Whealton, & W.L. Stirling, (1997). Effect of emission aperture shape upon ion optics, *Rev. Sci Instrum*, 48(8)
  8. M.M. Menon, C.C. Tsai, et al. (1985). Quasi-steady-state multimegawatt ion source for neutral beam injection, *Rev. Sci Instrum*, 56(2)

## Chapter 4. Six Ion Gun Fusion Experiment (SIGFE) design and construction

The Six Ion Gun Fusion Experiment (SIGFE) was designed and built to reproduce and extend the experiment published by Hirsch in 1967. [1] Several features of the Hirsch device that were incorporated into the SIGFE included 1) the use of six focused ion guns, 2) a cathode design that prevented electrons from escaping the inside of the cathode, and 3) a simple ion source extraction system that allowed the extraction of millamps of ion current at main chamber pressures as low as 6.7 mPa. The SIGFE extended beyond the Hirsch design with the addition of several features including: 1) adding focus lenses to the ion guns to allow beam focusing independent of the cathode potential, 2) improved mounting and alignment systems for the electrostatic lenses, 3) improved vacuum systems to achieve lower operating pressures, 4) improved instrumentation to aid in beam diagnostics, and 5) silicon-based charged particle detectors for detailed diagnoses of the experiment.

The first steps in the design process of the SIGFE was to develop a detailed understanding of the original Hirsch experiment and to identify critical design features from the body of theoretical papers reviewed in Chapter 2. The main design criterion taken from the literature review was the importance of well-aligned, well-focused mono-energetic beams to reduce the ion current required to produce virtual potential wells. A detailed three dimensional computer model was created in SolidWorks® [2] based on the original drawings published by Hirsch. From this model, simulations of the ion trajectories were conducted using SIMION® [3] to predict the performance of the ion optics of the Hirsch device. The knowledge gained from the previous publications and the reverse engineering of the Hirsch device was used as a starting point for designing the SIGFE. Figure 4-1 compares the final design of the SIGFE device to the recreated CAD model of the Hirsch device.

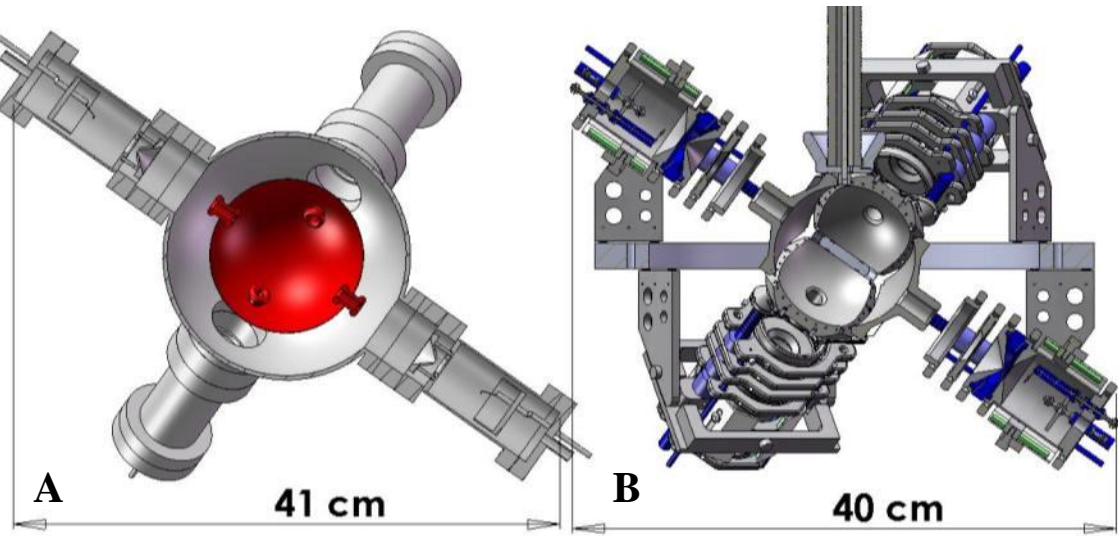


Figure 4-1: Comparison of the CAD models of the Hirsch device (A) to the final SIGFE design (B)

The development of the SIGFE was divided into three phases or major components:

- 1) the modular ion gun, and 2) infrastructure for all six ion gun modules, and 3) diagnostics.

The symmetry of the six gun design allowed a single ion gun to be designed and prototyped as an independent module that was replicated for the full experiment. This phased approach reduced development time. Figure 4-2 shows a pictorial timeline. SIGFE started as a concept in December of 2007 and was operational twelve months later in December of 2008.

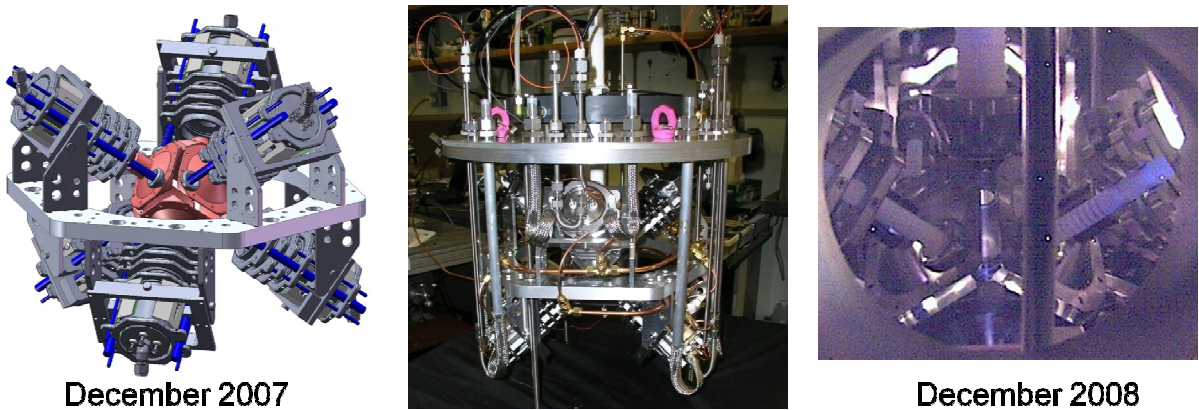


Figure 4-2: Pictorial timeline of the SIGFE development.

#### 4.1. Ion gun module design and construction

The purpose of the ion gun module was to produce, focus, and accelerate one to five millamps of D or  $^3\text{He}$  ions to the center of the full device, which was approximately 20 cm from the ion source. There were several distinct systems within each module: 1) the ion source plasma, 2) the ion extraction electrodes, 3) the ion focusing lenses, and 4) the main accelerating cathode. Figure 4-3 shows a cross-section view of the ion gun module. The inside shape of the cathode lens was machined to produced a 110 mm diameter sphere when all six modules were assembled together.

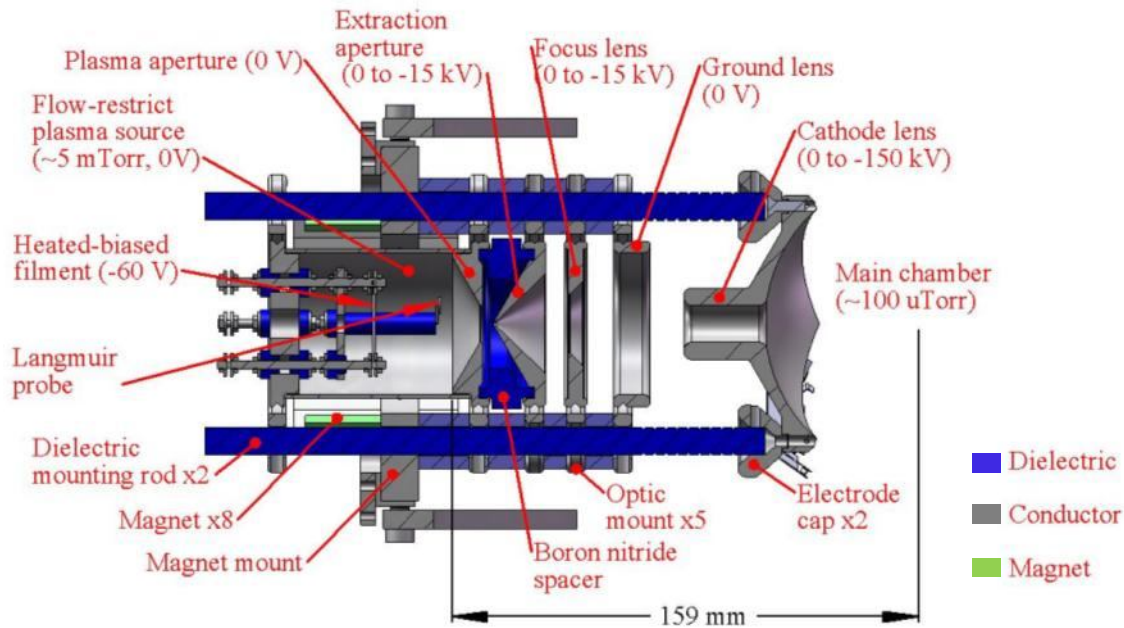


Figure 4-3: Cross-section drawing of ion gun module. Major components highlighted with operating voltages and pressures listed where appropriate.

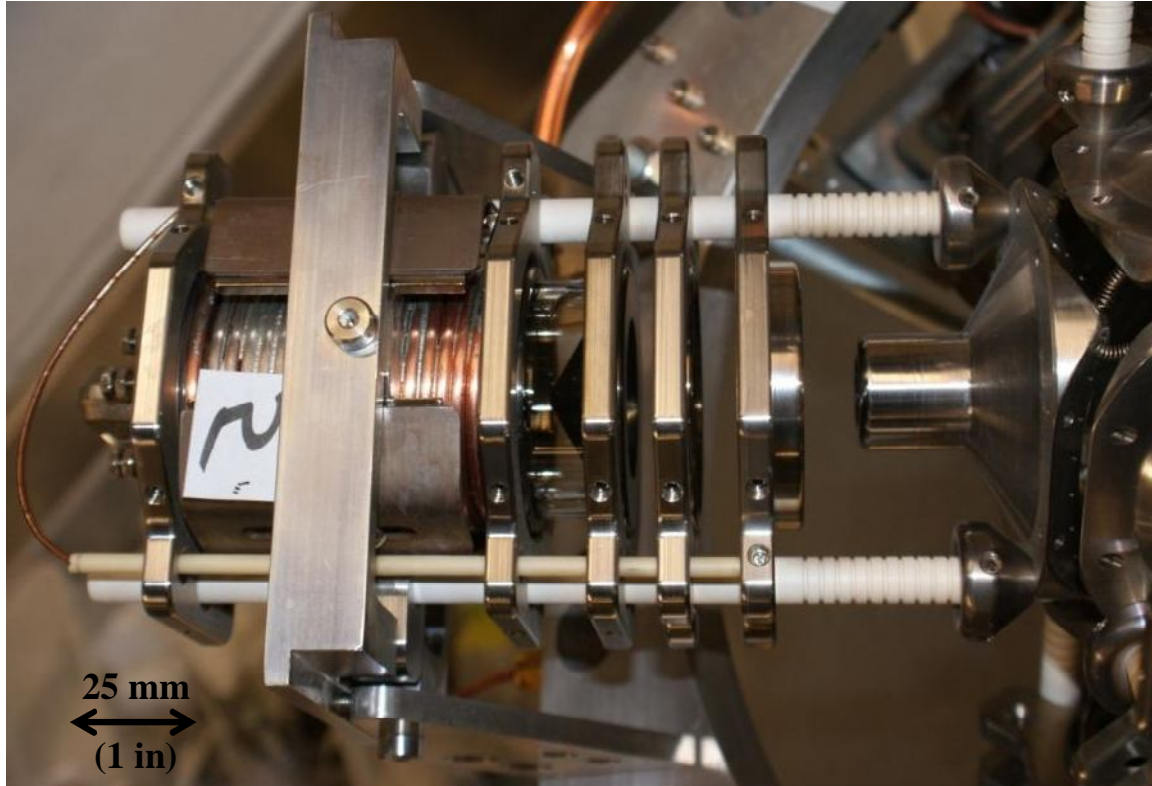


Figure 4-4: Photo of an ion gun module. White paper square is for scale and is 25 x 25 mm (1 x 1 inch). Boron nitride spacer replaced with quartz spacer to show extraction electrode.

#### 4.1.1. Plasma source and extraction

The source of the ions was a filament-assisted DC-discharge plasma with a 0 to -15 kV extraction electrode. To produce the required plasma density, which was on the order of  $10^9 \text{ cm}^{-3}$ , a neutral gas pressure of a few hundred mPa was required. In a competing requirement, the acceleration region of the gun required approximately 0.1 Pa or less of neutral gas pressure to minimize ion collisions with the background gas. To satisfy both requirements, the plasma source was fully contained in a stainless steel tube. A pressure difference between the plasma source and the main chamber was maintained by directly feeding the gas into the tube. The only intentional exit path for the gas was a 1.8 mm diameter hole in the center of the extraction electrode. A circular hole of that size was calculated to maintain a 38:1 pressure differential; see Section 4.2.7 for the complete calculation.

The extraction of millamps of ion current from a  $10^9 \text{ cm}^{-3}$  plasma required an emissive surface area much larger than afforded by the  $2.5 \text{ mm}^2$  hole in the extraction electrode. Therefore, the shape and voltage of the extraction electrodes were chosen to force the emissive surface, which was approximately the plasma sheath, to form a concave surface. The theory of how the shape and position of the plasma sheath was determined is described in Chapter 3. The experimental results, with comparison to the theory, are detailed in Chapter 5. This section will detail several of the engineering challenges and main components associated with the ion extraction system.

The source plasma was formed by feeding gas into a 48 mm diameter by 64 mm long stainless steel tube that contained a tungsten filament. The filament from a standard 300 W incandescent light bulb was used and was connected to the floating DC power supply. The power supply could maintain a 0 to 150 V DC across the filament while floating the entire filament at 0 to -400 V DC from the grounded stainless steel tube. A photo of the filament mount and the Langmuir probe is shown in Figure 4-5. The efficiency of the plasma source was enhanced by surrounding the tube with a cusp magnetic field. The magnetic field increased the lifetime of the electrons emitted from the filament and thus increased the ionization rate for a given filament power. Eight 51 x 6 x 3 mm super high temperature neodymium block magnets with alternating poles produced a cusp field of 0 to 250 G inside the tube. Steel shields were placed between the outwardly facing magnetic poles to increase the magnets' efficiency, minimize stray magnetic fields, and prevent stray electrons from directly heating the magnetic material.

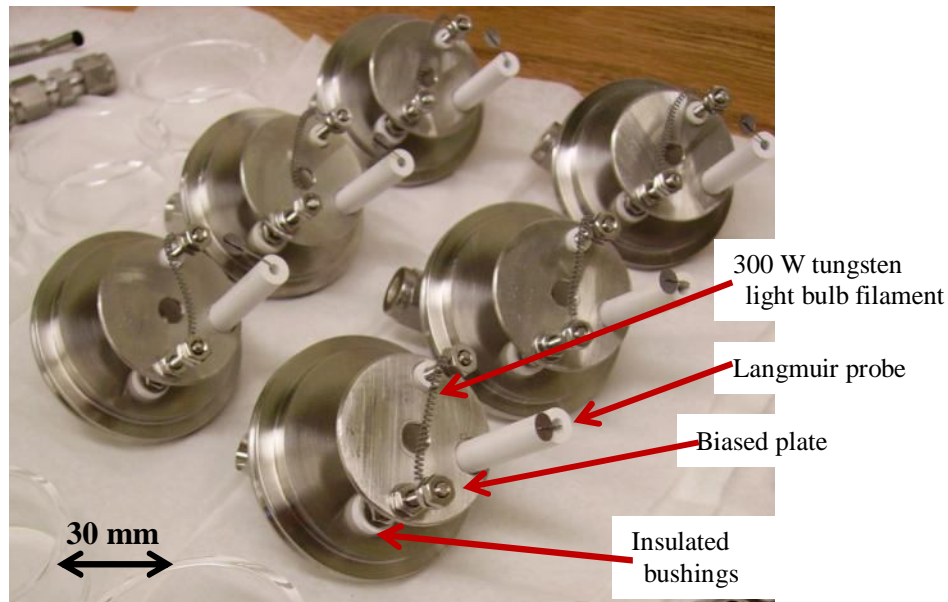


Figure 4-5: Photo of internal components of plasma source, including the tungsten filament and Langmuir probe.

The permanent magnets used for the cusp field had a maximum operating temperature of 150 °C, which is nearly twice the maximum temperature of standard neodymium magnets. However, the plasma tube had little innate cooling other than radiative cooling to dissipate the up to 300 W of power from the filament. Therefore, the source was actively water cooled with 3 mm diameter copper piping tightly wrapped and soldered to the exterior of the 48 mm diameter stainless steel tube. To maintain the temperature of the outside surface of the plasma tube below 100 °C, each module required a flow of water at 50 °C or less, at a minimum flow rate of 5.5 liters per hour per module. Without adequate water cooling it was found, by unfortunate and time-consuming experience, that the stainless steel and copper wrap tube could reach the melting point of copper, approximately 1000 °C.

A Langmuir probe was installed in each plasma source to measure the density and electron temperature of the plasma. The probe was a thin circular metal disc with a surface area of 25.4 mm<sup>2</sup> attached to a wire. A boron nitride insulating tube both supported the connecting wire and shielded it from the plasma. The position and orientation of the disc in the tube was selected to minimize the effects of the cusp magnetic field on its measurements;

it was placed parallel to the magnetic field lines and near the center where the field approaches zero. A LabVIEW® program was written to decipher the voltage-current traces of the probe into plasma density and electron temperature in near real-time. The Langmuir probed data was used to compare the plasma emissive surface theory to the experimental ion current.

The connection between the stainless steel tube and the extraction electrode needed to prevent gas from escaping while preventing electrical breakdown between the -15 kV extraction electrode and the grounded plasma aperture. The first prototype used a machinable ceramic material called Macor, which has a maximum temperature of 1000 °C and a bulk dielectric strength of 39.4 kV/mm. [4] The Macor spacer failed when the ceramic binder melted and became a conductive path. It was replaced with a quartz tube, which had a maximum temperature of 1150 °C and a dielectric strength of 55 kV/mm. [5] The quartz spacer performed well until the straight, polished interior surface became coated with a conductive metallic coating sputtered from the extraction aperture. The third and final spacer was made from the machinable ceramic boron nitride, grade HP. It has an 1150 °C maximum temperature and a 66.9 kV/mm dielectric strength. [6] Boron nitride HP is a soft, porous material that has shown a resistance to forming a conductive metallic coating in previous applications. [7] When a metallic coating did eventually form, it was easily removed with a coarse paper towel or fine sandpaper. Additionally, the boron nitride spacer was designed with angled surfaces out of the line-of-sight of sputtering metal, thus slowing the formation of a continuous conductive coating. At the time of writing, the boron nitride HP spacers have performed well up to the designed voltages of -15 kV. However, the 1150 °C maximum temperature was still a concern; the recommendations for future work will include an upgrade to boron nitride AX05. AX05 has an 1800 °C maximum temperature and

factor of 4 higher thermal conductive. [6] The higher thermal conductivity would increase the heat conduction from the extraction electrode to the water-cooled plasma tube.

Excessive heating was also an issue for the extraction electrode. The extraction electrode could not be actively water cooled due to its tight physical location and its need to be at -15 kV. This electrode had a major heat source from both inside and outside the plasma tube. Ions from the plasma that were not focused through the extraction aperture hit the tip of the electrode at energies up to 15 keV. The inside surface was also exposed to radiative heating from the tungsten filament. In addition, the exterior side of the electrode was struck by the ion beam from the opposing ion gun and secondary electrons accelerated back from the cathode. Depending on the focus of the opposing gun, those ions could have been localized at the tip of the electrode as well. The first extraction apertures were machined from 303 stainless steel, which has a melting point of 1350 °C. Several of the stainless steel electrodes melted when the complete six gun system was running at a total cathode current of 15 mA and cathode potential of 150 kV. The extraction electrodes were replaced with the Molybdenum alloy TZM. Pure Molybdenum has a melting point of 2610 °C and a thermal conductivity of  $0.35 \text{ cal cm}^{-3} \text{ }^{\circ}\text{C}^{-1} \text{ s}^{-1}$ . The thermal conductivity of the TZM lenses, which is approximately a factor of 4 higher than stainless steel, allowed the heat load directed at the small tip of the electrode to be distributed more evenly over the entire part, thus increasing the effective radiative surface area. [8]

The material, optics, and vacuum pumping design challenges of the ion source and extraction system were met with a combination of theoretical calculations and experimentation to determine what worked. The end result was a system that met the design requirements and performed reliably over multiple experimental campaigns.

#### 4.1.2. Electrostatic optics design and ion trajectory simulations

Three electrostatic lenses were used to accelerate and focus the ions extracted from the plasma source: the focus lens, the ground lens, and the cathode lens. Sorting through the vast number of design options associated with the shape, spacing, and electrical potential of each lens required detailed simulations of the optics used in the Hirsch device [1], a review of published empirical relationships for ion optics [9], an extensive campaign of simulating the proposed SIGFE designs, and lastly experimental testing of a prototype ion gun.

A three-dimensional CAD model of the original Hirsch device was created by scaling the drawings included in the two papers published on the Hirsch ion guns. [1,10] Figure 4-6 shows the original drawings published by Hirsch, while Figure 4-1 A shows the CAD model of the Hirsch device reproduced for this dissertation. The Hirsch device used the spherical vacuum chamber as the anode. On the other hand, the SIGFE was designed to fit inside of an existing cylinder vacuum chamber. The SIGFE's ground lens, best seen in Figure 4-3, produced the same electrostatic forces as the vacuum flange in Hirsch's spherical vacuum chamber.

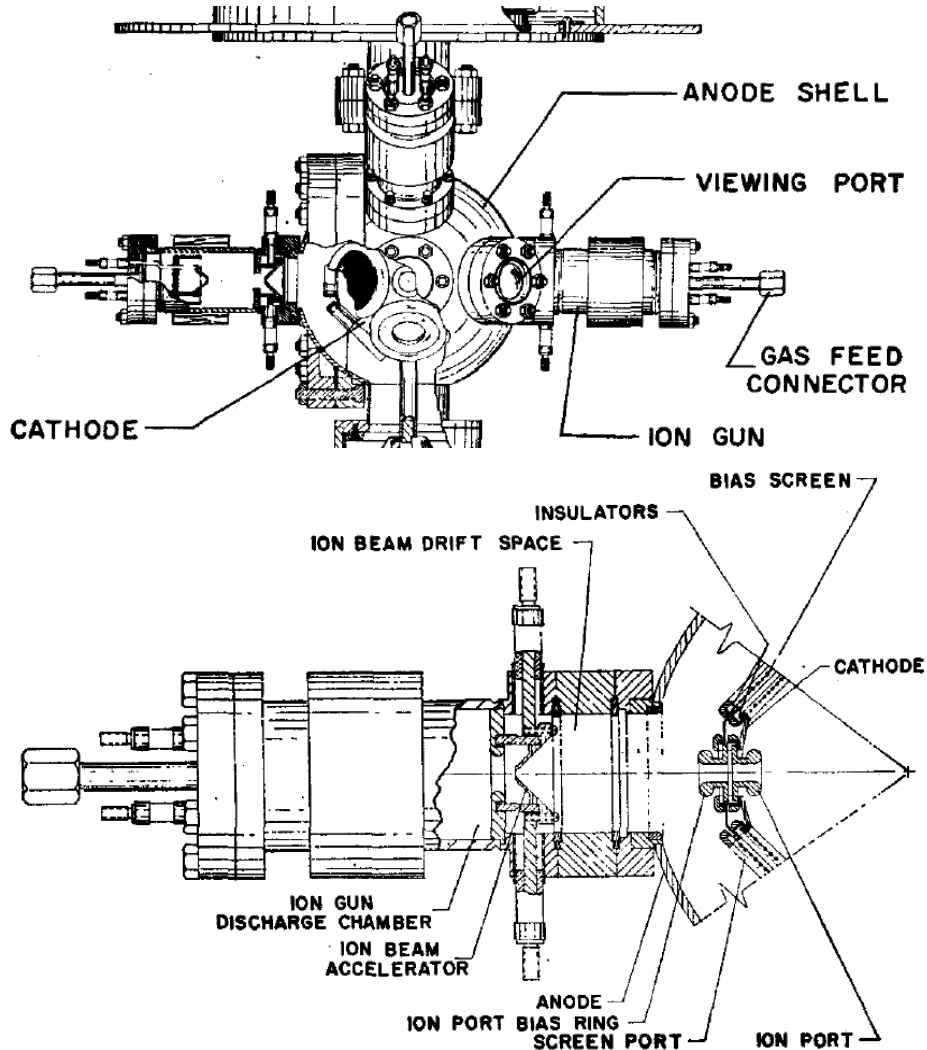


Figure 4-6: Original drawings of the Hirsch device, reproduced from Hirsch (1967) [10, 11]

The Hirsch device did not have a means of easily adjusting the focal point of the ion beams; it could only be adjusted by changing the length between the extraction lens and the cathode. This required adding a spacer at the vacuum flange. This method gave only a coarse adjustment and was time consuming. [11] The SIGFE added an electrostatic focus lens that adjusted the focal point in real-time, with fine resolution over a wide range of extraction and cathode parameters. Figure 4-7 compares the Hirsch device with the added spacer to the SIGFE with the focus lens set to a voltage of 7.2 kV and the cathode lens at -150 kV. With the addition of the focus lens, the majority of the ions in the SIGFE design

were predicted to be within 0.5 mm of the center of the device for cathode voltages from -80 to -150 kV. At a cathode voltage of 150 kV, the Hirsch device was predicted to place the ions within 8.5 mm of the center. This is greater than a factor of 10 difference in the radius of convergences, which was hypothesized to be an important parameter in enabling virtual potential well formation. The ion trajectories shown in Figure 4-7 were simulated without space charge effects using the charge particle tracking software SIMION®. [3]

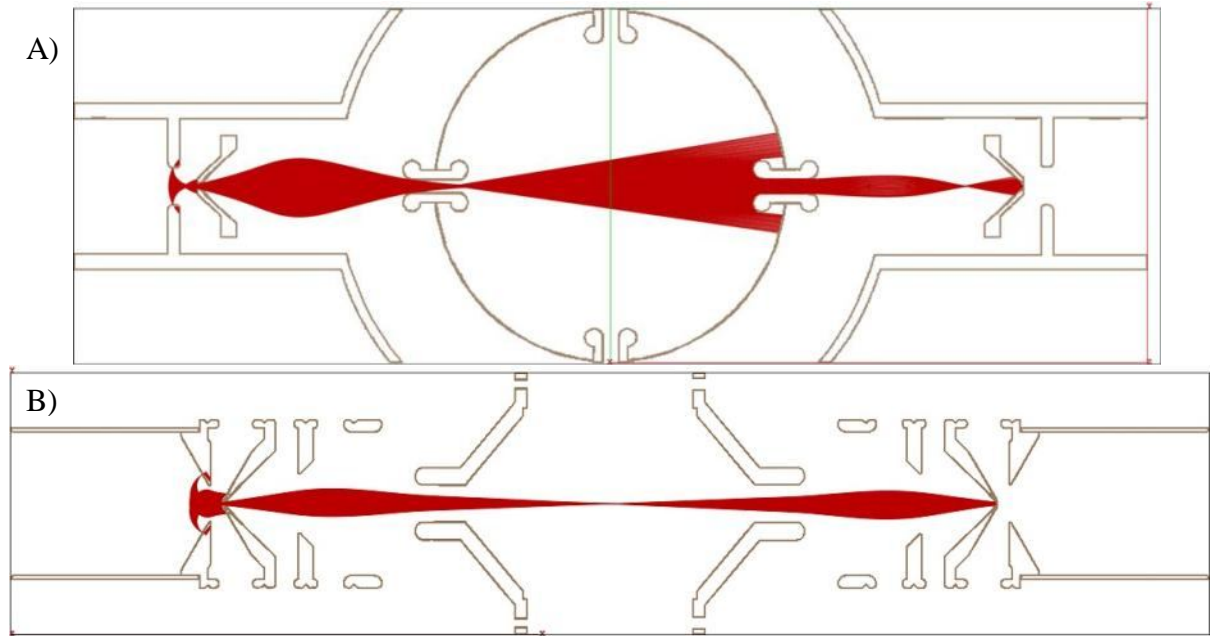


Figure 4-7: Comparison of simulated ion optics between A) the Hirsch device with spacer added to adjust focal length [11] and B) the SIGFE device with the focus lens set to 7.2 kV. Both cathode voltages set to 150 kV.

The optics design for SIGFE was evaluated by the SIMION® software and analysis of variance (ANOVA) statistical techniques. Various lens geometries and spacings, as prescribed by the Design of Experiments (DOE) package Design-Expert®, [12] were simulated in SIMION®. Design-Expert® is a software package that incorporates multiple advanced ANOVA techniques to calculate the relationships between multiple independent and dependent variables. Using this technique, the relationship between the variables was determined without the need to simulate all of the thousands of combinations of different

variables. With the assistance of the optimization routine included in the Design-Expert<sup>®</sup> software, the distance between extraction and focus lenses was chosen. The statistical analysis found that the most significant variables in determining the ion beam focal point were the *focus voltage*, *cathode voltage*, the cross-term of *cathode voltage* x *ground-to-cathode spacing*, and the cross-term of *focus voltage* x *ground-to-cathode spacing*. The optimized spacing values were experimentally proven in the prototype ion gun testing and the significances of the different variables helped to concentrate the experimental studies.

Based on the final optics design, a detailed study of the trajectory of the ions was conducted. Table 4-1 shows a sample of these results for a cathode voltage of 100 kV and an extraction voltage of 10 kV. The ion trajectories predicted by SIMION<sup>®</sup> are shown at various focus voltages, and are compared to the model of the Hirsch device. Figure 4-8 graphs the relative quantity of ions that were predicted to strike the different electrode surfaces for a range of focus voltages. The results of this simulation were used in chapter to explain the experimental results.

The extensive amount of time spent simulating both the previous experiment and proposed ion optic designs allowed the prototype ion gun to successfully focus ions on target on its first attempt. The prototype construction and testing will be discussed in more detail in the following sections. In addition to several other benefits, the prototype testing validated the SIMION and statistical modeling discussed in this section.

Table 4-1: Visual representation of ion trajectory simulations at various focus lens voltages

Ion trajectory simulations Cathode voltage 100 kV, Extraction voltage 10 kV		Focus percent / voltage
<b>Ion direction</b> →	<b>Upstream lenses</b>	<b>Downstream lenses</b>
		2.50 kV
		70% 3.27 kV
		100% 4.70 kV <i>Best Focus</i>
		130% 6.12 kV
		8.00 kV
		Hirsch device No focus lens

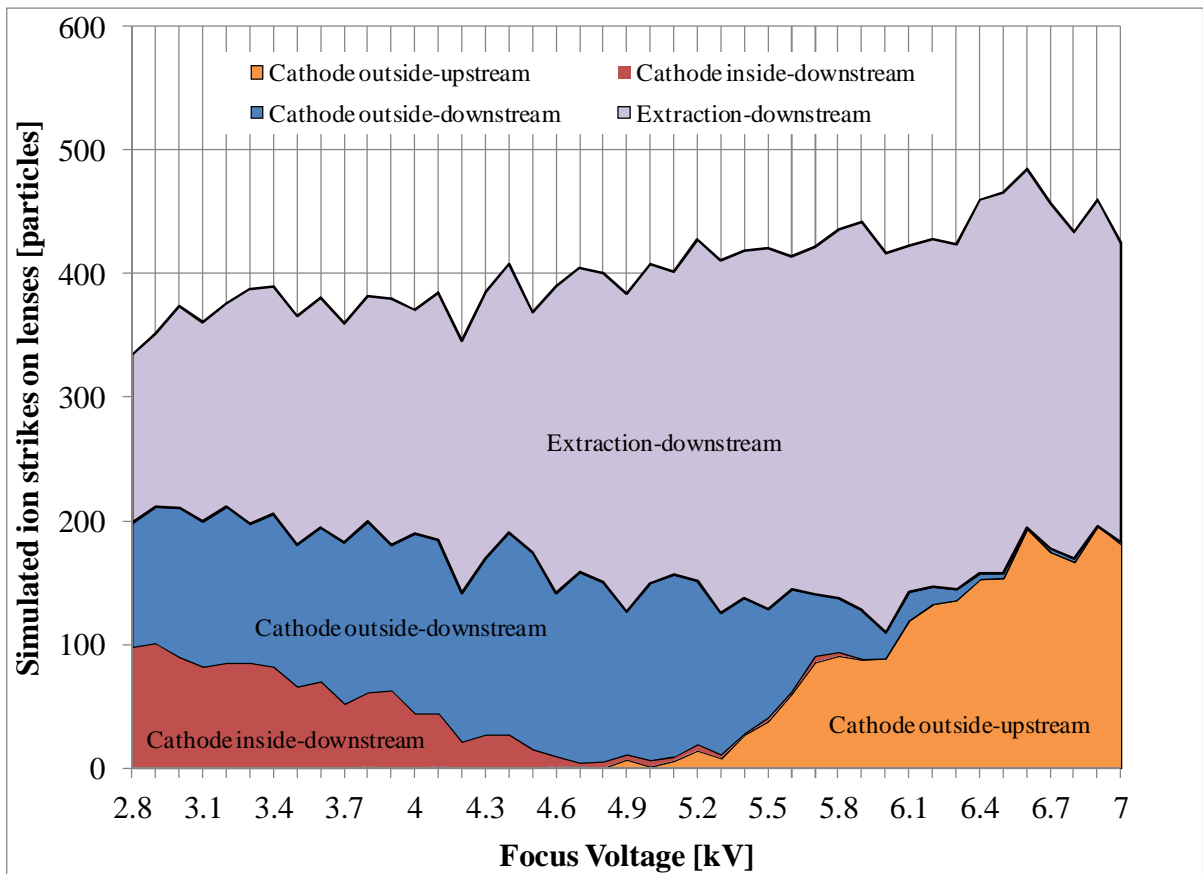


Figure 4-8: Graph of ion trajectory simulation results showing the relative number of particles that were predicted to strike the different lens surfaces defined in Table 4-1.

#### 4.1.3. Assembly and alignment techniques

The project goal of aligning six independent ions beams to within 0.5 mm required a design with sufficient adjustment, precision component fabrication, and a meticulous assembly process. The modular design of the ion guns allowed the position along the z-axis and the concentricity of the individual lens to be set independent of the larger six gun system.

The backbone of the module was two mounting rods made of 9.5 mm diameter boron nitride; boron nitride is a machinable ceramic with a high dielectric strength. The parallelism of the mounting rods was constrained at only two points: at the cathode lens, and the magnet mount. These two mounting points are shown in Figure 4-9 B and D. The attachment system of the optic mounts, shown in Figure 4-9 C, was designed to prevent over-constraining the rods. One attachment point is a circle while the second point was a slot.

Additionally, the set screws that contacted the rods were placed on orthogonal axes. This resolved a major issue of breaking the mounting rods experienced with the prototype ion gun.

The z-position of lenses was set by permanent boron nitride spacers placed between the optic mounts as shown in Figure 4-9 A. The final distance between the cathode lens and the ground lens was set by a removable shim. With the spacers and shim in place the unit was firmly pressed together and the set screws were tightened in order: first the cathode lens screws, then the magnet mount screws to set the parallelism of the two mounting rods. With the rods in place, the screws of the optic mounts were tightened in the following order: 1) loosely tighten the x-axis screw, 2) loosely tighten y-axis screw, and 3) fully tighten screws in same order. This technique was developed to minimize the stress induced in the mounting rods. After tightening, the gaps between each optic mount were measured on each of the four corners. If any gaps were not within 0.25 mm of the specified dimension, the module was disassembled and the process was started over

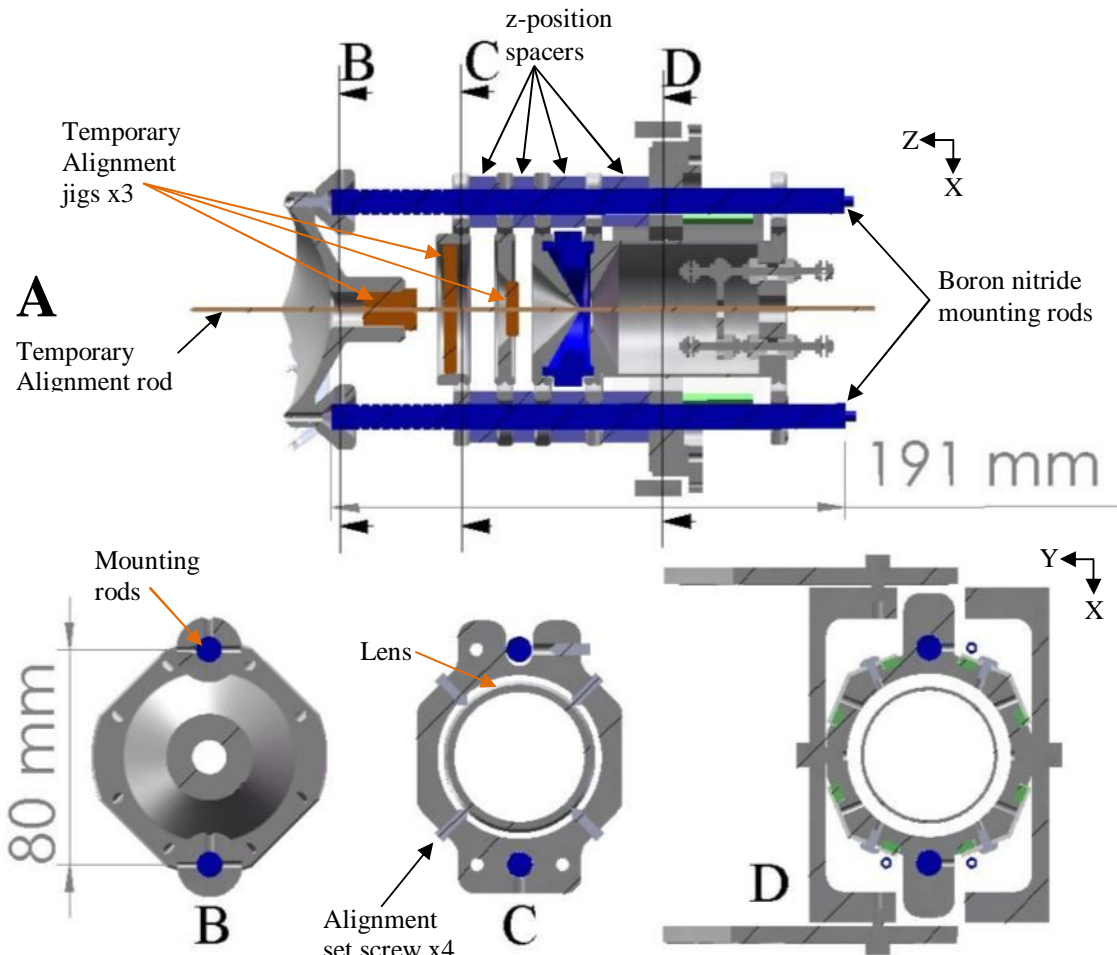


Figure 4-9: Ion gun module alignment details. A) Cross-section view of the full module showing boron nitride mounting rods, alignment rod and jigs, B) cross-section view of cathode lens highlighting mounting rod attachment, C) view of 1 of 5 optic mounts with lens alignment set screws shown, and D) view of magnet mount

The concentricity of the lenses was adjusted with the four alignment set screws in each optic mount. The set screws had a conical point that locked into a groove machined in each lens. The inside diameter of the cathode lens was used as the main datum. Precision jigs were machined to tolerances less than 0.025 mm. These jigs had center holes that matched the diameter of the extraction aperture, and were placed inside each lens as shown in Figure 4-9 A. The alignment screws of each lens were adjusted until a precision-ground steel rod could be smoothly slid though all of the jigs. This was a painstaking process that could take between 15 minutes and 2 hours per ion gun module.

Great care was taken in the design, machining, and assembly of the ion gun modules to achieve a high level of precision and accuracy. The measured z-position of the lenses was accurate to less than 0.25 mm. The concentricity error of the lenses was estimated to be less than 0.5 mm. The results presented in Chapter 6 confirm the importance of this level of accuracy. For example, Figure 6-11 shows a decrease in the device's fusion rate when the lenses shifted out of position for various reasons.

#### *4.1.4. Electrode and insulator design and fabrication*

The backbone of the modular ion gun design was the two 9.5 mm diameter boron nitride (BN) insulating rod that held the lenses in place. Electrical breakdown along the surface of these rods was identified as a major risk to the success of the overall design. This risk was minimized by reviewing existing literature on surface breakdown, simulations of the proposed designs, and experimental prototype testing. The area of greatest concern was the span between the cathode and ground lens, see Figure 4-3. A voltage potential difference of up to 150 kV was successively maintained across this 40 mm span.

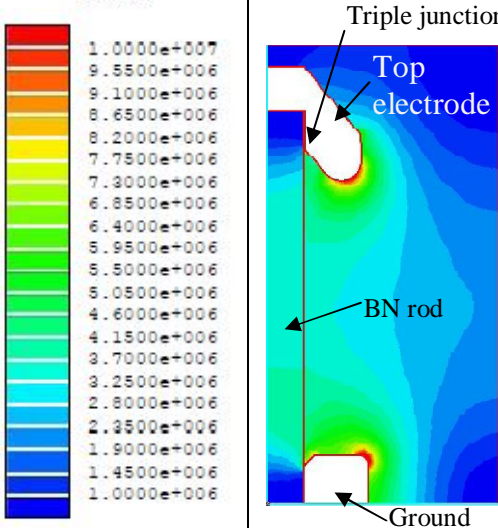
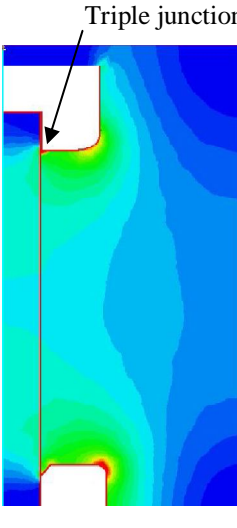
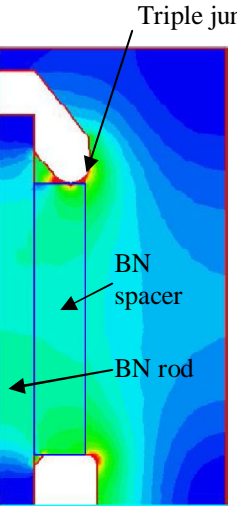
Based on previous experience with high voltage in vacuum, it was assumed that the most likely path for electrical breakdown was not though the bulk vacuum, but along the surface of the insulators. In a 1993 article, H.C Miller [13] provided a summary of the leading theories of surface flashover. In many of the theories, the phenomenon of flashover was separated into three phases: initiation, propagation and discharge. It was generally agreed that flashover is initiated by electrons emitted at the triple junction where the cathode, insulator, and vacuum meet. These free electrons may be a result of field emission, which is directly related to the electric field at the triple junction. According to this theory, a reduction in the electric field in this critical region would result in a lower probability of a flashover occurring.

There appears to be considerable disagreement on the mechanism of the propagation and discharge phases of flashover. The most generally accepted mechanism according to Miller, is the secondary electron emission avalanche (SEEA) theory. In this theory, the electrons emitted at the triple junction impact the insulator. These impacts produce more electrons that are turned around by the electric field to also impact the insulator. This can create a chain reaction of multiple generations of every increasing numbers of electrons and a large amount of surface charge on the insulator. The surface charge enhances the strength of the electric field and accelerates the process. The electron impacts liberate gas absorbed in the insulator to form a layer of gas. A discharge between the two electrodes eventually occurs as the front of the electron avalanche and the gas cloud progress towards the anode.

[13,14]

The ideas of SEEA were used to inform the design of the attachments to the boron nitride mounting rods. The first priority was to reduce the electric field at the cathode-insulator-vacuum triple junction. The designed labeled “bell shaped” in Table 4-2 was used for the device. In this design, the junction of the electrode to the insulator was at a 45 degree angle. This angle reduced the magnitude of the electric field by more than a factor of 2 over a simple 90 degree interface. Both the bell shaped case and 90 degree case were modeled with a 0.1 mm gap between the insulator and the electrode. This small gap simulated the fabrication tolerances and increased the electric field by a factor of 10. This indicates an opportunity for further increasing surface flashover standoff by developing fabrication techniques to eliminate this gap. The swept back design also shadowed the insulator from ion impacts and sputtered metal that would eventually form a conductive coating along the rod.

Table 4-2: Simulation and experimental comparison of three cathode electrode designs. The lower electrode was set to 0 V and the upper electrode was at -150 kV. A 0.1 mm vertical gap was modeled between the insulating rod and the top electrode to represent fabrication tolerances. Simulations performed in Ansoft Maxwell SV® [15]

Top electrode shape:	Bell shaped	90 degree	Bell shaped with boron nitride spacer
E [V/m]			
<b>Electric field at triple point with -150 kV applied to top electrode</b>	$1.2 \times 10^7$ V/m	$2.7 \times 10^7$ V/m	$4.2 \times 10^7$ V/m
<b>Maximum experimental voltage</b>	-150 kV	not tested	-50 kV

During the course of experimenting with the SIGFE, an additional boron nitride spacer was added between the ground lens and the cathode lens, as shown in the last column of Table 4-2. The intention of the spacer was to assist in accurately setting the z-position of the lenses. The unintended consequence was a factor of 3.5 increase in the electric field at the cathode triple junction. With these spacers in place, the cathode had difficulty reaching -50 kV, without the spacer the cathode could stably operate at -150 kV, a factor of 3 difference.

The boron nitride mounting rods and electrodes had several other empirically based features to improve performance. Grooves were machined in the rods as shown in Figure

4-3. The intention of the grooves was to increase surface path length between the two electrodes. However, the grooves may cause field concentration points that could increase the electric field as the insulator builds up surface charge. The harm or benefit of the grooves has not been proven. During fabrication, the semi-porous boron nitride rods are carefully handled to avoid contamination and are baked to 400 °C in a vacuum oven to minimize the amount of gas absorbed in the material. The metal electrodes were carefully polished to reduce surface roughness, which could create electric field concentration point. The metal electrodes were machined smooth, then sanded with 600 grit sandpaper, and finally polished with crocus cloth to a near mirror finish.

It is this author's opinion that lessons learned from reviewing the mechanism of surface flashover and the electrostatic simulations contributed to the success of the SIGFE device. Being able to maintain up to -150 kV over a 40 mm long insulator was viewed as a difficult challenge at the beginning of the project. Through careful design and fabrication the SIGFE was able to stably operate at -150 kV.

#### *4.1.5. Prototype ion gun*

A prototype ion gun module was built and operated to its full design parameters before constructing the full six gun experiment. It was used to prove that the insulator designs could operate to at least -150 kV, and that the electrostatic optics had adequate control of the focus of the ion beams. Data from the prototype validated the simulations and analytic calculations used in the design process. The prototype found and helped to resolve several issues that could have been major problems had they been repeated six times in the much more complex SIGFE device. In a spinoff of this work, the prototype was converted into a materials test facility for the testing the first wall armor materials for inertial fusion reactors.

The prototype ion gun shown in Figure 4-10 varies from the final SIGFE design in only a couple of ways. The most obvious difference is the cathode. After the cathode lens, which was nearly identical to the final SIGFE lens, the ions entered a stainless steel tube with a quartz window on the end. The quartz was placed where the center of the cathode would be on the full SIGFE device. As the ions were accelerated and focused they struck the quartz window and fluoresced. This was used to diagnose the diameter of the ion beam and the performance of the electrostatic optics system. The source plasma tube was conductively cooled with a passive copper strap; this was replaced with an active water cooling system in the final design.

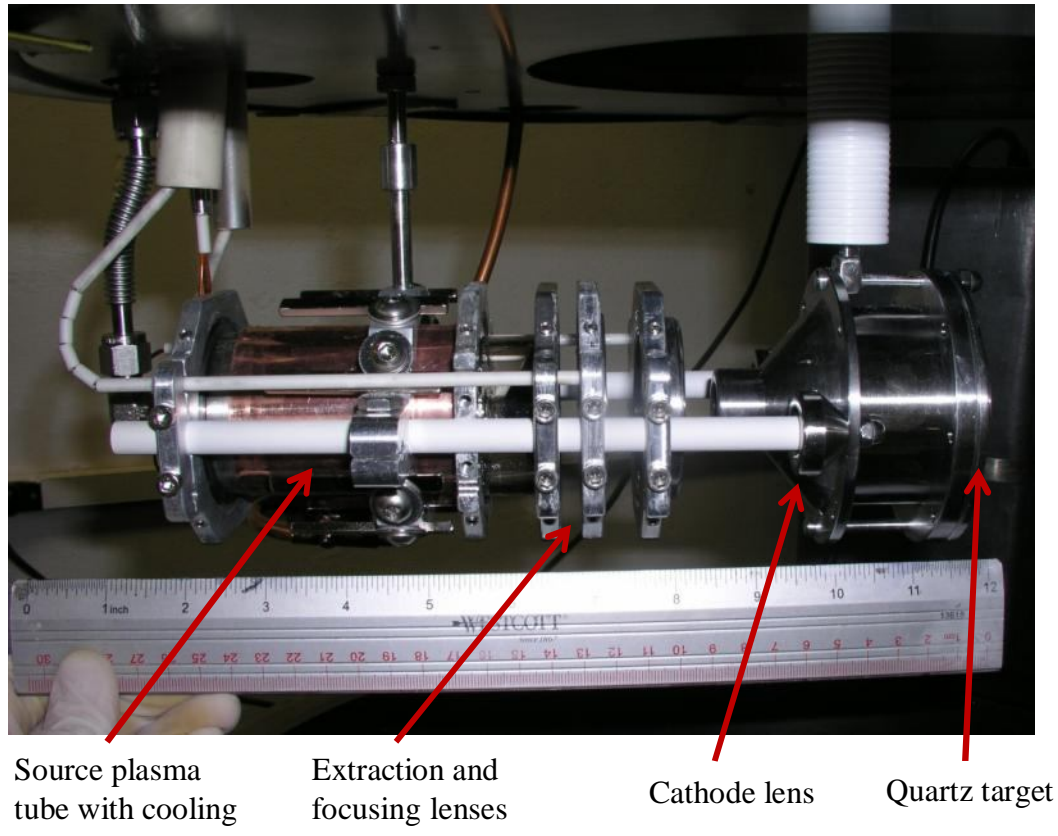


Figure 4-10: Picture of the prototype ion gun

Another major difference between the prototype shown in Figure 4-10 and the final SIGFE device was the design of the optic mounts holding the lenses. This was one of the

major issues discovered and resolved during the construction of the prototype ion gun. The original mount used a saddle clamp to tightly hold to the rod. However, when more than two of this style clamp was used the mounting rods often broke. Both of the clamps on all of the optic mounts completely constrained the rods. Small variations, ~0.1 mm, in the distance between the saddle clamps were enough to flex and snap the boron nitride rods. The final design changed one of the mounting holes to a slot. The final optic mount design was described in section 4.1.3.

The prototype ion gun achieved its main goals of testing the performance of the ion optic system and to prove that the electrode and insulator designs were capable of cathode voltages up to -150 kV. Figure 4-11 show two views of the ion gun in operation. The left hand photo shows an example of the quartz target fluorescing as the ions struck it. At cathode voltages from -70 to -150 kV, the voltage applied to the focus lens was change and the resulting size of the image on the quartz was recorded. During an experiment a 2 mm diameter hole was melted in the quartz target at a cathode voltage of -65 kV and 5 mA of total cathode current. After the target was replaced, the ion current was maintained below 0.5 mA for the remaining prototype experiments.

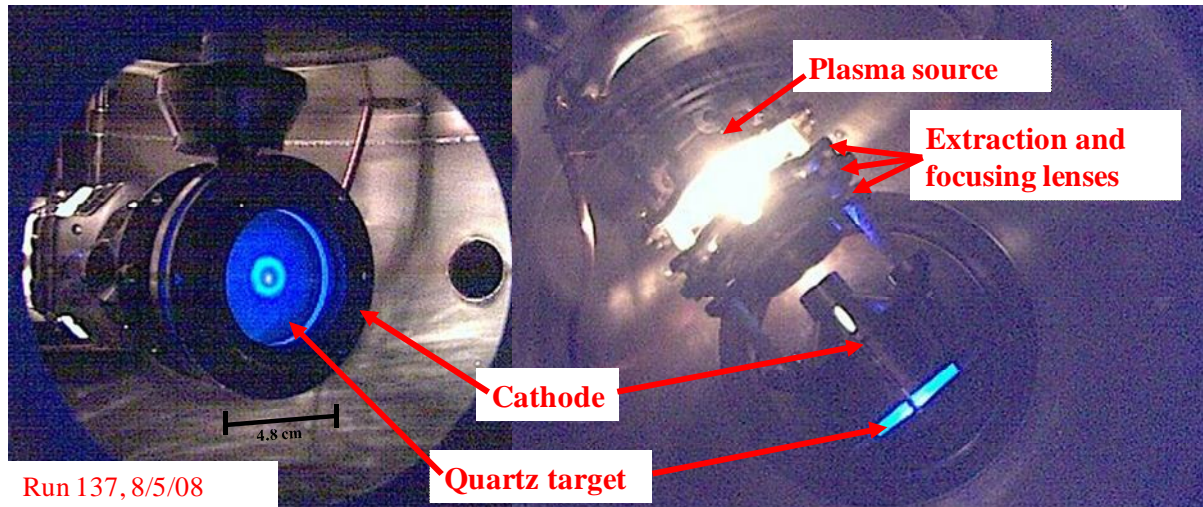


Figure 4-11: Pictures of the prototype ion gun in operation. A) View of the quartz target placed at future center of SIGFE device. B) View from below the ion gun.

A set of experiments was performed on the prototype ion gun to measure the performance of the ion extraction system. The focus lens was replaced with a solid blank to act as a collector. The setup is drawn in Figure 3-1. At a fixed voltage on the extraction electrode, the voltage on the collector was varied. Figure 4-12 shows a typical graph of a scan of the collector voltage versus the current collected. For collector voltages more positive than the extraction electrode, the system acted as a faraday cup and recorded only the ion current extracted from the source. As the collector voltage was swept more negative than the extraction voltage, a sharp rise in total current was seen; the size of the jump was used to approximate the secondary electron coefficient of the stainless steel collector plate. For collector voltages near zero only a portion of the ions struck the collector plate. The voltage where the collected current plateaued was used to estimate the velocity component of the ions parallel to the gun's axis.

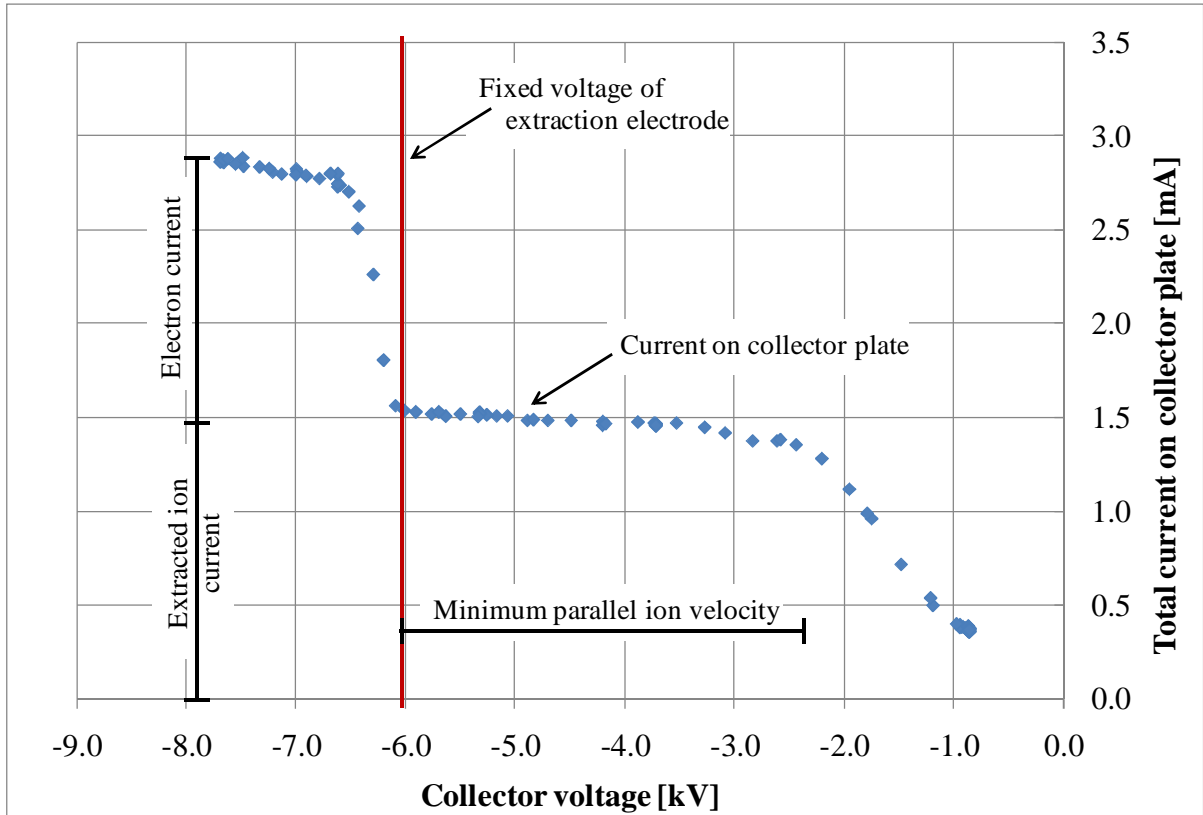


Figure 4-12: Typical result from a voltage scan of the collector voltage for a fixed extraction voltage.

In parallel with experiments involving the collector voltage, a Langmuir probe was used to measure the plasma density and electron temperature of the source plasma. The location of the Langmuir probe can be seen in Figure 4-3. Parameter studies of how the filament power, filament bias, gas flow, and extraction voltage affected the plasma characteristics and extractable ion current were conducted. The results of this study, along with a comparison to the extractable ion current described in Chapter 3 will be presented in Chapter 5.

An unexpected spinoff of the ion gun prototype was its use for materials testing. The UW IEC laboratory had a history of testing candidate first wall armor materials for inertial fusion reactors. The previous UW gridded IEC devices were used to simulate the lower energy (< 100 keV) threat spectrum of alpha particles resulting from the fusion burn of an

Inertial Confinement Fusion (ICF) target. [16, 17, 18] The quartz target of the prototype ion gun was replaced with a sample of a candidate material. The sample could then be implanted with 10 to 150 keV He<sup>+</sup> ions. Figure 4-13 shows a schematic of this setup and the results of the first sample tested by this method. At the time of this writing, another graduate student, Sam Zenobia, is converting the prototype ion gun hardware into a stand-alone device for the purpose of material testing. [19] This work was supported by the High Average Power Laser (HAPL) at the Naval Research Laboratory.

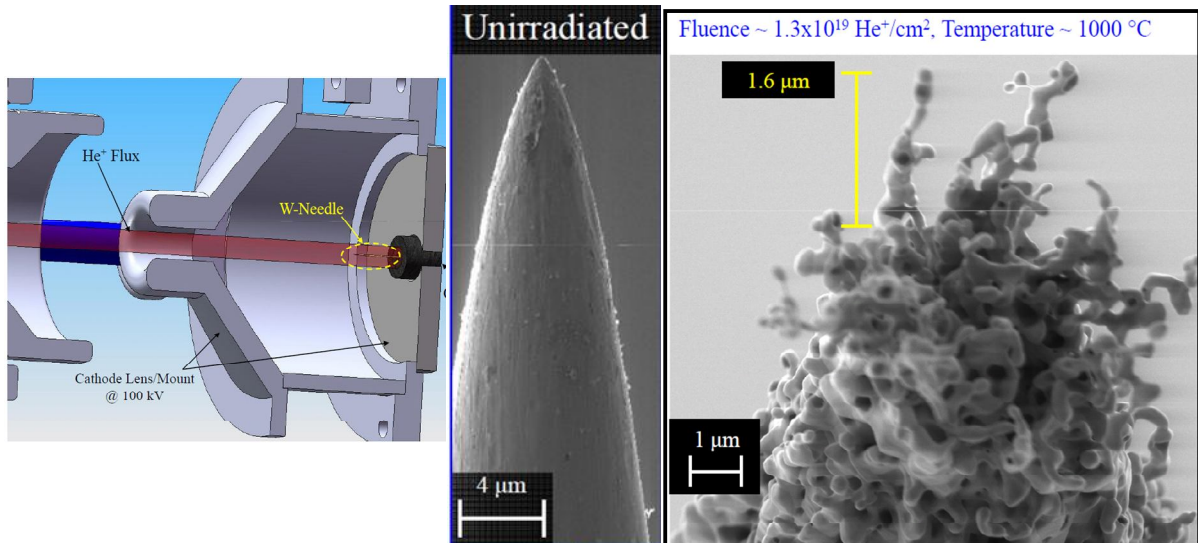


Figure 4-13: A) Schematic of materials test setup. The quartz target seen in Figure 4-11A was replaced with a test sample. B) Micrograph of the unirradiated W-needle to be tested. C) Micrograph of the W-needle after a fluence of  $1.3 \times 10^{19}$  He<sup>+</sup> ions per cm<sup>2</sup>. Pictures courtesy of Sam Zenobia. [19]

The prototype ion gun proved to be a valuable stand alone experiment as well as a stepping stone to the Six Ion Gun Fusion Experiment. It proved the viability of the ion gun module design without the risk of building the complete six gun device. It was a proof-of-concept for the new material testing device under-construction by another graduate student. In addition, it provided experimental data to compare to the extractable ion current calculated in chapter 3.

## 4.2. SIGFE infrastructure

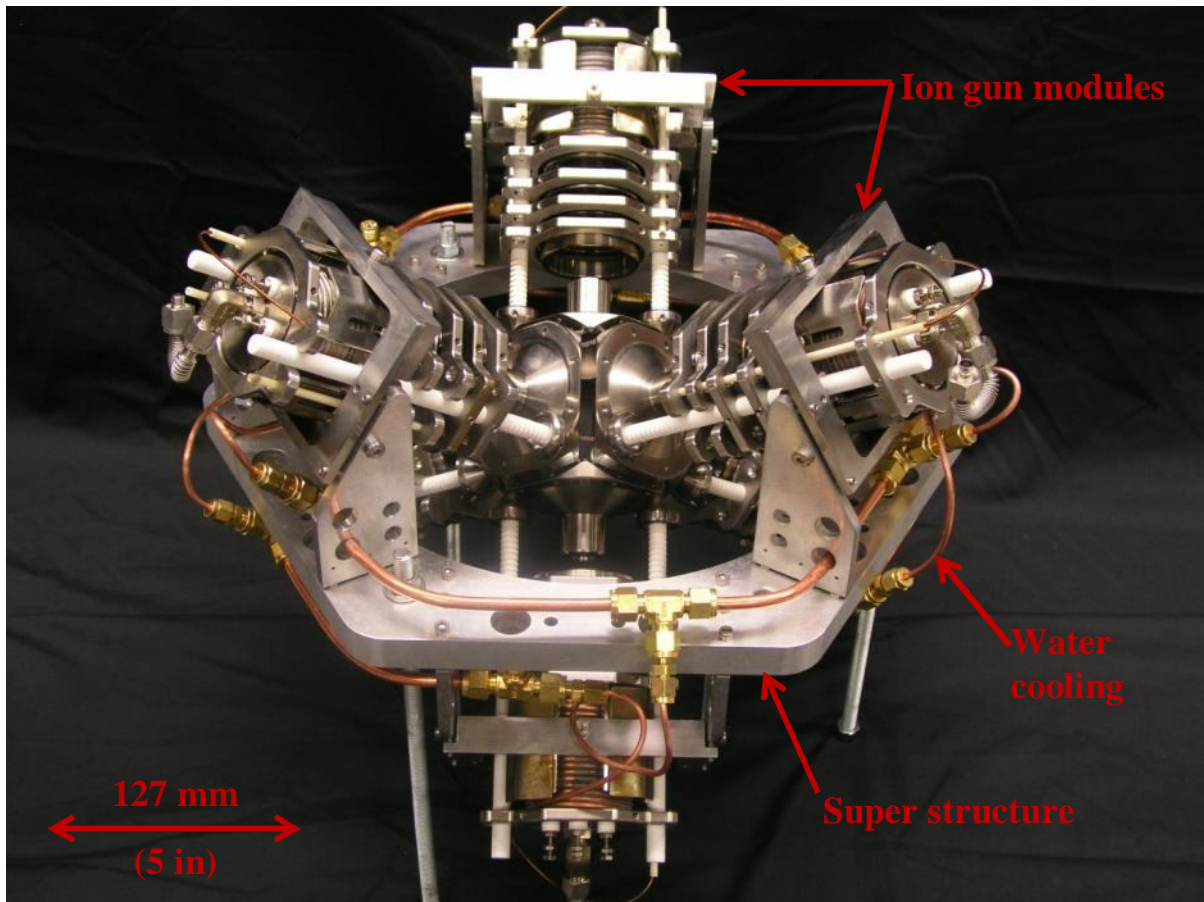


Figure 4-14: Photo of the internal components of the Six Ion Gun Fusion Experiment. All six ion gun modules are shown in their adjustable mounts attached to the super structure.

The Six Ion Gun Fusion Experiment had several key engineering challenges that needed to be solved. The ion gun modules required a stable mounting platform that included adjustment mechanisms that could finely position and align each module to within 0.1 mm. The ion gun modules and mounting hardware needed to be housed in a vacuum system that could reach base vacuum pressures of approximately  $2 \times 10^{-4}$  Pa ( $2 \times 10^{-6}$  Torr) with the capacity to handle the gas flow rates required for the ion sources. High voltage electrical power (-150 kV and -15 kV) had to be delivered to the lenses inside the vacuum chamber. To enable quick upgrades and maintenance, the whole experiment system needed to be easy to remove from the vacuum chamber. Finally computer hardware and software had to be

procured and developed that could remotely control the electrostatic lenses and continuously monitor the entire experiment. Photos of the internal and external components with key components highlighted are shown in Figure 4-14 and Figure 4-15.

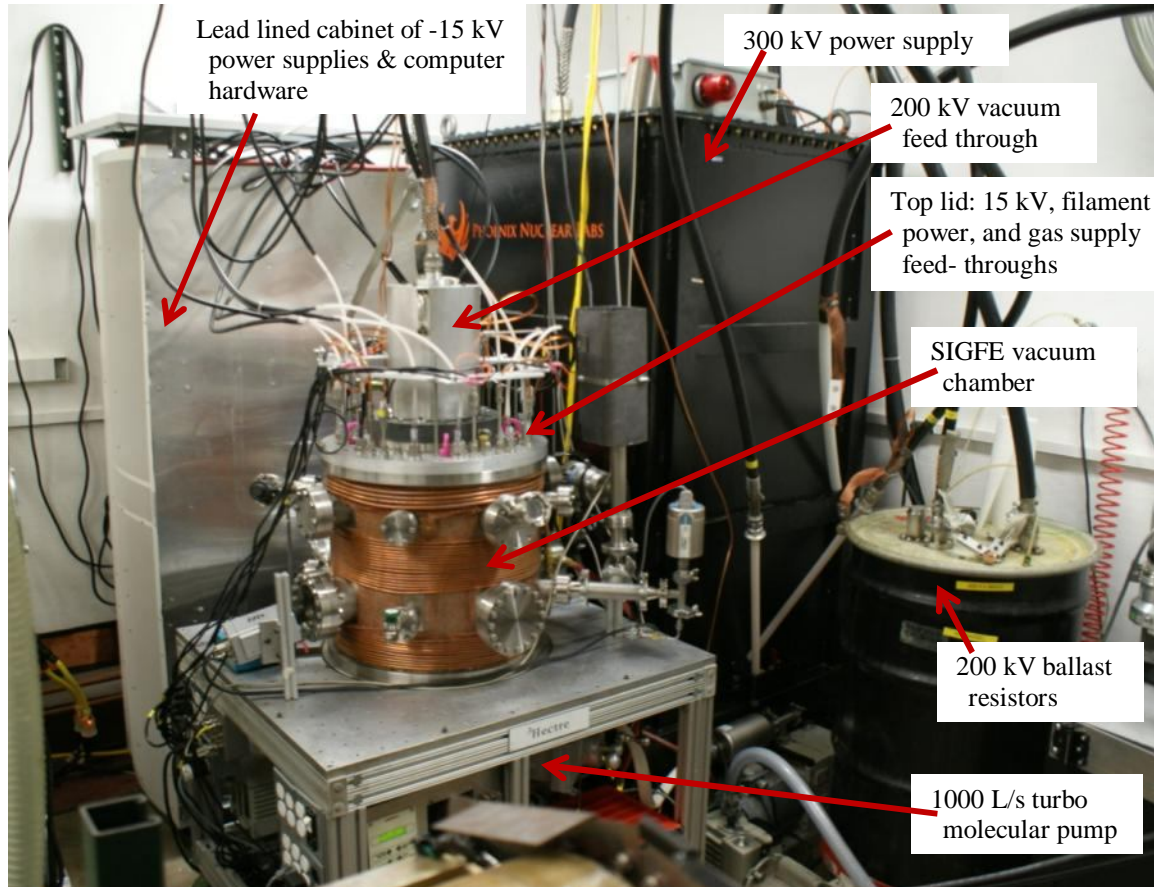


Figure 4-15: Photo of external SIGFE infrastructure.

#### 4.2.1. Ion gun mounting and alignment

The ion gun modules are attached to a 19 mm thick aluminum super structure by a mounting system that can pivot the module in two axes. Figure 4-16 shows the details this system. Two vertical sides are bolted to the main frame. Nominally 1.27 mm of shims were placed between the side mounts and the frame to allow an additional direction of adjustment. The swivel plate was attached between sides by a single shoulder bolt through each side. Shims were also included between the sides and the swivel plate. Set screws located on

either side the shoulder bolts created a finely adjustable pivot point that was used to aim the gun. The magnet mount, which was integrated into the ion gun module assembly, was attached to the swivel plate with a similar shoulder bolt set screw system.

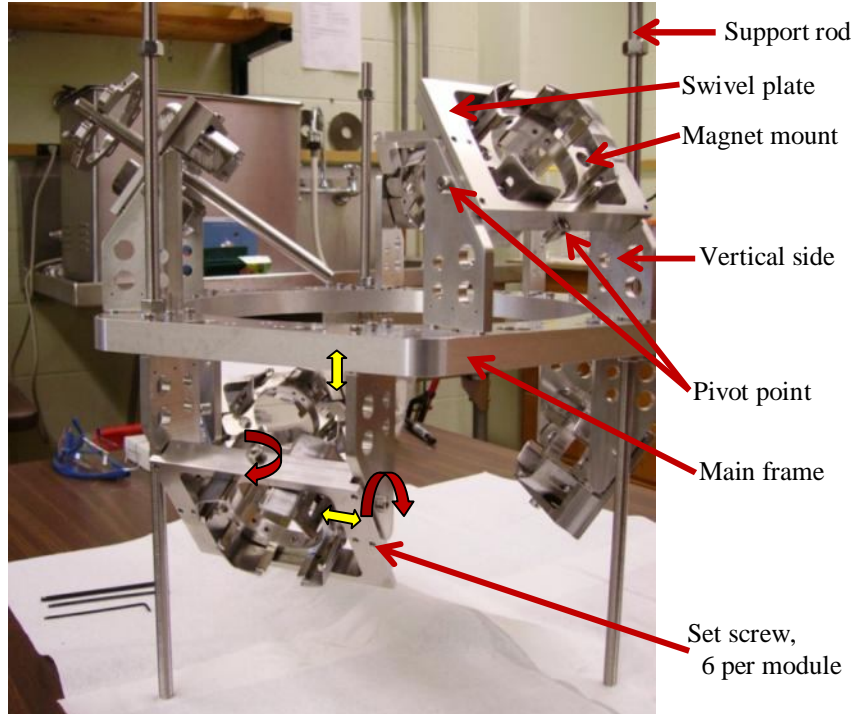


Figure 4-16: Details of the ion gun module mounting and adjustment hardware. Yellow straight arrows denote adjustment by adding or removing shims. Red curved arrows denote set screw adjust around the pivot points.

The three support rods shown in Figure 4-16 were used to hang the entire ion gun assembly from the top lid of the vacuum chamber. All of the electrical, gas, and water cooling connections were made through the top lid. The fact that no connections were made to the assembly except through the top lid allowed the whole assembly to be easily removed for maintenance and upgrades. The vacuum chamber could be vented to dry nitrogen, the assembly removed, necessary adjustment made, and the chamber resealed to vacuum in less than 20 minutes. Designing the equipment to be easily maintained increased the time available to run experiments.

It was estimated that the modules were aligned to within 0.2 mm (0.010 in) of the device center. Achieving this level of alignment was not a trivial task. First, the lenses of each individual module were aligned as described in section 4.1.3. The same precision ground steel rods and cathode insert jigs used for the lens alignment and shown in Figure 4-9 A were used to aim the modules. The alignment rod was held between the cathode jig and the extraction aperture. The set screws in the swivel plate were adjusted until the sharpened tips of the alignment rods in each gun touched. Figure 4-17 is a photo of this setup with one of the modules removed for better viewing. The photo in Figure 4-18 is zoomed in to show the level of accuracy that was met. As a second check, the alignment rod had to pass between the two opposing modules with minimal resistances. Finally, the alignment of two opposing modules was checked by visually sighting down its axis. With the cathode jigs in place a full circle of light should be visible through both modules. If any of these checks failed, alignment of the all the modules was revisited. Successive attempts to aim each gun using the other guns as guides eventually refined the aim to the exact center of the device. Figure 4-19 shows the results of this painstaking process; it is a photo taken of the ions beams of all six guns converging at the center.

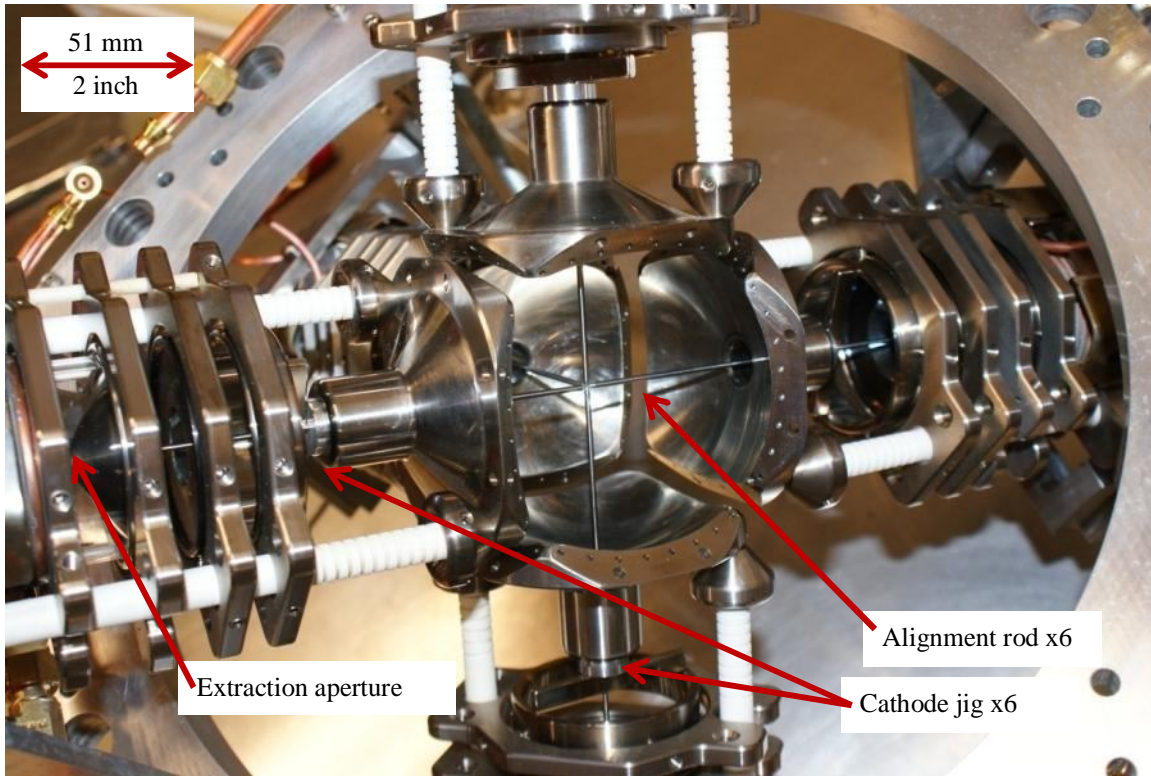


Figure 4-17: Photo illustrating the technique used to align the ion gun modules. Note that the location of each alignment rods was constrained by the extraction aperture and the cathode lens.

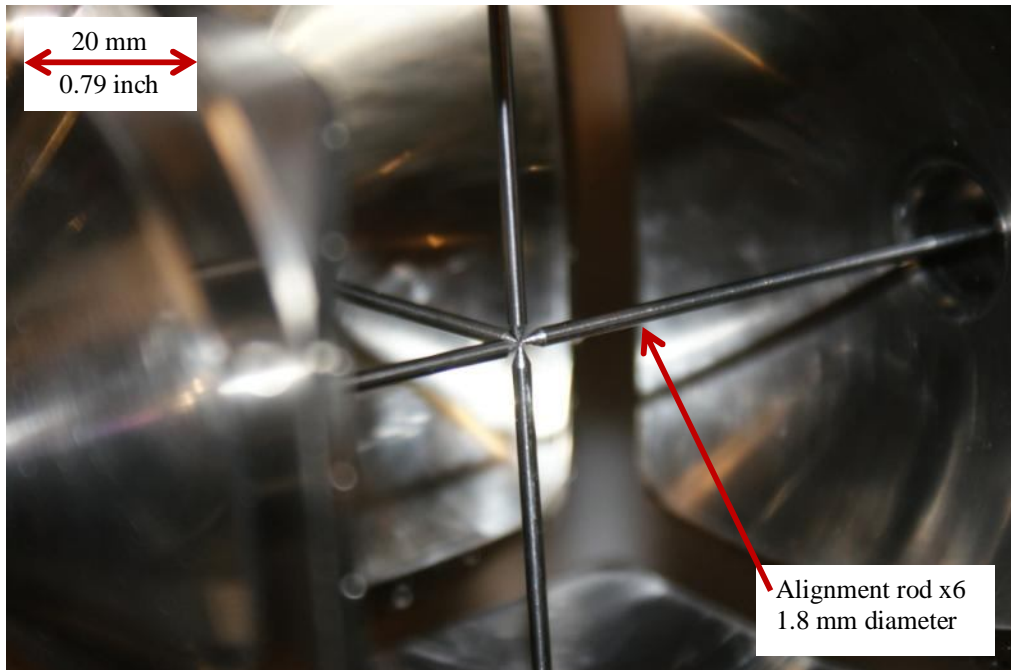


Figure 4-18: Photo of the alignment rods to show the level of accuracy the modules were aligned to. The rods are precision ground to  $1.829 \pm 0.008$  mm ( $0.072 \pm 0.0003$  inch).

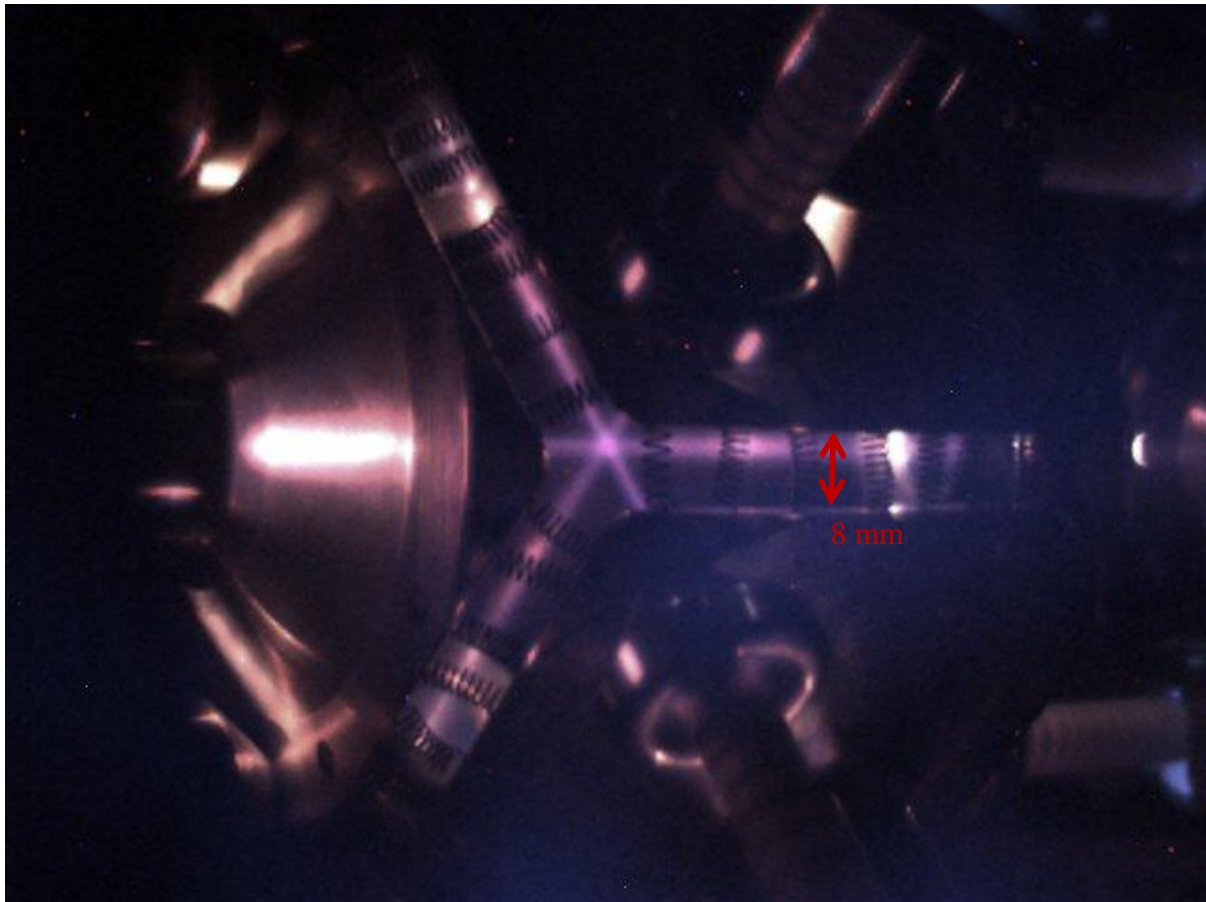


Figure 4-19: Photo of ion beams of all six ion gun modules converging at the center of the SIGFE device. The width of the beams just before the center is estimated at 1.6 mm.

#### 4.2.2. 200 kV high-voltage feed-through

A significant amount of effort was invested in developing an electrical vacuum feed-through that could withstand up to 200 kV of potential difference and survive the plasma environment of an IEC device. The design of the feed-through for the SIGFE is an extension of the design used on the previous two UW IEC devices, HOMER and HELIOS. The heart of both designs is a 2.5 cm diameter boron nitride insulating rod with a 0.48 cm diameter molybdenum conductor at the center. This is held in place by a Swaglok compression fitting. Sketches of both designs are shown in Figure 4-21.

A review of the past decade of experimental data from HOMER showed a high concentration of failures in the boron nitride insulator at or near the Swaglok fitting, which is

grounded in the HOMER design. Using the commercial code Maxwell 3D<sup>®</sup>, the electrostatic fields were simulated for a -1000 kV arc. Even though the power supply used was only capable of -300 kV, evidence of much stronger -1000 kV arcs was observed. These strong arcs may have been a result of transient voltages induced during an arcing event inside the IEC device. Simulation of the electric field strength in the insulator material near the Swaglok<sup>®</sup> fitting was higher than 66.9 kV/mm. 66.9 kV/mm is the dielectric strength of boron nitride. [6] Figure 4-22 A shows the results of this study for the HOMER feed-through. As the localized field strength exceeded the dielectric strength, the insulator material could become permanently damaged. This could contribute to the eventual failure of the insulator. The high localized field strength is likely a contributing factor in the larger number of failures observed in close proximity to the Swaglok fitting.

Assisted by the Maxwell 3D<sup>®</sup> code and SolidWorks<sup>®</sup>, a new feed-through was developed to reduce the electric field in the insulator. This was accomplished by electrically isolating the Swaglok<sup>®</sup> fitting with a ceramic plate, thus allowing it to electrically float.

Figure 4-20 is a detailed view of this design. Analytic calculations predicted the nut would float to approximately one half the applied potential. This design lowered the maximum electric field strength by a factor of 2.2 over the HOMER feed-through. The results of this simulation are shown in Figure 4-22 B for comparison.

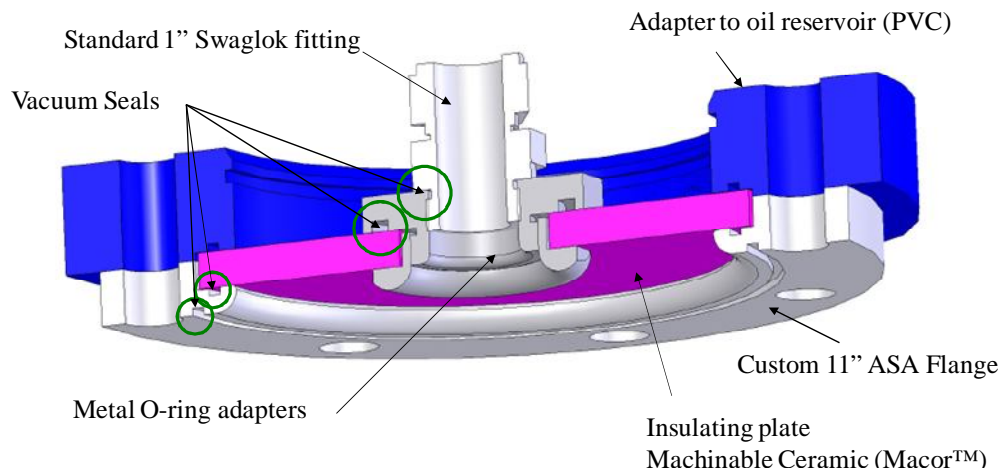


Figure 4-20: Details of the isolated nut high voltage feed-through design

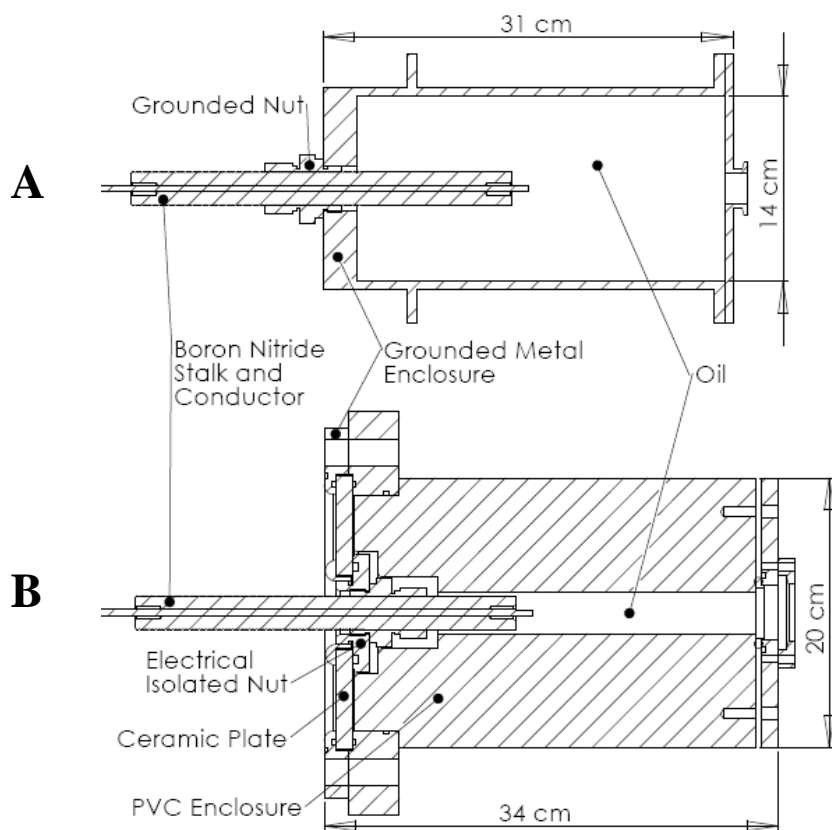


Figure 4-21: Cross-section views of the high-voltage feed though for A) HOMER and B) SIGFE

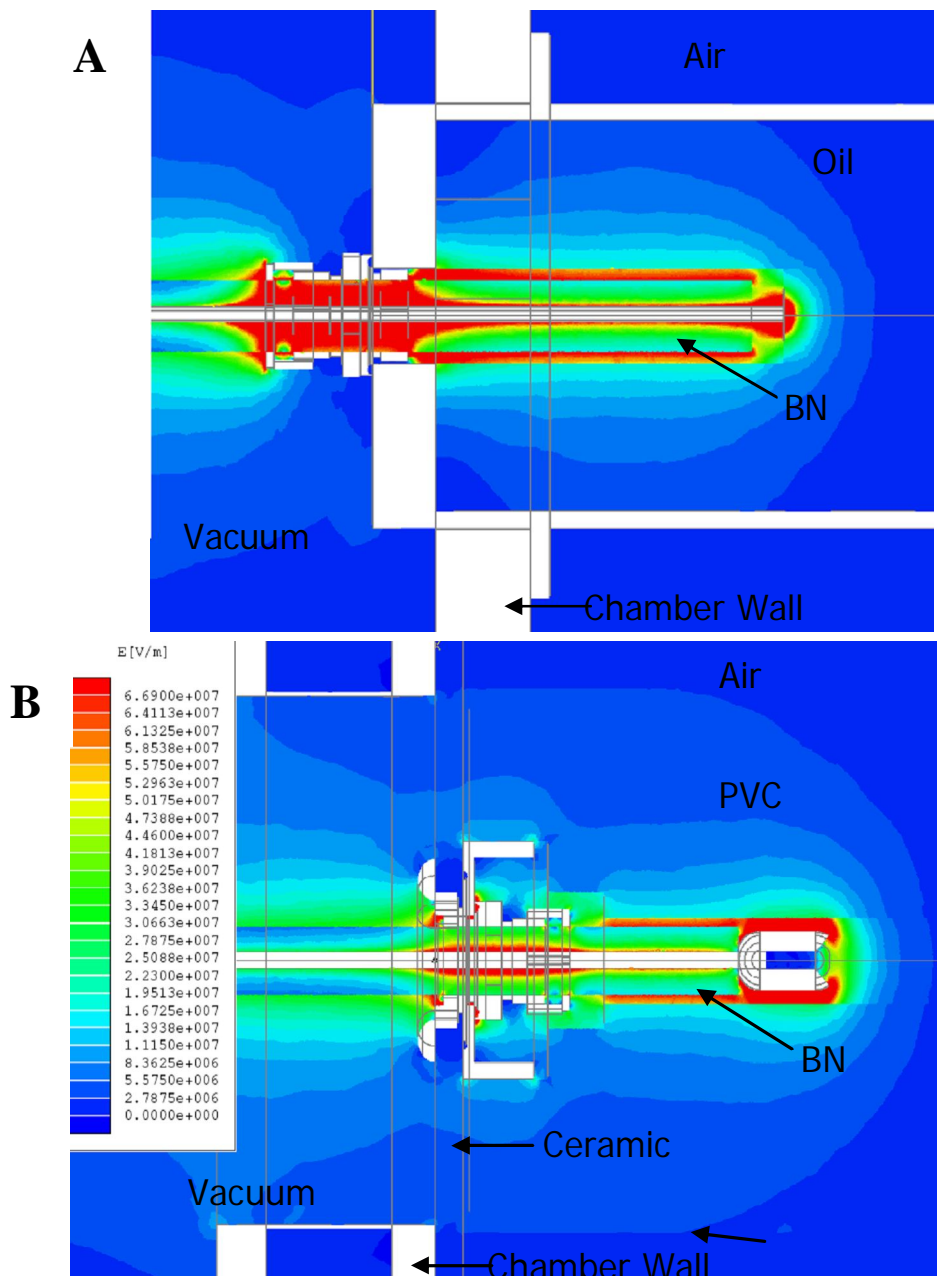


Figure 4-22: Simulated electric field strength for an applied voltage of -1000 kV for A) HOMER and B) SIGFE. The areas shown in red are above the dielectric strength of boron nitride at  $6.69 \times 10^7$  V/m. The SIGFE design showed a factor of 2.2 improvement in the maximum magnitude of the electric field

The new feed-through design has been tested to an applied voltage of -150 kV. The ceramic plate used to isolate the fitting has experienced two failures; both were cracks in the plate after high power experimental runs with a cylindrical gridded cathode. The shape of the cylindrical cathode caused electron beams to be accelerated out of the cathode in focused jets. These electron jets could have caused non-uniform heating of the ceramic plate that resulted in fatal thermal stresses. For the data reported for SIGFE, the ceramic plate was replaced with an aluminum plate to eliminate the risk of cracking and thus the risk of oil contamination of the intricate components of the SIGFE located directly below the feed-through.

#### *4.2.3. Boron nitride 200 kV insulator design*

In addition to the insulator failure mode detailed in the previous section, “treeing” is also a likely cause of long term failures of the insulator. [20] Treeing occurs when an electrode and a dielectric have a small vacuum gap between them. A strong electric field occurs in the vacuum gap that can induce arcing across that gap. This repeated arcing can continually degrade the dielectric material and formed a conducting path into the insulator. Eventually the conducting path can extend through the entire insulator, and results in a failure.

Gaps between the solid dielectric and the electrode are unavoidable due to the fabrication tolerances of the materials and processes that were used. To understand the severity of the problem and to engineer a solution, an analytic solution to the electric field in the system was developed. The electric field,  $E(r)$ , inside the infinitely long, cylindrical geometry shown in Figure 4-23 was found using the electric displacement,  $D(r)$ , the permittivity of free space,  $\epsilon_0$ , and the dielectric constant of the mediums,  $\epsilon_r$ .

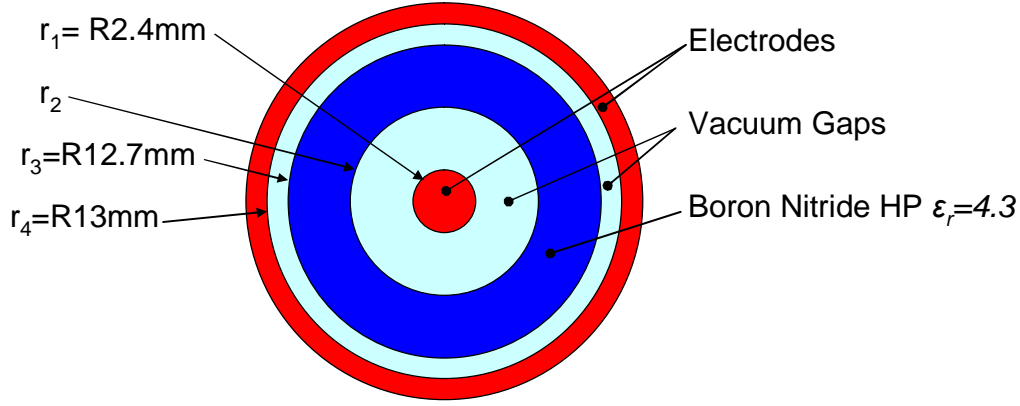


Figure 4-23: Infinitely long cylindrical geometry used for the analytic calculations of the electric field inside the high voltage stalk

Beginning with Gauss's law and assuming a linear dielectric, the electric displacement can be found by

$$\nabla \cdot \vec{D} = \rho_f \quad \text{Eqn 4-1}$$

where

$$\vec{D} = \epsilon_0 \epsilon_r \vec{E}, \quad \text{Eqn 4-2}$$

and  $\rho_f$  is the free charge. Integrating equation 4-1 in only the  $\hat{r}$  cylindrical coordinate yields

$$\vec{D}(r) = \frac{\lambda}{2\pi r} \hat{r}. \quad \text{Eqn 4-3}$$

Substituting Eqn 4-2 into Eqn 4-3 gives the electrical field as shown below.

$$\vec{E}(r) = \frac{\lambda}{2\pi\epsilon_0 r} \begin{cases} 0, & r < r_1 \\ 1, & r_1 < r < r_2 \\ \frac{1}{\epsilon_r}, & r_2 < r < r_3 \\ 1, & r_3 < r < r_4 \\ 0, & r_4 < r \end{cases} \hat{r} \quad \text{Eqn 4-4}$$

The cylindrical charge density,  $\lambda$ , was found from the boundary conditions of the applied electric potential,  $V(0)=V_o$  and  $V(r_4)=0$ .

$$\vec{E}(r) = -\nabla V(r)$$

$$V(r_4) - V(0) = \frac{-\lambda}{2\pi\epsilon_o} \left( \int_0^{r_1} 0 + \int_{r_1}^{r_2} \frac{1}{r} dr + \int_{r_2}^{r_3} \frac{1}{r\epsilon_r} dr + \int_{r_3}^{r_4} \frac{1}{r} dr \right)$$

$$\lambda = \frac{2\pi\epsilon_o V_o}{\ln\left(\frac{r_2 r_4}{r_1 r_3}\right) + \frac{1}{\epsilon_r} \ln\left(\frac{r_3}{r_2}\right)}$$
Eqn 4-5

Substituting  $\lambda$  into Eqn 4-4 gives the electric field as a function of the applied voltage and radial position in the system.

$$\vec{E}(r) = \frac{V_o}{r} \frac{1}{\left[ \ln\left(\frac{r_2 r_4}{r_1 r_3}\right) + \frac{1}{\epsilon_r} \ln\left(\frac{r_3}{r_2}\right) \right]} \begin{cases} 0, r < r_1 \\ 1, r_1 < r < r_2 \\ \frac{1}{\epsilon_r}, r_2 < r < r_3 \\ 1, r_3 < r < r_4 \\ 0, r_4 < r \end{cases} \hat{r}$$
Eqn 4-6

Equation 4-6 satisfies the boundary conditions and shows that the electric field is discontinuous at the boundary of the vacuum and the insulator by a factor of the dielectric constant. Figure 4-24 shows this discontinuity in the electric field for the design values in Figure 4-23 and various sizes of the vacuum gap between the inner electrode and the inside diameter of the dielectric ( $gap=r_2-r_1$ ). For an applied voltage,  $V_o$ , of 300 kV, the maximum field in the vacuum gap approaches 300 kV/mm as the gap size approaches 0. As the gap increases in size the field in the gap approaches the pure vacuum solution without a dielectric present. These results are consistent with a computation analysis performed in the commercial electrostatic solver Maxwell SV®.

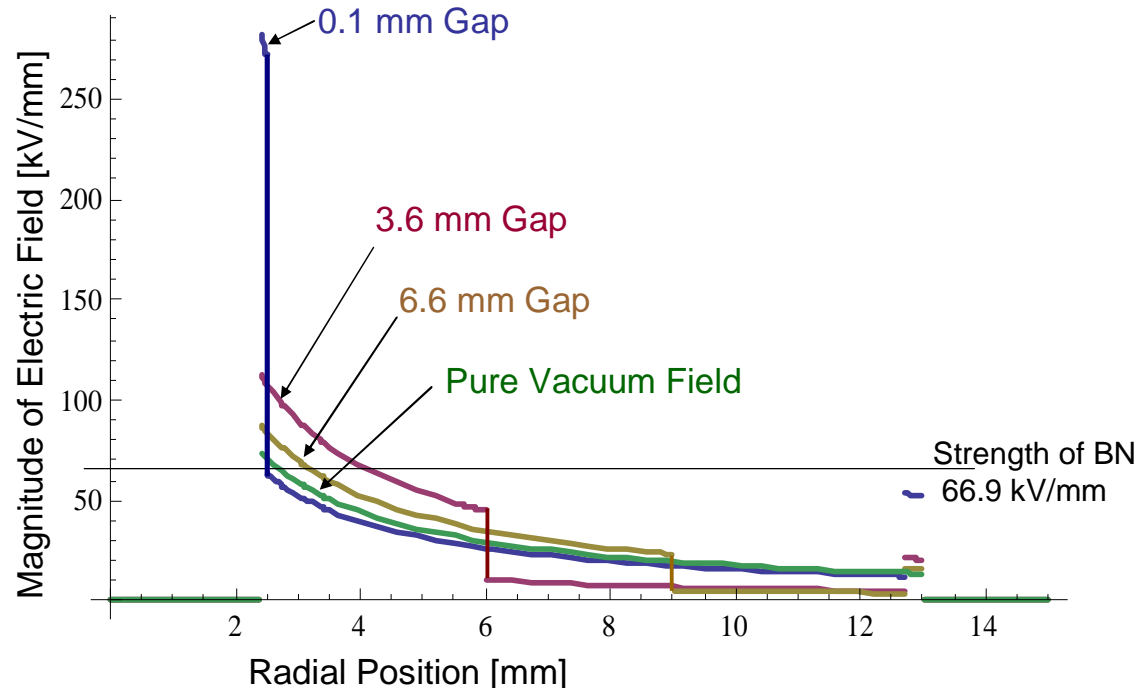


Figure 4-24: Radial electric field for an applied voltage of 300 kV and dimensions of  $r_1=2.4$  mm,  $r_3=12.7$  mm, and  $r_4=13$  mm. The size of the vacuum gap between the inner electrode and the inside diameter of the dielectric ( $gap=r_2-r_1$ ) was varied.

The maximum electric field for both the inner vacuum gap and the dielectric occur at the surface of the inner electrode and the inner diameter of the dielectric respectively; these values are plotted in Figure 4-25. In the previous stalk design, the size of the vacuum gap is held at the minimum achievable. This results in localized electric fields in the insulator which approach the dielectric strength of boron nitride, 66.9 kV/mm; the field in the vacuum gap at small gap sizes is a factor of 4.3 higher. This high electric field could initiate arcing between the inner electrode and the insulator, and could lead to a failure of the insulator due to treeing.

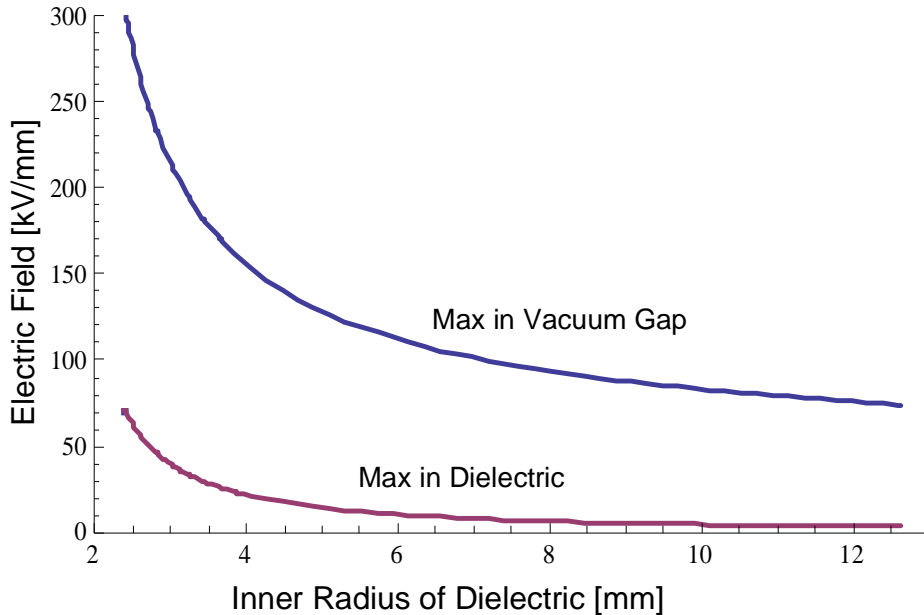


Figure 4-25: Maximum electric fields in the dielectric and vacuum gap as a function of the inner radius of the dielectric for an applied voltage of 300 kV, and dimensions of  $r_1=2.4$  mm,  $r_3=12.7$  mm, and  $r_4=13$  mm.

To minimize the electric fields in the system, a new insulator was designed with a larger inner diameter. As a tradeoff between the mechanical strength of the insulator and the electric field strength, an inner radius of 6.3 mm was chosen. Figure 4-26 shows the details of this design. The inner conductor was centered inside the insulator by two spacers. Inside the oil filled portion of the feed-through a metal spacer was used. The field at this spacer was not a large concern since it was far away from the electrical ground. The first stalk produced with this design used a stainless steel spacer on the vacuum side. However, during operation the spacer thermally expanded at a different rate than the boron nitride material and cracked the stalk. Subsequent stalks formed the vacuum side spacer from a bridge of boron nitride that was not completely bored out near the end of the stalk.

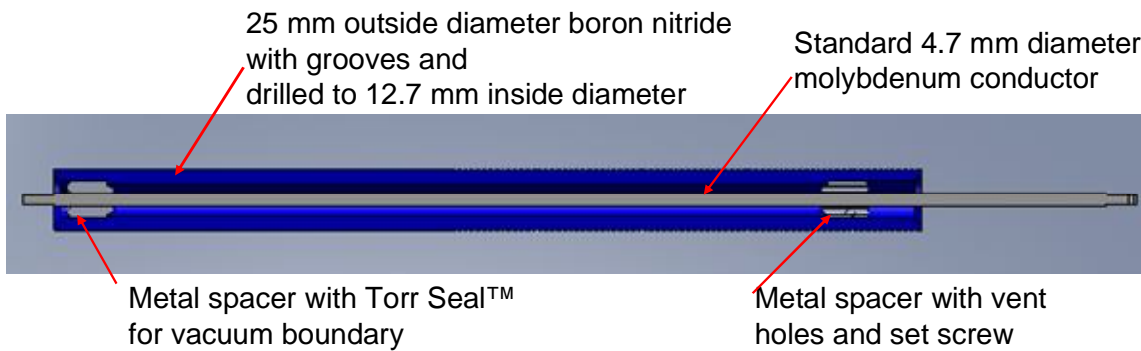


Figure 4-26: Sketch of the new high voltage stalk design

Comparing the 0.1 mm gap size case, which simulated the prior stalk designs, to the new design shown in Figure 4-26 resulted in a reduction of the maximum field in the gap by a factor of 2.6, from 283 kV/mm to 108 kV/mm. The maximum field in the boron nitride was reduced from 63 to 9 kV/mm, a factor of 7. Incorporating this design with the high voltage feed-through described in section 4.2.2, the maximum field in the gap could be reduced to 88 kV/mm and the field in the boron nitride becomes 8 kV/mm. These results were calculated for an applied voltage of -300 kV.

This new stalk design was first tested on the UW IEC device HOMER. As of the time of this writing it has been installed for 19 months with 130 run hours and has achieved an applied voltage of 160 kV. Applied voltages greater than 160 kV have not yet been attempted for reasons not related to the stalk design.

The stalk design used on the SIGFE device changed the vacuum end spacer to an external bell shaped electrode. In addition to centering the main conductor, the shape of this conductor acted to reduce the electric field at the cathode-vacuum-insulator triple point and to shadow the surface from sputtered metal. The reduction of the electric field at the triple point reduced the initiation of electrical breakdown along the surface of the stalk. This concept was detailed in section 4.1.4. The stalk used for all of the data collected for this dissertation was the original stalk and was still operational at the time of this writing. It has

achieved stable operation at an applied voltage of 150 kV, and has approximately 75 hours of run time.

#### *4.2.4. Cathode design for electron trapping*

One of the features that distinguish the SIGFE and Hirsch devices from the gridded IEC devices is the design of the cathode. The cathodes in most gridded IEC systems were simple grids of metal wire formed and welded into a spherical shape. The cathodes in the Hirsch and SIGFE devices acted as both a lens and an opaque boundary for containing electrons. The theory of operation behind the SIGFE cathode lenses was that ions would be accelerated and focused through the 12.7 mm diameter beam ports. Stray ions that were not perfectly focused or that were deflected by space charge would strike the inside of the opposite cathode lens and create secondary electrons. Since the electrodes forming the cathode region were mostly opaque, the electrons would not see any of the external electric field and would remain in the cathode region.

The design of the SIGFE cathode lens used the upstream side of the cathode as the final electrostatic lens and the downstream side was one-sixth of a sphere. When all six ion gun modules were mounted together their inside surfaces enclosed a 110 mm diameter spherical space. The photo in Figure 4-27 shows the inside of the cathode region with five of the six ion gun modules in place. The edges between the cathode lenses were 8 mm apart, and were intended to allow access to the core region for the various diagnostics and to allow for neutral gas pumping while limiting the number of electrons that escaped the cathode region.

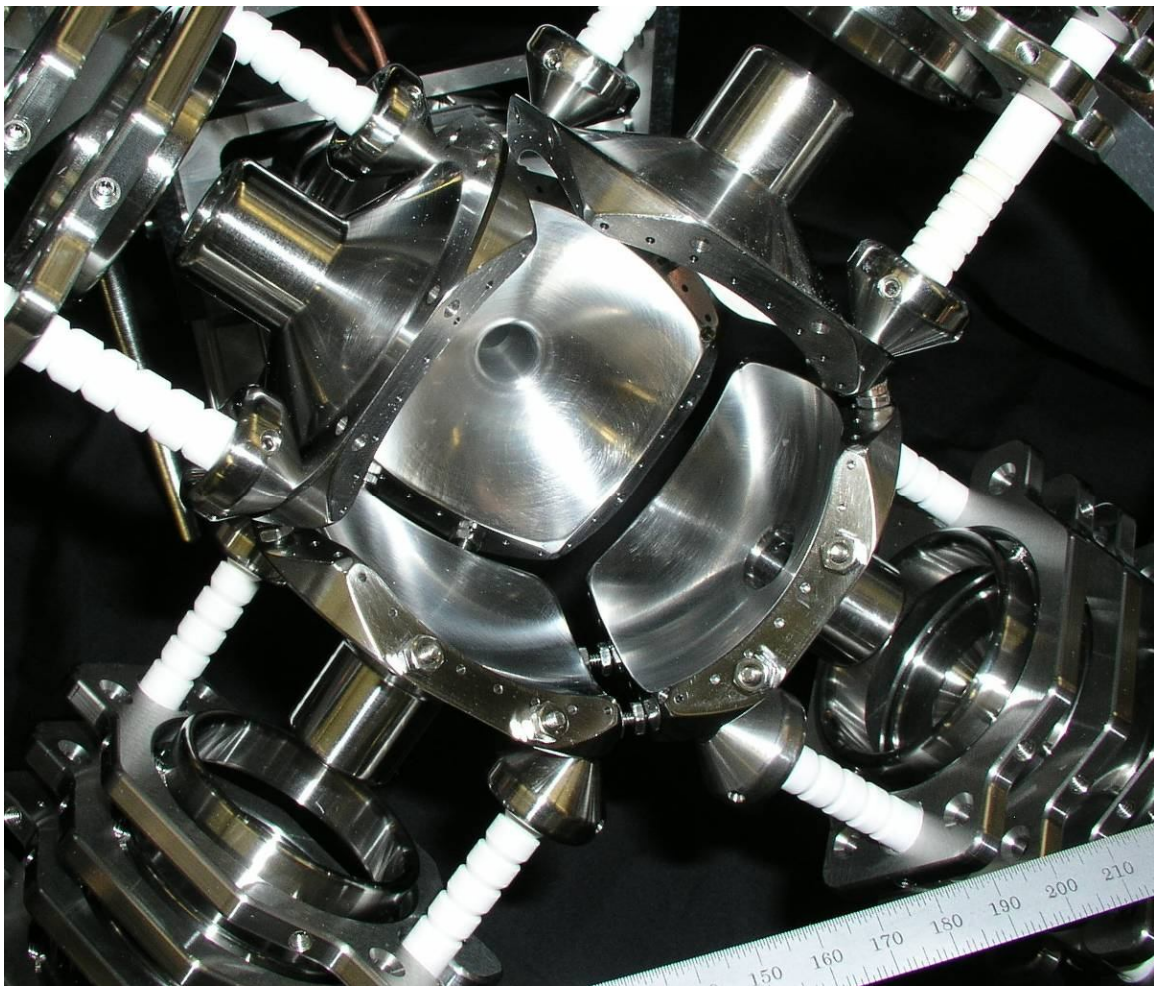


Figure 4-27: Photo of the 110 mm diameter spherical cathode region form by the final electrostatic lenses of the ion gun modules. One of the modules was removed for viewing.

In practice it was believed that the 8 mm gaps between the cathode lenses were allowing too many electrons to leak out of the cathode region. Escaping electrons would be accelerated back towards ground and waste high voltage power, thus reducing the machines neutron rate per power efficiency. To reduce the external electric field seen inside the cathode region the stainless steel shields seen in Figure 4-28 were snapped into place to cover the gap. The shields were made to block line-of-sight out of the cathode region. However, they had to have a gap between them and the cathode lenses in order for the neutral gas in the cathode to be pumped out. Without a gap, D and  $^3\text{He}$  gas or containment gases could build up inside the region and interact with the ion beams. There was approximately a

3 mm gap between the shield and the lenses; this provided at least 1260 mm<sup>2</sup> of open surface area. This amount of surface area was predicted to provide adequate pumping to the region, therefore only a negligible amount of pressure difference was expected between the pressure gauge and the cathode region.

At the corners of the cathode lenses various types of shields were installed. Figure 4-28 shows a quartz window and an 8  $\mu\text{m}$  Al corner shield. The thin Al foil shield was used to allow fusion protons to pass with minimal interaction, but to stop secondary electrons from escaping. The corner at the bottom of the device had a quartz window installed for optical viewing. Corners that did not line up with a diagnostic port had simple thick stainless steel shields.

Despite the sharp edges the shields introduced to the high voltage cathode, they did not significantly reduce the high voltage performance of the system. In qualitative terms, the high voltage performance may have improved slightly since fewer electrons were freely streaming around and striking the insulators. As will be presented in more detail in the results section, the addition of the electron shields improved the neutron rate by approximately a factor of 2 for the same operating conditions.

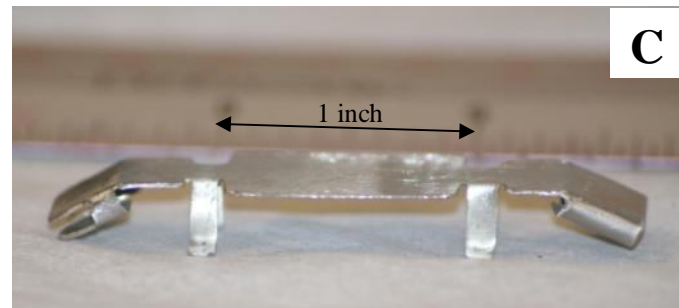
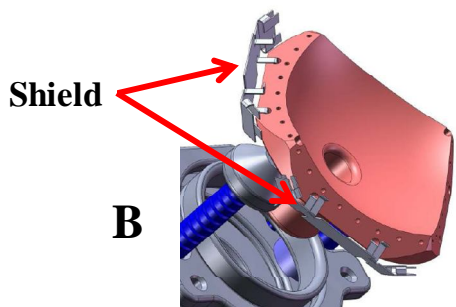
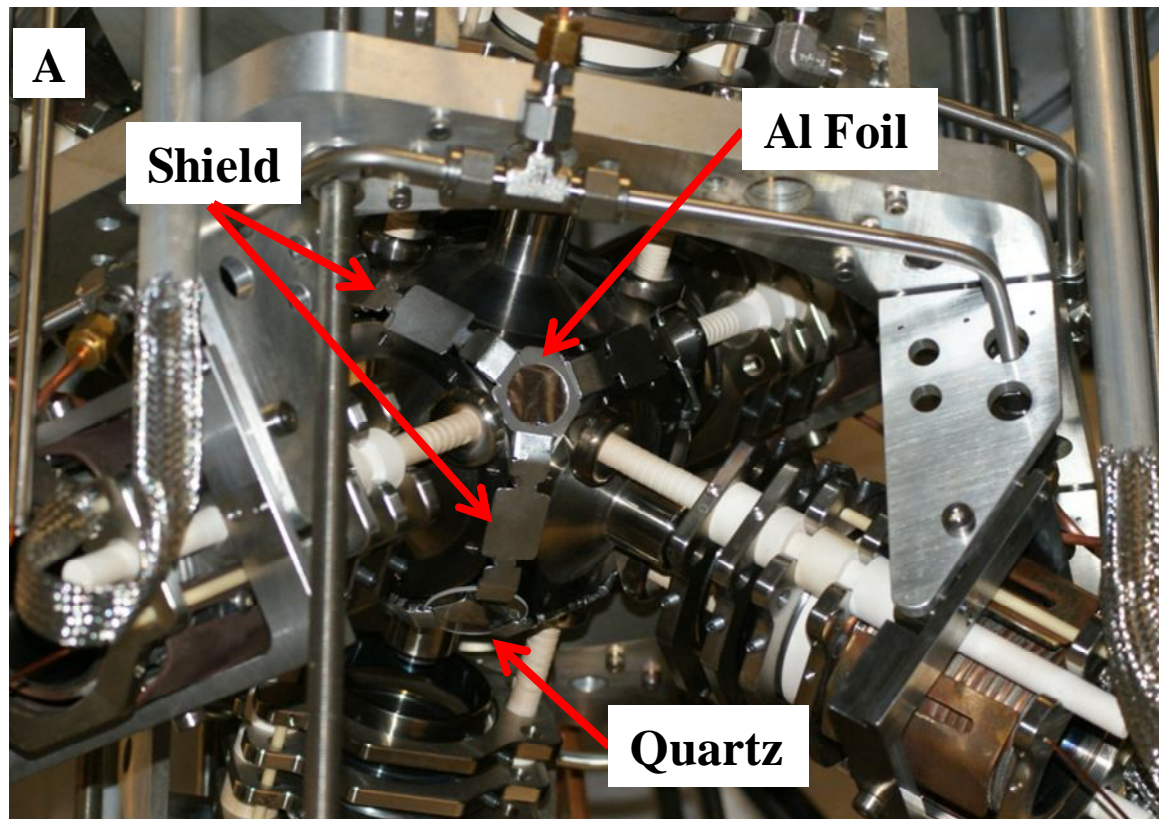


Figure 4-28: A) Photo of the electron shields installed. An 8  $\mu\text{m}$  Al foil is shown at the corner of the lenses to allow fusion protons to reach the detectors, and a quartz window was installed for optical viewing inside the cathode. B) Illustration of the fit of the shields, note the gap between the shield and the lens. C) Photo of the electron shield. The ends of the shields were formed to hold the various styles of corner shields

#### 4.2.5. Power supplies

The Six Ion Gun Fusion Experiment required a sophisticated array of power supplies. Each ion gun module had independent control for the extraction lens voltage, focus lens voltage, and plasma filament heating power. The cathode lenses shared a -300 kV, 200 mA DC power supply.

The -300 kV power supply was designed and built by Phoenix Nuclear Labs [21] for the specific purpose of powering IEC type devices. The supply could continuously deliver -300 kV DC and 200 mA with less than 1% ripple. To protect the delicate components inside the SIGFE device, the power supply had a very low stored energy, less than 200 J, and could sense and shutdown from an arc in less than 50  $\mu$ sec. These features delivered less energy to an arc and therefore limited the amount of permanent damage to the insulators and electrodes. The oil filled tank that held the high voltage components for this power supply can be seen in Figure 4-15.

To further protect the high voltage components, a set of 250  $k\Omega$  ballast resistors was installed in series between the Phoenix supply and the cathode. This resistor set along with the power supply's internal 45.5  $k\Omega$  resistor limited the maximum current draw during a direct short to ground to 0.5 Amps for an applied voltage of -150 kV. Without the external ballast resistors the maximum current would have been 3.3 Amps, a factor of 6.6 higher. In addition to protecting the components, the 250  $k\Omega$  ballast resistors made the system 6.6 times more resistance to small arcs that would have otherwise caused the power supply to trip its overload circuit and shutdown. Since small arcs were unavoidable, the additional resistance gave the system the stability required to take 10 to 1000 second long uninterrupted data sets. The ballast resistor however, caused a voltage drop between the power supply and the cathode. Since both the voltage and current from the supply were monitored, the actual cathode voltage was easily calculated in real-time by the LabVIEW control program.

The extraction electrode of each of the six ion gun modules were powered by independent Glassman MK15N5 power supplies. The Glassman supplies were rated for continuous DC power up to -15 kV and 5 mA with less than 0.03% ripple and less than 0.8 J of stored energy. [22] They used a simple air-insulated brick design with all of the control

and monitoring performed through 0 to 10 V analog signals. The supplies were fully controlled by the main LabVIEW program by connecting these remote signals to the cRIO LabVIEW controller. Similar to the Phoenix supply,  $3\text{ k}\Omega$  of ballast resistors were placed between the supply and the lenses. This limited the peak discharge current at full power to 5 A versus 500 A. At  $3\text{ k}\Omega$  and 5 mA, the voltage drop across the external resistors during operation was negligible.

Controlling the voltage applied to the focus lenses was a more difficult task than originally expected. As ions struck the cathode, secondary electrons were formed and a significant current of these electrons were accelerated into the focus lenses. The only path to ground for the cathode supplied electrons was through the focus lenses' negative high voltage power supplies. Standard DC power supplies use a network of diodes and capacitors to convert the AC power from a high voltage isolation transformer into DC power. The diode rectifiers only allow electrons to flow to the lenses and could not allow the cathode generated electrons to pass through. In the first SIGFE experiments with a standard DC supply, the cathode electrons did not have a path to ground. This caused the focus lens voltage to runaway to increasing negative potentials until the breakdown voltage of the system was exceeded and arcing occurred. This run-away voltage until breakdown was quickly repeated multiple times a second until a component failed or the system was shutdown.

The initial solution to the buildup of electrons on the focus lenses was to attach high power resistors in parallel with the power supply. This provided a path for the cathode generated electrons to reach ground, however it did not discriminate between the cathode electrons and the power supply electrons. Thus, a large portion of the power supplies energy was dumped to ground. This heated the resistors to high temperatures and greatly increased the power requirement. A high voltage power supply manufacturer, Gamma High Voltage

Research [23], developed a custom solution to this problem. The custom Gamma High Voltage supplies placed a ladder of zenor diodes and MOSFETs at the output of standard -15 kV, 5 mA supplies. The MOSFETs acted as variable resistors that maintained a constant current to ground independent of the output voltage or current source. These power supplies were capable of sinking or sourcing 2.5 mA of current at voltages from -2.5 kV to -15 kV.

The system integration of the focus lens supplies was similar to the extraction lens power supplies. They were remotely monitored and controlled via 0 to 10 V analog connections to the cRIO LabVIEW controller. Ballast resistors valued at  $3\text{ k}\Omega$  were placed in series between the focus lenses and the power supplies to limit the peek current during an arc.

The electrons that initiated the plasma in the ion source of each ion gun module were produced by a heated, negatively biased tungsten filament. The experiment used the tungsten filament from a standard commercial 300 W incandescent light bulb. These filaments required 0 to 130 V DC across the filament for heating and needed to be biased negative with respect to the grounded tube enclosing the plasma source; the filament arrangement was shown in Figure 4-3 and Figure 4-5. Two separate, but identical power supplies were designed and built by Richard Bonomo for the filaments. [24] The supplies used isolated variac transformers and a network of diodes, inductors, and capacitors to provide 0 to 130 V DC across the filaments and bias voltage to the entire filament from 0 to -250 V DC with respect to the chamber ground. For example, if 100 V was applied across a filament that was biased at -60 V; the two ends of the filament would be at -60 and -160 V with respect to ground. The supplies had a measured ripple from pure DC of less than 1%, and were rated for 10 A of filament heating current and 10 A of bias current. Additionally, each supply had four output channels. The first channel was the direct output and the other three channels

were connected through a rheostat that added a variable resistance in series with the filament heating. This allowed the heating power of each filament to be varied slightly with respect to the others; this feature helped to balance small variations in the fabrication of the experiment and to provide more balanced ion current from each ion gun module.

The filament power supplies were manually controlled, but were heavily instrumented for monitoring with the LabVIEW software. The filament heating voltage and heating current for each of the four channels was able to be monitored via a 0 to 10 V analog signal. The bias voltage from ground and bias current for the entire supply was also monitored. Two identical filament supplies were placed in the same structure and each was used to power one half of the ion gun modules. Having two separate supplies allowed for the filament heating power and bias to be adjusted depending on what fuel gas was flowed into that set of guns.

#### *4.2.6. Computerized control, monitoring and data logging*

An advanced computer based monitoring and machine control system was developed for the SIGFE. Inputs and outputs from multiple hardware components were integrated into a custom computer program written on the LabVIEW® software platform. The three main functions of the system were to 1) provide real-time monitoring of the operation and performance of the experiment, 2) provide automatic and manual control of the twelve -15 kV power supplies used for the ion gun lenses, and 3) to provide a consistent record of the entire experimental run for later analysis.

The UW IEC laboratory has developed a flexible set of hardware for monitoring and controlling its experimental devices. Three input/output devices are directly installed in one Windows XP based computer. These devices include a wide range of functions, which include the following: 4 analog input channels for true simultaneous sampling up to 5 MHz,

90 analog input channels at  $\sim$ 10 kHz, and 6 counter/timers. A fourth device was a CompactRIO (cRIO) programmable automation controller. The cRIO is a standalone device that runs a compact version of the LabVIEW software on an onboard computer processor with a field programmable gate array (FPGA). The device communicates with the main PC based LabVIEW program via Ethernet. The cRIO chassis can accept up to 8 expansion modules. The four modules installed were a 16 channel analog output, a 32 channel analog input, an 8 channel counter/timer, and a 4 channel thermal couple.

LabVIEW® is a high-level graphical program language that specializes in data collection and machine control in a laboratory environment. Table 4-3 is a list of the experiment parameter monitored by the program for the SIGFE. Most of the more than 50 measurements were read into the program from -10 to 10 V analog signals. The signals were continuously sampled at 1000 Hz. Several signals were displayed in an on-screen chart at the full 1000 Hz rate to assess the stability of the experiment's high voltage system. Ten times a second (10 Hz), 100 samples of each parameter were averaged and displayed to on-screen numeric indicators. The averaging eliminated much of the fluttering and noise in the measurements and made the screen easier to read. These values were also stored in memory to be further averaged, charted on screen and recorded into a text file along with the results of the radiation counters.

Table 4-3: Experimental parameters displayed and recorded by custom LabVIEW® program

<b>Monitored experiment parameter</b>	<b>Measurement Source</b>
Run time	System clock
Raw cathode voltage	300 kV supply
Cathode current	300 kV supply
Adjusted cathode voltage	Calculation
Flow rate of He-3	Flow controller 2
Flow rate of D	Flow controller 3
Flow rate of He-4	Flow controller 4
Chamber pressure from ion gauge	Ion gauge
Chamber pressure from baratron gauge	Baratron
Foreline pressure	Thermal couple
Filament heating voltage chn A&B	Filament power supply
Filament heating current chn A&B	Filament power supply
Filament Bias voltage chn A&B	Filament power supply
Filament Bias current chn A&B	Filament power supply
Extraction lens voltage (separate for each of 6 guns)	Extraction power supplies
Extraction lens current (separate for each of 6 guns)	Extraction power supplies
Focus lens voltage (separate for each of 6 guns)	Focus power supplies
Focus lens current (separate for each of 6 guns)	Focus power supplies
Neutron counts from detector 1	SCA
Neutron counts from detector 2	SCA
Proton counts	SCA
Proton detector position	Servo motor
Detector count time	Hardware clock

Digital counters were integrated into the LabVIEW program that recorded the results of several single channel analyzers (SCA) connected to the radiation detection electronics. To ensure an accurate counting time, the counters were enabled and disabled with an external hardware gate. The gate was connected to a LabVIEW controlled pulse generator that created a stable square wave pulse with software adjustable frequency and duty cycle. The accuracy of the counters was tested to be better than 1 $\mu$ sec, which was better than the integration time of the detector electronics. In typical operation, the counters were enabled

for 3 seconds and disabled for 1 second. While enabled, data from the counters and all other data sources was accumulated. When the gate pulse went low, the counters' values were recorded and corrected for detector dead-time and calibration. The accumulated analog data points were further averaged to the detector count time. All of this data, plus several other sources and the standard deviation of key parameters, was recorded to a single comma-delimited line in a text file. The text file acted as a complete record of entire experimental run with a typical resolution of four seconds. Selected count time averaged data was displayed to on-screen charts to aid in the immediate identification of trends during an experimental run.

The voltage output of the twelve -15 kV extraction and focus lens power supplies was designed to be remotely controlled via a 0 to 10 V signal. The 12 control signals were generated by the cRIO's 16-channel analog output module. The flexibility of having the focus lens supplies controlled by the LabVIEW program was utilized in several ways. The voltage of each lens could be independently adjusted in real time to account for small variation in the fabrication of each ion gun module. Secondly, an option in the program could be enabled to automatically adjust the focus voltage to track changes in the cathode voltage. This was important since the focus voltage required to focus the ion beams was a function of the cathode voltage. Lastly, data on the effects of changing the focus voltage was collected automatically. For a given set of conditions, the focus voltage was set to auto scan mode. During the off time of the counters, the program changed the focus supplies to a new setting; data was collected during the counter's on-time, and the cycle repeated itself at the start of the next off time. This greatly increased the speed and accuracy of these data sets.

The most sophisticated portion of the LabVIEW program controlled the movable-collimated proton detector described in the diagnostic section. The program communicated

with a servo motor that positioned the detector. When the servo indicated it was in position, the counters on the cRio device were enabled for a preset time. When the counters finished, LabVIEW communicated the number of degrees of rotation for the next location to the servo motor and repeated the process. At the start of the program, the servo was automatically homed by moving it on to, then just off of, a limit switch built into the detectors movable mount. This feature provided a detector position repeatability of less than 0.3 mm between runs.

LabVIEW and its associated hardware were extensively used during this research to increase the level of detail and accuracy of the collected data. The value of the effort invested was overwhelmingly realized while analyzing the data.

#### *4.2.7. Vacuum system*

The gas metering and vacuum pumping system of the SIGFE was designed to maintain a 38:1 pressure differential between the plasma source region and the rest of the device. This was accomplished by piping the D or  $^3\text{He}$  fuel gas directly in to the plasma source region and restricting the flow out of each source through a 1.8 mm diameter thin circular aperture. The main chamber of the experiment was evacuated with a 1000 L/sec turbo molecular pump. Without gas flow the system maintained a base pressure of approximately  $2 \times 10^{-4}$  Pa ( $2 \times 10^{-6}$  Torr). In operation, ion beams were produced at main chamber pressures from 6.7 mPa to 270 mPa.

The vacuum system that supported the SIGFE was made up of several pressure gauges, pumps and a residual gas analyzer (RGA). The cylindrical stainless steel vacuum chamber had a diameter of 46 cm and was 45 cm tall. It had multiple CF flanged ports every 45 degrees around the circumference and used large viton O-ring seal on the top and bottom. A Leybold 1000C turbo-molecular pump was mounted with a gate valve on the bottom of the

vacuum chamber; this pump had a rated volumetric pumping speed of 1100 L/sec in N<sub>2</sub>. A Leybold D25B rotary vane fore line pump was used to back the turbo pump; it was rated at 7 L/sec.

The pressure in the main chamber was measured by two independent gauges, a Varian Bayard-Alpert ionization gauge and a MKS 627C capacitance manometer. The ionization gauge was used for pressures below 0.08 Pa ( $6 \times 10^{-4}$  Torr). Ionization gauges are sensitive to the gas species. The ion gauge in the SIGFE was calibrated to N<sub>2</sub>, however all of the data presented in this dissertation has been corrected for D<sub>2</sub> gas. The location of the ion gauge relative to the pump is shown in Figure 4-29. The capacitance manometer was used for pressures between 13 mPa and 13 Pa (0.1 to 100 mTorr). Capacitance manometers read in absolute pressure and are not affected by the gas species being measured. A thermal couple gauge was installed near the outlet of the turbo-molecular pump to monitor the pressure in the fore line. The measurements of all three pressure gauges were recorded by the LabVIEW control program.

Before the experiment was constructed, rough calculations of vacuum system's expected performance was made in order to properly size the components. The pressure at various locations in the design was calculated and the pressure difference between the main chamber and the ion source region was estimated. Figure 4-29 is schematic used for these approximate calculations.

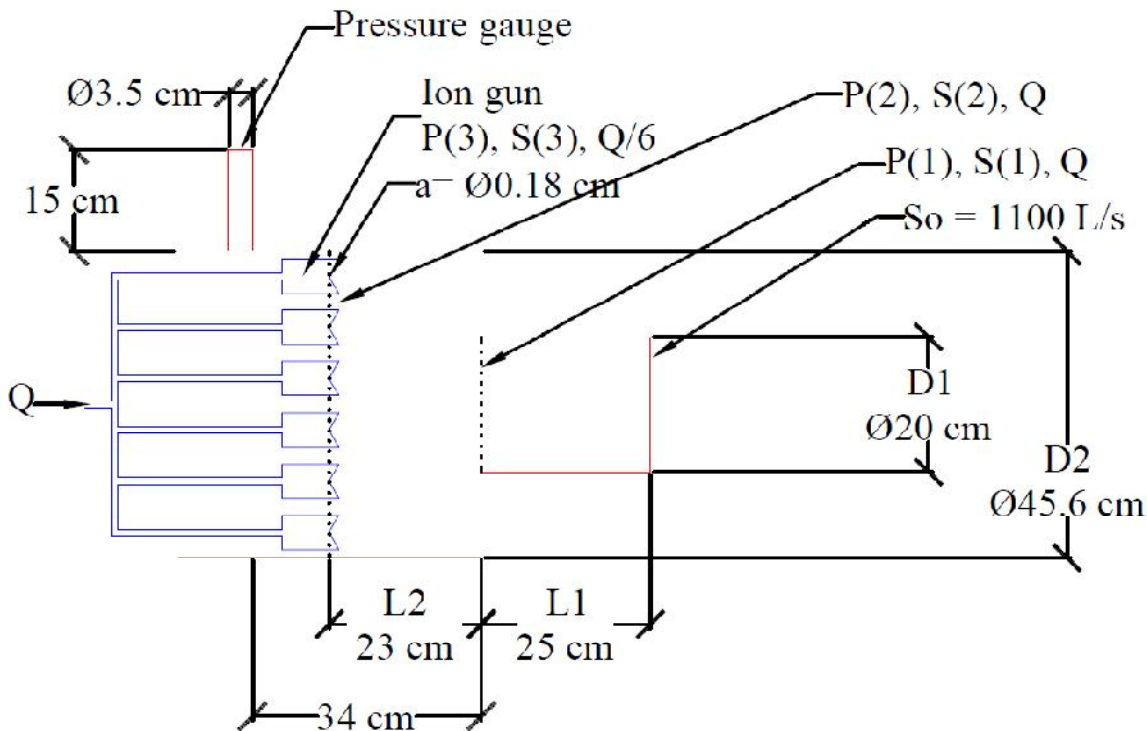


Figure 4-29: Schematic of vacuum system for vacuum conductance calculations.

The pressure in a vacuum system at any location,  $P(x)$ , can be calculated from eqn 4-7. Where  $Q(x)$  is the total gas flow,  $S(x)$  is the effective pumping speed, and  $x$  indicates the location in the system.

$$P(x) = \frac{Q(x)}{S(x)} \quad \text{Eqn 4-7}$$

$Q$  is the total gas flow in the system from all sources, and is a conserved quantity in steady-state; the total gas flow into a system must equal the gas flow out. The relationship between the gas flow in the various regions of SIGFE is given in eqn 4-8. Note that the flow in each ion gun, region 3, is 1/6 the total flow since it was divided into six parallel paths. Sources of gas can include out-gassing of the vacuum components, containments, leaks in the vacuum chamber, and the gas intentionally flowed into the ion guns. For this analysis, the intentional gas flow was assumed to be much larger than the other sources; therefore the other sources were neglected.

$$Q = Q(1) = Q(2) = 6 Q(3)$$

Eqn 4-8

The effective pumping speed at any location is a function of the vacuum pump speed,  $S_o$ , and the parallel and series conductance between that location and the pump. For components in series, the effective pumping speed can be calculated from eqn 4-9 where  $C(x)$  is the conductance through that region.

$$\frac{1}{S(x)} = \frac{1}{C(x)} + \frac{1}{C(x-1)} + \dots + \frac{1}{S_o} \quad \text{Eqn 4-9}$$

The conductance of a straight circular tube is found from eqn 4-10, where  $C_t$  is the conductance constant for a given gas,  $D$  is the tube diameter, and  $L$  is the length of the tube.

$$C_{tube} = C_t \frac{D^3}{L} \quad \text{Eqn 4-10}$$

The conductance of a thin circular aperture is given by eqn 4-11, where  $a$  is the diameter of the aperture and  $C_o$  is the conductance constant for a given gas.

$$C_{aperture} = 4 C_o a^2 \quad \text{Eqn 4-11}$$

The effective pumping speed at the most upstream point of each region, as describe in Figure 4-29, was calculated from eqn 4-12. Note that region 3 is a point immediately upstream of the aperture and is only one of the six guns.

$$\text{region 1: } \frac{1}{S(1)} = \frac{L_1}{C_t D^3} + \frac{1}{S_o}$$

$$\text{region 2: } \frac{1}{S(2)} = \frac{L_2}{C_t D_2^3} + \frac{L_1}{C_t D_1^3} + \frac{1}{S_o} \quad \text{Eqn 4-12}$$

$$\text{region 3: } \frac{1}{S(3)} = \frac{1}{4 C_o a^2} + \frac{L_2}{C_t D_2^3} + \frac{L_1}{C_t D_1^3} + \frac{1}{S_o}$$

Combining the equations of 4-8 and 4-12 yields the pressure at upstream point of each region.

$$\text{region 1: } P(1) = Q \left( \frac{L_1}{C_t D^3} + \frac{1}{S_o} \right)$$

$$\text{region 2: } P(2) = Q \left( \frac{L_2}{C_t D_2^3} + \frac{L_1}{C_t D_1^3} + \frac{1}{S_o} \right) \quad \text{Eqn 4-13}$$

$$\text{region 3: } P(3) = \frac{Q}{6} \left( \frac{1}{4 C_o a^2} + \frac{L_2}{C_t D_2^3} + \frac{L_1}{C_t D_1^3} + \frac{1}{S_o} \right)$$

The pressure ratio between the plasma source and the chamber (region 3 and 2) can then be calculated from eqn 4-14. Note that the pressure ratio is not directly dependent on the flow rate.

$$\frac{P(3)}{P(2)} = \frac{1}{6} \left[ \frac{C_t S_o}{4 C_o a^2 \left[ S_o \left( \frac{L_2}{D_2^3} + \frac{L_1}{D_1^3} \right) + C_t \right]} + 1 \right] \quad \text{Eqn 4-14}$$

The designed values for the variables in eqn 4-14 are shown in Figure 4-29, and are listed in Table 4-4. The pressure difference between the ion source region and the main chamber was estimated to be 38:1. Therefore for an experimental chamber pressure of 13 mPa (100  $\mu$ Torr) the ion source pressure was estimated to be 500 mPa (3.8 mTorr).

Table 4-4: Values of variables for the pressure difference calculation. \*for hydrogen

Variable	Value
$C_t^*$	$46 \frac{L}{\text{sec cm}^2}$
$C_o^*$	$35 \frac{L}{\text{sec cm}^2}$
a	0.18 cm
$S_o$	$1100 \frac{L}{\text{sec}}$
$L_1$	25 cm
$D_1$	20 cm
$L_2$	23 cm
$D_2$	45.7 cm
$\frac{P(3)}{P(2)}$	38

### 4.3. Diagnostics

The diagnostics used on the SIGFE consisted of two neutron detectors, three proton detectors, two visible light cameras, and a residual gas analyzer (RGA). This array of diagnostics was able to observe the performance and operation of the experiment from several different perspectives. In most cases, data for each diagnostic was collected simultaneously with the other diagnostics and real-time experimental parameters. The analysis of this data and comparisons drawn between the different perspectives provided insight into the different physical mechanisms that were responsible for the  $D(d, n)^3He$ ,  $D(d, p)T$ , and  $^3He(d, p)^4He$  nuclear fusion reactions inside the SIGFE.

#### 4.3.1. Neutron detection

The 3.2 MeV neutrons produced from the  $D(d, n)^3He$  reaction were detected using two independent neutron detector setups. Both setups were similar in their use of  $^3He$  fill detection tubes, standard nuclear instrumentation modules (NIM) electronics, and the method used to record the results. The only difference was the location and size of the  $^3He$  detectors. Figure 4-30 shows the location of the detectors relative to the SIGFE vacuum chamber.

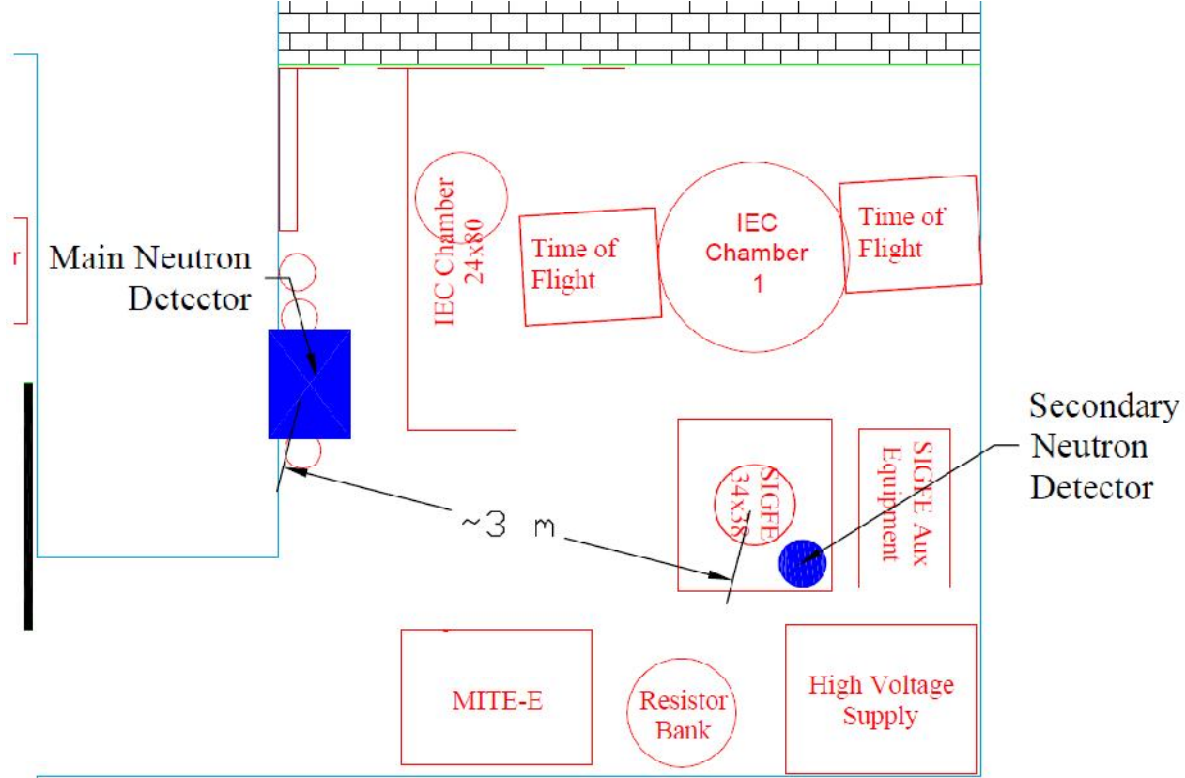


Figure 4-30: Layout of UW-IEC's hot cell. The location of the two neutron detectors is shown in relation to the SIGFE experiment.

For the main detector, the relationship between the number of counts detected and the total number of neutrons produced was determined by placing a PuBe neutron check source at the center of the SIGFE vacuum chamber. The PuBe source produced  $2.23 \times 10^6$  neutrons per second. [25] The counts detected from the calibration source were recorded by both the MCA and the LabVIEW counter for a known period of time. The main neutron detector was 2.9 m from the center of the SIGFE chamber; this was more than a factor of 10 greater than the 0.23 m radius of the device. The maximum error that could be due to the spatial distribution of fusion reactions was estimated by comparing the  $1/r^2$  falloff in neutron flux from the center of the chamber to the detector versus the closest and furthest points in the chamber; this was +14% and -18% respectively. Additionally, there were no obstacles between any location in the SIGFE device and the detector that could have

significantly attenuated 3.2 MeV neutrons. Therefore, the calibration factor determined from the equation below was a good estimate of the total neutron production rate regardless of the spatial distribution of fusion reactions. The calibration factors used for this dissertation are shown in Table 4-5.

$$\text{Calibration factor } \left[ \frac{\text{neutrons}}{\text{count}} \right] = \frac{\text{events counted [counts]}}{\text{count time [seconds]}} \Bigg/ \text{PuBe source strength } \left[ \frac{\text{neutrons}}{\text{second}} \right]$$

Due to its close proximity to the SIGFE device, the secondary neutron detector had a much higher count rate than the main detector for the same total neutron rate. The purpose of this detector was to identify small changes in the neutron rate on time scales that would have had too large of counting error to distinguish in the main detector. This low counting error was obtained at the expense of larger error in the calibration factor. The distance from the chamber to the detector was smaller than the chamber's diameter. A neutron generated at the closest point in the chamber was a factor of 10 more likely to be detected than a neutron generated at the opposite wall. Therefore, a calibration factor of this detector was not determined.

Figure 4-31 is a schematic of the setup of the detector electronics and Table 4-5 gives the details of equipment and settings used for each detector setup. The output of the main detector was recorded by two means. First, the output signal of the amplifier was fed to a PC based multi-channel analyzer (MCA). The total number of counts recorded by the MCA over a 10 second time window was manually recorded in the experimental log book. Additionally, the amplifier signal was fed into a single channel analyzer (SCA) whose digital logic pulse output was connected to a LabVIEW controlled counter. The counting time of the LabVIEW counter was typically 3 seconds with a 1 second wait time between counting

windows. The value of the LabVIEW counter was automatically recorded along with many other experimental parameters into a text file. The details of the LabVIEW program and text file were discussed in Section 4.2.6. Generally, the LabVIEW counter data was used in the results section of this dissertation. The MCA data was used as a backup and to watch for excess noise on the setup. The output of the secondary neutron detector was typically recorded only by a LabVIEW counter, but could be looked at with the MCA if necessary.

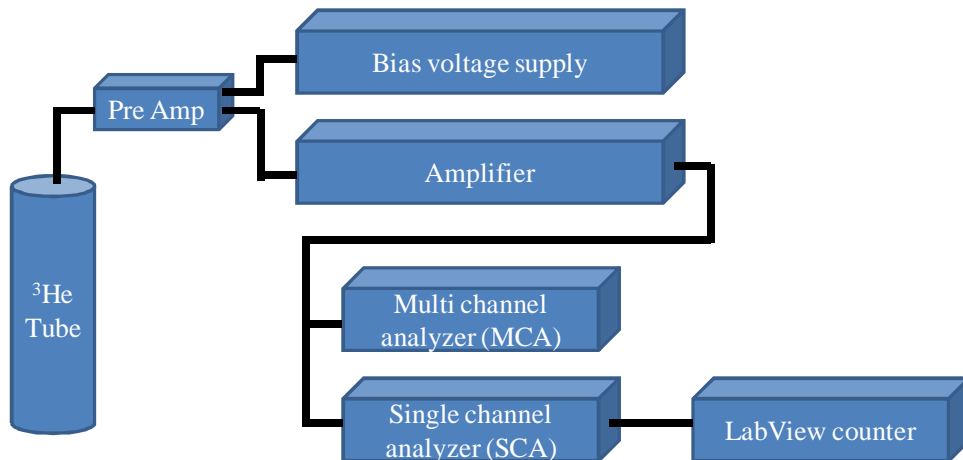


Figure 4-31: Schematic of electronics used for both the main and secondary neutron detector setups.

Table 4-5: Details of the two neutron detector systems including model number and settings of equipment. LLD and ULD are the Lower and Upper Level Discriminator setting for the Single Channel Analyzer (SCA). Note that the TC246 is a combination amplifier and SCA.  
 \*Values of the coarse adjust, multi-turn potentiometer, \*\*Value of the multi-turn potentiometer.

	Main detector	Secondary detector
<b><sup>3</sup>He Tube, LND Inc model:</b>	#2804	#25291
<b>Preamp model</b>	TC preamp	Ortec 142PC
<b>Amplifier / SCA model</b>	TC246	TC246
Amp setting	500, 10-0*	100, 5-0*
LLD setting	1-48**	1-48**
ULD setting	10-0**	10-0**
<b>Bias supply model</b>	Mech 256	TC952
Bias setting	1400 V	1300 V
<b>Multichannel analyzer</b>	Ortec PCI Trump	
LLD setting	300	
<b>MCA calibration factor [n/cnt]</b>	39188.3	NA
<b>LabVIEW calibration factor [n/cnt]</b>	38847.2	NA

The  $^3\text{He}$  based neutron detectors were extensively used during this dissertation to judge the performance of the SIGFE. The majority of the data shown in chapter 6 was generated using the main neutron detector setup described above. The measurement of the fusion neutron production rate was important, because unlike the fusion protons, the neutrons were not significantly attenuated by the structure of the equipment and therefore a true total  $\text{D}(\text{d},\text{n})^3\text{He}$  reaction rate could be determined.

#### *4.3.2. Fusion ion Doppler shift (FIDO) diagnostic*

The fusion ion Doppler shift (FIDO) diagnostic is a silicon based proton detector bent by an electromagnet out of the line-of-sight of the bremsstrahlung radiation generated in an IEC style device. The FIDO diagnostic was developed in 2008 by David Boris as a portion of his PhD dissertation in the UW-IEC laboratory. [26] Removing the detector from the line-of-sight of the chamber eliminated the need for the Al or Pb foil shields normally placed in front of the detector to attenuate the x-rays. [16] The amount of Pb required to shield the x-rays in a line-of-sight detector system degraded the resolutions of the proton spectrum, which would make the Doppler shift of the fusion protons difficult to resolve.

In the  $\text{D}(\text{d}, \text{p})\text{T}$  fusion reaction a 3.02 MeV proton is produced in the center-of-mass frame. The lab frame energy of the proton is Doppler shifted by the center-of-mass energy of the reacting particles. The velocity of this proton in the lab frame,  $v_t$ , can be found from the equation 4-15, where  $v_f$  is the velocity imparted to the proton from the fusion reaction,  $v_{cm}$  is the velocity of the center-of-mass of the reacting particles, and  $\theta$  is the angle between  $v_f$  and  $v_{cm}$ .

$$v_t = \sqrt{v_f^2 + v_{cm}^2 + 2 v_f v_{cm} \cos \theta} \quad \text{Eqn 4-15}$$

If two equally energetic particles react, the Doppler shift would be zero and  $v_t$  would equal  $v_f$ ; and that would be the expected signature of the beam-beam fusion mode. If one particle is approximately stationary, as expected in the beam-background fusion mode, the center-of-mass energy can be found from equation 4-16. Where  $E_{cm}$  is the center-of-mass energy;  $E_A$  and  $m_A$  are the energy and mass of the moving particle and  $m_B$  is the mass of the stationary particle.  $E_A$  can be converted to the velocity  $v_{cm}$  by equation 4-17.

$$E_{cm} = E_A \left( \frac{m_B}{m_A + m_B} \right) \quad \text{Eqn 4-16}$$

$$V_{cm} = \sqrt{\left( \frac{2 E_{cm}}{m_A + m_B} \right)} = \sqrt{\left( \frac{2 m_B E_A}{(m_A + m_B)^2} \right)} \quad \text{Eqn 4-17}$$

For the D(d, p)T fusion reaction, the moving mass,  $m_A$ , depends on the ion species, which can be  $D_1^+$ ,  $D_2^+$ , or  $D_3^+$ . If the mass of D is denoted  $m_D$ , then  $m_A$  can be written as equation 4-18 where  $x$  is species of the ion: 1, 2, or 3.

$$m_A = x m_D \quad \text{Eqn 4-18}$$

Even though the stationary target is likely molecular deuterium,  $D_2^0$ ,  $m_B$  is assumed to be the mass of atomic deuterium,  $m_D$ , since the kinetic energy and the energy of the molecular bond are negligible. Then equation 4-17 can be rewritten as

$$V_{cm} = \sqrt{\frac{2 E_A}{m_D (1+x)^2}} \quad \text{Eqn 4-19}$$

Equation 4-15 can be rewritten in terms of energy where  $m_p$  is the mass of the fusion proton,  $E_f$  is the energy of the fusion proton in center-of-mass frame, and  $E_t$  is the energy of the proton in the lab frame.

$$E_t = E_f + \frac{m_p}{m_D} \frac{E_A}{(1+x)^2} \pm 2 \sqrt{\frac{m_p E_f E_A}{m_D (1+x)^2}} \cos \theta \quad \text{Eqn 4-20}$$

The ions in the SIGFE were predominantly traveling along distinct trajectories as defined by the ion guns. Therefore, the angle between ion's velocity and a proton that could

reach the detector was well defined. The FIDO diagnostic was mounted on a custom vacuum port whose axis was designed to be an equal angle from the axis of all six guns. Based on the CAD model shown in Figure 4-32, the angle  $\theta$  was found to be  $54.7^\circ \pm 1.5^\circ$ . The error of  $1.5^\circ$  equated to less than a 0.2% change in the proton energy. This well defined angle improved the resolution of the proton spectrum so that it was easier to determine information about the reacting ions.

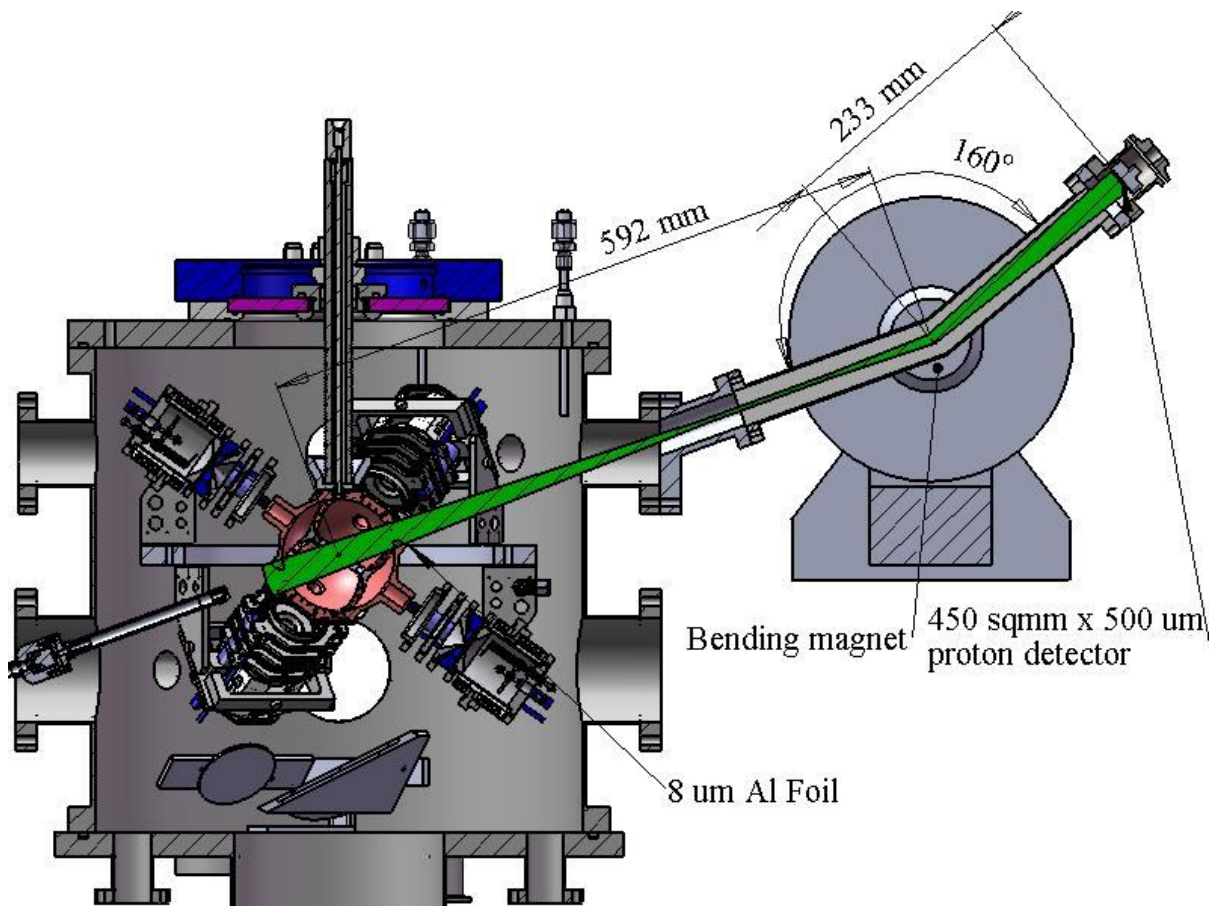


Figure 4-32: Cross-section view of the Fusion Ion Doppler Shift (FIDO) diagnostic installed on SIGFE. The cone-of-view of the system is highlighted. The distance from the detector face to the device center was 825 mm. An  $8\text{ }\mu\text{m}$  Al foil was placed between the device center and the detector.

Table 4-6 shows the Doppler shift for  $D_1^+$ ,  $D_2^+$ , and  $D_3^+$  ions as calculated by equation 4-20. At the operating pressures of the SIGFE, the mean-free path of the ions was calculated to be longer than the device dimensions and the ion energy spectrum was expected

to be approximately equal to the energy corresponding to the cathode potential. One of the goals of the FIDO experiments was to determine the validity of this assumption.

To prevent secondary electrons from escaping the inside of the cathode, an 8  $\mu\text{m}$  Al foil was placed in the gap in the cathode that was aligned with the FIDO diagnostic. Figure 4-33 shows the estimated downshift and energy spread of the proton through the foil as predicted by SRIM®[27]; this was done for the initial energies of protons Doppler shifted by  $D_1^+$ ,  $D_2^+$ , and  $D_3^+$  ions for ion energies of 70 keV, 100 keV, and 125 keV.

Table 4-6: Energy of fusion protons in the lab frame after the Doppler shift as calculated by Eqn 4-20 for 70, 100 and 125 keV ions with stationary  $D^0$ . The average proton energy after attenuation through 8  $\mu\text{m}$  of Al foil is also shown as calculated by SRIM. [27] All energy values are in MeV and masses are in AMU.

Ion energy	Ion species	Initial fusion proton energy			After 8um Al foil		
		$E_t^+$	$E_t^-$	Difference	$E_t^+$	$E_t^-$	Difference
0.070	$D_1^+$	3.22	2.84	0.38	3.05	2.65	0.40
	$D_2^+$	3.15	2.90	0.25	2.98	2.72	0.26
	$D_3^+$	3.12	2.93	0.19	2.94	2.74	0.20
0.100	$D_1^+$	3.26	2.81	0.45	3.09	2.62	0.47
	$D_2^+$	3.18	2.88	0.30	3.01	2.68	0.33
	$D_3^+$	3.14	2.91	0.22	2.98	2.72	0.27
0.125	$D_1^+$	3.29	2.78	0.50	3.12	2.59	0.52
	$D_2^+$	3.19	2.86	0.33	3.02	2.67	0.35
	$D_3^+$	3.15	2.90	0.25	2.98	2.72	0.26

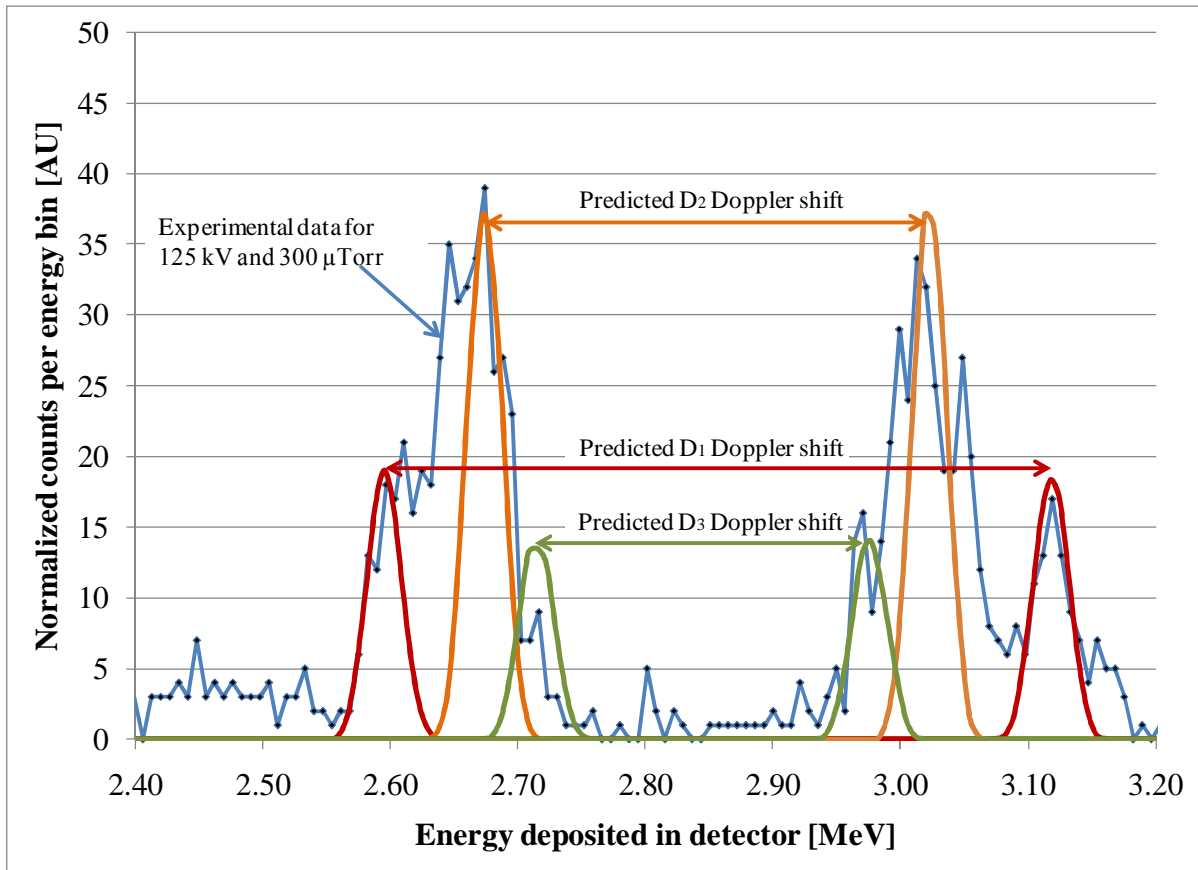


Figure 4-33: Predicted fusion proton spectrum for 125 keV  $\text{D}_1^+$ ,  $\text{D}_2^+$ , and  $\text{D}_3^+$  ions after passing through 8  $\mu\text{m}$  of Al foil. Energy loss through foil was simulated in SRIM. [27] The height of the predicted peaks were adjust to match experimental data. Experimental data set shown was taken at a cathode voltage of 125 kV and 40 mPa (300  $\mu\text{Torr}$ ).

The setup up of FIDO diagnostic is shown in Figure 4-32. The FIDO arm was a piece of stainless steel rectangular tubing cut and welded to form a 20° bend. The protons were bent through this angle by a 1.5 T electromagnet with 76 mm diameter pole faces. The magnet was set to 0.79 T; this optimal magnet field was found though simulations and previous experimental trials performed by Boris. [26] The silicon proton detector used was an Ortec Ultra Series BU-XXX-450-500-S with a light tight coating; the face of the detector had a surface area of 450  $\text{mm}^2$  and thickness of 500  $\mu\text{m}$ . The light tight coating was a 300 nm Si equivalent reflective coating to prevent visible light from being detected while minimizing the disruption to the proton energy. The outside of the FIDO arm and the detector mount was wrapped with a minimum of 3 mm of Pb to shield the detector from x-

rays. To minimize electrical noise on the system, the detector mount was electrically isolated from the rest of the chamber and was only grounded through the detector electronics.

A calibration factor was estimated for the number of protons counted and the total fusion protons produced by assuming a point source of protons at the center of the cathode. The distance from the center of the device to the detector,  $d$ , was 825 mm and the radius of the detector face,  $a$ , was 12 mm. The calibration factor for a point source located at the center of the chamber was found from Eqn 4-15.

$$\frac{1}{\text{calibration factor}} = \frac{1}{2} \left( 1 - \frac{d}{\sqrt{a^2 + d^2}} \right) \quad \text{Eqn 4-15}$$

The result was a calibration factor of 18910 reactions per count. Note that, as seen in Figure 4-32, the FIDO diagnostic could only see a small portion of the geometric area of the SIGFE device. Fusion reactions that did not occur near the center of the SIGFE device could not be detected by the FIDO diagnostic, whereas the neutron detectors could detect neutrons produced at any location. This distinction will be used in the results section to calculate the percentage of fusion reactions that occurred in the center.

The FIDO diagnostic provided a means of measuring the energy spectrum of the fusion proton to a degree of precision that revealed significant information about the reacting particles. This level of precision was made possible by the technique of bending the proton to a detector that was well protected for x-ray noise. Also, the limited geometric volume from which the diagnostic could detect fusion reactions was compared to the neutron diagnostic to determine the fraction of the fusion reactions that occurred at the cathode center versus the rest of the chamber.

### 4.3.3. One-axis movable collimated proton detector

The theory of virtual electrode formation reviewed in chapter 2 suggested that a spatial variation in the fusion reactions at the center of the cathode should exist. Using a collimated neutron detector, Hirsch observed variations at the center of his device that were on the scale of 1 cm; the theory suggested that the variations should be on the millimeter scale. To look for spatial variations in the proton production in the SIGFE, a movable, collimated, silicon based charged particle detection system was designed and constructed. This proton detector was able to be positioned with an accuracy of less than 1 mm and initially had a viewing radius of 1.5 mm on a plane through the origin of the SIGFE device.

Several parameters and constraints were balanced to optimize the performance of this diagnostic. Increasing the count rate required increasing the aperture size and decreasing the distance between the detector and the center of the device. Conversely, to achieve a small spatial resolution the aperture size had to be reduced and the distance between the two collimation apertures had to be increased. Figure 4-34 is the schematic used to optimize these constraints. The relationship between the aperture size,  $a$ , and the viewing radius,  $b$ , at a distance  $d_1$  from the center is given by

$$b = a \left( 2 \frac{d_1}{d_2} - 1 \right) \quad \text{Eqn 4-16}$$

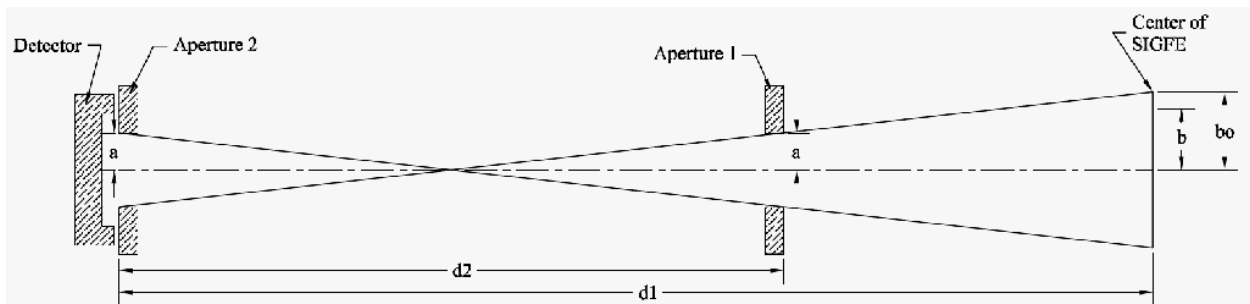


Figure 4-34: Schematic of collimated detector system

The probability of an isotropically generated fusion proton reaching the detector from a point located a distance  $d_1$  from the detector and a distance  $b$  off axis was calculated by eqn 4-17, for  $b$  less than  $a$ . The units of  $P_o$  are *detector event per source event*.  $P_o$  is related to the common parameter of solid angle,  $\Omega$ , in steradians by eqn 4-18.

$$P_o = \frac{1}{2} \left( 1 - \frac{d_1}{\sqrt{a^2 + d_1^2}} \right) \quad \text{Eqn 4-17}$$

$$\Omega = 4\pi P_o = 2\pi \left( 1 - \frac{d_1}{\sqrt{a^2 + d_1^2}} \right) \quad \text{Eqn 4-18}$$

To prevent arcing from the high voltage cathode to the detection assembly the first aperture had to be at least 100 mm from the center of the cathode,  $d_1 - d_2 = 100$  mm. A design target for the viewing cone at the center of the device was chosen as  $b = 1.5$  mm. Table 4-7 shows the resolution,  $b$ , and counting time required to observe 1000 counts assuming a point source of  $10^7$  protons per second. Initially, assuming a fusion rate of  $10^7$  protons per second (p/s), case 3 was chosen as the best balance between low counting times and resolution. Unfortunately, the fusion rate from the center of the device was observed to be on the order of  $10^4$  p/s and the small aperture could not produce a distinguishable proton signal above the x-ray noise. Therefore the apertures were enlarged to a radius of 2 mm (case 7).

Table 4-7: The effect of multiple design parameter choices on the spatial resolution and required count times for the collimated detector setup.

Case	<b>a</b> [mm]	<b>d<sub>1</sub></b> [mm]	<b>d<sub>2</sub></b> [mm]	<b>b<sub>o</sub></b> [mm]	<b>P<sub>o</sub></b> [cnts x 10 <sup>-6</sup> / fusion]	<b>Seconds needed for 1000 cnts @ 10<sup>7</sup> fusions / sec</b>
1	0.5	270	170	1.09	0.86	117
2	0.5	200	100	1.50	1.56	64
3	0.7	270	170	1.52	1.68	60
4	0.7	200	100	2.10	3.06	33
5	1.0	270	170	2.18	3.43	29
6	1.0	200	100	3.00	6.25	16
7	2.0	270	170	4.35	13.7	7.3

Positions inside the viewing cone where  $b$  was greater than  $a$  could only see a portion of the detector because of shadowing from aperture 1. A correction factor to  $P_o$  was derived by dividing the area of the detector visible at a point  $(d_1, b)$  by the total detector area. Eqn 4-19 is the probability of a proton striking the detector from an isotropic point source located at  $(d_1, b)$ . Figure 4-35 graphs  $P(d_1, b)$  for the different cases in Table 4-7. This graph shows the effects of the edges of the viewing cone on the detection system. In practice, as the detector is moved across a fixed point source it will not detect a sharp edge, but rather a gradual increase in counts corresponding with Eqn 4-19.

$$0 \leq b \leq a \quad P(d_1, b) = P_o(d_1)$$

$$a \leq b \leq a \frac{d_1}{d_2} \quad P(d_1, b) = \frac{P_o(d_1)}{2} \left[ 1 + \left( 1 + \frac{d_2(1-\frac{b}{a})}{d_1-d_2} \right)^2 \right] \quad \text{Eqn 4-19}$$

$$a \frac{d_1}{d_2} \leq b \leq a \left( 2 \frac{d_1}{d_2} - 1 \right) \quad P(d_1, b) = \frac{P_o(d_1)}{2} \left[ 1 - \left( 1 + \frac{d_2(1-\frac{b}{a})}{d_1-d_2} \right)^2 \right]$$

$$b > a \left( 2 \frac{d_1}{d_2} - 1 \right) \quad P(d_1, b) = 0$$

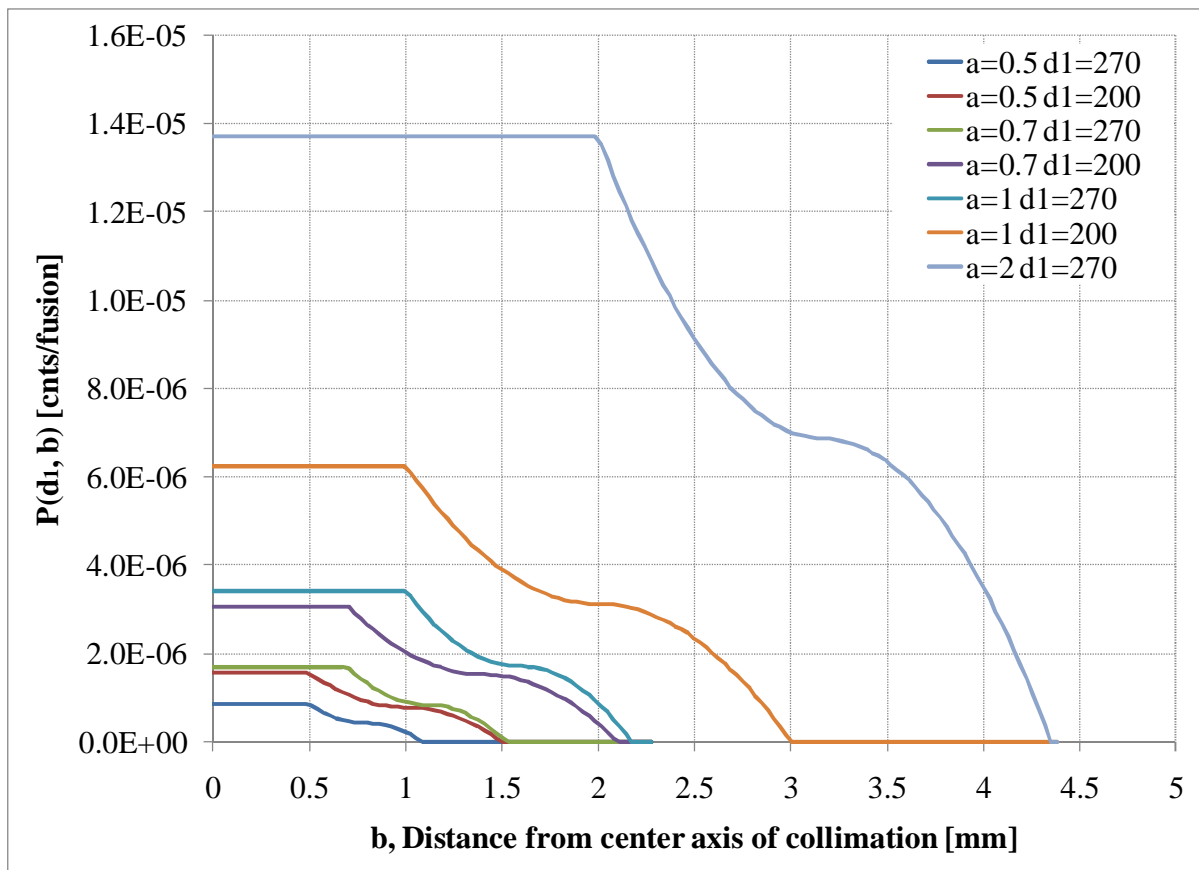


Figure 4-35: Probability of a proton striking the detector from a distance  $b$  from the axis of collimation and on a plane perpendicular to that axis and that intersected the origin of the SIGFE device. All of the cases in Table 4-7 are plotted. Note that the distance between aperture 1 and the origin remained fixed while aperture 2 was moved in the various cases.

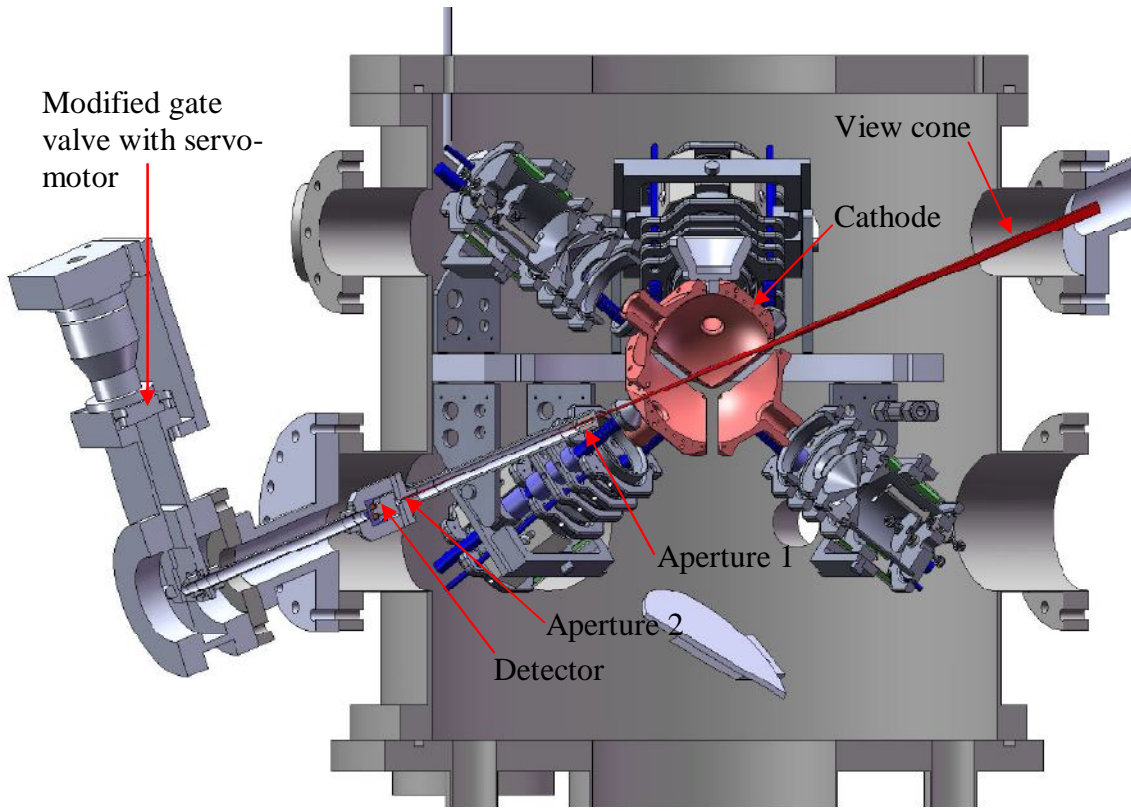


Figure 4-36: Cut-away view of the movable collimated detector system installed on the SIGFE. The inside diameter of the cathode was 110 mm, and the gaps between the cathode lenses were 8 mm.

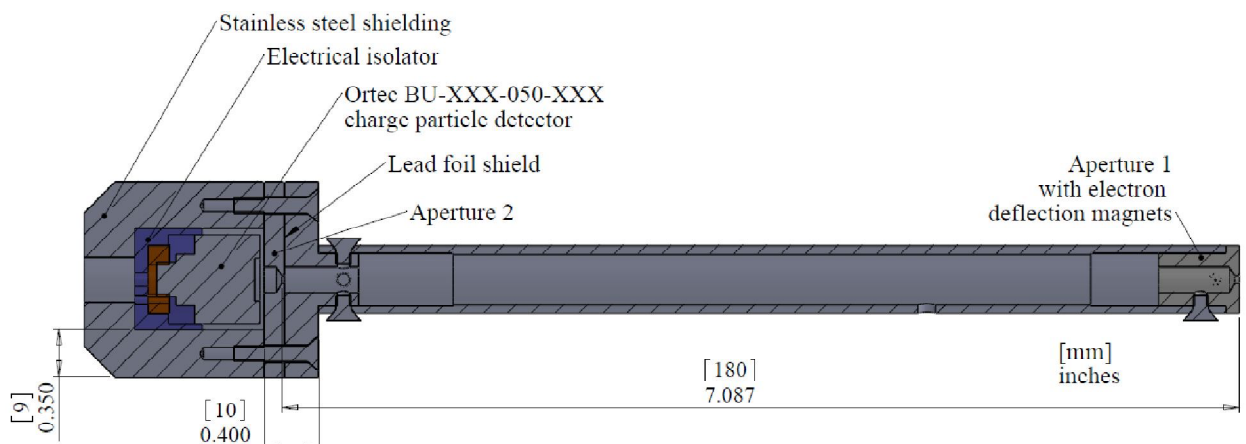


Figure 4-37: Cross-section view of the collimated detector head assembly.

The physical detector system was based on an Ortec Ultra Series charged particle detector mounted to the carriage of a standard vacuum gate valve. For the D-D fusion experiments, a BU-012-050-100 detector was chosen. The detector is surrounded by a

minimum of 9 mm of stainless steel to attenuate the x-rays generated in the device, and was nested in an electrically insulating sleeve to isolate it from the shielding and protect it from high voltage arcing to the collimation assembly. Aperture 1 and its mounting tube are made of aluminum to reduce the amount of bremsstrahlung radiation generated by energetic secondary electrons. A pair of permanent magnets was mounted behind aperture 1 to deflect secondary electrons that would have otherwise struck the detector. The lengths of the apertures were kept as short as possible (0.7 mm) to minimize the effects of slight misalignments between them. Aperture 2 consisted of two pieces to hold the Pb foil shield. The deflection magnet and foil shield prevented or reduced the amount of visible light, x-rays, negative ions and neutral particles that reached the detector while minimizing the attenuation of the fusion protons.

The thickness of the detector and the thickness of the Pb foil shield were chosen as a balance between attenuating the x-rays while not overly degrading the proton energy. A 100  $\mu\text{m}$  thick Si detector was chosen over a 500 or 700  $\mu\text{m}$  detector. The thinner detector was adequate to fully stop 3.0 MeV protons but had less material to interact with the x-rays. A 3.0 MeV proton is fully stopped in 50  $\mu\text{m}$  of Pb, whereas after 10  $\mu\text{m}$  of Pb the proton has an average energy of 2.57 MeV. The detector was built with 10  $\mu\text{m}$  of Pb foil; however the x-ray spectrum still overwhelmed the proton spectrum.

The positioning of the detector and collimation assembly was achieved by modifying a standard manually operated CF 4.5 inch vacuum gate valve. The movable carriage inside the valve was modified to hold the detector assembly. A National Aperture MM-4M-R Rotary MicroMini® stage was mounted to the external hand crank of the valve. Over the 24 mm of travel, the repeatability of the detector's position was measured to be less than 0.3 mm. This level of repeatability was achieved in several ways. 1) At the beginning of

each run, the servo motor was automatically homed by moving the detector assembly on to, then just off of, a limit switch built into the detectors movable mount. 2) Counts were only taken in one direction, so the slack in the linkages was always in the same direction. 3) The actual position of the detector was mapped every 1 mm along its length of travel. This map created a more accurate correlation between the servo's rotary position and the linear position of the detector.

The detector positioning and counting of radiation events was controlled, monitored, and logged using the custom LabVIEW® computer program described in section 4.2.6. The program communicated with the rotary table to move to and verify a new position. When in position, the program begins counting for a designated amount of time. When the counting is complete, the detector is moved to the next location, and the number of counts was recorded in a text file with all of the other operating parameters of the SIGFE. These other parameters include the counts from the two neutron detectors and the D-<sup>3</sup>He proton detector also installed on the system. This integrated strategy allows for the collimated data to be correlated to the other operating parameters from the exact same time period.

The system was capable of monitoring multiple single channel analyzers (SCA) connected to the collimated detector at the same time; however this had not been utilized at the time of this writing. The design was for the energy spectrum from the detector to be analyzed by three SCAs. One SCA tuned for the energy of D-D fusion protons. The other two channels were tuned for different energy ranges in the x-ray portion of the spectrum. Monitoring the points in the x-ray spectrum would have allowed an estimate x-rays of the produced. This would have helped to separate the x-ray spectrum from the proton spectrum without collecting data on a full MCA. The complete detector electronics setup for this system is shown in Figure 4-38.

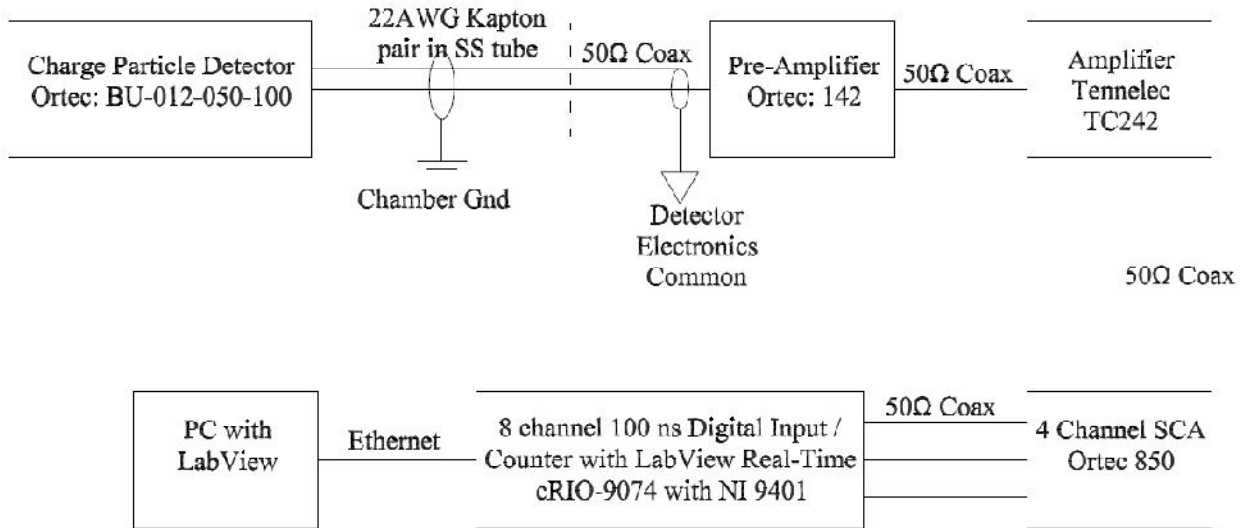


Figure 4-38: Schematic of the collimated proton detector electronics

The collimated proton detector system was designed and built to measure spatial variations in the proton rate in the center region of the cathode. The equipment was capable of automatically positioning the collimated assembly within 0.3 mm. Bench tests with an  $^{241}\text{Am}$  alpha source were successful. Unfortunately when installed on the SIGFE, the actual proton rate in the cathode region was lower than expected and the x-ray noise was higher. This resulted in a lower proton signal to noise ratio and made the automatically collected data unreliable. The future work section will discuss an idea for reducing the x-ray noise with a compact, permanent magnet variation of the FIDO diagnostic.

#### 4.3.4. Proton detector for $D-^3\text{He}$ fusion reactions

Detection of the proton from the  $^3\text{He}(\text{d}, \text{p})^4\text{He}$  fusion reaction required a different detector setup than the collimated and FIDO systems described in the previous two sections. The 14.7 MeV D- $^3\text{He}$  protons were much harder to stop in the Si detector than the 3.02 MeV D-D protons. The energy deposited by a D- $^3\text{He}$  proton in the 100  $\mu\text{m}$  thick detector used in the collimated setup would be less than 1 MeV. Therefore, the detector used for the D- $^3\text{He}$  experiments was 700  $\mu\text{m}$  thick, in which without addition shielding would collect less than

5 MeV of the proton energy. The FIDO diagnostic could not be used, because the 1.5 T bending magnet was not strong enough to bend the D-<sup>3</sup>He proton through the 20 degree arc of the FIDO arm.

The difficulty of stopping the D-<sup>3</sup>He proton was used as an advantage since more x-ray shielding could be placed in front of the detector. Figure 4-39 shows the location of the 360  $\mu\text{m}$  of Pd and 8  $\mu\text{m}$  of Al foil that was placed between the detector and the center of the device. With this amount of shielding, the D-<sup>3</sup>He proton was completely stopped in the detector. The deposited energy was high enough so the proton spectrum was above the remaining x-ray energy. With this shielding and the 700  $\mu\text{m}$  thick detector, an average of 7.86 MeV was predicted to be deposited in the detector.

The electronics used for this system were arranged similarly to those shown in Figure 4-31 with the <sup>3</sup>He tube replaced by a 1200  $\text{mm}^2$  x 700  $\mu\text{m}$  Si based proton detector. Table 4-8 lists the specific nuclear instrumentation modules used and their settings.

Table 4-8: Details of D-<sup>3</sup>He proton detector equipment and settings. \*Values of the coarse adjust, multi-turn potentiometer.

	<b>Model # / settings</b>
<b>Si detector</b>	Canberra PD 1200-33-700 AB
<b>Preamp model</b>	Ortec 142
<b>Amplifier</b>	Ortec 570
Amp setting	20, 11-50*
<b>SCA</b>	Ortec 850
LLD setting	3.66
ULD setting	10.0
<b>Bias supply model</b>	TC 953
Bias setting	120 V
<b>MCA</b>	Canberra ASA-100

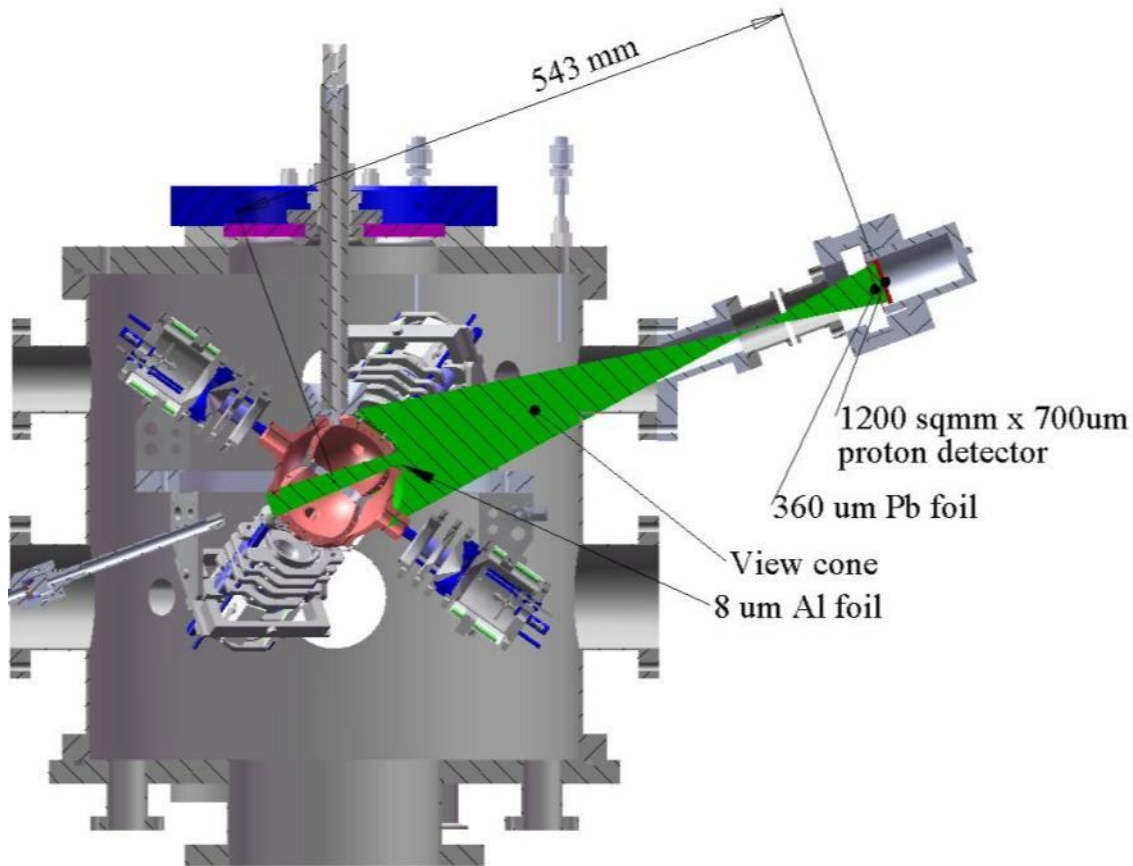


Figure 4-39: Diagram of wide-view D- $^3$ He proton detector setup. The 1200 mm $^2$  x 700  $\mu\text{m}$  thick Si based detector had 360  $\mu\text{m}$  of Pd and 8  $\mu\text{m}$  of Al between it and the center of the device, which was 543 mm away.

The relationship between the total number of  ${}^3\text{He}(\text{d}, \text{p}){}^4\text{He}$  fusion reactions and the number of protons counted was estimated using Eqn 4-15 and assuming a point source of protons originating at the center of the SIGFE device. The distance from the detector to the center was 543 mm and the radius of the detectors was 19.5 mm. This resulted in a calibration factor of 3105 D- $^3$ He reactions per count. The calibration factor would change by approximately 20% for protons originating from the closest or furthest points inside the cathode. Based on the size of the view cone and the geometry of the SIGFE device shown in Figure 4-39, the detector was expected to detect fusion reactions that mainly occurred near

the center of the cathode. It was unlikely that fusion resulting from ions embedded in the surfaces of the lenses could have been detected.

The spectrum of energy deposited in the detector from D-<sup>3</sup>He protons showed the distinct twin peak structure associated with Doppler shifting as energetic ions fused with stationary targets. Equation 4-20 is a rewriting of the equations in section 4.3.2 for the lab frame energy of fusion protons,  $E_t$ , for arbitrary ion and target masses;  $E_a$  and  $m_a$  are the energy and mass of the ion respectively,  $m_b$  is the mass of the stationary target,  $m_p$  is the mass of a proton, and  $E_f$  is the energy released in the fusion reaction.

$$E_t = E_f + \frac{m_b m_p E_a}{(m_a+m_b)^2} \pm 2 \sqrt{\frac{m_p m_b E_f E_a}{(m_a+m_b)^2}} \cos \theta \quad \text{Eqn 4-20}$$

Table 4-9 shows the result of these calculations for <sup>3</sup>He+ and D<sub>2</sub><sup>+</sup> ions on <sup>3</sup>He and D targets at 100, 130 and 150 keV ion energies. Using SRIM [27], the amount of energy deposited in the detector after the Al and Pb shielding was predicted for each case. Figure 4-40 shows the energy spectrum predicted for all four ion-target combinations for 130 keV ions. The energy spread for each case was more than 1 MeV. This spread was greater than the difference between the cases; therefore identification of the dominant ion-target combination could not be determined. However, the spread of the up-shifted versus down-shifted Doppler peaks was still resolvable and was used to estimate the order of magnitude of the energy of the reacting ions.

Table 4-9: Energy of a 14.7 MeV D- $^3\text{He}$  fusion proton in the lab frame after the Doppler shift resulting from 100, 130, and 150 keV ions reacting with stationary targets. The proton energy after 8  $\mu\text{m}$  of Al and 360  $\mu\text{m}$  of Pb was determined by SRIM [27]. The 700  $\mu\text{m}$  thick Si detector was predicted to completely stop the proton after the foils. All energy values are in MeV and masses are in AMU.

$E_a$	Ion species / target	$m_a$	$m_b$	Initial fusion proton energy			After 8 $\mu\text{m}$ Al and 360 $\mu\text{m}$ Pb foil		
				$E_t^+$	$E_t^-$	Difference	$E_t^+$	$E_t^-$	Difference
0.100	$\text{D}_1^+ / ^3\text{He}$	2	3	15.20	14.23	0.97			
	$\text{D}_2^+ / ^3\text{He}$	4	3	15.05	14.36	0.69	8.47	7.40	1.07
	$\text{D}_3^+ / ^3\text{He}$	6	3	14.97	14.43	0.54			
	$^3\text{He}^+ / \text{D}$	3	2	15.10	14.31	0.79	8.46	7.29	1.17
0.130	$\text{D}_1^+ / ^3\text{He}$	2	3	15.27	14.16	1.11	8.79	7.06	1.73
	$\text{D}_2^+ / ^3\text{He}$	4	3	15.10	14.31	0.79	8.46	7.29	1.17
	$\text{D}_3^+ / ^3\text{He}$	6	3	15.01	14.40	0.61	8.36	7.53	0.84
	$^3\text{He}^+ / \text{D}$	3	2	15.16	14.26	0.90	8.52	7.17	1.35
0.150	$\text{D}_1^+ / ^3\text{He}$	2	3	15.31	14.12	1.19			
	$\text{D}_2^+ / ^3\text{He}$	4	3	15.13	14.28	0.85	8.55	7.16	1.39
	$\text{D}_3^+ / ^3\text{He}$	6	3	15.04	14.38	0.66	8.66	7.13	1.52
	$^3\text{He}^+ / \text{D}$	3	2	15.20	14.23	0.97			
No Shift				14.70			7.86		

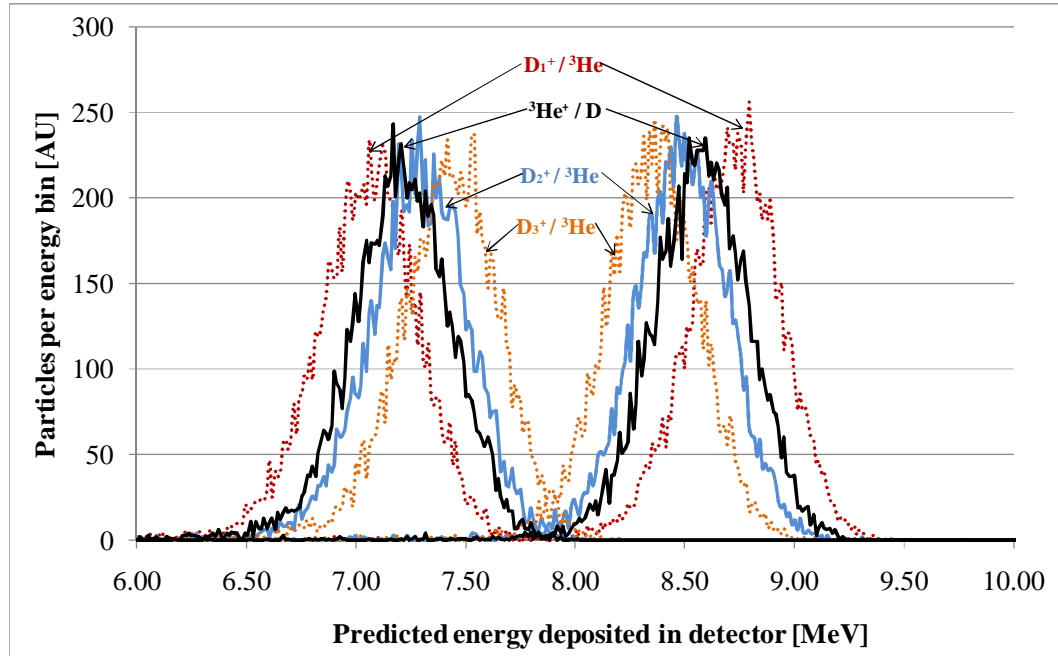


Figure 4-40: Predicted energy spectrum deposited in a 700  $\mu\text{m}$  thick Si detector after 8  $\mu\text{m}$  of Al and 360  $\mu\text{m}$  of Pb for 14.7 MeV  $^3\text{He}(d, p)^4\text{He}$  fusion protons resulting from 130 keV ions fusing with stationary targets. All four combinations of  $^3\text{He}^+$ ,  $\text{D}_1^+$ ,  $\text{D}_2^+$ , and  $\text{D}_3^+$  ions on  $^3\text{He}$  and D targets are plotted

Several of the properties of the D-<sup>3</sup>He fusion protons were effectively measured by this simple Si based proton detector setup. The well defined angle between the ion trajectories and the proton detector allowed the Doppler shift (caused by the reacting particles) to be detected. With the assumption that this detector could only detect fusion reactions from the cathode region, the total <sup>3</sup>He(d, p)<sup>4</sup>He reaction rate in that region was estimated.

#### *4.3.5. Optical cameras*

The operation of the SIGFE device was constantly monitored by two visible light cameras. The first camera was a Point Greys Research Grasshopper camera with macro zoom lenses. This camera had extensive software control of its shutter speed, frame rate, and other features. The ability to set long shutter speeds made it valuable for observing the low levels of light emitted as the ion beams passed through the low pressure background gas. Figure 4-41B shows an example frame from this camera at a frame rate of approximately 3 frames per second.

The purpose of the first camera was to zoom in on the converging ion beams evaluate the focus and the alignment of the ion beams. The three ports that had a direct line-of-sight into the cathode were occupied by either proton detectors or the main vacuum pump. Therefore, two mirrors were used to reflect the light so that a direct view of the cathode center was seen. Figure 4-41A shows this setup. As described in section 4.2.4, a quartz window was placed on the bottom of the cathode to prevent secondary electrons from escaping while providing a viewing port for visible light. The edges of the quartz glowed blue and blue streaks were visible on the quartz; this can be seen in Figure 4-41B.

The second camera was an Axis communications model 207 Ethernet based security camera. The view angle from this camera's position is noted in Figure 4-41A. It was used to

give a wide angle view of the various components during operation. The camera was designed for low light conditions and was sensitive in the infrared range; this proved useful in detecting heating of the ion gun lenses. Experience in operating the equipment showed that if the lenses heated to the point of showing color on the camera, the equipment was approaching a temperature that could cause damage.

The visible light cameras mounted on the SIGFE device were useful for monitoring the health of the equipment and as a diagnostic. The zoomed in Grasshopper camera could detect changes in the ion beams as the focus lens voltages were adjusted. In extreme cases, the misalignment of the ion beams was visible. Visible monitoring of the equipment was important to the safety of the equipment. The experiment was never run without at least one operating camera.

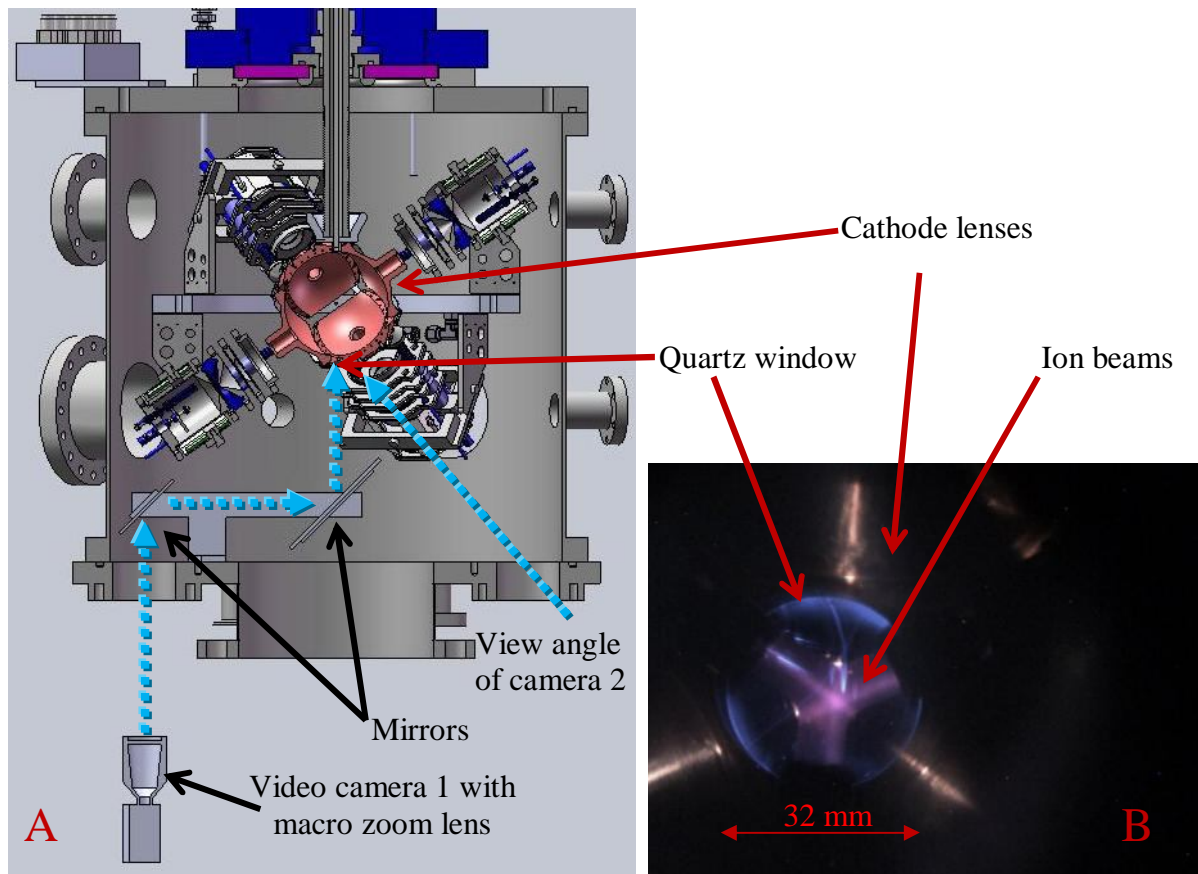


Figure 4-41: A) Diagram of video camera setup showing the mirrors used to direct the camera view through quartz window at the bottom of the cathode electrode. B) Photo of typical view from camera 1.

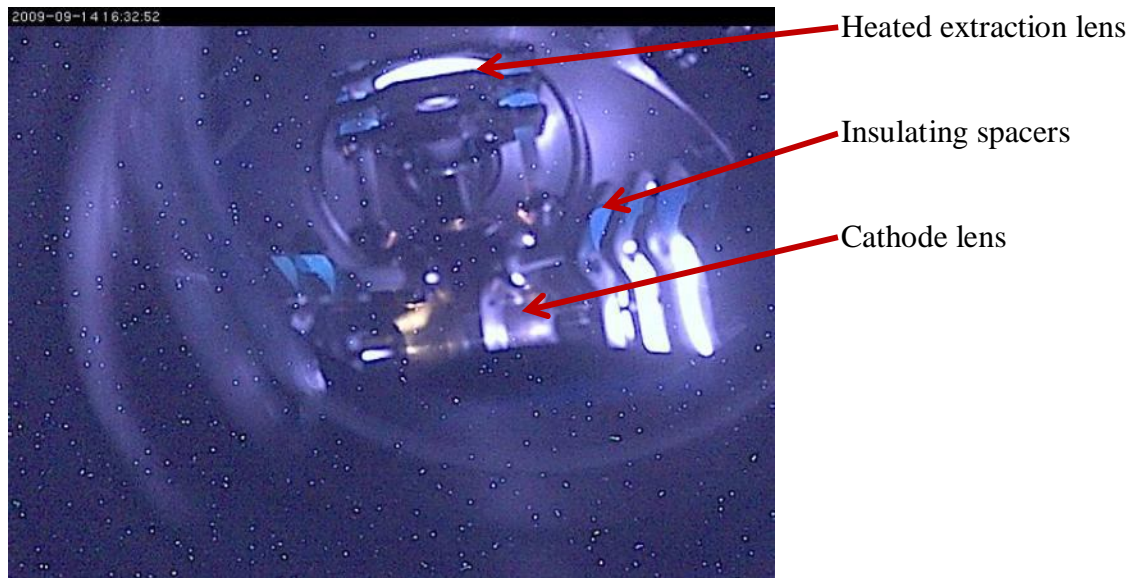


Figure 4-42: Still photo taken from camera 2. Light emitted from the heated extraction lenses was visible along with DC plasma discharges along the insulating spacers.

#### 4.4. References for Chapter 4

1. Hirsch, R. L. (1967). Inertial-electrostatic confinement of ionized fusion gases. *Journal of Applied Physics*, 38(11), 4522-4534.
2. *SolidWorks Student Version 2009-2010*, (2009). Dassault Systems SolidWorks Corp, Concord, MA, [www.solidworks.com](http://www.solidworks.com)
3. *SIMION Version 8.0*, (2009). Scientific Instrument Services, Inc, Ringoes, NJ, [www.simion.com](http://www.simion.com)
4. Accuratus Corporation, (2002). Macor properties. Retrieved February 2, 2010, from [www.accuratus.com/macorprps1.html](http://www.accuratus.com/macorprps1.html)
5. National Scientific Company, (1995). Fused quartz properties and usage guide: GE type 214, 214LD, and 124. Retrieved February 2, 2010, from [www.quartz.com/gedata.html](http://www.quartz.com/gedata.html)
6. Saint-Gobain Ceramics, (2003). Combat® solid boron nitride: technical overview datasheet. Retrieved February 2, 2010, from [www.bn.saint-gobain.com](http://www.bn.saint-gobain.com)
7. Peifer, G. R. (2006). Performance of a low-pressure, helicon driven IEC  $^3\text{He}$  fusion device. (PhD dissertation, University of Wisconsin – Madison)
8. The REMBAR Company, Inc, Physical properties of Molybdenum. Retrieved January 1, 2010, from [www.rembar.com/molybdenum.htm](http://www.rembar.com/molybdenum.htm)
9. Zhang, H., (1999) *Ion Sources*. Science Press Beijing. ISBN: 7-03-007351-7/O-1092
10. Hirsch, R.L., & Meeks, G.A., (1967) “Highly Efficient, Inexpensive, Medium Current Ion Sources.” *The Review of Scientific Instruments*. Volume 38, number 5, page 621 to 624
11. Hirsch, R.L, (2009) Personal email correspondence
12. *Design-Expert® Version 8*, (2009). Stat-Ease Inc, Minneapolis, MN, [www.statease.com](http://www.statease.com)
13. Miller, H.C. (1993). Flashover of insulators in vacuum, review of the phenomena and techniques to improve holdoff voltage, *IEEE Transactions on Electrical Insulation*, 28(4)
14. Anderson, R.A., (1974). Mechanism of fast surface flashover in vacuum, *Applied Physics Letters*, 24(2)
15. *Maxwell® 2D SV*, (2002). Ansoft, Pittsburg, PA, [www.ansoft.com](http://www.ansoft.com)
16. Cipiti, B. B. (2004). The fusion of advanced fuels to produce medical isotopes using inertial electrostatic confinement. (PhD dissertation, University of Wisconsin – Madison)
17. Radel, R., & Kulcinski, G. L., (2007). Effects implantation of  $\text{He}^+$  in candidate fusion first wall materials, *Journal of Nuclear Materials*, 367-370(1), pg 434-439
18. Zenobia, S.J., Radel, R.F., Cipiti B.B., & Kulcinski, G.L., (2009). High temperature surface effects of  $\text{He}^+$  implantation in ICF fusion first wall materials. *Journal of Nuclear Materials*, 389(2), pg 213-220

19. Zenobia, S. J. (2009). Personal correspondence
20. Naidu, M.S., & Kamaraju, V., (1996) *High Voltage Engineering* (2<sup>nd</sup> ed.). McGraw-Hill.  
ISBN: 0-07-462286
21. Phoenix Nuclear labs, Product specifications, Retrieved January 13, 2010, from  
[www.phoenixnuclearlabs.com/products.php](http://www.phoenixnuclearlabs.com/products.php)
22. Glassman High Voltage Inc, MD Series 75 watt, MK15N5, Retrieved January 13, 2010,  
from [www.glassmanhv.com/pds/mk\\_series.pdf](http://www.glassmanhv.com/pds/mk_series.pdf)
23. Gamma High Voltage Research, (2009) personal correspondence,  
[www.gammahighvoltage.com](http://www.gammahighvoltage.com)
24. Bonomo, R., (2009) personal correspondence, UW-Madison
25. University of Wisconsin Nuclear Reactor Lab, (2009) personal correspondence for PuBe  
source #516, as of 8-11-2009
26. Boris, D.R. (2009). Novel diagnostic approaches to characterizing the performance of the  
Wisconsin Inertial Electrostatic Confinement plasma. (PhD dissertation, University of  
Wisconsin – Madison)
27. Ziegler, J. F., (2010). *SRIM Version 2010*, [www.srim.org](http://www.srim.org)

## Chapter 5. Extractable ion current from the ion source and extraction system

A Langmuir probe was installed in the plasma source of each ion gun module to measure the density and electron temperature of the plasma. The measurements from this probe were used to compare the theoretically predicted extractable ion current to the experimentally measured ion current. The experimental data also shows an optimal plasma density at which a maximum ion current was focused though the small aperture in the extraction electrode. This was consistent with the hypothesis in chapter 3 that described how the shape of the emissive surface of the plasma could act as a lens to focus the ions.

### 5.1. Results of plasma parameter study of the ion source

A study of the plasma parameters versus the input parameters of the ion source was conducted using the Langmuir probe shown in Figure 4-3 and Figure 4-5. The probe was a thin circular metal disc with a surface area of  $25 \text{ mm}^2$  attached to a wire. The position and orientation of the disc in the tube was selected to minimize the effects of the cusp magnetic field on its measurements; it was placed parallel to the magnetic field lines and near the center where the field approached zero. A LabVIEW® program was written to decipher the voltage-current traces of the probe into plasma density, electron temperature, and plasma potential in near real-time.

The Design of Experiment software package described in section 6.1 was used to determine the relationship between the multiple input parameters of the ion source and the plasma parameters calculated from the measured Langmuir probe trace. The input parameters studied were 1) the filament voltage, 2) the filament bias voltage, and 3) gas flow. The plasma parameters recorded were the 1) plasma density, 2) electron temperature, 3) plasma potential, and 4) floating potential. The plasma density was calculated independently from both the electron saturation current and the ion saturation current of the Langmuir probe

trace. The ion saturation current proved to be a more repeatable method of calculating the density; therefore it was used for the results below.

The filament voltage drop was observed to be the most significant input parameter of all of the plasma parameters. The filament voltage drop was defined as the voltage difference between the two ends of the filament. The voltage drop across the filament changes the temperature of the filament and therefore controls the electron current available. The plasma density (calculated from ion saturation current) versus filament voltage drop and gas flow is shown in the contour plot in Figure 5-1. The gas flow was shown to have a linear relationship with the neutral gas pressure in the source region as described in section 4.2.7. The highest plasma density observed was  $5.0 \times 10^{10} \text{ cm}^{-3}$ , which was at a filament drop of 110 V and a gas flow rate of 0.7 sccm (7.5 uncalibrated sccm).

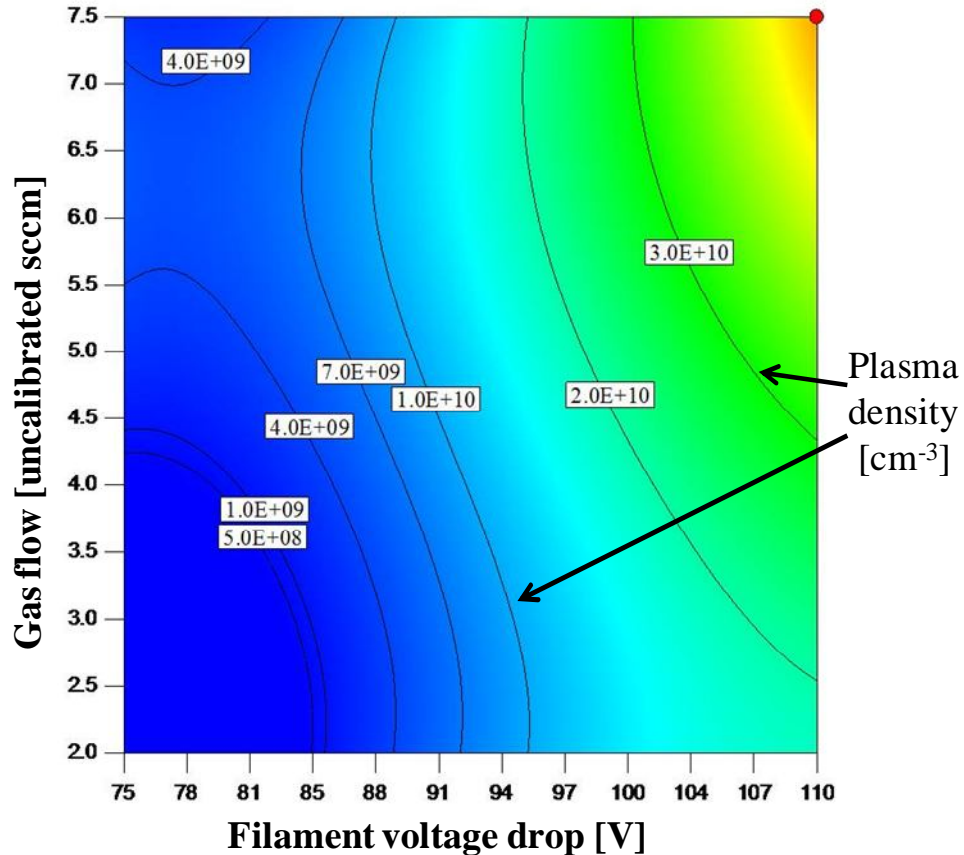


Figure 5-1: Contour plot of the plasma density versus filament voltage drop and gas flow. The red dot on the plot represents an experimental data point. (10 uncalibrated sccm = 0.9 sccm)

Figure 5-2 shows the contour plot of the plasma density versus filament drop and filament bias voltage. The bias voltage is the potential between the filament and the grounded tube surrounding the plasma source. In typical operation, the plasma source is operated at plasma densities between  $2 \times 10^9$  and  $1 \times 10^{10}$  cm<sup>-3</sup> and a filament bias voltage of -60 V. In this region, the plasma density is relatively insensitive to the bias voltage.

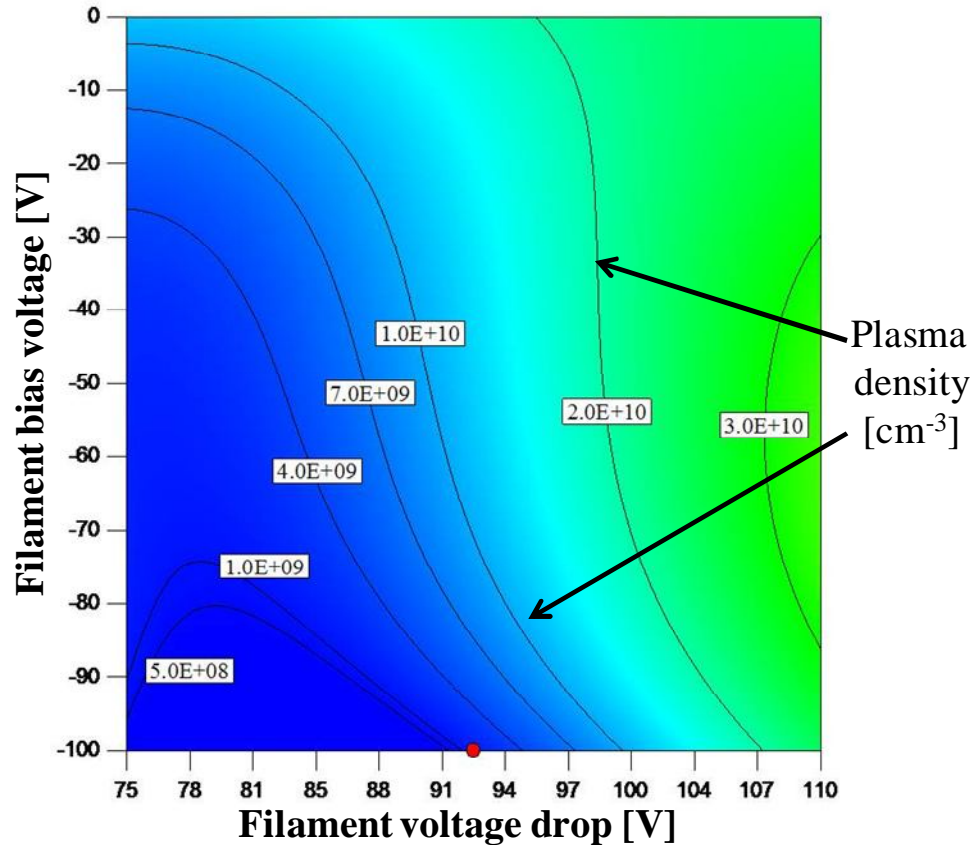


Figure 5-2: Contour plot of the plasma density versus filament voltage drop and filament bias voltage. The red dot on the plot represents an experimental data point.

The electron temperature and the plasma potential are both relatively insensitive to the filament bias and gas flow. The plasma electron temperature is shown in Figure 5-3 versus filament drop and filament bias voltage. The plasma potential is shown in Figure 5-4 versus filament drop and gas flow.

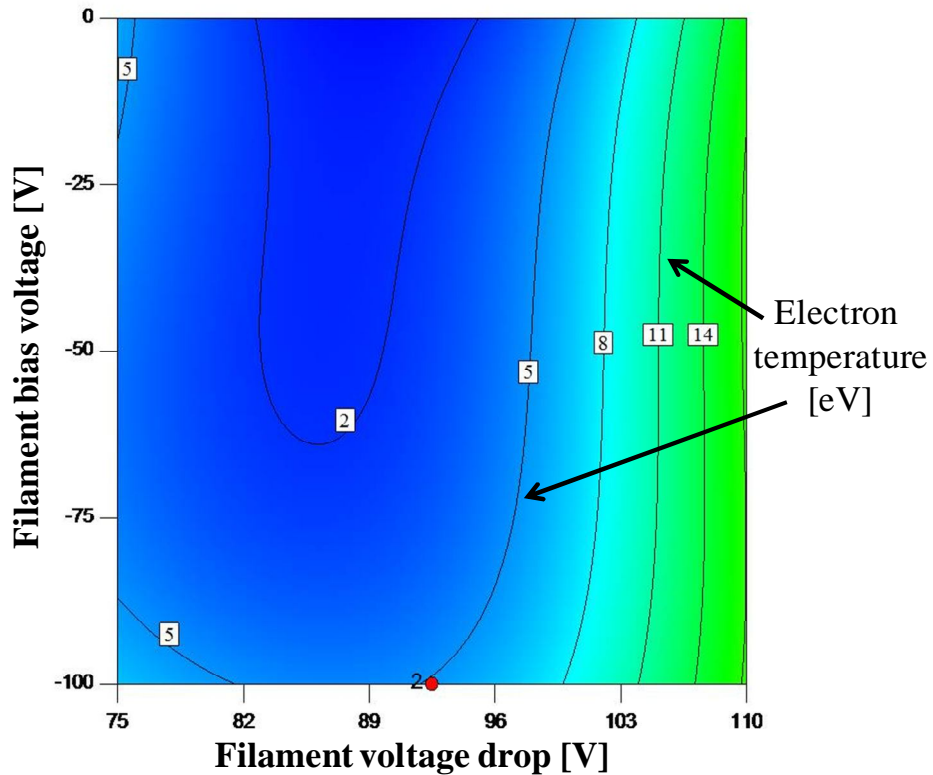


Figure 5-3: Contour plot of the plasma electron temperature versus filament voltage drop and filament bias voltage.

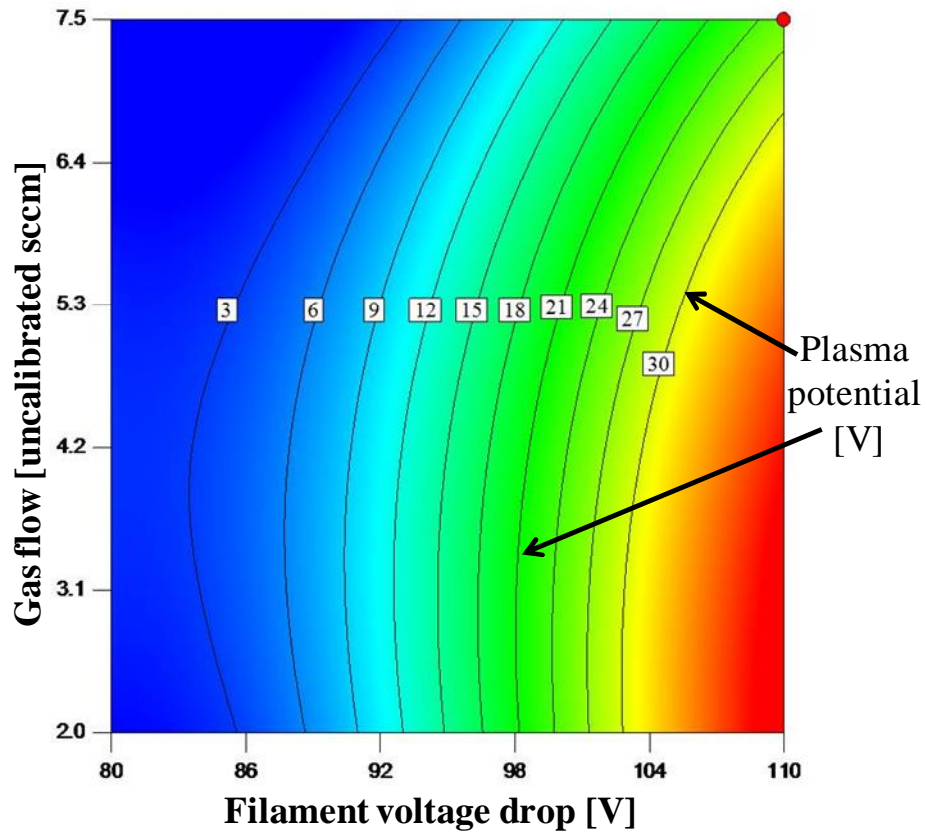


Figure 5-4: Contour plot of the plasma potential versus filament voltage drop and gas flow.  
(10 uncalibrated sccm = 0.9 sccm)

## 5.2. Extractable ion current

The amount of extracted ion current was measured by replacing the focus lens of one of the ion gun modules with a flat polished stainless steel plate as shown in Figure 5-5 and described in section 4.1.5. To measure only the ion current, the voltage on the collection electrode was maintained more positive than the extraction electrode. This prevented the majority of the secondary electrons generated at the collection electrode from leaving this electrode and causing a non-ion current to be measured.

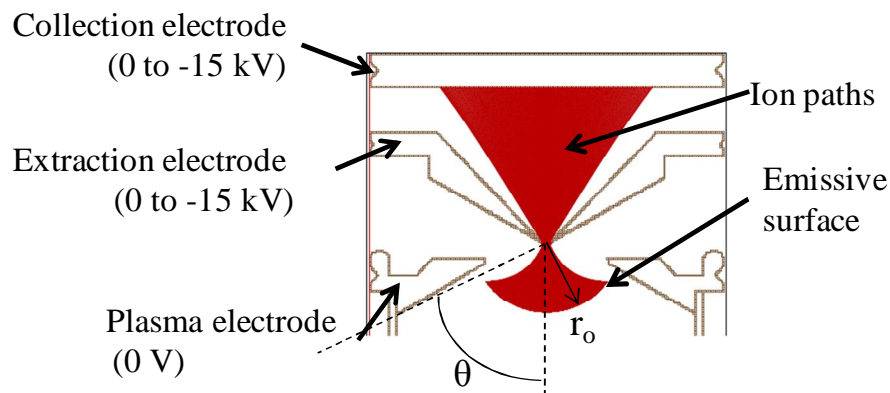


Figure 5-5: Schematic of the ion extraction test setup with simulated ion trajectories

At a fixed voltage on the extraction and collection electrodes, the filament voltage drop was increased to increase the plasma density and electron temperature as shown in section 5.1. Figure 5-6 shows the current on both the collector plate and the extraction lens for an extraction voltage of -7 kV. The extraction lens current included the secondary electron current. Figure 5-7 shows the extracted ion current (current to the collection plate) at three extraction lens voltages.

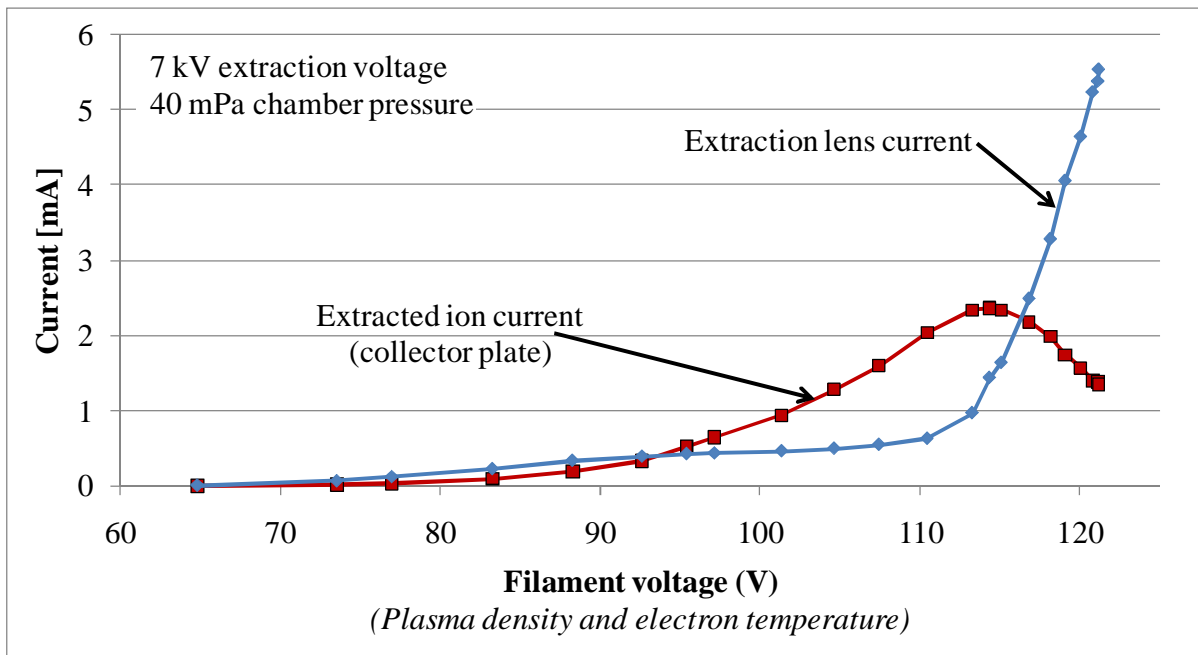


Figure 5-6: Extracted ion current and the total current on the extraction lens plotted versus the voltage across the filament. Relationship between the filament voltage and the plasma density was described in section 4.1.

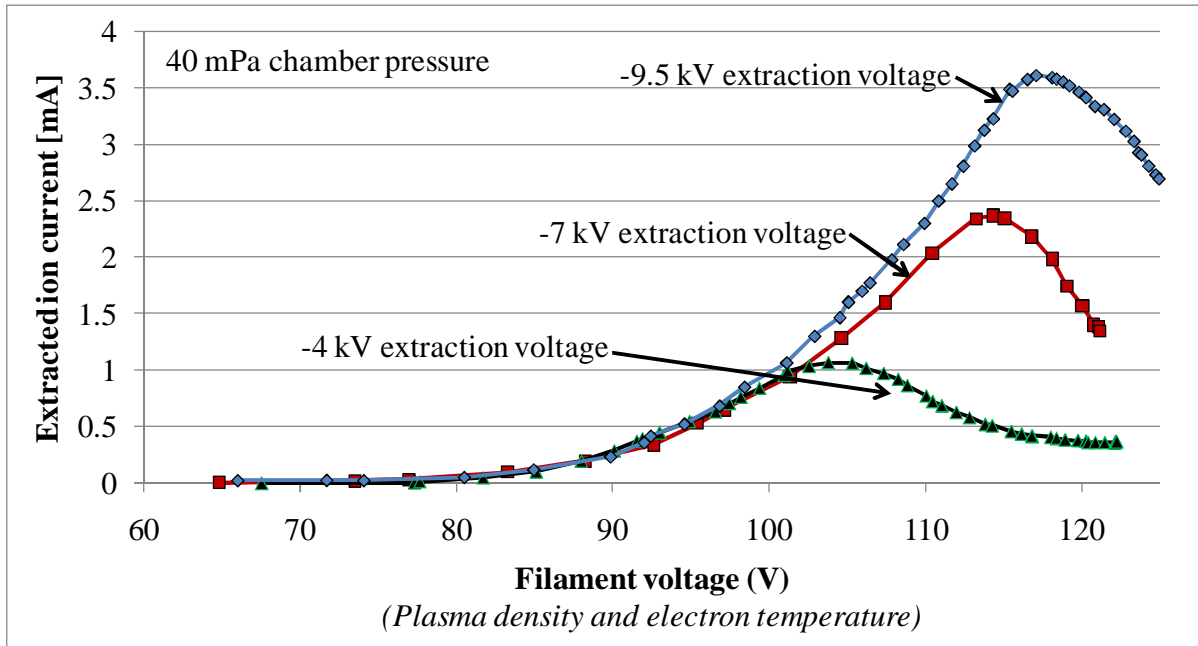


Figure 5-7: Extracted ion current for three extraction lens voltages versus the filament voltage.

At the several extraction voltages between -4 kV and -9.5 kV the filament voltage drop and filament bias voltage were adjusted to the maximum extracted ion current. At these

settings the plasma density, electron temperature, and plasma voltage were measured with the Langmuir probe. Figure 5-8 plots both the maximum measured ion current and the corresponding plasma density.

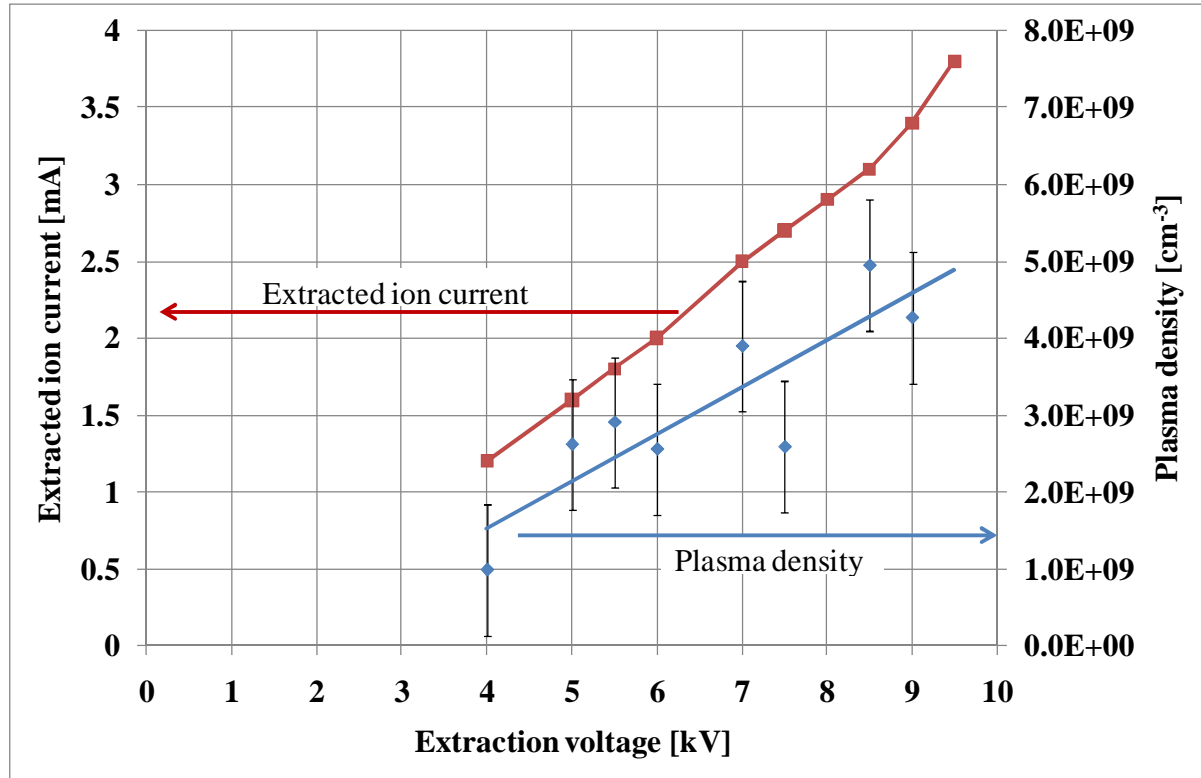


Figure 5-8: Maximum extracted ion current and corresponding plasma density at various extraction electrode voltages.

### 5.3. Discussion of plasma parameters and extractable ion current

The accuracy of the equations used to determine the extractable ion current for the SIGFE sources was evaluated using the experimentally measured plasma density, electron temperature, extraction voltage and extracted ion current presented earlier in this chapter. The plasma density measurements shown in Figure 5-8 exhibited a large amount of variation. The plasma density was calculated independently from both the electron saturation current and the ion saturation current of the Langmuir trace. The two calculations differed from one another by as much as a factor of 5. The ion saturation current calculation was more repeatable and therefore was used in this analysis. The variation in the density measurements

may have been caused by the following complications. 1) The mass of the ions was assumed to be 4 AMU; however the exact mixture of  $D_1^+$ ,  $D_2^+$ , and  $D_3^+$  was unknown. The effective ion mass could have been between 2 and 6 AMU. 2) Due to the compact size of the ion source, the Langmuir probe was located within 2 cm of the filament; the effects of primary electrons from the filaments could be seen on the probe traces. 3) Further complicating the probe measurements was the effect of the magnetic field on the collection of electrons to the probe surface. Even though the probe was located near a minimum in the magnetic field, the magnetic field was still a likely cause of the non-repeatability of the density measurements from the electron saturation current.

Chapter 3 described the calculation of the theoretical ion current that could be extracted from a plasma in a system with geometry similar to the shape of the electrodes in the SIGFE ion source. Eqn 3-13 is reproduced from chapter 3 for the reader's convenience.

$$I \text{ [amps]} = 1.05 \times 10^{-9} \frac{(1-\cos\theta)}{\sqrt{M_{iAMU}}} ( n_e \sqrt{T_e} )^{0.452} r_e^{0.902} V_e^{0.822} \quad \text{Eqn 3-13}$$

For this analysis the ion species was assumed to be  $D_2^+$ , so  $M_{iAMU} = 4$ . The values  $\theta = 55^\circ$  and  $r_e = 0.09$  cm were estimated from the geometry of the electrodes. The current calculated by Eqn 3-13 is the total ion current from the plasma, which included both the extracted ion current and the ion current to the extraction electrode. The measured extraction electrode current was corrected for the secondary electron coefficient. The secondary electron coefficient was determined to be 0.9 from Figure 4-12.

Figure 5-9 graphs both the measured ion current from the plasma and the current calculated by Eqn 3-13 for the plasma conditions measured at each experimental point. The measured and calculated values consistently differ by approximately a factor of two. Considering the error in measuring the plasma density previously described and the assumptions made in the derivation of Eqn 3-13, this was a relatively good agreement

between experimental and theoretical results. There are several likely sources of error in the theoretical calculation. The first is the lack of knowledge of the mix of D ion species in the plasma; a mass of 4 AMU was used, but as stated previously a mass of 2 to 6 AMU was possible. The other most likely source is the coefficient of the Bohm current density in Eqn 3-1. The value of 0.4 was arbitrarily chosen because it was the most common value used in the literature, but it could be between 0.3 and 0.9. It is likely that other sources of error existed, however these two sources of error could account for the factor of two difference between the experimental and theoretical results.

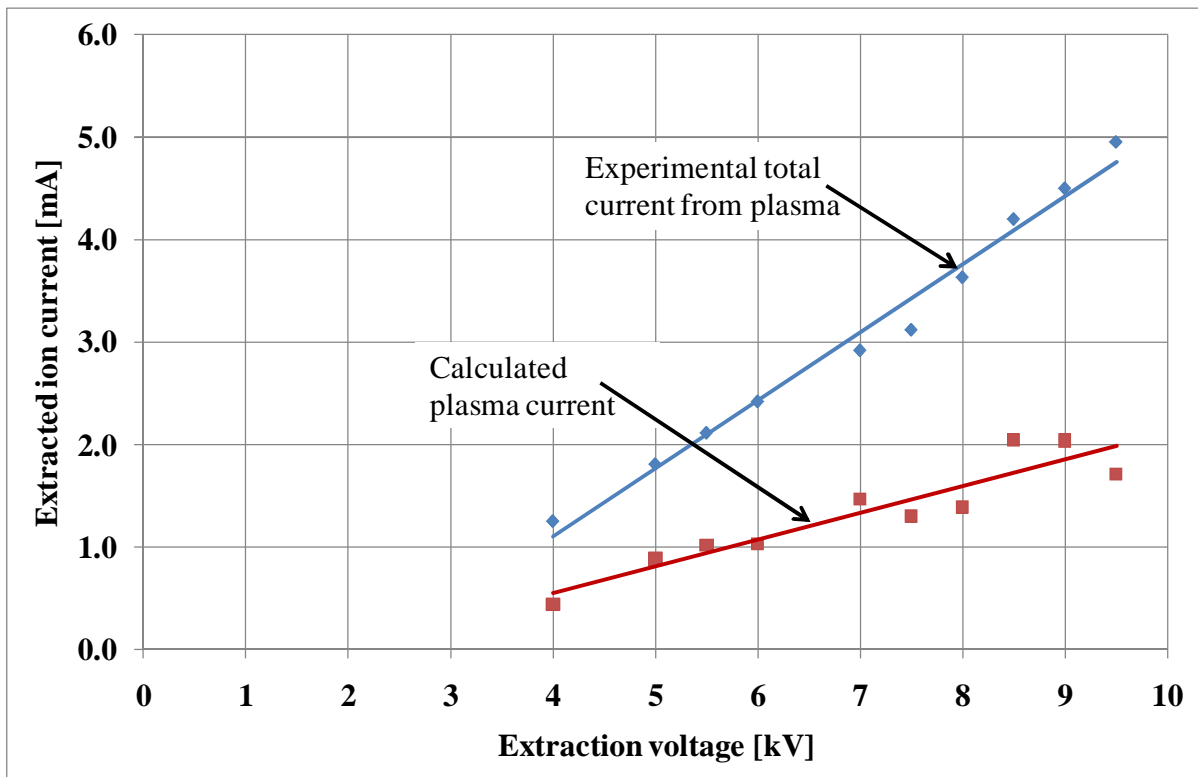


Figure 5-9: Comparison of the experimental current extracted from the plasma and the theoretical current calculated by Eqn 3-13.

The relationship between the experimental collector plate current and the extraction lens current shown in Figure 5-6 supported the hypothesis developed at the end of chapter 3 describing how an optimal size and shape of the plasma emissive surface existed in which the

majority of the ions were focused though the 1.8 mm aperture in the extraction electrode. The geometry of the emissive surface was a balance between the extraction voltage and the plasma density and electron temperature. As the plasma density increased beyond this optimal balance point, the concave shape of the emissive surface flattened and an increased number of ions that struck the extraction lens. This hypothesis was consistent with the observation seen in Figure 5-6 as the filament voltage was increased past the optimal point.



## Chapter 6. Six Ion Gun Fusion Experiment results and discussion

The mechanisms that produced the D(d, p)T, D(d, n)<sup>3</sup>He, and <sup>3</sup>He(d, p)<sup>4</sup>He fusion reactions in the Six Ion Gun Fusion Experiment were investigated using the instrumentation and diagnostics described in the previous chapters. Data on the total neutron production rate, the proton production rate in the cathode core region, and the energy spectrum of the cathode region fusion protons were collected. The result of changing the cathode voltage, total cathode current, pressure and ion beam focus were investigated. In addition to studying the properties of the fusion reactions, experimental data was collected about the operation and performance of the ion source extraction system.

The Six Ion Gun Fusion Experiment successfully accomplished many of the engineering challenges that were identified at the beginning of the project. These challenges were systematically approached during the 12 months between the initial project planning and the first operation of the full six gun system. The device was further refined during the next 12 month period of developing the diagnostics, debugging the equipment, and collecting data. The following is a sample of the challenges met. 1) The ion optics system was able to independently control six multi-milliamp ion beams from an under-focused, focused, to over-focused state. When focused at the center of the device, the beam was estimated to be 1.6 mm wide. 2) The compact ion gun modules and supporting systems were able to reliably operate to a cathode voltage of -150 kV in both D and D-<sup>3</sup>He environments; this electrical potential difference was maintained across a surface distance of 40 mm. 3) Through careful design and fabrication, the ion beams were aligned to within 0.2 mm of each other. 4) The active water cooling system and the selection of materials allowed the experiment to continuously operate for more than 1000 seconds per experimental run.

The majority of the data presented in the following sections was collected using the custom LabVIEW computer program discussed in section 4.2.6, with the exception of the proton energy spectrum data. The automated system collected and recorded operating parameters simultaneously with neutron and proton diagnostic results. This enabled data points whose parameters deviated too far from the set point to be excluded from the analysis. As a general rule, the error of the cathode voltage was within  $\pm 1$  kV and the errors of the total cathode current was within  $\pm 0.5$  mA. When multiple observation points were combined into one reported data point, the error bars for the neutron production rate were reported as the greater of either the standard deviation between the observed points or the square root of the total number of counts.

### 6.1. D-D fusion results

The SIGFE logged more than 75 hours and 250 runs in a deuterium environment. During those runs, the chamber pressure was varied across two orders of magnitude with a total cathode current (current from ions plus electrons) of 2 to 31 mA. The ion gun modules could focus the ions at the center of the device for cathode voltages between -50 kV to -150 kV. Figure 6-1 graphically shows the parameter space investigated during this dissertation.

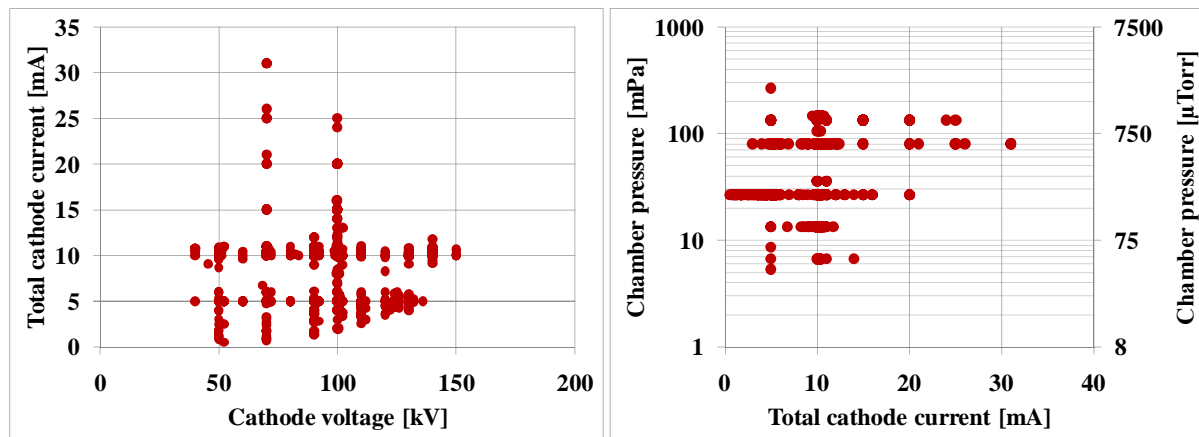


Figure 6-1: Parameter space of the Six Ion Gun Fusion Experiment.

The highest neutron production rate observed in a deuterium environment was  $4.3 \times 10^7$  neutrons per second (n/s) at a cathode voltage of -130 kV and a total cathode current (ions plus electrons) of 10 mA; this equated to  $3.3 \times 10^7$  neutrons per second per kilowatt. The neutron production rate was highly dependent on the focusing of the ion beams; results typical of this relationship are shown in Figure 6-2. The neutron rate increased as the focal point was adjusted away from the cathode center and closer to the upstream lenses; this setting of the focal point was called “low focus voltage” and is the 70% focus case shown in the figure. The ion trajectories predicted by the simulation software SIMION® at various focus settings are shown in Table 4-1. The relationship between the higher neutron rates and the prediction that more ions struck the cathode lenses at lower percent focus will be expanded upon in the discussion section (section 6.3).

Of note in Figure 6-2, is the noticeable change in slope of the 70% focus data series between -100 and -110 kV. This change in slope was typical of data that was taken sequentially from low voltage to higher voltage. In qualitative observations, the ion gun lenses would glow increasingly bright with temperature as the run progressed. When the lenses glowed brightly the neutron rates would start to drop. The lower percent focus runs seemed to heat more quickly. A more quantitative study of the lens heat versus neutron rate was limited by the availability of a pyrometer that could read below 500 °C through a glass vacuum window. Figure 6-10 will explore the trend of the neutron rate with run time in more detail. To minimize the heating and/or time effect on the results, the data was taken as quickly as possible. The time between the start of each data point was approximately 15 to 45 seconds.

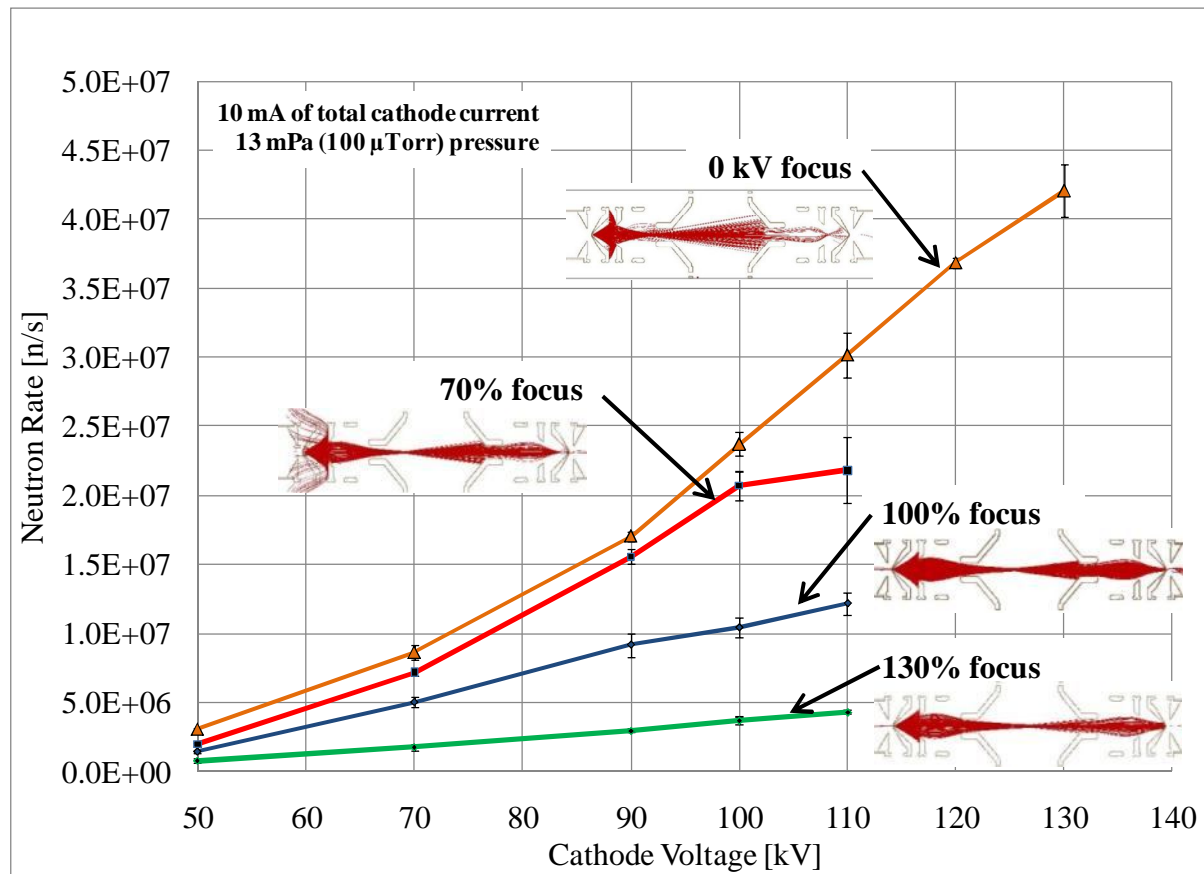


Figure 6-2: D-D neutron production rate in the SIGFE versus cathode voltage at different focus lens voltages.

The focus setting of the ion beams had an effect on the scaling of the neutron rate as a function of chamber pressure; this is shown in Figure 6-3. At low focus the neutron rate showed an inverse relationship with pressure. At 100% focus, the focal point was at the cathode center and there was little change in neutron rate with pressure. At 130% focus the neutron rate decreased with decreased chamber pressure.

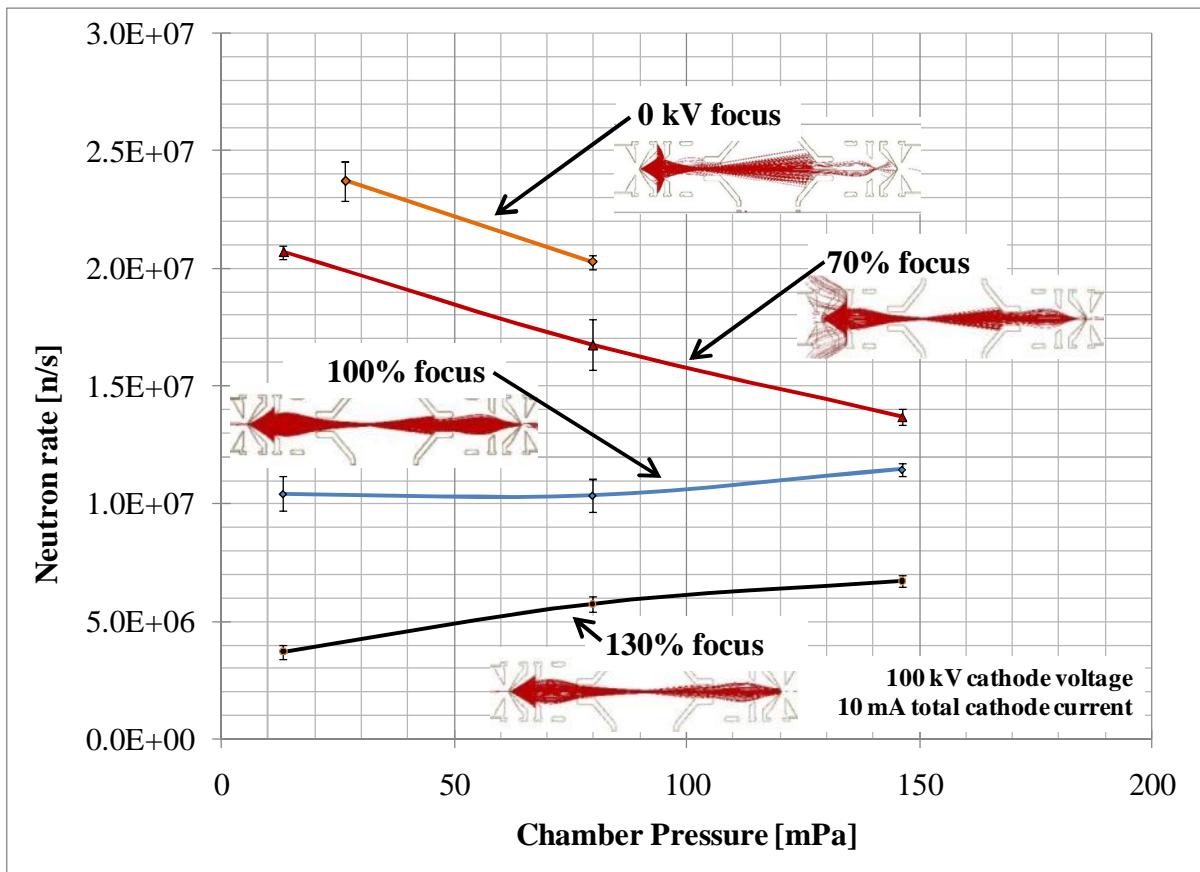


Figure 6-3: D-D neutron production rate from the SIGFE versus pressure at 3 different focus lens voltages.

The direct effect of the ion beam focal point on the neutron rate was explored by holding all other settings constant while the focus voltage was changed. Figure 6-4 shows how the neutron rate decreased as the focal point moved from low focus, through the device center at approximately -4.7 kV, to high focus. As the neutron rate decreased, the total current on the cathode increased. Since the plasma source and ion extraction settings were constant, the ion current from the sources was assumed to be constant; however the current measured was the total cathode current, which included the secondary electron current.

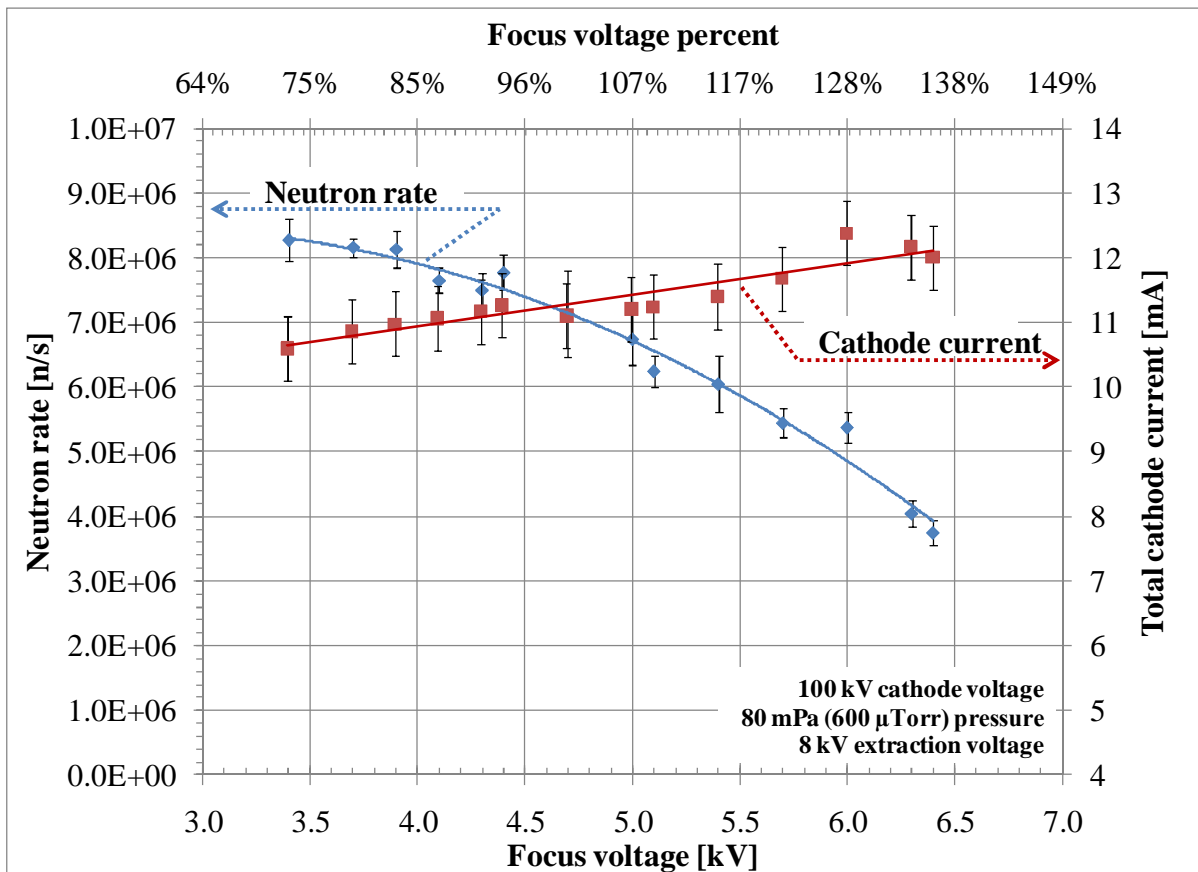


Figure 6-4: Result of a focus lens voltage scan showing the neutron rate and total cathode current. The cathode voltage was -100 kV, chamber pressure was 80 mPa, and the extraction voltage was -8 kV. The extraction and ion source input parameters were constant. The total cathode current was the sum of the ion to and secondary electron current from the cathode.

The interaction between the focus lens voltage and the extraction lens voltage was investigated with a statistical method called the Response Surface Method (RSM), which is a subset of the statistical tools of Design of Experiments (DOE). [1] RSM is a method of mapping a parameter space based on a mathematical model that gives statistical validity while minimizing the number of experimental data points required. The software package Design-Expert<sup>®</sup> [1] was used to setup and analyze the DOE conducted to determine the dependence of the neutron rate on a combination of the extraction lens voltages and the focus lens voltages. The data points were taken at random to isolate the effect that run time and run sequence may have on the results. Figure 6-5 shows the resulting contour plot for this

analysis. The study showed the neutron rate had only a minor dependence on the extraction voltage and confirmed the major dependence on the focus voltage.

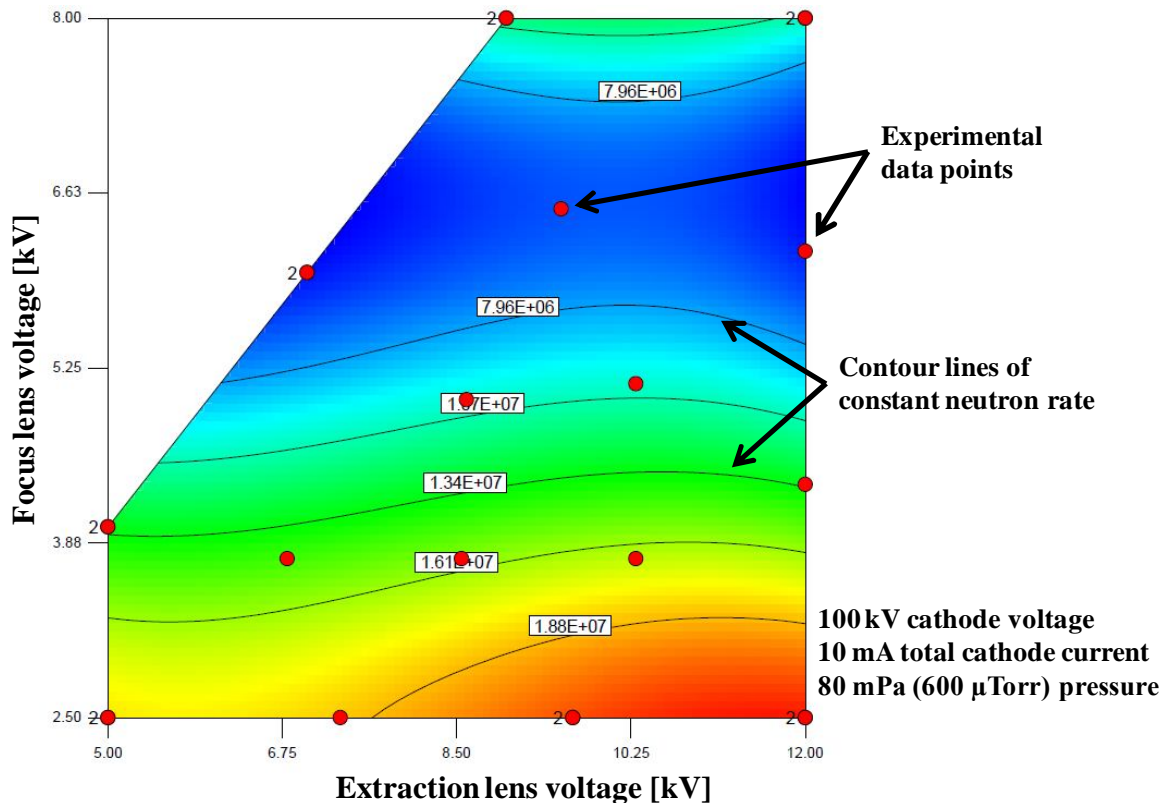


Figure 6-5: Contour plot showing lines of equal neutron rate for combinations of different voltages applied to the focus and extraction lenses. Contours are the result of a Design of Experiment that was setup and analyzed in the statistical software package Design-Expert® [1]

Figure 6-6 shows a subset of the DOE analysis at an extraction voltage of approximately -10 kV. A minimum in the neutron rate was observed. At focus voltages more negative than -6.5 kV the neutron rate increased. The discussion chapter will compare this minimum with the results of the ion trajectory simulations shown in Figure 4-8.

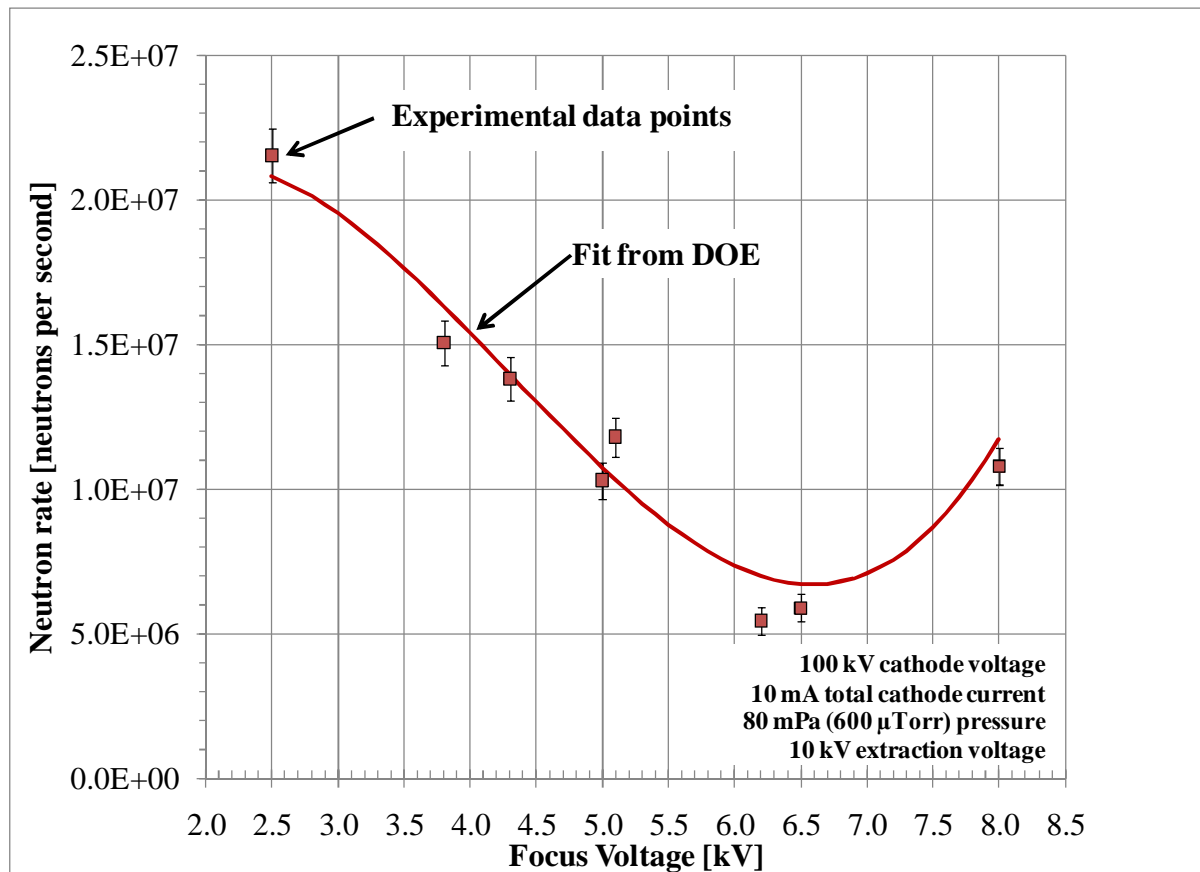


Figure 6-6: Plot of neutron rate versus focus voltage. The plasma source parameters were adjusted to provide a total cathode current of 10 mA for each data point. The experimental data and fit curve are a subset of the data shown in Figure 6-5 at an extraction voltage of 10 kV.

Experimental runs in which a scan of the focus settings was conducted for the full SIGFE system and then for each ion gun operating by itself. The neutron rate from each gun operating individually was approximately one sixth of the neutron rate of all guns operating together. The comparison of all six ion guns operating versus a single gun is shown in Figure 6-7.

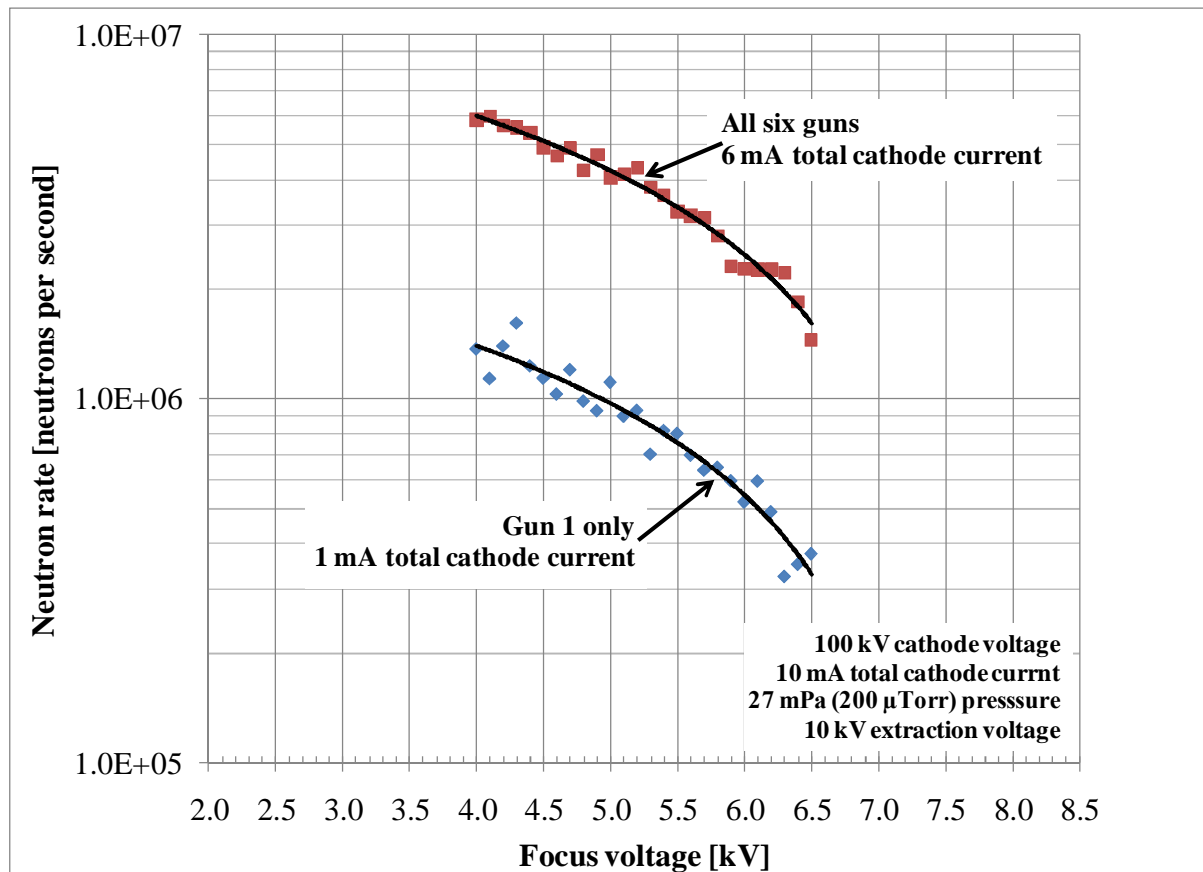


Figure 6-7: Single ion gun operation compared to full six ion gun operation as a function of focus.

The scaling of the neutron rate as a function of total cathode current is shown in Figure 6-8 and Figure 6-9. The data in the two graphs shows a linear scaling of the neutron rate with current. Neither the focus voltage nor the pressure in the chamber had a significant effect on the scaling of neutron rate with current.

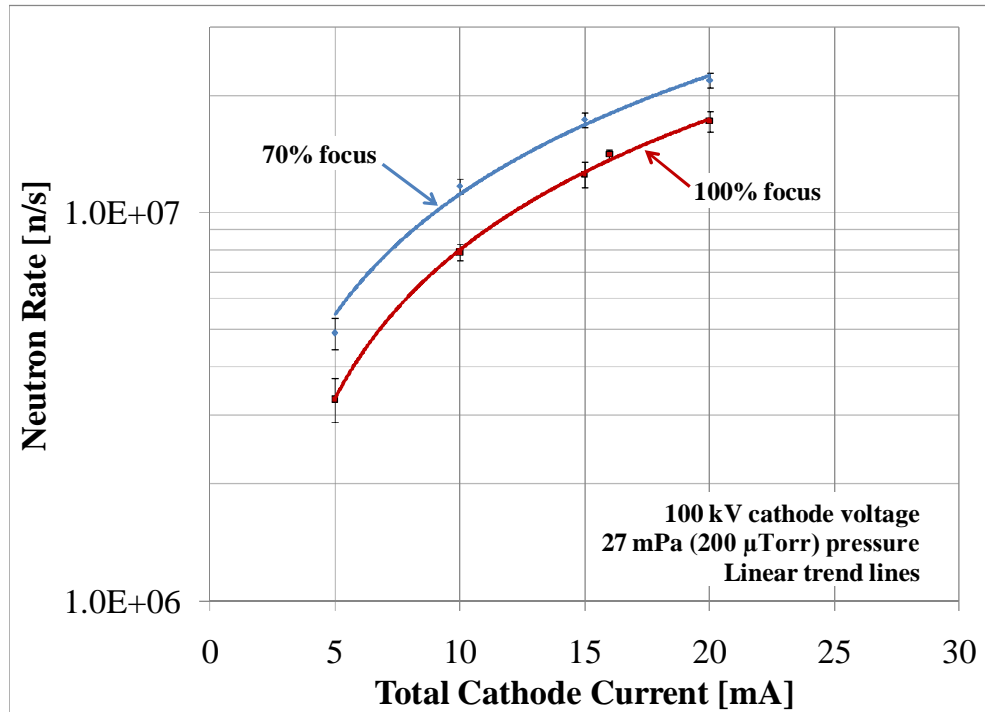


Figure 6-8: D-D neutron production rate versus total cathode current at two focus lens voltages. Data was taken at a cathode voltage of -100 kV and a chamber pressure of 27 mPa. The total cathode current was the sum of the ion current to and secondary electron from the cathode.

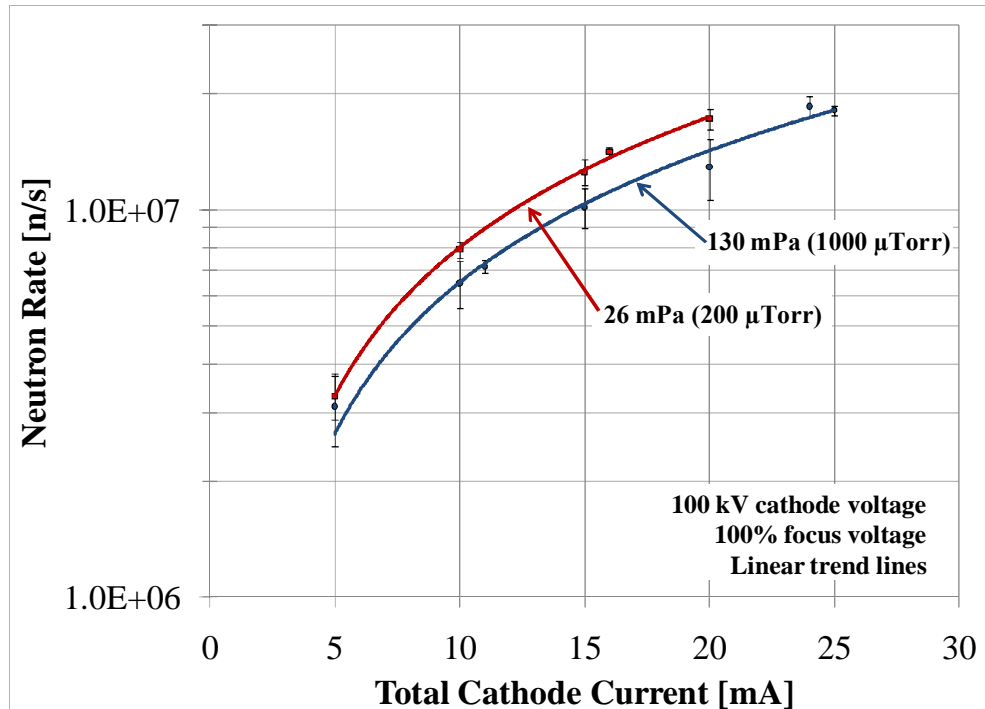


Figure 6-9: D-D neutron production rate versus total cathode current at two chamber pressures. Data was taken at a cathode voltage of -100 kV and a focus lens voltage of 100%. The total cathode current was the sum of the ion current to and secondary electron current from the cathode.

The time dependence of the neutron rate complicated the comparison of different data points taken throughout this dissertation. To investigate this, several experimental runs were conducted where the device was quickly (~30 seconds) brought up to the desired power level and maintained at those settings for 1000 seconds. In most cases, these runs were coupled with the collection of proton data from the FIDO and/or collimated proton detector. Figure 6-10 shows a sample of this data. A maximum in the neutron rate was normally observed between 400 and 500 seconds. The measured chamber pressure is not shown, but remained relatively constant until approximately 750 seconds. The neutron rate maximum was most noticeable in the 70% focused case where Figure 4-8 predicted more ions would be striking the cathode lenses.

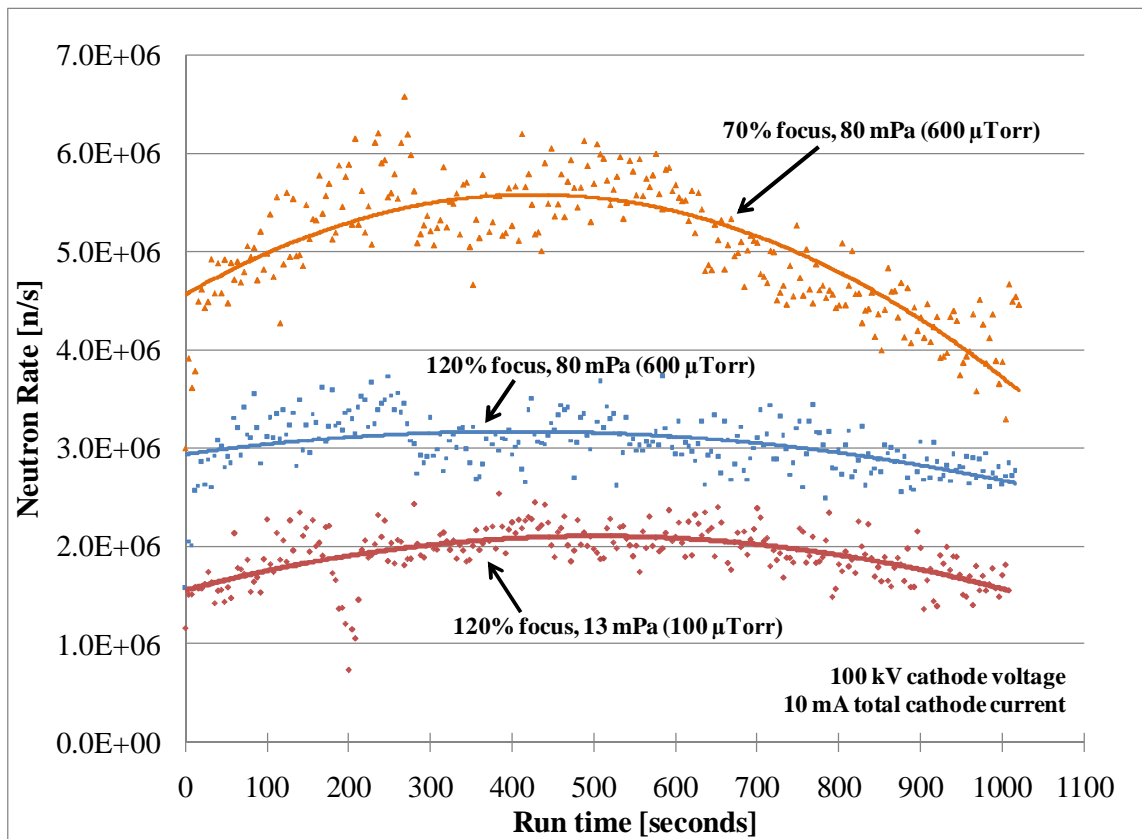


Figure 6-10: Time dependence of the neutron rate.

The neutron production rate was dependent on the alignment of the ion gun lenses. The lenses were aligned using the techniques discussed in sections 4.1.3 and 4.2.1. The lenses could become misaligned if they were allowed to get too hot. The repeated thermal expansions of the lenses appeared to loosen the lenses in their mounts and caused misalignments of approximately 1 mm. The extraction lenses had the highest heat load and were the most likely components to be out of alignment. Figure 6-11 shows two examples of the effect of lens alignment on the neutron rate. An approximate factor of two difference was observed in neutron rates between the aligned and misaligned cases.

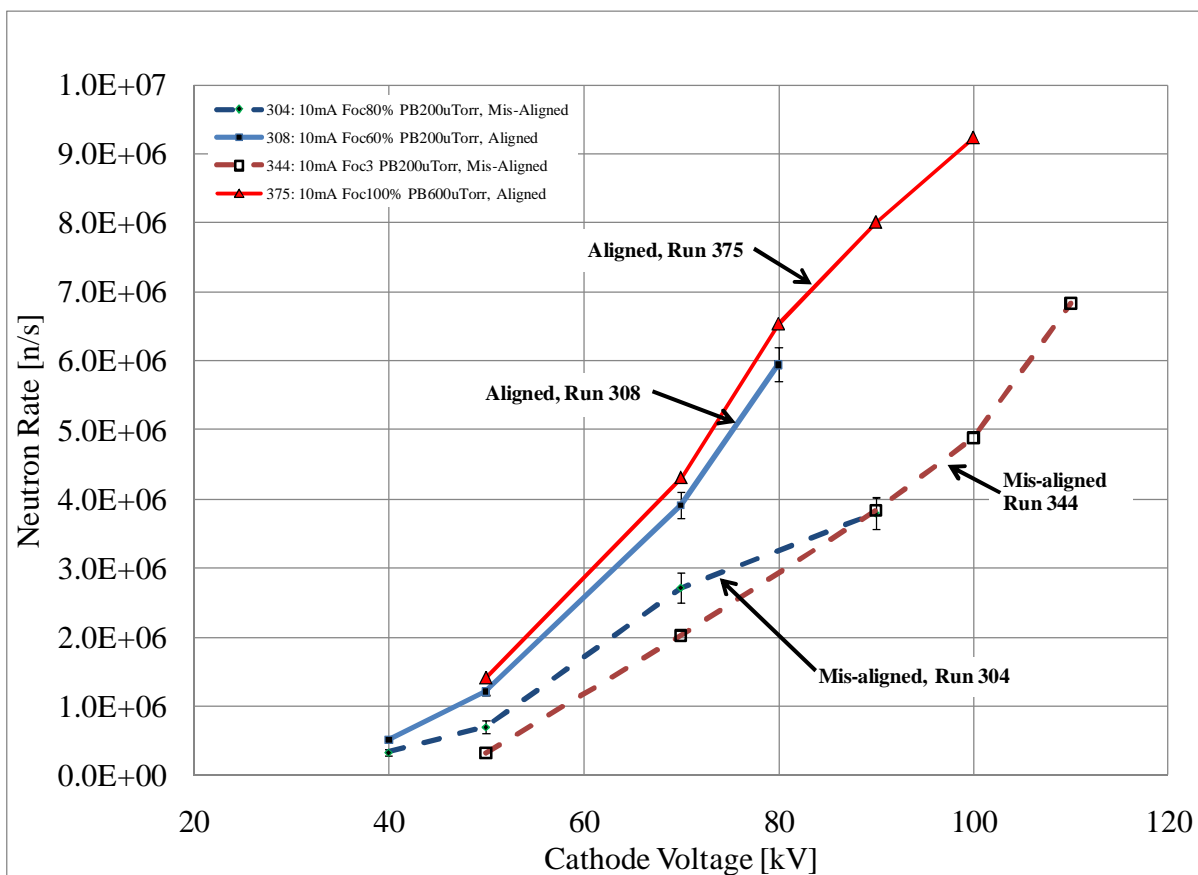


Figure 6-11: Effects of lens alignment on neutron rate. Misalignment of the extraction lenses was on the order of 1 mm.

The addition of electron shields reduce the loss of electrons from the cathode region and increased the neutron rates by a factor of more than two for the same high voltage power.

Figure 6-12 shows two comparable data sets before and after the installation of the shields. Section 4.2.4 gives a detailed description of the design and installation of these shields. Qualitative observations of the 8  $\mu\text{m}$  thick Al foils at the corners of the shields showed no signs of damage or discoloration from heating. Damage and heating would be expected if the foils were impacted by energetic ions or electrons.

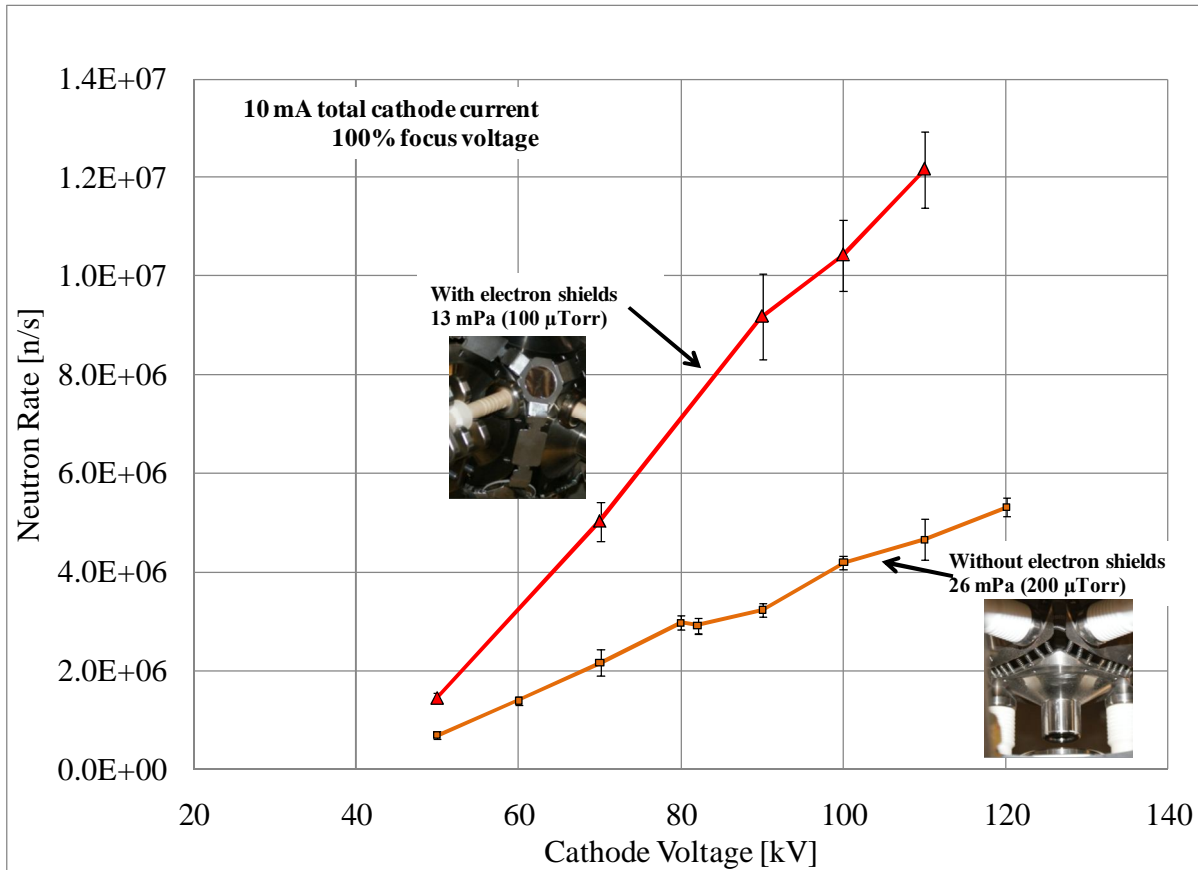


Figure 6-12: Comparison the neutron rate performance before and after the installation of the electron shields at the seams of the cathode.

### 6.1.1. Energy spectrum of D-D fusion protons

The Fusion Ion Doppler Shift (FIDO) diagnostic [2] was installed on the SIGFE to measure the energy and production rate of the 3.02 MeV D-D fusion protons. The FIDO diagnostic measured the energy of the protons with a resolution of 7 keV, which allowed the Doppler shift caused by the center-of-mass velocity of the reacting particles to be observed. A complete description of the FIDO diagnostic and its installation on the SIGFE device was

given in Section 4.3.2; Figure 6-13 is reproduced from that section for the reader's convenience. The green cone in the figure depicts the geometric volume where the protons could have been observed from.

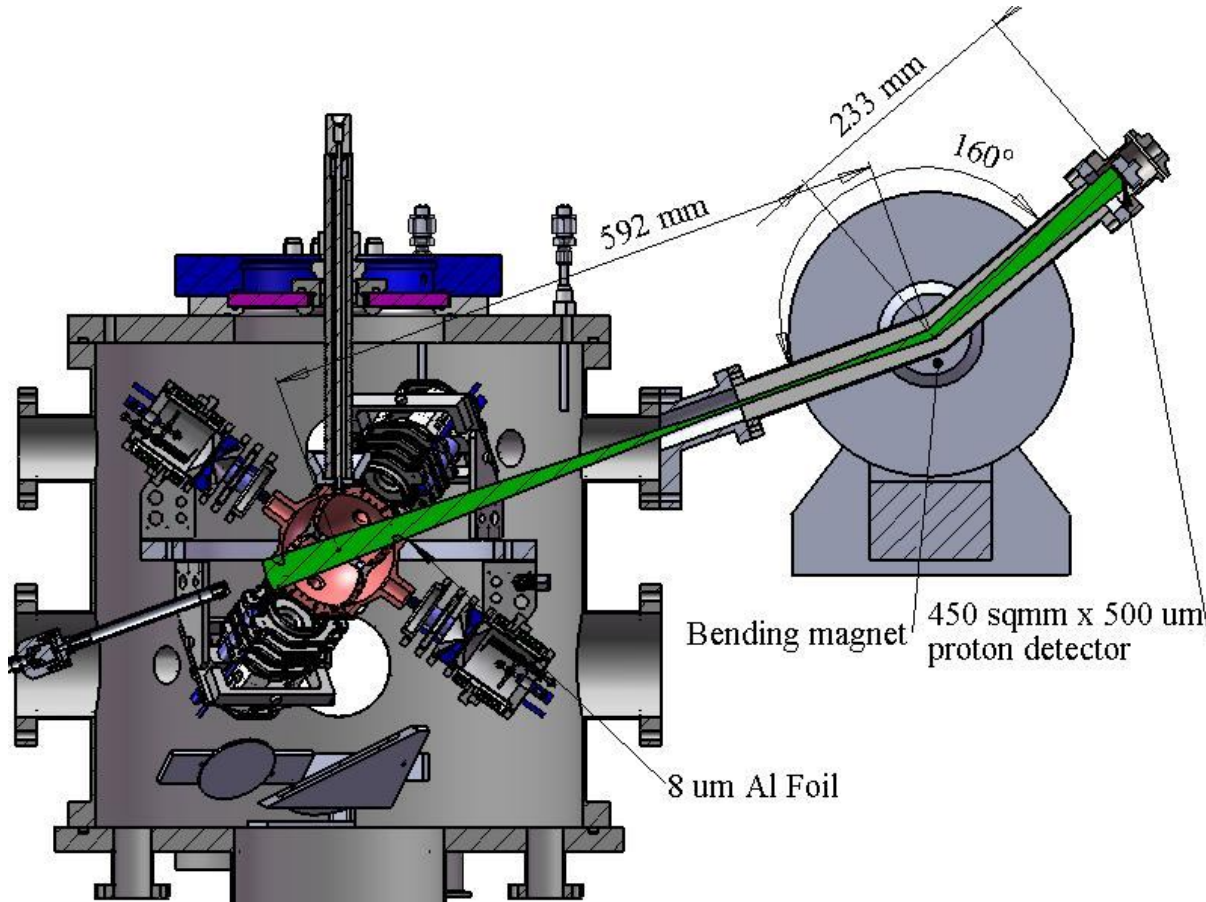


Figure 6-13: Cross-section of fusion ion Doppler shift diagnostic (FIDO) installed on SIGFE. The cone-of-view of the system is highlighted in green. The distance from the detector face to the device center is 825 mm. An  $8 \mu\text{m}$  Al foil was between the device center and the detector.

Measurements of the proton energy spectra at different cathode voltages, chamber pressures, and focus voltages were taken. The operating parameters were held constant for a 1000 second count time at each setting, and the equipment was allowed to cool for approximate two hours or more between each data set. This long period of time between data points and concerns for fatigue on the equipment limited the number of data points collected to three pressures, three cathode voltages, and two focus voltages.

Figure 6-14 shows the raw proton count results for the -125 kV cathode voltage case, which included two separate 1000 second experimental runs to improve the counting statistics. Two distinct energy groups were observed, along with smaller features visible inside each group. Few protons were observed near 2.84 MeV, which is the expected energy of non-Doppler shifted 3.02 MeV protons through the Al foil. Figure 6-15 shows the predicted energy spectrum of D-D fusion protons Doppler shifted by full cathode energy  $D_1^+$ ,  $D_2^+$ , and  $D_3^+$  ions after passing through the Al foil. The heights of the peaks in Figure 6-15 were adjusted for clarity to approximately match the experimental results in Figure 6-14.

The proton rate shown in the following experimental graphs was multiplied by the calibration factor calculated in section 4.3.2, which was 18909 protons per count. The energy spectra at the three different cathode voltages are shown in Figure 6-16. The distance between the twin energy peaks and the total proton production rate increased as the cathode voltage increased. The expected shift in the peaks for full cathode energy  $D_2^+$  ions was simulated using SRIM® and is displayed in Figure 6-17.

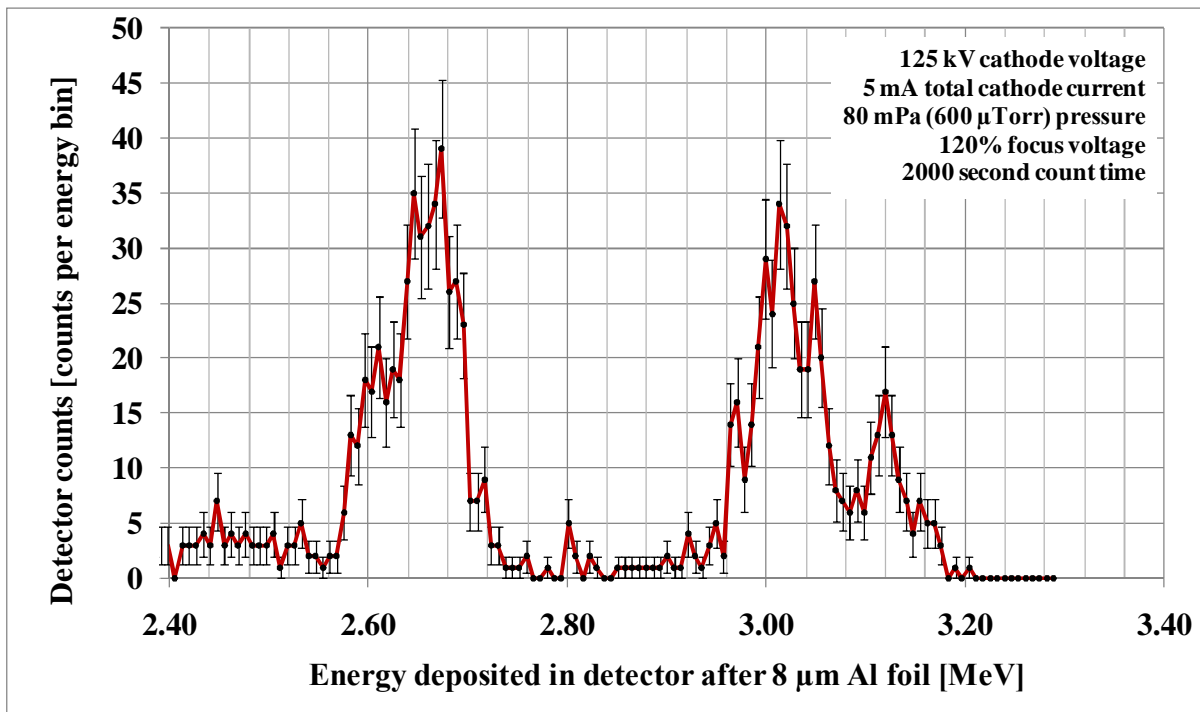


Figure 6-14: Energy spectrum for 3.02 MeV D-D fusion protons deposited in a 500  $\mu$ m thick Si detector after an 8  $\mu$ m thick Al foil. Data was obtained with the FIDO diagnostic at a cathode voltage of -125 kV and count time of 2000 seconds.

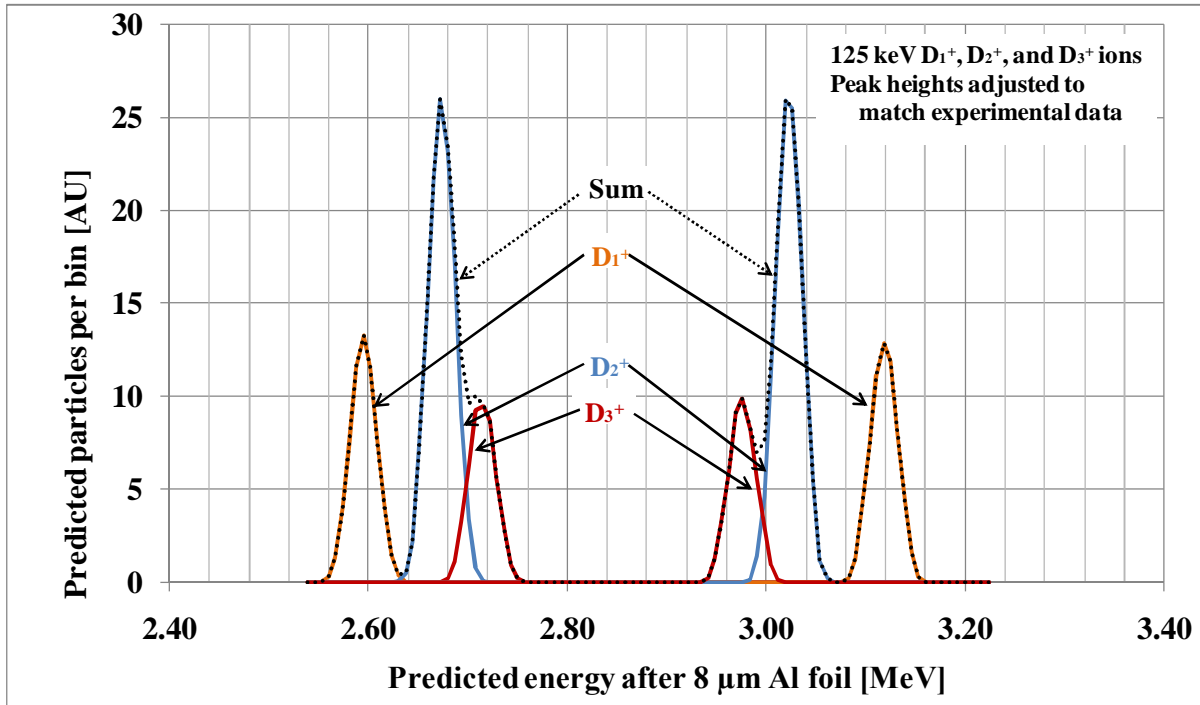


Figure 6-15: Predicted energy deposited in a detector by D-D fusion protons after a Doppler shift from 125 keV D<sub>1</sub><sup>+</sup>, D<sub>2</sub><sup>+</sup>, and D<sub>3</sub><sup>+</sup> ions and after 8  $\mu$ m thick Al foil. Initial ion energies after Doppler shift used in SRIM simulations are shown in Table 4-6. The peak heights of the various ions are adjusted for clarity to match experimental peak heights in Figure 6-14.

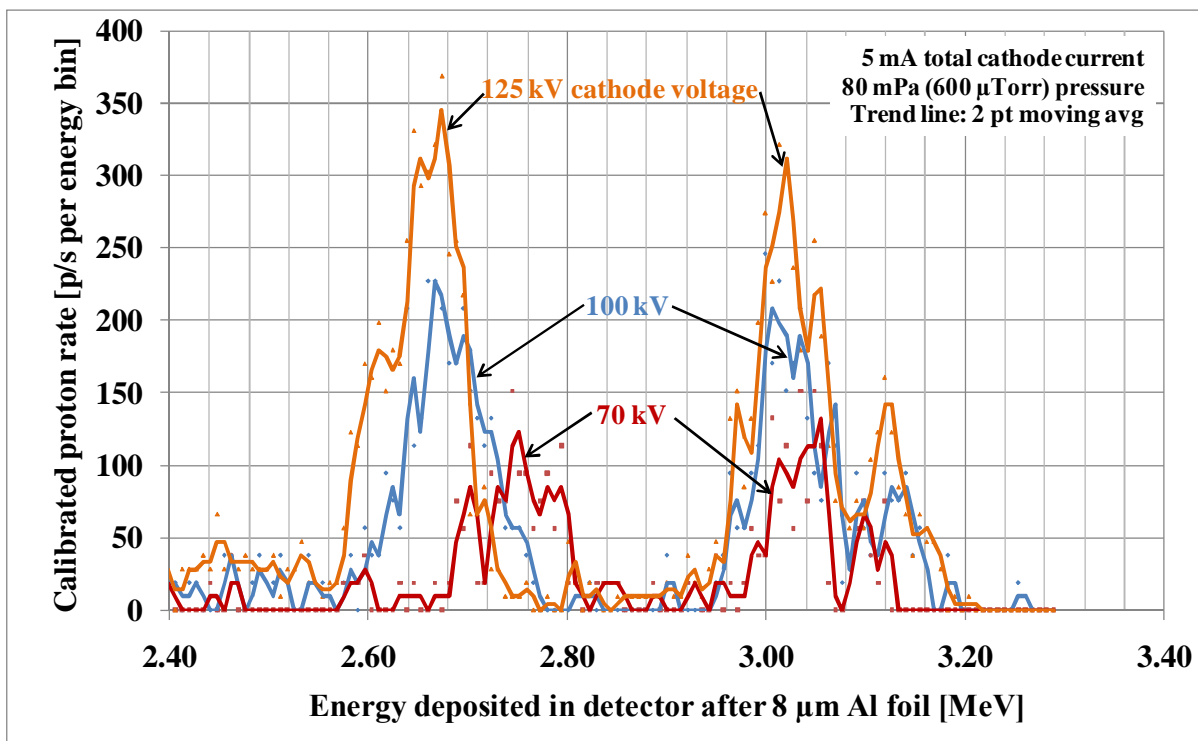


Figure 6-16: Comparison of the energy spectra of D-D protons collected by the FIDO diagnostic at three different cathode voltages. An 8 μm Al foil was between the cathode region and the detector.

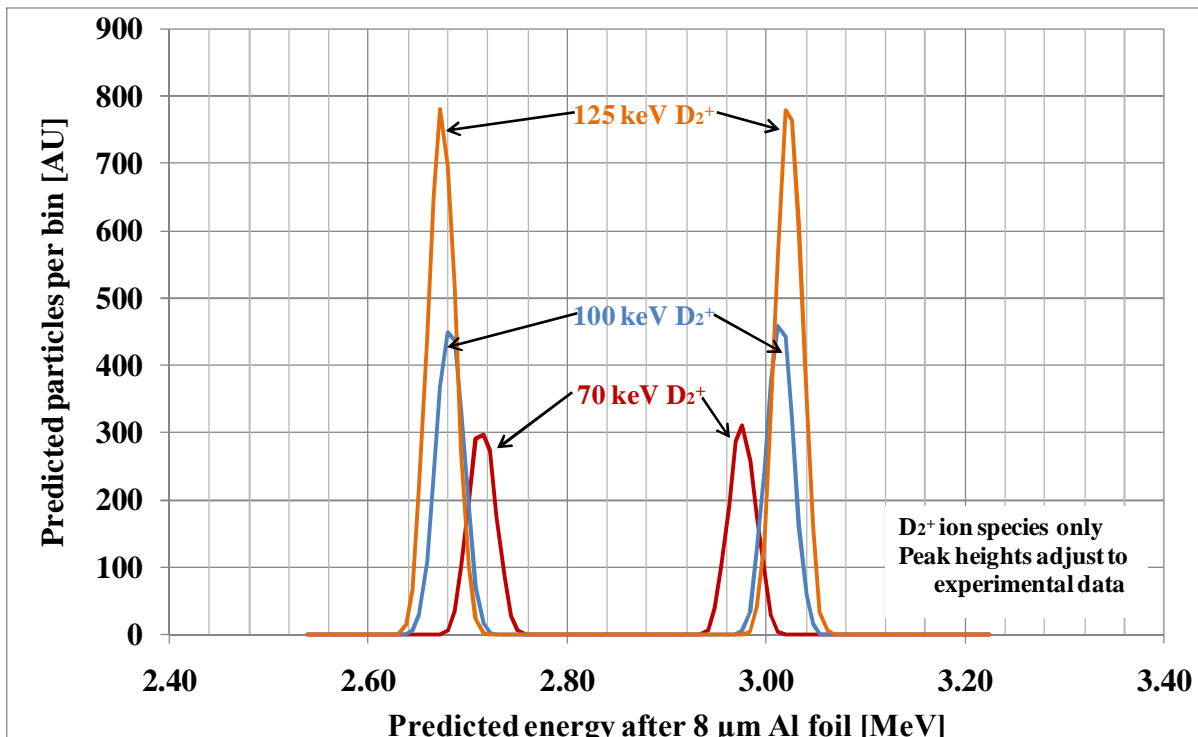


Figure 6-17: Predicted energy deposited by  $D_2^+$  ions into a 500 μm thick Si detector after an 8 μm thick Al foil. Initial ion energies after Doppler shift used in SRIM simulations are shown in Table 4-6. The peak heights of the various energy ions adjusted for clarity to match experimental peak heights in Figure 6-16.

The comparison of the energy spectra with changing pressure is shown in Figure 6-18. The width of the energy spectrum did not significantly change as the chamber pressure was increased from 80 mPa to 130 mPa. The total number of counts collected in the 13 mPa cases was too low to allow for an accurate comparison.

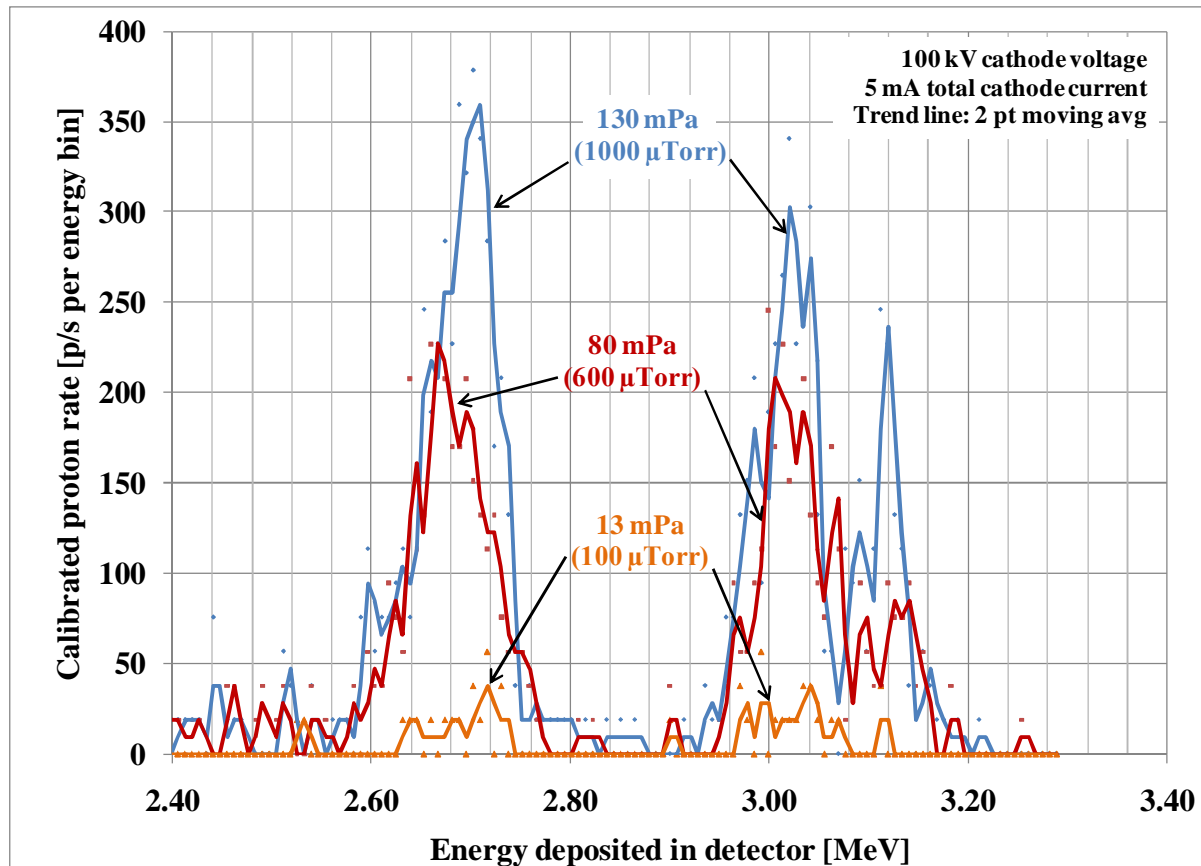


Figure 6-18: Comparison of the energy spectrum of the 3.02 MeV D-D protons collected by the FIDO diagnostic at three different chamber pressures. An 8  $\mu\text{m}$  Al foil was between the cathode region and the detector.

Since the FIDO diagnostic was only able to observe the D(d, p)T fusion rate for a limited volume that included the center of the cathode region, it was interesting to compare the proton rate from FIDO with the total D(d, n) $^3\text{He}$  neutron rate for the same experimental data set. The neutron detector was able to observe fusion reactions from anywhere in the device, and the branching ratio between the D(d, p)T and D(d, n) $^3\text{He}$  reactions is nearly 50%.

[3] With these assumptions, the fusion reactions that occurred in the center of the cathode were estimated to be less than 0.2% of the total amount of fusion that occurred in the entire device.

Figure 6-19 compares the calibrated proton and neutron rates at two focus settings; note the three orders of magnitude difference between scales of the proton and neutron data. The change in the proton rate with focus voltage was less than the error bars, and therefore may not have been significant. This is in contrast to the neutron rate that increased as the focus voltage was decreased, which was consistent with the more detailed neutron rate versus focus voltage studies shown in Figure 6-4.

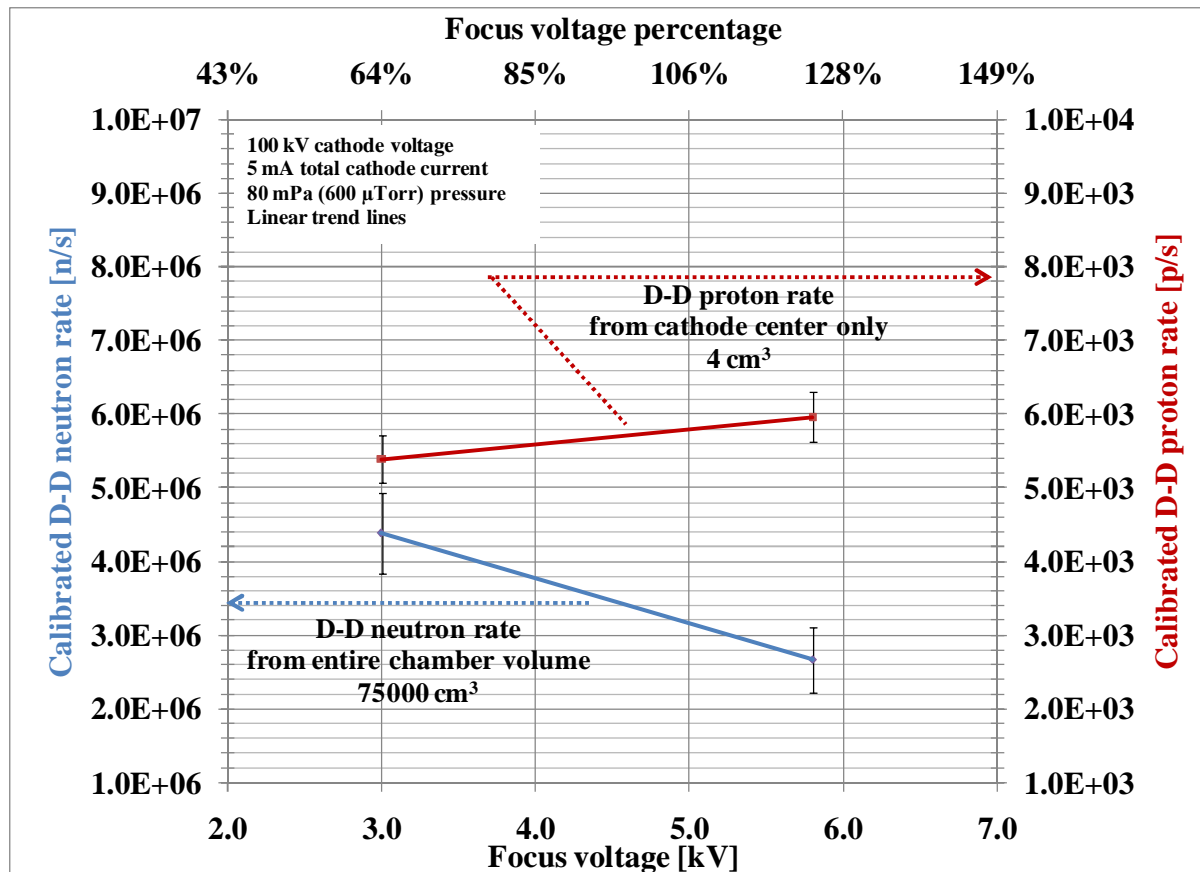


Figure 6-19: Calibrated D-D proton rate from the cone-of-view defined in Figure 6-13, which included the center of the cathode, compared to the total calibrated neutron rate at focus voltages of 3.0 keV (65% focus) and 5.8 keV (125% focus).

The proton rate observed by the FIDO diagnostic increased approximately linearly with increased chamber pressure. The neutron rate increased at a slower linear rate than the proton rate with pressure. The three pressure data points are shown in Figure 6-20.

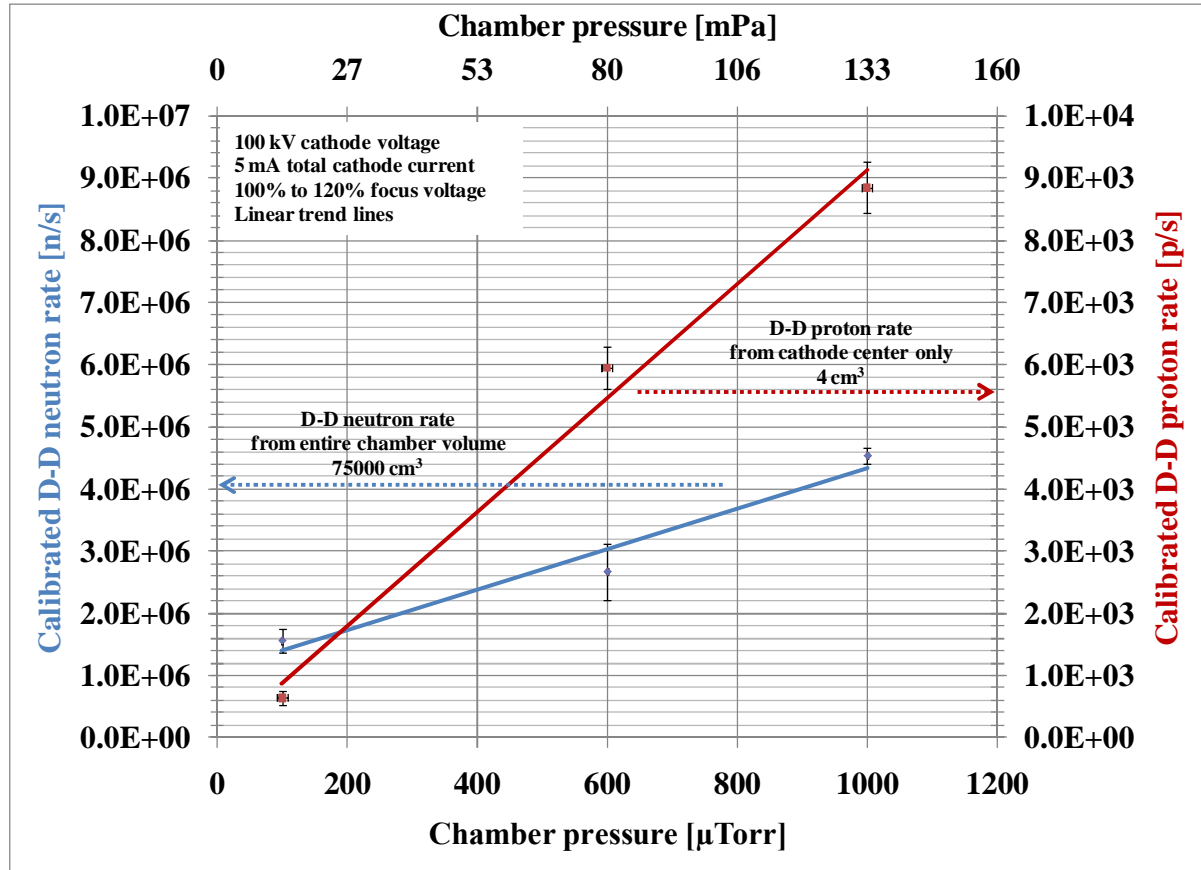


Figure 6-20: Calibrated D-D proton rate from the cone-of-view defined in Figure 6-13, which included the center of the cathode, compared to the total calibrated neutron rate for three different chamber pressures.

## 6.2. D-<sup>3</sup>He fusion results

The detector system described in section 4.3.4 was the only diagnostic included on the SIGFE that was able to detect the <sup>3</sup>He(d, p)<sup>4</sup>He reactions. It replaced the FIDO diagnostic on a vacuum port with a view of the center of the cathode through an 8 μm Al foil. Therefore it could detect fusion protons from a similar region as the FIDO diagnostic; as seen in Figure 4-39. As mentioned in the early description of this detector system, 360 μm of Pb was placed in front of the detector to reduce the x-rays detected. The Doppler shift resulting

for the center-of-mass energy of the reacting particles was detectable even with the spread of proton energy though the Al and Pb foils. Figure 6-21 shows the raw results from this detector with the twin peak structure characteristic of Doppler shifting visible. Similar to the analyses performed for the D-D fusion protons, Figure 6-22 plots the predicted energy spectra deposited in the detector for all four combinations of the  $D_x^+$  and  ${}^3He^+$  ion species. A qualitative comparison of the raw proton data and the predicted spectrum suggests that the ion energy is near the full cathode energy for a singly charged ion.

The count rate of the  $D-{}^3He$  protons was between 0.21 counts per second (c/s) and 4.3 c/s. A counting time of 500 seconds was required to obtain the level of error shown in Figure 6-21, which had a total of 1185 counts. Longer counting times were not taken due to concerns of damage to the electrodes. Prolonged exposure to He ions had been shown in previous experiments in the UW IEC lab to erode the electrode surfaces at a microscopic level and decrease their high voltage standoff performance. [4]

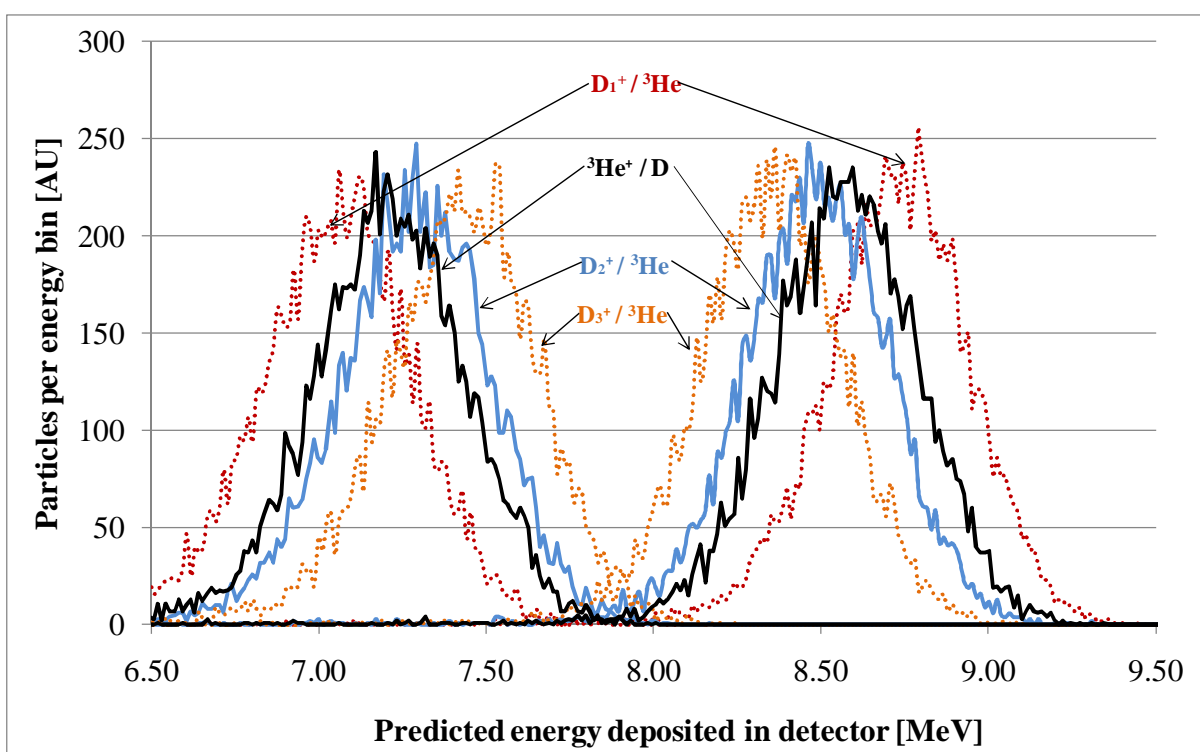
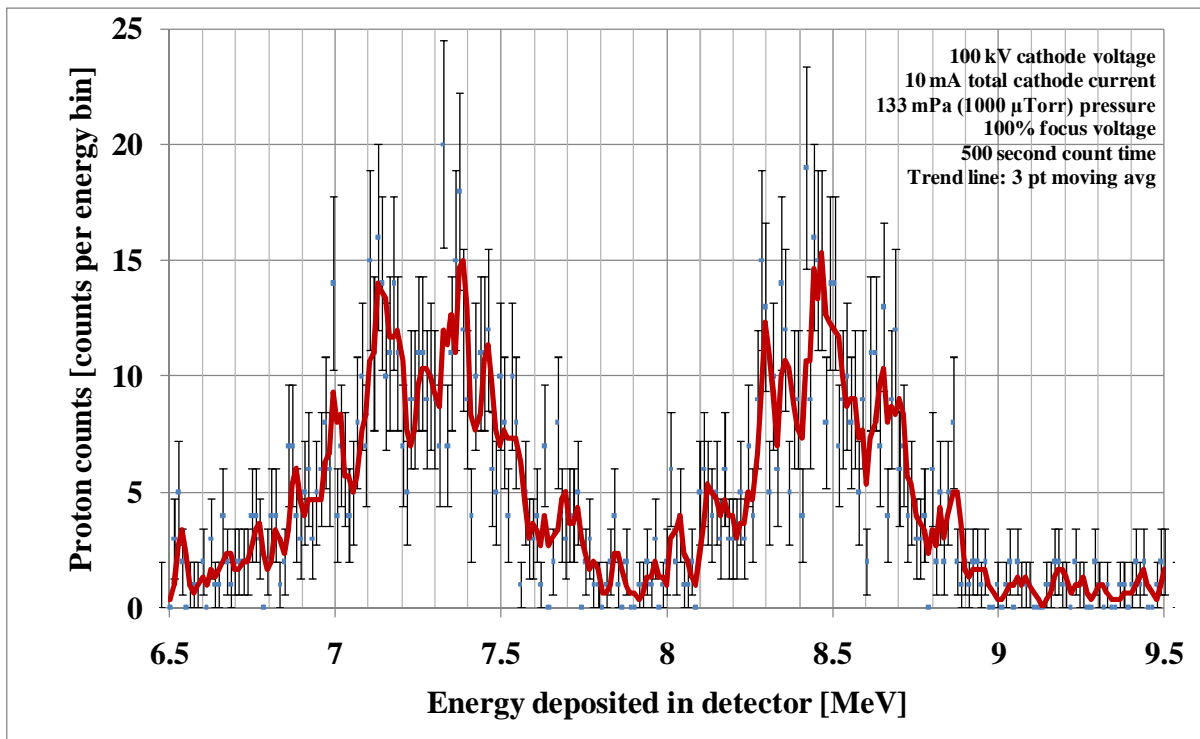


Figure 6-22: Predicted energy spectrum deposited in a 700  $\mu\text{m}$  thick Si detector after 8  $\mu\text{m}$  of Al and 360  $\mu\text{m}$  of Pb for 14.7 MeV <sup>3</sup>He(d, p)<sup>4</sup>He protons resulting from 130 keV ions fusing with stationary targets. All four combinations of <sup>3</sup>He+, D<sub>1</sub>+, D<sub>2</sub>+, and D<sub>3</sub>+ ions on <sup>3</sup>He and D targets are plotted

A total of five experimental runs were conducted with a 1:1 ratio of  ${}^3\text{He}^+$  to  $\text{D}_x^+$  ion current and a ratio of 1:1  ${}^3\text{He}$  to D gas mixture. Figure 6-23 shows the results of a voltage scan performed at 133 mPa. The proton rate was corrected using the calibration factor calculated in Section 4.3.4, which was 3105. The results showed broadening of the gap between the peaks as the cathode voltage was increased. However, a detailed quantitative analysis would have required much longer counting times to improve the counting error of the data. Figure 6-24 compares the calibrated  $\text{D}-{}^3\text{He}$  proton rate from the center of the cathode to the calibrated D-D neutron rate for the cathode voltage scan. Between two and three orders of magnitude less  $\text{D}-{}^3\text{He}$  protons were detected compared to the D-D neutrons.

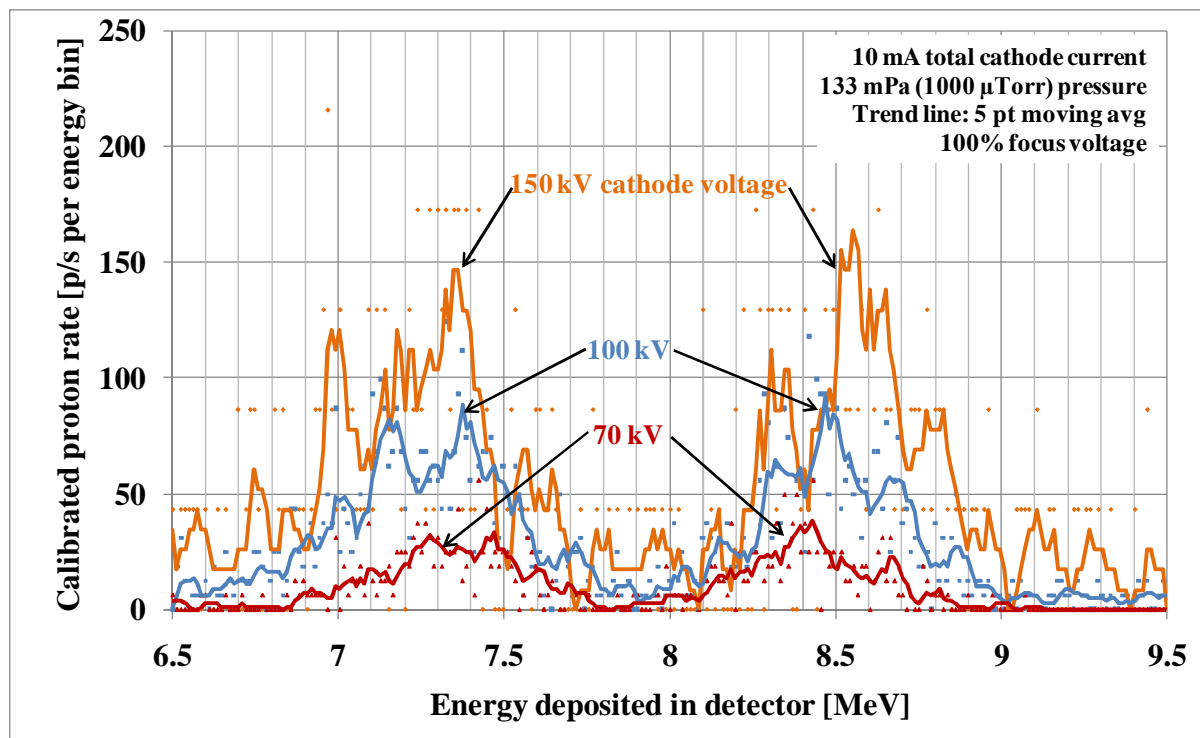


Figure 6-23: Comparison of the energy spectra of  $\text{D}-{}^3\text{He}$  fusion protons at three cathode voltages. 8  $\mu\text{m}$  of Al foil and 360  $\mu\text{m}$  of Pb foil were between the center of the cathode and the detector.

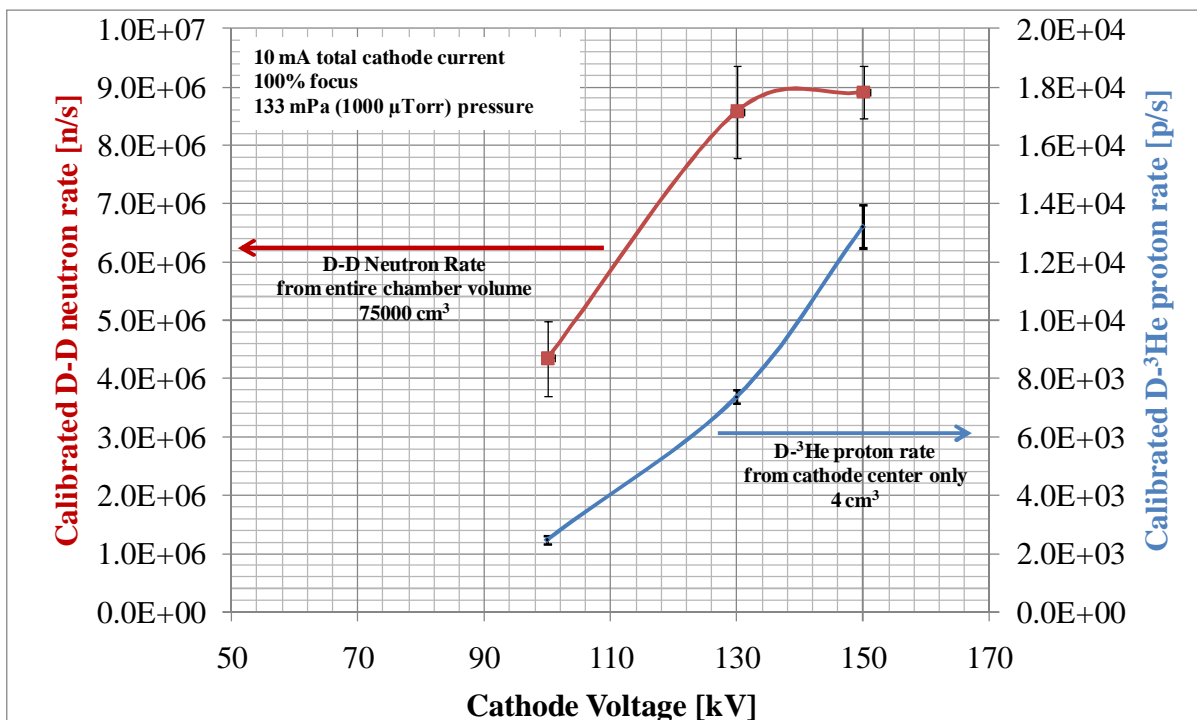


Figure 6-24: Calibrated D-<sup>3</sup>He fusion proton rate from the cone-of-view defined in Figure 4-39, which included the center of the cathode, compared to the total calibrated D-D neutron rate for the three cathode voltages.

At a cathode voltage of -100 kV, the pressure in the chamber was varied while maintaining the 1:1 D to <sup>3</sup>He gas mixture. Figure 6-24 and Figure 6-25 show the results of this study. Within the accuracy allowed by the counting statistics of the data, a noticeable widening of the Doppler peaks was not observed. The total number of calibrated D-<sup>3</sup>He protons observed at the center of the device increased linearly with pressure while the D-D neutrons had a weak inverse relationship with the pressure.

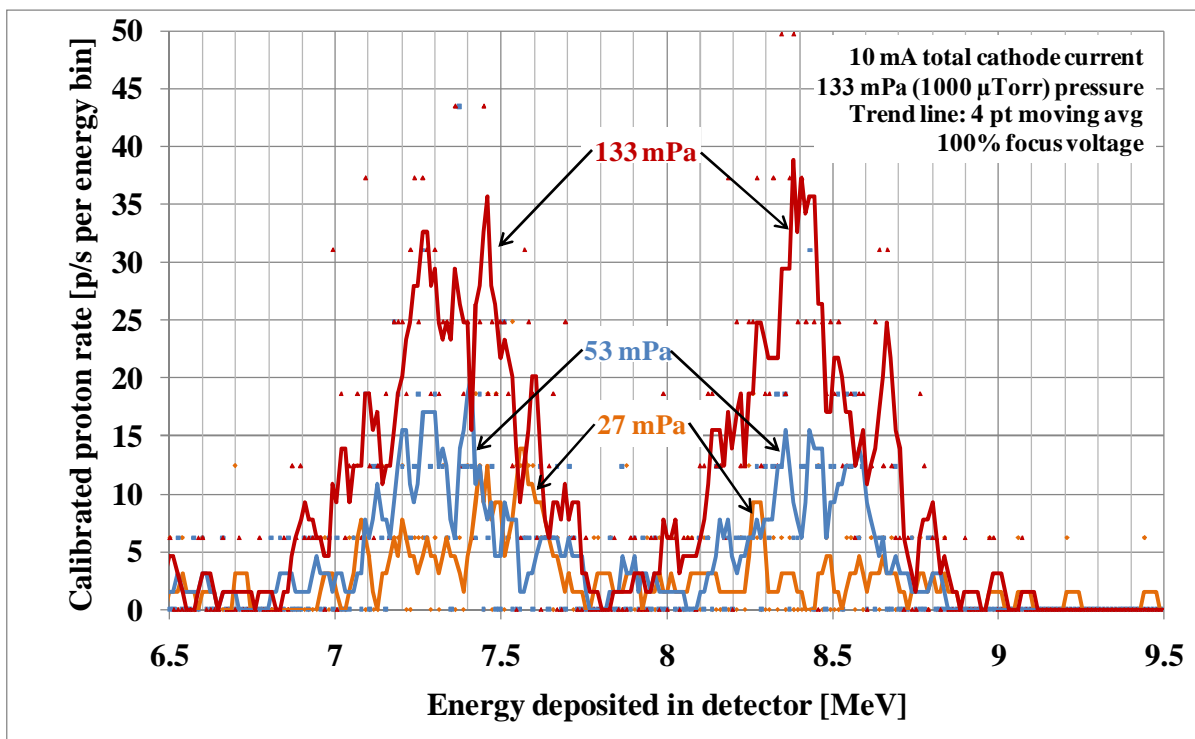


Figure 6-25: Comparison of the energy spectra of the 14.7 MeV D- $^3$ He fusion protons at three chamber pressures with a 1:1 mixture of D and  $^3$ He gas. 8  $\mu$ m of Al foil and 360  $\mu$ m of Pb foil were between the center of the cathode and the detector.

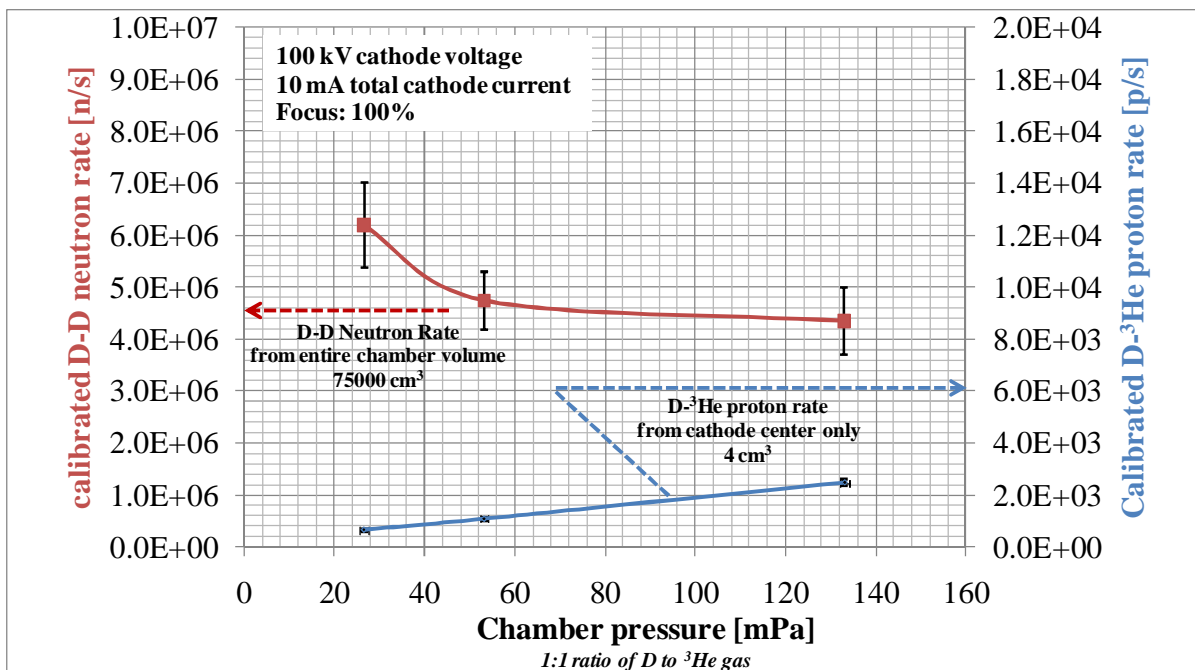


Figure 6-26: Calibrated D- $^3$ He fusion proton rate from the cone-of-view defined in Figure 4-39, which included the center of the cathode, compared to the total calibrated D-D neutron rate for the three chamber pressures.

### 6.3. Discussion of SIGFE results

#### 6.3.1. Implications for the existence of potential well structures in the SIGFE device

Nuclear fusion from the formation of virtual potential well structures at the center of the cathode was not a significant mechanism by which fusion reactions were generated in the SIGFE device at total cathode currents below 30 mA and cathode voltages between -50 kV and -150 kV. This was evident by the low number of D-D protons observed from the center of the cathode compared to the total number of D-D neutrons observed. Had a majority of the fusion reactions been occurring in the center where virtual potential wells should have formed, the calibrated proton rate and calibrated total neutron rate should have been approximately equal, given that the branching ratio between the D(d, p)T and D(d, n)<sup>3</sup>He reactions is nearly equal. [3] However, the calibrated D-D proton rate was less than 0.2% of the calibrated D-D neutron rate.

The relationship between the focus of the ion beams and the D-D neutron production rate was also inconsistent with virtual potential well structures being a significant source of fusion in the SIGFE device. The experiments showed that the neutron rate decreased as the ion beams were focused at the cathode center. The theory of virtual potential well formation described in chapter 2 predicted the opposite. As the beams are focused, more space charge is injected into a smaller area and the probability of a potential well forming should have increased. If this had occurred in the experiment, a marked increase in neutron production should have resulted as the intersecting beams focused on one another, however this was not the case.

The characteristics of the D-D fusion protons that originated from the center of the cathode were consistent with what would be expected from energetic ions reacting with the background gas. The energy spectra of the protons collected by the FIDO diagnostic showed

a shift in the energy away from what would have been expected from pure 3.02 MeV D-D fusion protons. The energy shifts were consistent with the center-of-mass energy of near full cathode energy  $D_1^+$ ,  $D_2^+$ , and  $D_3^+$  ions reacting with stationary  $D_1^0$ , as shown in Figure 6-27.

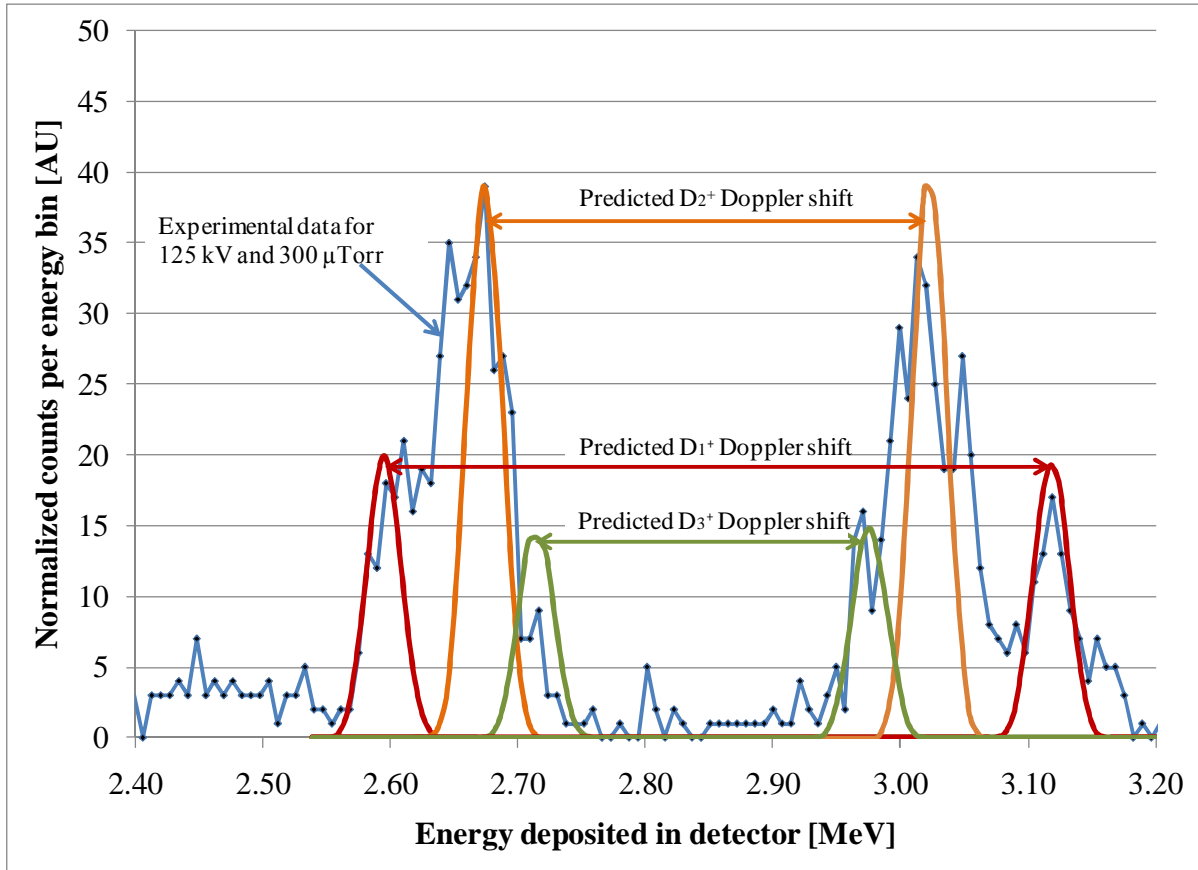


Figure 6-27: Experimental and predicted fusion proton spectrum of D-D fusion protons Doppler shifted by 125 keV  $D_1^+$ ,  $D_2^+$ , and  $D_3^+$  ions after passing through 8  $\mu\text{m}$  of Al foil. Energy loss through foil was simulated in SRIM. [27] The height of the predicted peaks were adjusted to match experimental data. Experimental data set shown was taken at a cathode voltage of -125 kV and 40 mPa (300  $\mu\text{Torr}$ ).

The weak dependence of the proton rate on the focus voltage, seen in Figure 6-19, was also consistent with beam-background gas reactions. Beam-background reactions should only be dependent on the number of energetic particles and the number of targets, not on the focusing of the ion beams. As long as the ion current through the center of the device remained constant, the protons from beam-background fusion should also remain constant, as was seen in the experimental results.

The majority of the protons observed by the FIDO diagnostic originated from near the center of the cathode. The 8  $\mu\text{m}$  Al foil at the perimeter of the cathode down-shifted the observed energy spectrum. If a fusion reaction occurred in the region between the outside of the cathode and the detector it would not have this shift, and peaks in the spectrum would be expected near 2.9 MeV and 3.2 MeV for the 125 keV case shown in Figure 6-27. Since these additional peaks were not observed, the majority of the fusion must have originated from inside the cathode. The point of origin of the fusion protons observed by the FIDO diagnostic can be further estimated by the angular dependence of the Doppler shift shown in eqn 4-20. Fusion that would have occurred by stray ions would not have a well defined angle between their trajectory and the detector, whereas the ions in the beams did have that relationship. If the majority of fusion was from particles not in the ion beams, the random angle between their trajectories and the detector would have caused more spreading in the energy spectrum than was observed. Therefore, the majority of the fusion protons observed by the FIDO diagnostic must have originated from particles that were within the beams produced by the ion gun modules.

The total fusion from beam-background interactions within the ion beams can be estimated with the assumption that the protons observed by the FIDO diagnostic were from ions contained within the beams reacting with the background gas. The FIDO diagnostic could detect protons from 9.5 mm of each beam's 289 mm path between the two opposing extraction electrodes; this was 3.3% of the total path. Note that this analysis did not include the volume inside the ion sources, and assumed that the pressure between the extraction apertures is uniform. This estimate also assumed the ions were at the same energy over the entire path length; this is not true, but allowed for an upper bound of beam-background fusion rate to be determined. Based on these assumptions, Figure 6-28 shows the estimated

upper bound of the percentage of fusion reactions from the ion beams interacting with the background gas in the main vacuum chamber. The estimates ranged from 1% to 7%.

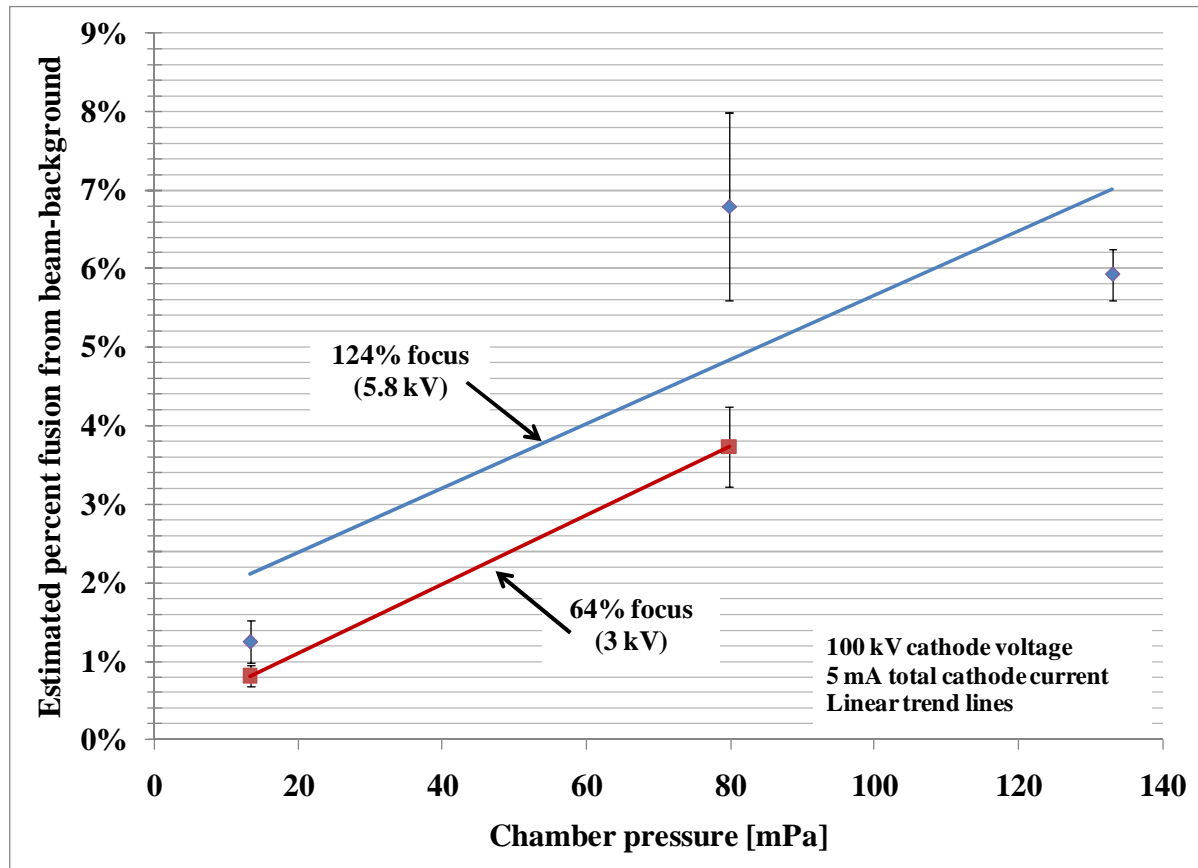


Figure 6-28: Estimated upper bound of the percentage of the total D-D fusion reactions that originated from reactions between the primary ion beams and the background gas in the main vacuum chamber.

The energy of the ions was estimated to be near the full energy of the cathode potential. This estimate was made by comparing the width of the experimental proton energy spectra to the spectrum predicted for Doppler shifted protons, and by comparing the experimental spectra at different chamber pressures. As the pressure increased the width of the spectra shown in Figure 6-18 did not noticeably increase. The lower bound of a noticeable shift in ion energy is 30 keV since a cathode voltage change from -100 kV to -70 kV was noticeable in Figure 6-16. Therefore for a -100 kV cathode voltage, the ion energy at the point of the fusion reaction was at least 70 keV and was likely higher.

Additionally, the larger peaks on both sides of the spectrum shown in Figure 6-27 are approximately twice as wide as the predicted  $D_2^+$  peak. However, the direction of the spreading appeared to be toward higher energy, not lower as would be expected from interactions with the background gas. The accuracy of these estimates was limited by the low number of counts in each energy bin and the energy calibration of the detection system.

With the exception of the center of the cathode, the fusion rates from localized regions in the SIGFE device were not directly measured. Therefore, the point of origin and reaction mechanism of the fusion reactions that were not from primary beam ions reacting with the background gas (93% to 99%) had to be inferred from the relationship between the fusion rate and the various parameters of the device. The most likely mechanisms for the fusion reactions in the SIGFE are:

- 1) Embedded fusion in the outside surfaces of the cathode lenses
- 2) Embedded fusion in the inside surfaces of the cathode lenses
- 3) Embedded fusion on both sides of the extraction lenses
- 4) Beam background fusion in the ion source region
- 5) Beam background fusion in the main chamber region (discussed previously)

In the hypothesis of embedded fusion in the lenses, the ions strike the metal electrode and become implanted. Over time the implanted concentration of reactants becomes high enough that subsequent ions strikes at the same location can fuse with the previously implanted reactants. The concentration of the reactants in the electrode surfaces would be dependent on the run time and the temperature of the lenses. [5] At the beginning of a run, the lenses would be cool and the desorption rate would be less than the ion flux; this would result in an increasing concentration of reactants in the surface. Above a certain temperature,

the desorption rate would become greater than the ion flux, and the concentration of reactants would decrease. The amount of fusion from this mechanism would be directly dependent on the concentration of the reactants in the lenses. This hypothesis is consistent with the time dependence of the neutron rate shown in Figure 6-10.

As the ions strike the metallic lenses, secondary electrons are ejected from the surface. The number of secondary electrons ejected, called the secondary electron coefficient, is highly dependent on several factors that include: angle of incidence, ion energy, surface condition, and material. [6] Previous work in the UW IEC laboratory has estimated the secondary electron coefficient to be between 2 and 3 for IEC relevant conditions. [4]

Secondary electrons generated when ions struck the outside surfaces of the cathode lenses were accelerated to ground, and were measured as part of the total cathode current. Secondary electrons liberated from the inside surface of the cathode were shielded from the external electric field. The electrons from inside the cathode were much less likely to be lost from the cathode region and contribute to the total cathode current. The effect of controlling the secondary electrons from inside the cathode is seen in Figure 6-12. The electron shields reduced the magnitude of the electric field that penetrated the seams in the cathode lenses; therefore less electrons were accelerated to ground for the same ion current. The data taken with the electron shields had a factor of two higher neutron rate than the data without the shields for the same total cathode current. It is estimated that a beam of ions focused to strike the inside the cathode lenses would produce approximately a factor of the secondary electron coefficient (2 to 3 times) more neutrons for the same total cathode current as an ion beam that was focused at the outside surface of the cathode.

Figure 6-29 compares the experimental scans of the focus voltage to the simulations described in section 4.1.2 and shown in Table 4-1 and Figure 6-30. Table 6-1 summarizes the characteristics of the ions that struck at various locations in the SIGFE device. The simulations predicted a minimum in the number of ions that would strike the cathode lenses as the focus voltage was varied over its experimental range. The similarities between the simulated cathode strikes and the neutron rate relationships with focus voltage further supports the hypothesis that the majority of the fusion reactions were from ions embedded in the surfaces of the cathode lenses.

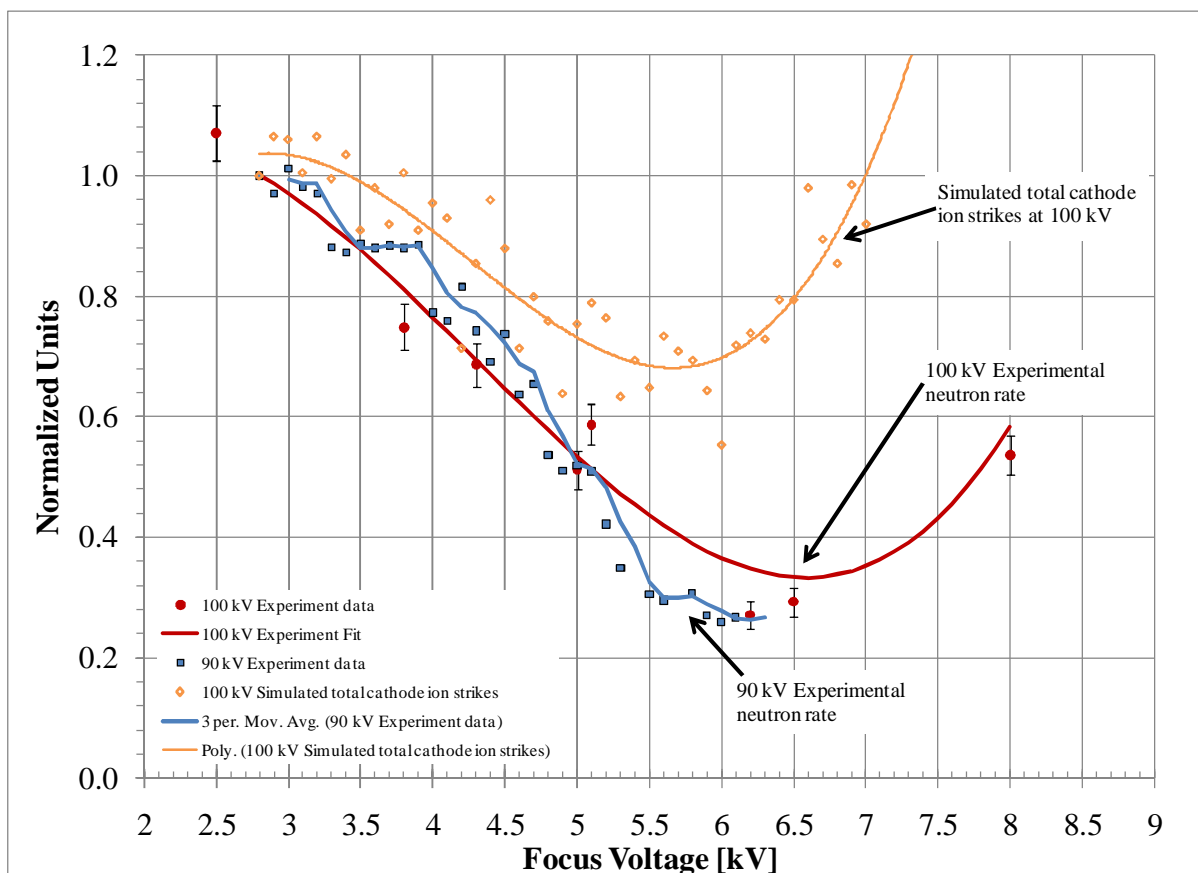


Figure 6-29: Comparison of experimental D-D neutron production rates at cathode voltages of -90 kV and -100 kV to the number of particles that strike all areas of the cathode lenses as predicted by the ion trajectory simulations

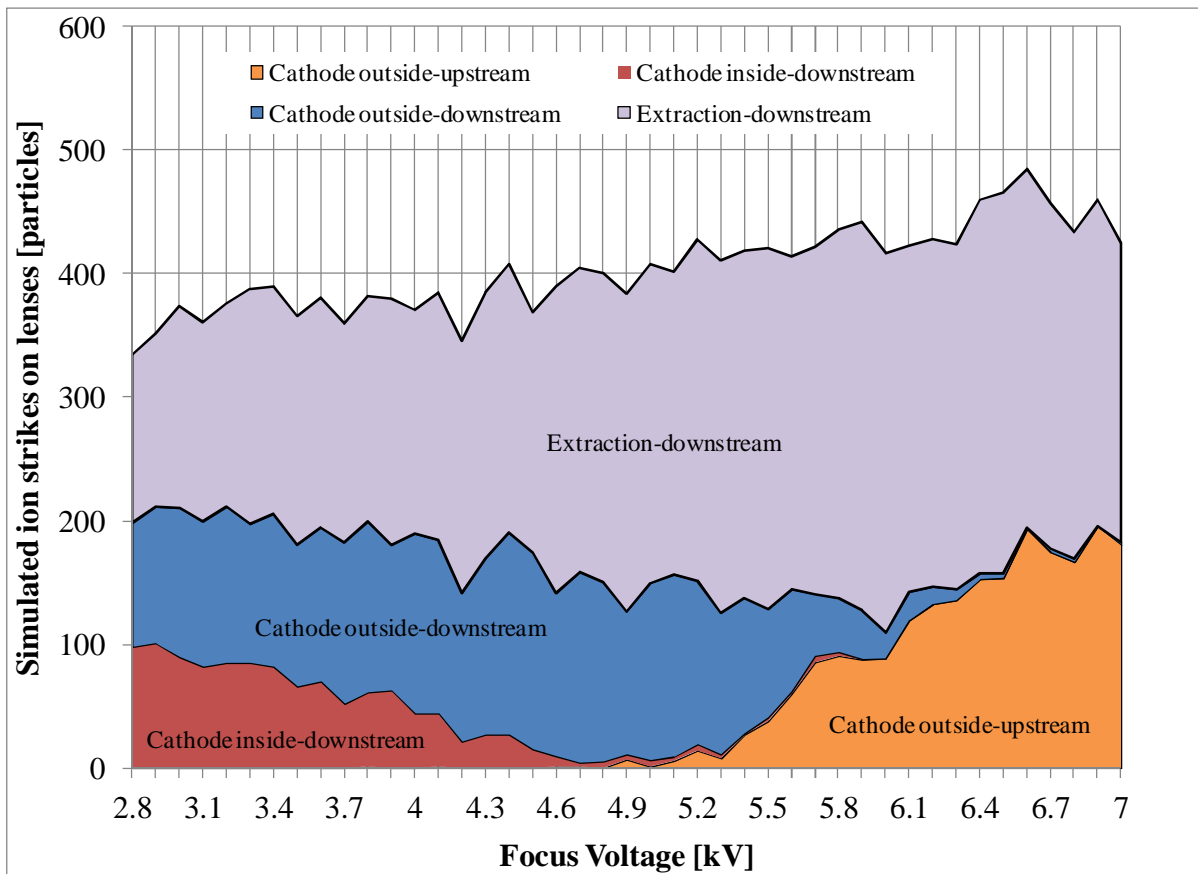


Figure 6-30: Graph of ion trajectory simulation results showing the relative number of particles that were predicted to strike the different lens surfaces defined in Table 4-1.

Table 6-1: Typical ion energy, fusion cross-section, and contribution to total cathode current for ions that struck various locations inside the SIGFE device. The locations are defined in Table 4-1.

Ion strike point	Typical ion energy [keV]	Fusion cross-section for $D_2^+$ on D [mb]	Total cathode current contribution, ion and electrons
Extraction-downstream	10	$5.59 \times 10^{-4}$	0
Cathode outside-downstream	100	8.42	~3 to 4
Cathode inside-downstream	100	8.42	~1
Cathode outside-upstream	100	8.42	~3 to 4

Embedded fusion reactions in the extraction electrode and in the high gas pressure region of the ion sources were also considered as possible sources of fusion. The voltage of the extraction electrode was typically set to -10 kV. Ions assumed to exit the 1.8 mm aperture in the extraction electrode with approximately 10 keV of energy. If the ions did not strike the cathode lenses or scatter on the background gas they would pass through the

cathode lenses, be decelerated, and strike the opposing ion gun module's extraction electrode or reenter the ion source region. In both cases, the ions would have the same energy they left the ion source with. The ion current that struck the extraction electrode or reentered the ion source may have been as high as 5 mA in each ion gun module, or 30 mA total, for a 10 mA total cathode current. This estimate was based on the measured current to extraction electrodes with cathode voltages set to 0, and the ion current that was predicted in Figure 4-8 to completely pass through the cathode lenses. Even though the ion current to the extraction lenses and ion sources was approximately a factor of 3 higher than the cathode current, the D-D fusion cross-section for a  $D_2^+$  at 10 keV is more than a factor of  $10^4$  less than at 100 keV. [3] This small difference in ion current and large difference in fusion cross-section makes it unlikely that reactions in the ion sources or embedded in the extraction electrodes were a significant source of fusion.

The extraction voltage was varied between -6 to -10 kV to experimentally prove that the embedded ions in the extraction electrode and that ions reentering the ion sources were not significant sources of fusion. The neutron rate did not significantly change with the extraction voltage. The cross-section of  $D_2^+$  ions on stationary D targets is  $6.2 \times 10^{-6}$  mb at 6 keV and  $5.59 \times 10^{-4}$  mb at 10 keV. [3] If the extraction electrodes and the ion source regions were significant sources of fusion, the neutron rate should have changed as the fusion cross-section changed by two orders of magnitude.

The drop in neutron rate as the ion beams became misaligned seen in Figure 6-11 may have suggested an interaction between the multiple beams. However, an alternate explanation may be that the misaligned beams caused more of the ions to hit the outside of the cathode; these ions would have otherwise hit the inside of the cathode. The difference in secondary electron current between the aligned and misaligned cases would have to have

been more than a factor of two to explain the approximate factor of two drop in neutron rate.

The misaligned ions would have struck the inside diameter of the beam ports on the cathode lenses at a shallow angle. The secondary electron coefficient increases as the incident angle changes from perpendicular to parallel. [6] Due to the shallow angle of incidence, the effect of secondary electrons in the misaligned case may have been enough to explain the drop in neutron rates; however that cannot be definitely determined with the data available.

The majority of the D-D fusion reactions were not occurring in the center of the device and therefore the formation of potential well structures proposed by Hirsch [7] was probably not the dominant mechanism by which the fusion reactions occurred in the SIGFE device within the parameter space explored for this dissertation. Table 6-2 summarizes the contribution to the total fusion rate of several possible mechanisms of fusion reactions as inferred in this discussion section. Based on the indirect experimental data, ions embedded in the cathode lenses are likely the dominant fusion mechanism in the SIGFE.

Table 6-2: Summary of the estimated percentage of fusion reactions from possible mechanisms of fusion reactions in the SIGFE device

Possible source of fusion reaction	Typical ion energy [keV]	Fusion cross-section for $D_2^+$ on D [mb]	Estimated percentage of total fusion reactions
Embedded in cathode lenses	100	8.42	90 to 99%
Embedded in extraction lenses	10	$5.59 \times 10^{-4}$	< 1%
Beam-background in ion source	< 10	$< 5.59 \times 10^{-4}$	< 1%
Beam-background in main chamber	100	8.42	1 to 7%
Beam-beam fusion	100 + 100	37	< 1%
Virtual potential well formation	NA	NA	< 1%

### 6.3.2. Comments on the $D-^3He$ fusion rate

The  $D-^3He$  proton results showed similar scaling with voltage and pressure as the D-D proton data. Therefore the discussion of the characteristics of the D-D protons also

applies to the D-<sup>3</sup>He protons observed, which were also only from the center of the cathode. As with the D-D protons, the D-<sup>3</sup>He proton production rate observed in the limited view of the detector was likely only a small percentage (less than 7%) of the total D-<sup>3</sup>He fusion that occurred in the device.

### *6.3.3. Scaling of D-D neutron rate with pressure and ion beam focus*

The exact cause of the different scaling of the neutron rate with pressure at different focus settings of the ion beams shown in Figure 6-3 could not be definitely determined in this dissertation. It was especially difficult to explain was the increased neutron rate with decreased pressure of the 70% focus case. However, the 70% case was similar to the results reported by Hirsch in 1967. [7]

In a 1982 paper, Baxter [8] attempted to explain the Hirsch pressure scaling results by arguing that the energy spectrum of the ions approached the full cathode energy as the pressure decreased. This increase in ion energy along with the higher D-D fusion cross-section may have caused the increased in the neutron rate. Baxter's analysis was based on the fusion of the ions with background gas, which was shown in the previous section to be less than 7% of the fusion rate in the SIGFE device.

The idea that the ion energy spectrum was softened as the pressure increased can be extended to embedded fusion in the surface of the cathode. From section 6.3.1, the energy spectrum of the ions at pressures from 13 mPa to 150 mPa was estimated to be at most 30 keV less than the full energy given by the cathode voltage. The difference in the D<sub>2</sub><sup>+</sup> on D<sup>0</sup> cross-section is 15% between 100 keV (full cathode energy) and 70 keV (minimum ion energy estimate) ions. However, the difference in neutron rates between 150 mPa and 13 mPa was 35%. The slowing down of the ion in the metal of the electrode was not accounted for in this simple analysis.

Also, the argument that the ion energy spectrum changes with the chamber pressure does not explain why the scaling of the neutron rate with pressure changed as the focus percentage was changed from 70% to 100%. If the energy spectrum was significantly changing, the change should have been the same at all focus settings.

Another explanation of the pressure scaling could be that the effect of the self-neutralization of the ion beams was changing with the pressure. As the ions pass through the background gas they ionize a portion of the gas and the freed electrons could be picked up by the ions and counteract the space charge spreading of the beams. As the pressure was increased the number of electrons picked up by the beams would have increased and the divergence of the beams would be less. In the less diverged beams, fewer ions would have struck the cathode lenses and therefore less fusion would have occurred. The number of ions that struck the cathode lenses would depend on both the focus lens settings and the pressure in the chamber.

The data presented in Figure 6-29 may indicate the effect of self-neutralization of the ion beams. The minimum number of particles predicted to strike the cathode is at a focus voltage of -5.7 kV, whereas the experimental data showed a minimum neutron rate near -6.6 kV. The difference between the simulations and the experimental results could be the result of space charge spreading of the ion beams.

The cause of the neutron rate scaling with pressure could not be definitely determined with experimental data available in this dissertation. It is this author's belief that the effect of the chamber pressure on the ion energy spectrum is not a major cause of the data observed. The hypothesis of the space-charge neutralization of the beam is plausible, but was not proven with the data available.

### 6.3.4. Comparison of the SIGFE to the Hirsch experiment

In the defocused (0 kV and 70% focus) cases, the SIGFE device was able to reproduce the total neutron rate, the relative neutron rate scaling, and the neutron rate scaling with pressure that were reported by Hirsch. [7] Figure 6-31 is a comparison of the total D-D neutron rate of the defocused SIGFE device to the Hirsch device at various pressures. At Hirsch's lowest pressure, 13 mPa, the SIGFE neutron rate and the scaling of the relative neutron rates (seen in Figure 6-32) was identical to the Hirsch results. At 150 mPa, both the absolute neutron rate and the relative scaling of the SIGFE neutron rate were 35% higher than that of the Hirsch device at -110 kV.

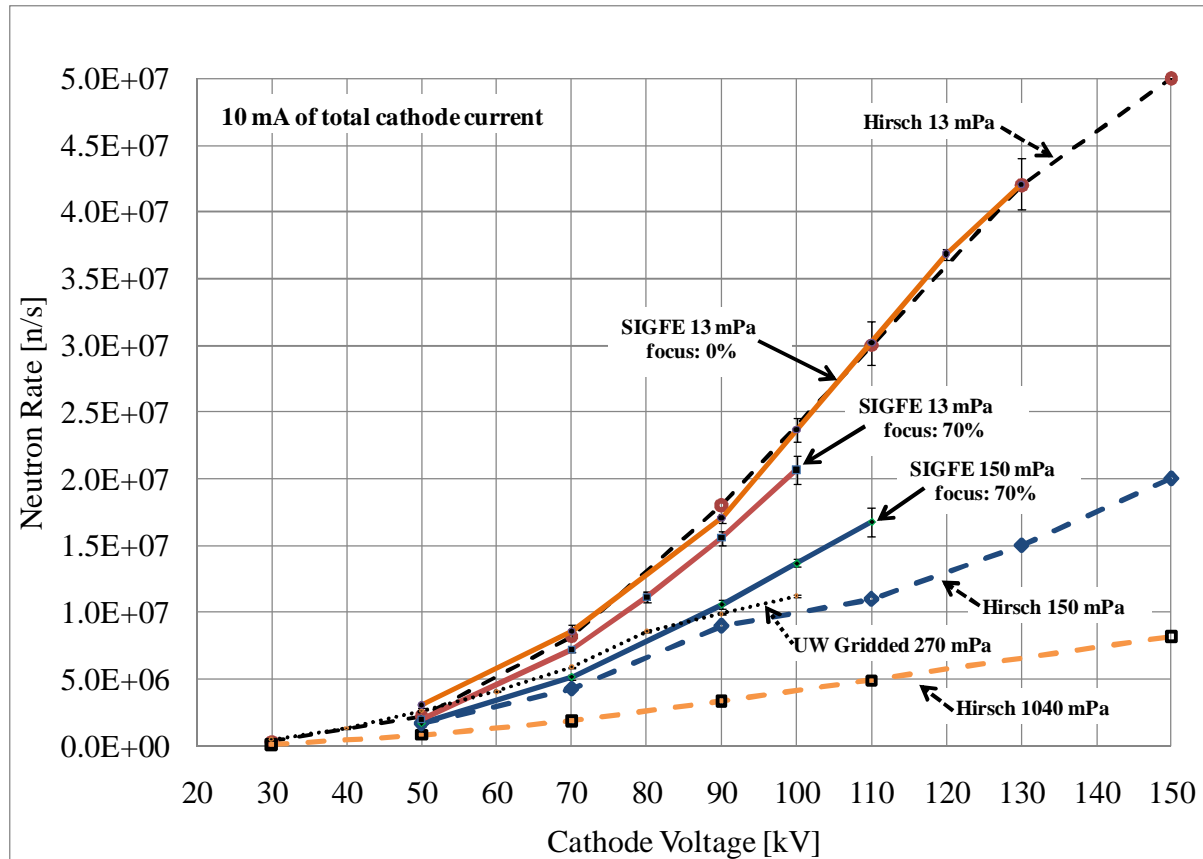


Figure 6-31: Experimental D-D neutron production rate versus cathode voltage at various pressures for comparison of the SIGFE, the Hirsch device, and the UW gridded IEC device. All data was taken at a total cathode current (including ion and electron current) of 10 mA.

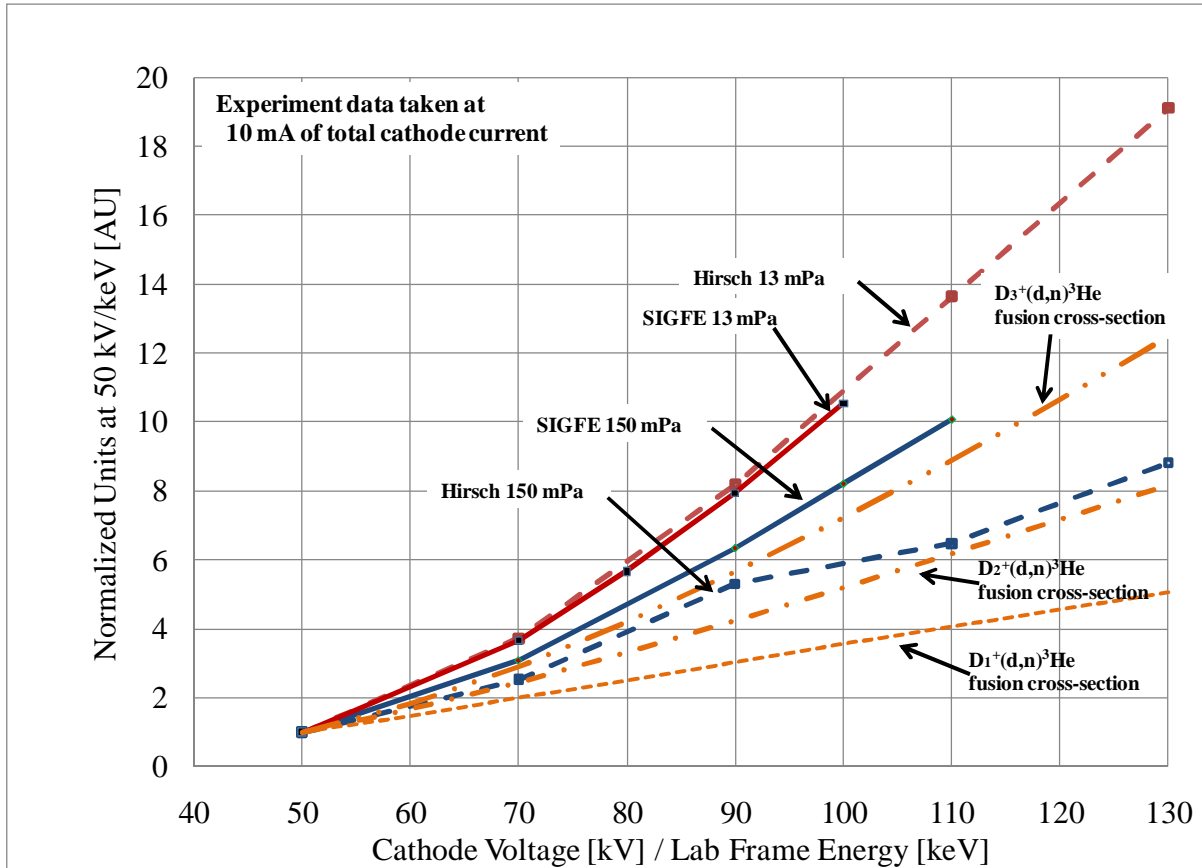


Figure 6-32: Normalized D-D neutron production and D-D fusion cross-sections for comparison of voltage scaling. Values normalized to 1 at a cathode voltage of -50 kV or a lab frame ion energy of 50 keV. The SIGFE data was taken at 70% focus. [3, 7]

The neutron rate scaling with pressure for the SIGFE, the Hirsch device and the UW-gridded IEC are shown Figure 6-33. At 70% focus, the SIGFE exhibited an increase in neutron rates with decreasing chamber pressure similar to the results reported by Hirsch. [7] The scaling of the neutron rate with pressure in the SIGFE was dependent on the focusing of the ion beams. The Hirsch device did not have independent control of the focus of the ion beams; therefore a comparison at different focus voltages was not possible.

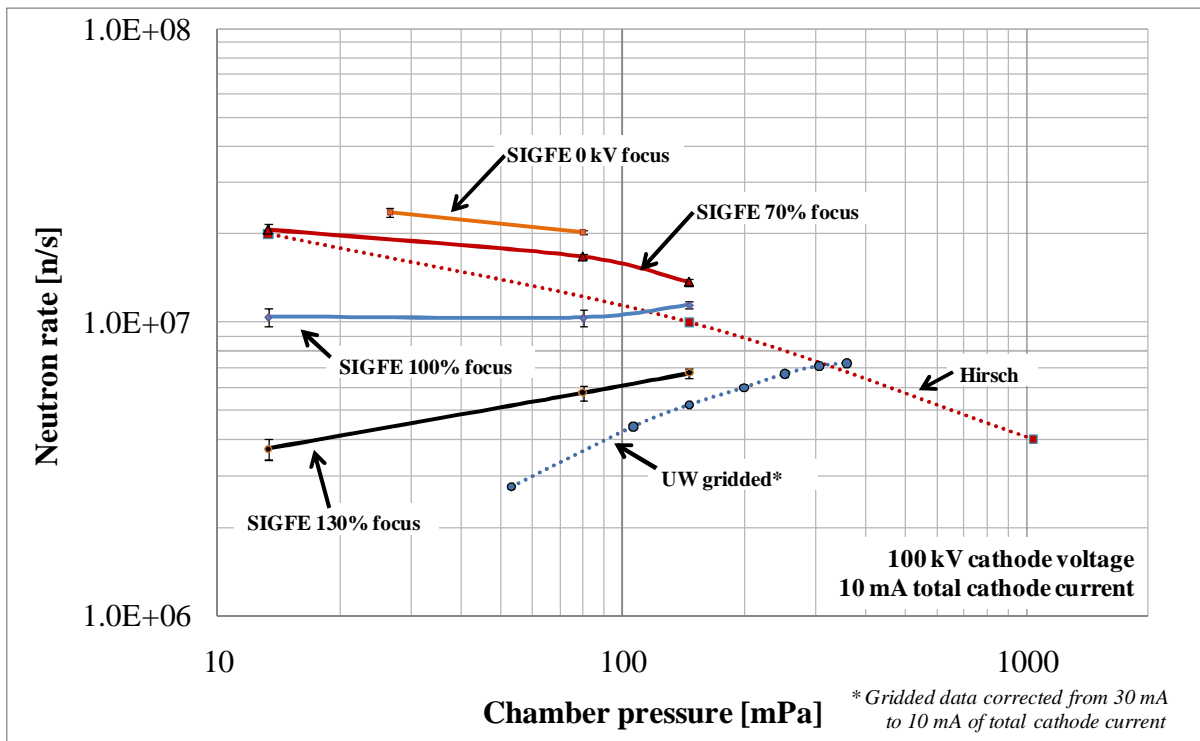
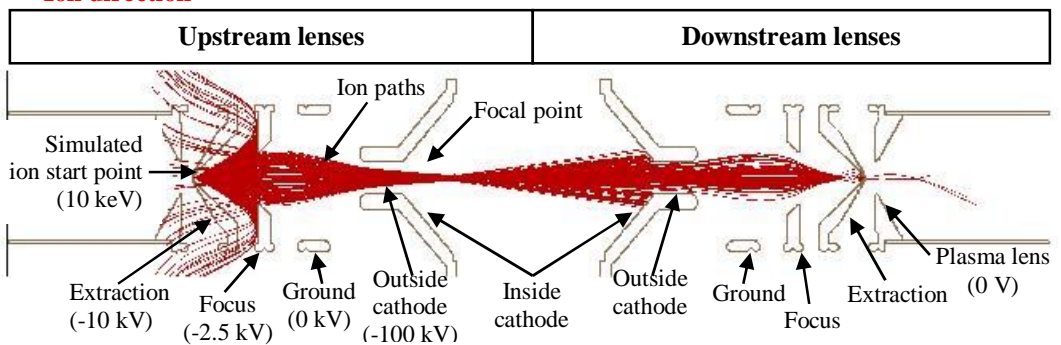
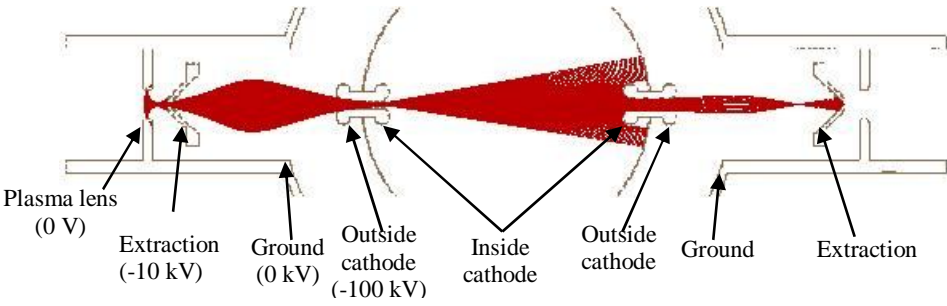


Figure 6-33: Comparison of D-D neutron production rate versus pressures for the SIGFE, the Hirsch device, and the UW gridded IEC device. The UW gridded data was linearly scaled down to 10 mA from 30 mA of total cathode current. The Hirsch data was interpolated to -100 kV from the data shown in Figure 6-31.

The simulations described in section 4.1.2 predicted the ion trajectories in both the SIGFE device at 70% and the Hirsch device were similar. Table 6-3 compares the visual results of the SIMION® study. A large amount of the ions are predicted to impact the inside surface of the cathode in both cases. The cathodes of both the SIGFE device and the Hirsch device were designed to prevent secondary electrons from leaving the cathode region and being accelerated to ground. This feature on both devices likely contributed to their high efficiency in terms of neutron rate per kilowatt of high voltage power.

Table 6-3: Visual comparison of the simulated ion trajectory of the SIGFE device at 70% focus to the Hirsch device. Simulation performed in SIMION® [9]

Ion trajectory simulations Cathode voltage 100 kV, Extraction voltage 10 kV		Focus percent / voltage
 <p><b>Ion direction</b> →</p> <p><b>Upstream lenses</b></p> <p><b>Downstream lenses</b></p> <p>Simulated ion start point (10 keV)</p> <p>Extraction (-10 kV)</p> <p>Focus (-2.5 kV)</p> <p>Ground (0 kV)</p> <p>Outside cathode (-100 kV)</p> <p>Inside cathode</p> <p>Focal point</p> <p>Outside cathode</p> <p>Ground</p> <p>Focus</p> <p>Extraction (0 V)</p> <p>Plasma lens</p>		70% 3.27 kV
 <p>Plasma lens (0 V)</p> <p>Extraction (-10 kV)</p> <p>Ground (0 kV)</p> <p>Outside cathode (-100 kV)</p> <p>Inside cathode</p> <p>Outside cathode</p> <p>Ground</p> <p>Extraction</p>		Hirsch device No focus lens

The Hirsch device and the SIGFE device are the two highest efficiency IEC devices published to date. Figure 6-34 compares the neutron rate per kilowatt of high voltage input power for several of the IEC experiments reported in the literature from around the world. These experiments vastly vary in their design and operating pressures, which made a direct comparison difficult. Hirsch, SIGFE, and Gardner were the only devices that did not use a wire gridded cathode. In comparison to the best gridded device, reported by Radel-2006 [10], the SIGFE is 50% more efficient. The Radel experiment operated at higher power levels than the SIGFE (-165 kV cathode voltage and 65 mA total cathode current) and produced a neutron rate of  $2.2 \times 10^8$  n/s. Extrapolating the SIGFE neutron rate to the same cathode voltage and total cathode current would predict a neutron rate for the SIGFE of  $3.5 \times 10^8$  n/s.

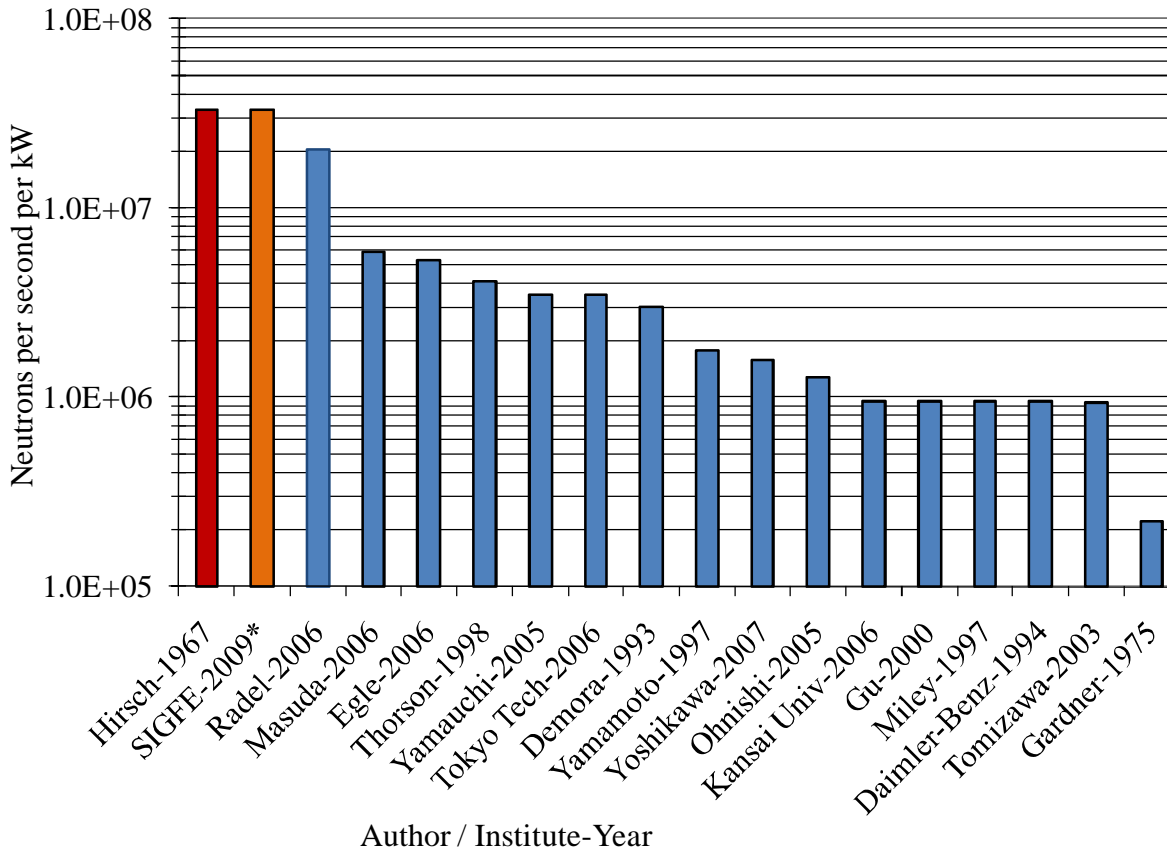


Figure 6-34: Comparison of steady-state D-D fusion neutron rates per kilowatt of high voltage power (meter current times cathode voltage) for various IEC experiments listed by author and year reported. [7, 10-23] \*SIGFE-2009 is the result of this dissertation.

In certain parameter ranges the SIGFE device was able to reproduce the neutron rate and neutron rate scaling results reported by Hirsch in 1967. [7] With these similarities of experimental results it is tempting to draw conclusions between the operation of the Hirsch device and the analysis of the SIGFE results in section 6.3.1. However, this would be speculative since the data used in the SIGFE analysis does not exist for the Hirsch device. Also, the centimeter scale spatial distribution of fusion products at the center of the cathode observed by Hirsch was not measured in the SIGFE device and cannot be explained with the data available.

## 6.4. References for Chapter 6

---

1. *Design-Expert® Version 8*, (2009). Stat-Ease Inc, Minneapolis, MN, [www.statease.com](http://www.statease.com)
2. Boris, D.R. (2009). Novel diagnostic approaches to characterizing the performance of the Wisconsin Inertial Electrostatic Confinement plasma. (PhD dissertation, University of Wisconsin – Madison)
3. Bosch, H. S., & Hale, G. M. (1992). Improved formulas for fusion cross-section and thermal reactivities. *Nuclear Fusion*, 32(4), 611-31.
4. Peifer, G. R. (2006). Performance of a low-pressure, helicon driven IEC  $^3\text{He}$  fusion device. (PhD dissertation, University of Wisconsin – Madison)
5. Yao, Z., Liu, C., & Jung, P. (2005). Diffusion and permeation of deuterium in Eurofer97: effect of irradiation and of implanted helium, *Fusion Science and Technology*, 48, 1285-1291
6. Svensson, B., Holmen, G., & Buren, A., (1981). Angular dependence of the ion-induced secondary-electron yield from solids, *Physics Review B (Condensed Matter)*, 24(7), 3749-3755
7. Hirsch, R. L. (1967). Inertial-electrostatic confinement of ionized fusion gases. *Journal of Applied Physics*, 38(11), 4522-4534.
8. Baxter, D.C., & Stuart, G.W. (1982). The effect of charge exchange on ion guns and an application to inertial electrostatic confinement devices. *Journal of Applied Physics*, 53(7), 4597-4601
9. *SIMION Version 8.0*, (2009). Scientific Instrument Services, Inc, Ringoes, NJ, [www.simion.com](http://www.simion.com)
10. Radel, R. F. (2007). Detection of highly enriched uranium and tungsten surface damage studies using a pulsed inertial electrostatic confinement fusion device. (Doctoral dissertation, University of Wisconsin - Madison).
11. Gardner, A. L., Hatch, D. M., Chan, A. I. Y., & Evans, R. P. (1974). Measurements on a Spherical Electrostatic Confinement System Employing Six Ion Guns. *Annals of the New York Academy of Sciences*, 251, 179-189.
12. University of Wisconsin-IEC Experimental Logbook.
13. Masuda, K. et. al., (2007), Anti-personnel landmine detection by use of an IEC neutron source, Presented at US-Japan IEC workshop 2007, Argonne National Lab
14. Thorson, T.A., Durst, R. D., Fonck, R.J., & Sontag, A.C., (1998). Fusion reactivity characteristics of a spherically convergent ion focus. *Nuclear Fusion*. 38(4), 495-507
15. Yamauchi, K., Tashiro, A., & Shura, S., (2005). Performance characteristics of ion-source-assisted cylindrical IEC fusion neutron/proton source, Presented at US-Japan IEC workshop 2005. Los Alamos National Lab
16. Demora, J. M., (1999). *Cathode grid optimization studies for the spherical IEC device*. (Master's thesis University of Illinois-Urbana)

- 
17. Yamamoto, Y., Hasegawa, M. and Ohnishi, M., (1997). Preliminary studies of potential well measurement in IEC fusion experiment, Presented at IEEE-SOFE 1998.
  18. Yoshikawa, K, Masuda, K, Takamatsu, T, et. al. (2007). Anti-personnel landmine detection by use of an IEC neutron source, presentation at the US-Japan IEC workshop- 2007, Argonne National Lab
  19. Ohnishi, M. Osawa, H. Tabata, T. & Yoshimura, S. (2005). Neutron yield in IEC fusion, presentation at the US-Japan IEC workshop-2005, Los Alamos National Lab
  20. Gu, Y., & Miley, G.H., (2000). Experimental study of potential structure in a spherical IEC fusion device, *IEEE Trans on Plasma Science*. 28(1) 331-346
  21. Miley, G. (1997). The IEC approach to fusion power, Current Trends in International Fusion Research edited by Panarella, *Plenum Press*, New York, NY
  22. Daimler-Benz Aerospace, (1994). Preliminary announcement: Fusion Star IEC-PS1, Bremen Germany
  23. Tomizawa, T., Higashi, T. Daino, M. & Yamamoto, Y., (2003). Characteristics of the cylindrical IECF experiments of low gas pressure operation, Presented at US-Japan IEC workshop-2003. Tokyo Institute of Technology.

## Chapter 7. Design and simulation for the production of radioisotopes from a D-<sup>3</sup>He fusion device

### 7.1. Radioisotope activity, cross-sections, and gas target design considerations

The initial goal of this dissertation was to show a path to the commercial production of the radioisotope <sup>11</sup>C using an IEC device. Based on the simulation work presented in this chapter, it was determined that the D-<sup>3</sup>He fusion rate in IEC devices needed to be increased by several orders of magnitude to be commercially viable. The SIGFE device became the main topic of this dissertation in order to explore a possible method of increasing the fusion rate required for this application.

Carbon-11 is produced from the <sup>14</sup>N(p,  $\alpha$ )<sup>11</sup>C reaction and has a 20.4 minute half-life. An activity of 2 to 10 mCi is required at the patient, and is normally administered in the form of carbon dioxide, hydrogen cyanide, or methane. [1] The activity, A(t), is a function of the production rate, R, and the decay constant,  $\lambda$ . For the purpose of this model the production rate was assumed to be, R=M S, where S was the known source rate of protons given in units of protons per second. The multiplication factor, M, was the number of radioactive nuclei produced for each source proton. The activity during irradiation as a function of time can be written as

$$A(t) = (M \cdot S)(1 - e^{-\lambda t}). \quad \text{Eqn 7-1}$$

At irradiation times greater than approximately six half-lives, the activity saturates to

$$A_{Max} = M \cdot S. \quad \text{Eqn 7-2}$$

The production of isotopes by leveraging D-<sup>3</sup>He fusion reactions is a multi-stage process and is summarized in Figure 7-1. D and <sup>3</sup>He gases are ionized and accelerated by an electrostatic field to energies where the <sup>3</sup>He(d, p)<sup>4</sup>He fusion reaction can occur. The fusion produced protons are collected by an array of nitrogen filled gas targets. The pressurized

nitrogen gas is separated from the low pressure D- $^3$ He environment by a thin metal foil. This foil attenuated the fusion protons, thus reducing the energy available for the  $^{14}\text{N}(\text{p}, \alpha)^{11}\text{C}$  reaction. The cross-section for the  $^{14}\text{N}(\text{p}, \alpha)^{11}\text{C}$  reaction is shown in Figure 7-2.

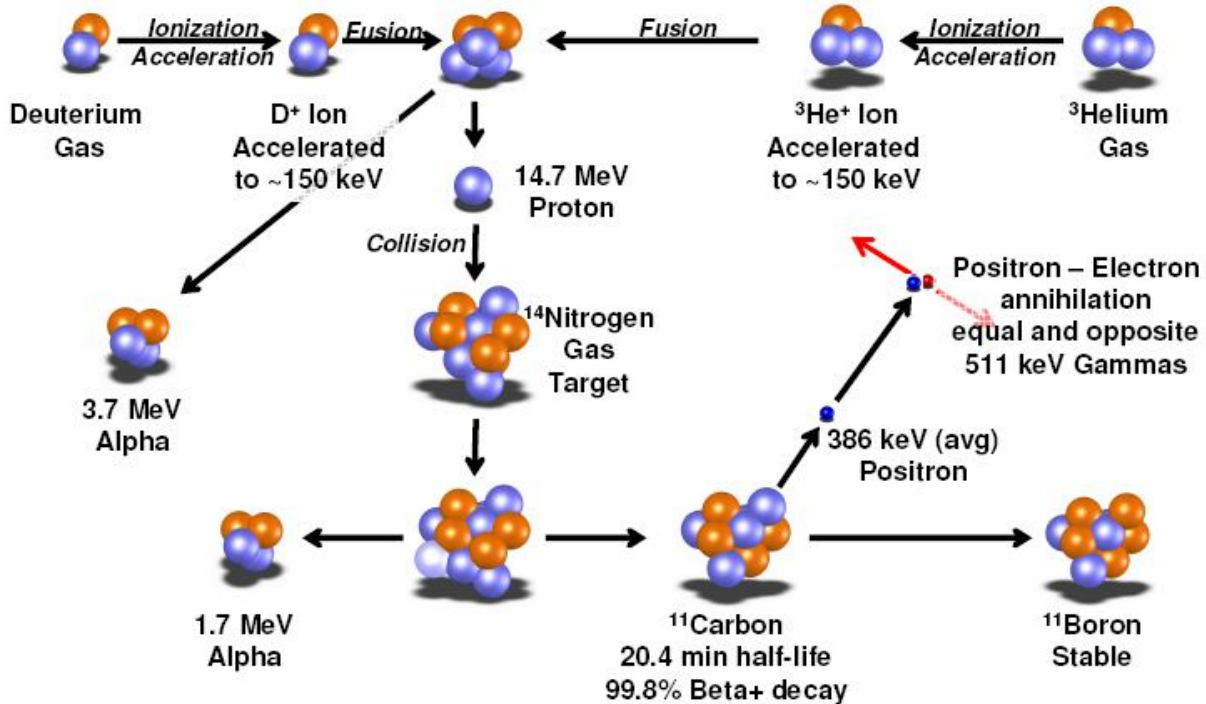


Figure 7-1: Summary of the multi-stage process for the production of  $^{11}\text{C}$  using the  $\text{D}-^3\text{He}$  fusion reaction.

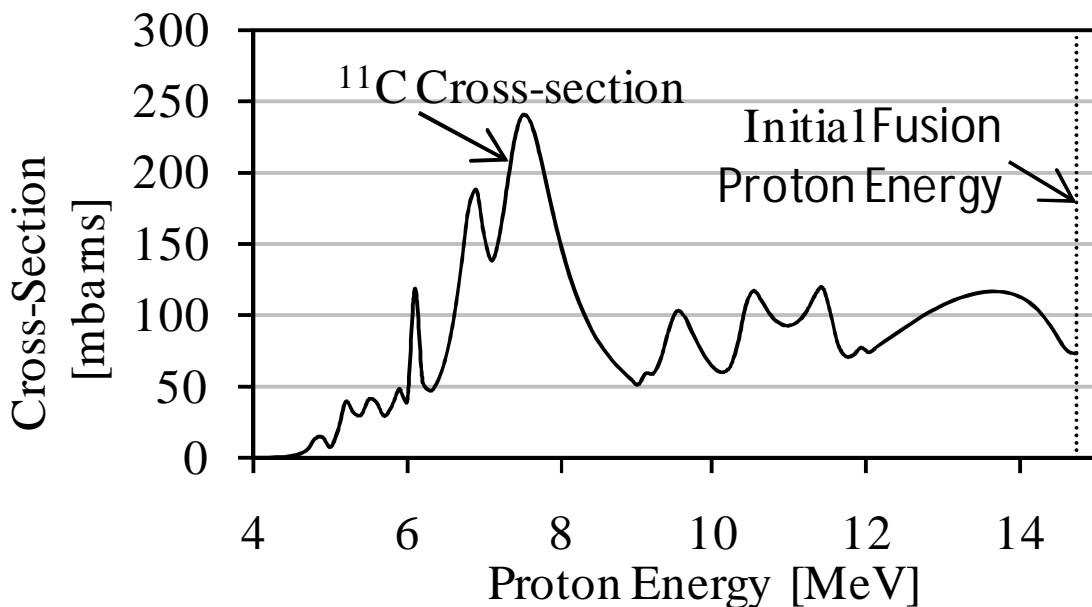


Figure 7-2: Cross-section of the  $^{14}\text{N}(\text{p}, \alpha)^{11}\text{C}$  reaction

## 7.2. Gas target design

The isotope production system was designed to fit into an existing experimental IEC device, named  $^3\text{HeCTRE}$ , which was encapsulated inside a 46 cm diameter by 46 cm long cylindrical vacuum chamber. [2]  $^3\text{HeCTRE}$  was the predecessor of the SIGFE. It was a gridded IEC device built in the same vacuum chamber that was eventually used for the SIGFE device. For a baseline study, the following models and simulations are based on design constraints of this vacuum chamber and gridded IEC device. Future work need not be limited by these dimensions.

The modeled isotope production system consisted of six gas targets equally spaced around the IEC device as shown in Figure 7-3 A and B. The gas targets were vacuum sealed rectangular boxes with inside dimensions of 8.5 cm by 39 cm by 7.75 cm deep. The side of the box that faced the proton source consisted of a thin titanium foil mechanically supported by a stainless steel grid on both sides. Figure 7-3 C shows a cutaway view of a gas target.

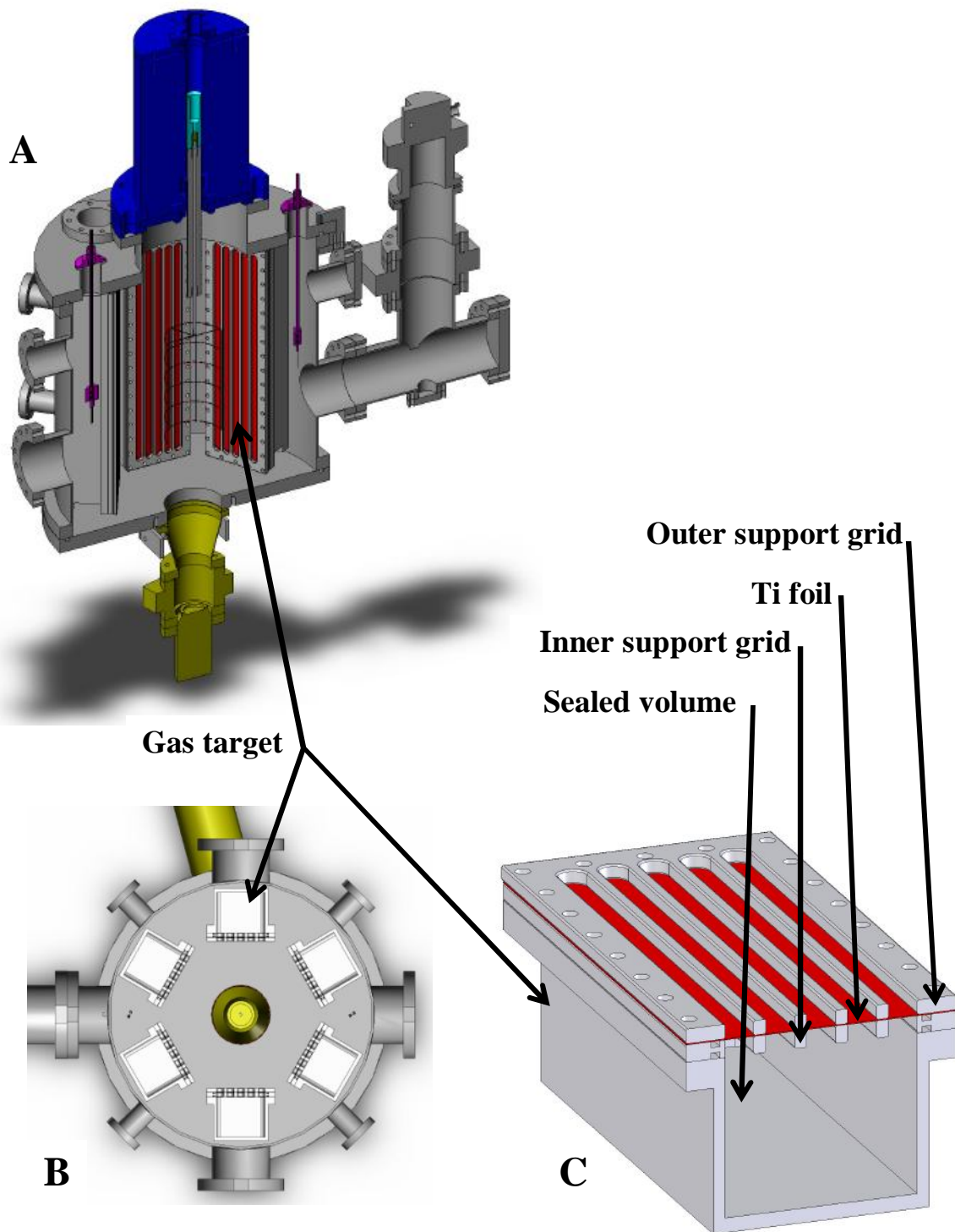


Figure 7-3: A) Cutaway view of the  ${}^3\text{He}$ CTRE IEC device with gas targets installed. B) Cross-section view of the IEC from the top. C) Cutaway view of the gas target

### 7.3. Monte Carlo simulations

#### 7.3.1. Model geometry, materials, and parameters

The Monte Carlo charged particle transport code MCNPX 2.5.0 [3] was used to determine the multiplication factor (M) needed to predict the activity of  $^{11}\text{C}$ . The gas targets were simplified to rectangular cells filled with gas and a thin foil of titanium on their front. The stainless steel support grids seen in Figure 7-2 C were not included in the MCNPX model. From the SolidWorks<sup>®</sup> model and the thickness of the grids, it was calculated that they block 50 percent of the incident protons; this was accounted for in the later activity calculations.

In MCNPX, a surface current tally, F11, was used to determine the solid angle subtended by the gas targets. Two more surface current tallies, F21 and F31, were placed after the foil and after the foil and gas to determine the proton energy spectra entering and exiting the gas cell. The energy spectrum was determined to a resolution of 0.5 MeV over the range of 4 MeV to 15 MeV using energy segmenting on the last two tallies. The tally of most interest was the F4 cell fluence tally that was used to calculate the  $^{14}\text{N}(\text{p}, \alpha)^{11}\text{C}$  reactions that occurred in the gas. The result of this tally is the multiplication factor, M, used in Eqn 7-1 and 7-2 for activity calculations. The tally locations are shown in Figure 7-4.

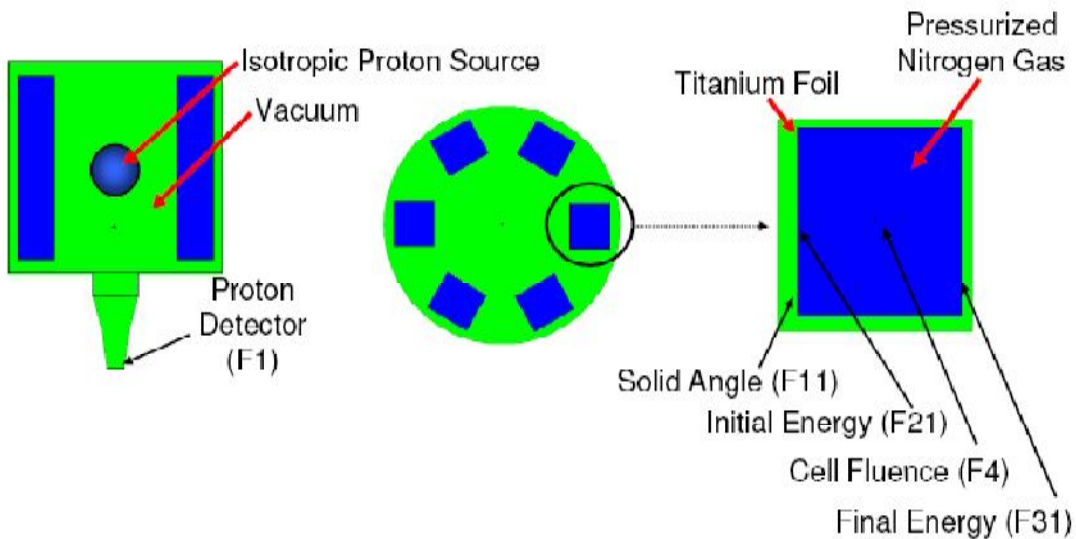


Figure 7-4: Simplified geometry for simulations showing tally locations

### 7.3.2. Results of the baseline (4 atm, 0.5 mm) design

A titanium foil thickness of 0.5 mm and a gas pressure of 4 atm was the baseline design. The simulation determined the multiplication factor to be  $7.40 \times 10^{-5}$  reactions per source proton. The highest D-<sup>3</sup>He fusion rate achieved in the IEC device being modeled was  $2 \times 10^7$  p/s. [2] This would result in a maximum activity of 10 nCi for the baseline case. To achieve an activation of 1 mCi, a D-<sup>3</sup>He fusion rate of  $1 \times 10^{12}$  p/s would be required.

The three surface current tallies, F11, F21, and F31, diagnosed how efficiently the fusion protons were utilized by the target design. The model predicted 52% of the source protons reached the face of the targets, 47% reached the gas, and 27% exited the gas cell. Figure 7-4 compares the energy spectrum of the protons entering and exiting the gas with the cross-section of the <sup>14</sup>N(p,  $\alpha$ )<sup>11</sup>C reaction. The peak of the entering spectrum was at 8.75 MeV, which was above the major peak in the cross-section. The protons were slowed down in the gas, which resulted in a reduced peak energy of 7.25 MeV by the time they exited the nitrogen gas.

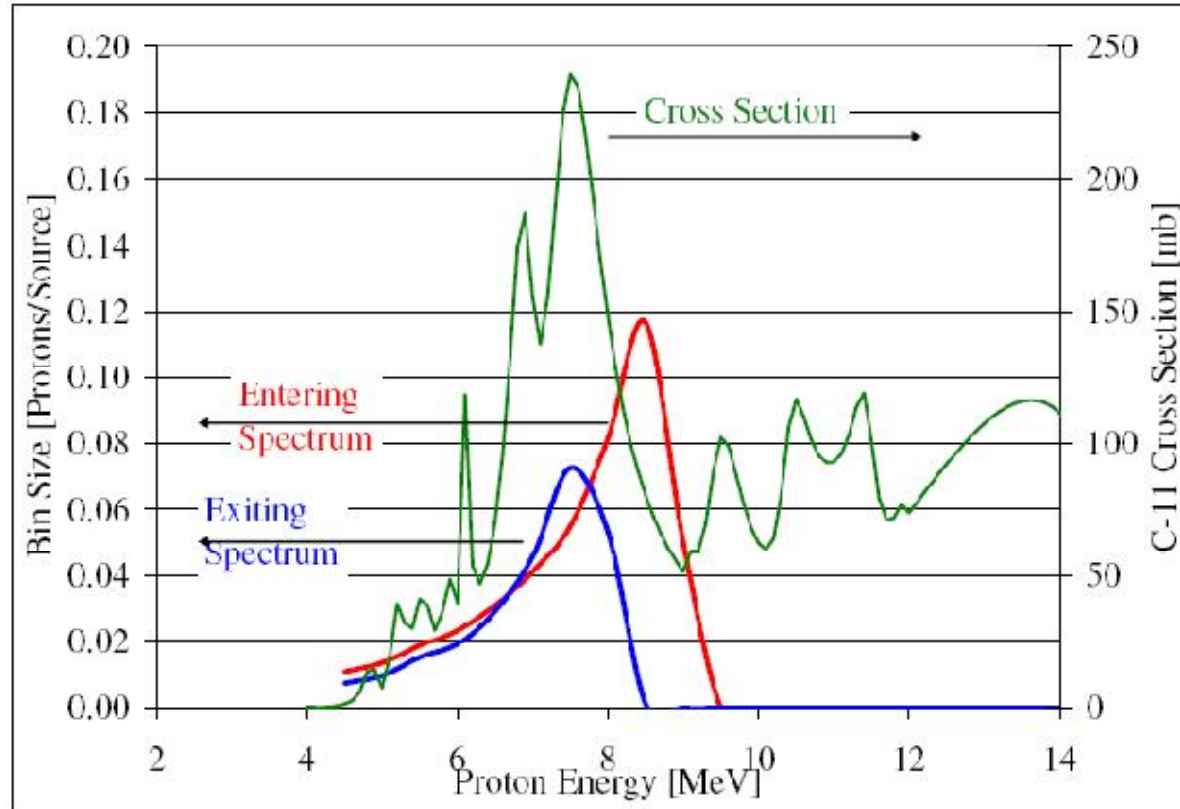


Figure 7-5: Comparison of proton spectrum entering the gas (after Ti foil) and exiting the gas (after Ti and gas) for 0.5 mm Ti foil and 4 atm of pure  $^{14}\text{N}$  gas with the  $^{14}\text{N}(\text{p}, \alpha)^{11}\text{C}$  cross-section.

### 7.3.3. Results of a pressure scan of the target gas pressure

The influence of the gas pressure on the activity of  $^{11}\text{C}$  was studied by varying the gas pressure while the Ti foil thickness and target depth were held constant at 0.5 mm and 77.5 mm respectively. Figure 7-6 shows the effect of pressure on the multiplication factor, M. As expected, M increased with pressure until the majority of the protons were stopped in the gas. At high pressure, above 10 atm, the maximum activity asymptotes to approximately 24 nCi at the present best experimental fusion rates. This is a factor of 2.4 increase over the baseline design. Figure 7-7 compares the peak energy of the exiting spectrum with the cross-section of the reaction.

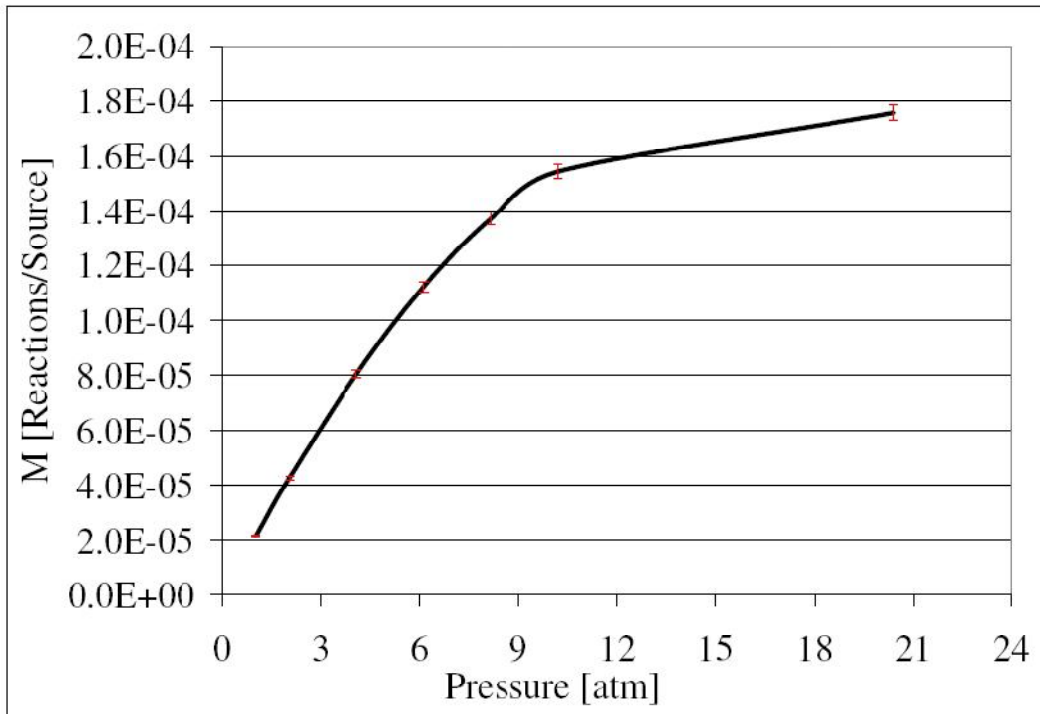


Figure 7-6: Multiplication factor,  $M$ , asymptotes above 10 atm. The Ti foil thickness held constant at 0.5 mm and target depth held at 77.5 mm.

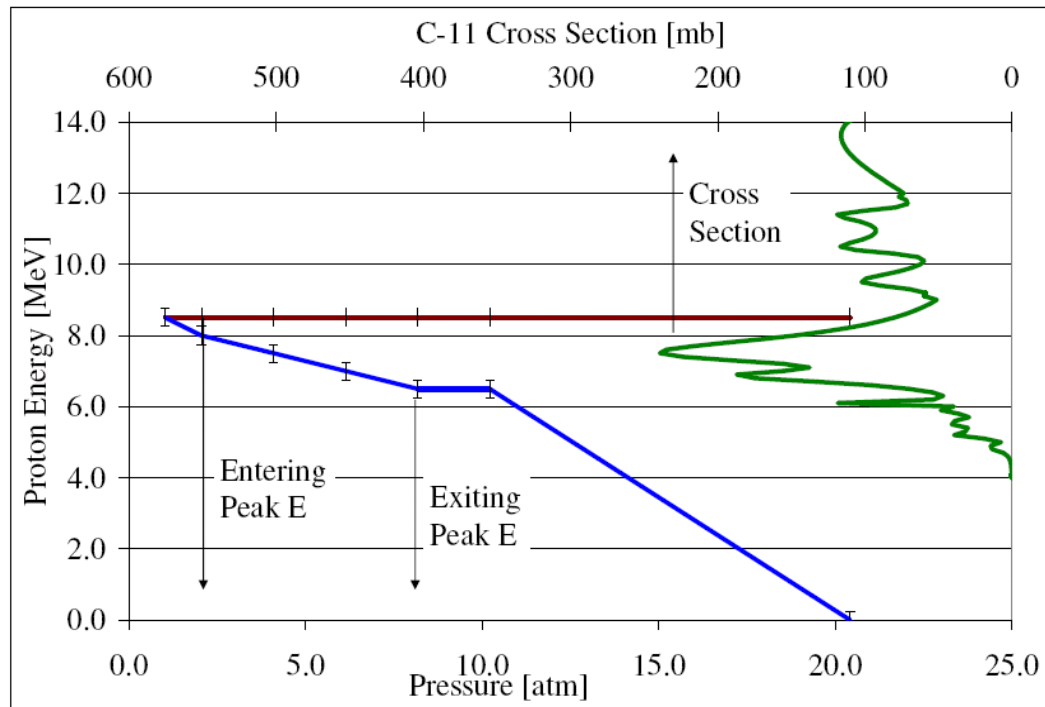


Figure 7-7: Comparison of peak energy entering (after Ti foil) and exiting gas cell (after foil and gas) as a function of gas pressure with the cross-section of the  $^{14}\text{N}(\text{p}, \alpha)^{11}\text{C}$  reaction. Ti foil thickness held constant at 0.5 mm and target depth held at 77.5 mm.

### 7.3.4. Results of titanium foil thickness scan

Different thicknesses of Ti foil were simulated to determine how this affected the maximum activity. The gas pressure and target depth were held constant at 4 atm and 77.5 mm respectively. With a thinner foil the peak energy of the proton spectrum entering the gas increased. Since the gas pressure and cell depth were constant, the average energy of the proton spectrum exiting the gas also increased. The roll off in M at thinner foil thicknesses, which is seen in Figure 7-8, can be explained by the peak of both the entering and exiting spectrum falling above the peak in the cross-section, as seen Figure 7-9. In order to achieve the benefit of a thinner foil, the gas pressure or the depth of the target must be increased.

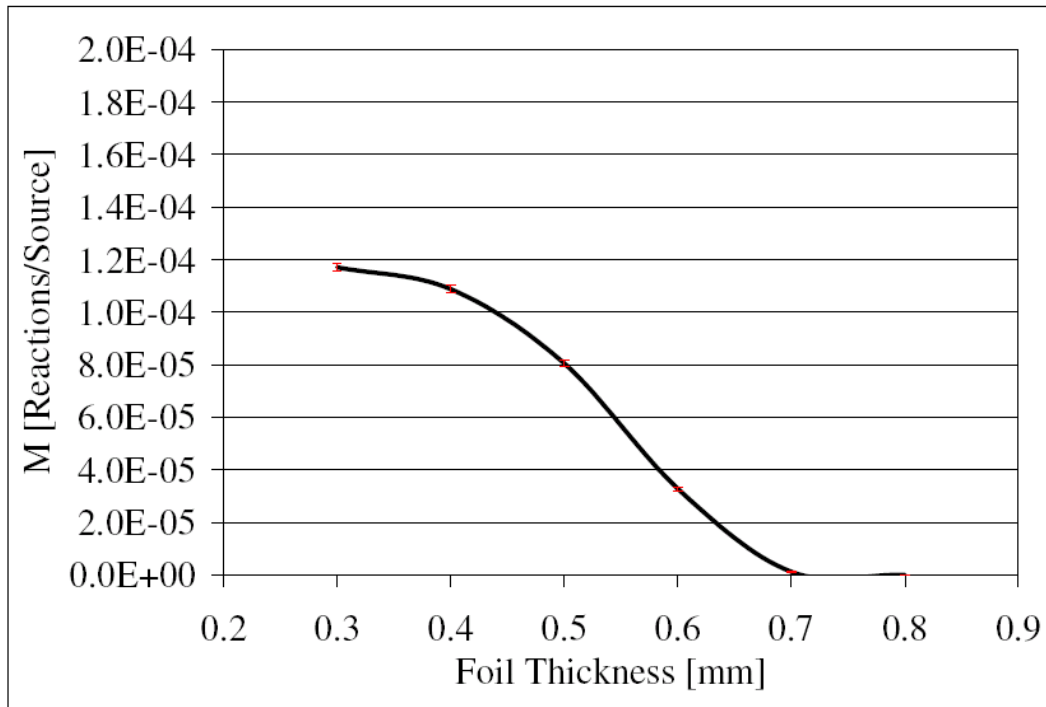


Figure 7-8: Multiplication factor, M, is reduced by increasing the Ti foil thickness. The gas pressure and cell depth held constant at 4 atm and 77.5 mm.

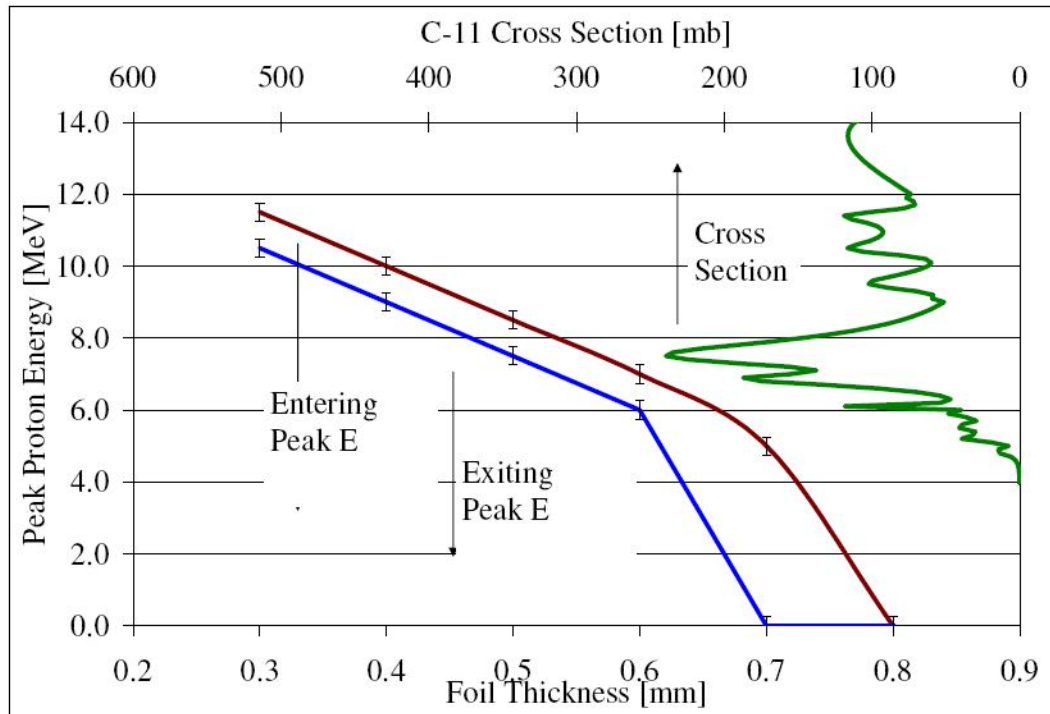


Figure 7-9: Comparison of peak proton energy entering (after Ti foil) and exiting the gas (after Ti foil and gas) as a function of foil thickness with the cross-section of the  $^{14}\text{N}(\text{p}, \alpha)^{11}\text{C}$  reaction. Gas pressure and cell depth held constant at 4 atm and 77.5 mm.

### 7.3.5. Results of the optimized case (10 atm, 0.3 mm)

Going to the extremes of the design space, a case was analyzed at 10 atm of gas pressure and 0.3 mm of Ti foil. This gave a maximum activity of 390 nCi at a D- $^3\text{He}$  fusion rate of  $2 \times 10^7$  p/s. This was an improvement of nearly a factor of 40 over the baseline case. Unfortunately, it is unlikely 0.3 mm of Ti can mechanically withstand the force exerted by 10 atm of gas. Since M is a function of pressure and distance, the depth of the gas target could be increased to achieve this optimization while maintaining its mechanical integrity.

## 7.4. Finite element analysis of mechanical strength and prototype testing

The MCNPX simulation showed the importance of maximizing the gas pressure and target thickness while minimizing the metal foil thickness. The values of these parameters were limited by the mechanical strength of the foil and support grids. To investigate this

limit, a finite element analysis (FEA) was performed using CosmoWorks<sup>®</sup> and a small prototype was built and pressure tested.

Titanium was chosen for the foil material since it had the best balance between low proton stopping power, high tensile strength and high melting point for commonly available materials. Aluminum, molybdenum, tungsten, and stainless steel were also considered. Melting of the metal foil by focused electron jets was a concern and was experienced by Weidner [4] in an aluminum version of his design. Weidner overcame this by switching to stainless steel. The melting point of Ti is 1650 °C, which is higher than common stainless steels at approximately 1350 °C. Therefore, Ti should perform at least equally as well as the stainless steel used by Weidner.

The FEA was a useful tool in developing the design of the stainless steel support grids. The mechanical strengths of several iterations were modeled. The final model was predicted to have a safety factor of 2.

A smaller version of the isotope panel was prototyped for mechanical pressure testing. A picture of the prototype is shown in Figure 7-10. It had a length of 18.6 cm, width of 10.1 cm, depth of 4 cm and a Ti foil thickness of 0.5 mm. It was filled with water and pressurized to 7 atm. No failures were detected and the maximum deflection was 1.6 mm. Since the actual unit will be installed in vacuum, the maximum test pressure is equivalent to 6 atm. This test validated the FEA model and showed that the concept was capable of meeting the mechanical requirements.

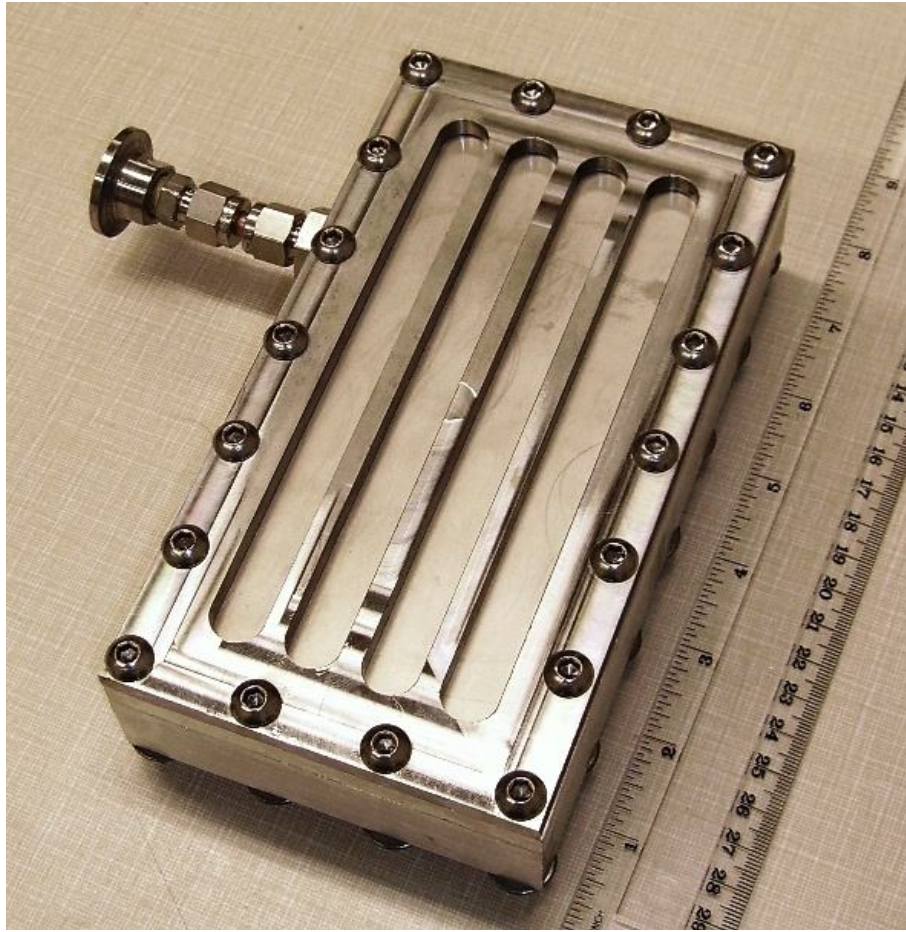


Figure 7-10: Picture of prototype gas target

### **7.5. Conclusions for the production of PET Radioisotopes in an IEC fusion device**

With the MCNPX simulation, FEA, prototype testing, and the previous proof-of-concept isotope production experiments of Cipiti [5] and Weidner [4] it can be concluded that the commercial production of radioisotopes in an IEC fusion device is feasible. With the present laboratory scale IEC device the production of approximately 400 nCi of  $^{11}\text{C}$  is possible. Scaling from the laboratory experiments to commercial systems requires an increase in the D- $^3\text{He}$  fusion reaction rate. This can be done by increasing the input power into the device and through advanced IEC concepts currently being pursued at the UW IEC laboratory. This simulation and modeling work has provided a valuable roadmap of the parameters required for producing medical radioisotopes in a D- $^3\text{He}$  nuclear fusion based device.

## 7.6. References for Chapter 7

- 
1. Cherry, S. R., Sorenson, J. A., & Phelps, M. E. (Eds.). (2003). *Physics in nuclear medicine* (3rd ed.). Philadelphia, Pennsylvania: Saunders.
  2. EGLE, B. J., SANTARIUS, J. F., & KULCINSKI, G. L, (2007). Comparison of spherical and cylindrical cathode geometries in IEC devices, *Fusion Science and Technology*, **52**, 4, 1110
  3. MCNPX Version 2.5.0 User's Manual, LA-CP-05-0369, Los Alamos National Laboratories, Los Alamos, New Mexico
  4. Weidner, J. W. (2003). The production of N-13 from inertial electrostatic confinement fusion. (M.S. dissertation, University of Wisconsin - Madison).
  5. Cipiti, B. B. (2004). The fusion of advanced fuels to produce medical isotopes using inertial electrostatic confinement. (PhD dissertation, University of Wisconsin – Madison)



## Chapter 8. Conclusions

This dissertation has experimentally explored the use of six spherically converging focused ion beams as a possible avenue for increasing the nuclear fusion reaction rate of advanced fuels (D-D and D-<sup>3</sup>He) to the levels required for several non-electric applications of nuclear fusion technology. The Six Ion Gun Fusion Experiment is the first experiment in over 40 years to recreate the seminal 1967 results of Hirsch. The careful design and fabrication of the SIGFE device provided confidence in the accuracy of the data collected and allowed a large parameter space to be explored. The SIGFE showed that virtual potential well structures, suggested by the Hirsch results, were not a significant mechanism for D-D fusion in the SIGFE device at total cathode currents below 30 mA and cathode voltages between -50 kV and -150 kV. Several major conclusions drawn from this dissertation are summarized below:

- 1) The SIGFE device met its engineering goals. The six ion beams of the SIGFE device were aligned to within 0.2 mm of each other, and were able to be focused to beam widths of less than 2 mm at cathode voltages ranging from -50 kV to -150 kV, at total cathode currents ranging from 2 mA to 30 mA and at chamber pressures from 5 mPa to 270 mPa.
- 2) The experimentally extracted ion current from each ion gun module was within approximately a factor of two of the theoretically predicted maximum value.
- 3) The SIGFE matched the Hirsch device as the most efficient steady-state IEC device in the world at the time of this writing. With the ion beams defocused, the SIGFE and Hirsch neutron production rates were identical. The maximum steady-state D-D

neutron production rate in the SIGFE was  $4.2 \times 10^7$  neutrons per second at a cathode voltage of -130 kV and a total cathode current of 10 mA; this was  $3.2 \times 10^7$  neutrons per second per kilowatt of high-voltage input power.

- 4) The D-D neutron rate in the SIGFE was highly dependent on the focusing of the ion beams. At a cathode voltage of -100 kV and total cathode current of 10 mA, the neutron rate varied from  $2.2 \times 10^7$  n/s to  $5.5 \times 10^6$  n/s as the ion beams were focused and defocused from the center of the device.
- 5) The D-D neutron rate in the SIGFE scaled linearly with the total cathode current within the parameter space explored. The neutron rate scaling with the total cathode current was independent of ion beam focusing, gas pressure, and cathode voltage.
- 6) Within the parameter space of this dissertation, less than 0.2% of the D-D fusion reactions occurred inside a 9.5 mm spherical volume at the center of the SIGFE cathode. Therefore, the formation of virtual potential well structures or other space-charge related physics that could occur at the center of the SIGFE device is not a significant source of fusion reactions at total cathode currents below 30 mA.
- 7) D- $^3$ He fusion reactions were produced in the SIGFE. The D- $^3$ He fusion reaction rate measured by the proton detector in a D- $^3$ He environment scaled similarly to the D-D fusion protons measured in a pure D-D environment. In both cases, the collimation of the proton detectors constrained the volume from which the fusion protons could be

observed to only a 9.5 mm diameter spherical volume at the center of the SIGFE cathode.

- 8) A concept was developed and evaluated, and an initial prototype was built for the production of radioisotopes from the 14.7 MeV D-<sup>3</sup>He fusion protons in an IEC device. Monte Carlo simulations of this concept determined that a D-<sup>3</sup>He fusion rate on the order of  $10^{11} \text{ s}^{-1}$  would be required for an IEC device to produce 1 mCi of the PET radioisotope <sup>11</sup>C.

The SIGFE device and the work of this dissertation has expanded upon the seminal IEC experiments of Hirsch by first matching the results of the previous work and then by using improved experimental capabilities to help explain the mechanism by which the SIGFE device is more efficient at producing D-D and D-<sup>3</sup>He fusion reactions than the other IEC experiments to date. This work has explored a possible avenue for developing IEC technology for several non-electric applications and will presumably help guide future work in this field.



## Chapter 9. Recommendation for future work

The conclusion that the formation of virtual potential well structures was not a significant mechanism for the production of D-D fusion in the SIGFE was limited to total cathode currents below 30 mA. The 1997 Ohnishi [1] paper predicted that virtual potential wells would not form below a certain threshold ion current. Above this threshold, Ohnishi predicted power law scaling of the neutron rate with current to powers as high as 3. Therefore, the most interesting next step for the SIGFE is to increase the available ion current and to search for this threshold.

Even at 10 mA, the SIGFE was plagued by overheating problems. To reach the currents required to form a potential well structure, which is anticipated to be ~1 A, several upgrades will be required. First, the ion gun modules will have to be operated in a pulsed mode. Even with relatively short pulses, upgrades to the extraction lenses will have to be performed to handle the heat load. The boron nitride grade HP spacers between the extraction and plasma lenses should be replaced with boron nitride grade AX05. AX05 has a maximum operating temperature of 1800 °C, which is 650 °C higher than HP. The AX05 also has a heat transfer coefficient approaching that of stainless steel, which is a factor of 4 higher than HP; this will allow the extraction lens to be conductively cooled by the water cooled plasma tube. It will have to be determined if the existing filament-assisted ion source will be able to supply the required ion current even in a pulsed mode.

The second major opportunity for the SIGFE is to determine the spatial distribution of the D-D fusion reactions within the entire SIGFE chamber. This dissertation determined that the center of the SIGFE cathode was not a major source of D-D neutrons, but did not definitively determine what the dominant mechanism of fusion was or where it was located.

The best way to determine this would be to build a collimated neutron detector that could scan the entire volume of the device from outside the vacuum chamber.

To determine the spatial distribution of the D-D fusion protons at the millimeter scale, the movable proton detector described in section 4.3.3 needs to be upgraded to improve its ratio of proton signal to x-ray signal. This could be accomplished by building a miniature version of the FIDO diagnostic using permanent magnets. With small aperture sizes the protons would only have to be bent through a few degrees to move the detector out of the line-of-sight of the x-rays. The counting statistics of this diagnostic would likely not be high enough to reliably determine the energy spectrum of the ions, but it would give a clean proton count. The device would likely be compact enough to be placed on a movable stage inside the vacuum chamber and be used to determine, with millimeter level accuracy, the origin of D-D protons. Both the mini-FIDO collimated proton detector and the collimated neutron detector would be useful on multiple experiments, not just the SIGFE.

## References for Chapter 9

- 
1. Ohnishi, M., Sato, K. H., Yamamoto, Y., & Yoshikawa, K. (1997). Correlation between potential well structure and neutron production in inertial electrostatic confinement fusion. *Nuclear Fusion*, 37(5), 611-619.